JSCSEN 86(1)1–113(2021)

ISSN 1820-7421(Online)

Journal of the Serbian Chemical Society

Electronic version

VOLUME 86

No 1

BELGRADE 2021

Available on line at

www.shd.org.rs/JSCS/

The full search of JSCS is available through

DOAJ DIRECTORY OF OPEN ACCESS JOURNALS

www.doaj.org

The **Journal of the Serbian Chemical Society** (formerly Glasnik Hemijskog društva Beograd), one volume (12 issues) per year, publishes articles from the fields of chemistry. The **Journal** is financially supported by the **Ministry of Education, Science and Technological Development of the Republic of Serbia.**

Articles published in the **Journal** are indexed in **Clarivate Analytics products: Science Citation Index-Expanded™** – accessed *via* **Web of Science®** and **Journal Citation Reports®**.

Impact Factor announced 2020: **1.097; 5-year Impact Factor**: **1.023**.

Articles appearing in the **Journal** are also abstracted by: **Scopus, Chemical Abstracts Plus (CAplus℠), Directory of Open Access Journals, Referativnii Zhurnal (VINITI), RSC Analytical Abstracts, EuroPub, Pro Quest** and **Asian Digital Library.**

Publisher:	**Serbian Chemical Society**, Karnegijeva 4/III, P. O. Box 36, 1120 Belgrade 35, Serbia tel./fax: +381–11–3370–467, E-mails: **Society** – shd@shd.org.rs; **Journal** – jscs@shd.org.rs Home Pages: **Society** – http://www.shd.org.rs/, **Journal** – http://www.shd.org.rs/JSCS/
Internet Service:	Contents, Abstracts and full papers (from Vol 64, No. 1, 1999) are available in the electronic form at the Web Site of the **Journal** (http://www.shd.org.rs/JSCS/).
Former Editors:	**Nikola A. Pušin** (1930–1947), **Aleksandar M. Leko** (1948–1954), **Panta S. Tutundžić** (1955**–**1961), **Miloš K. Mladenović** (1962–1964), **Đorđe M. Dimitrijević** (1965–1969), **Aleksandar R. Despić** (1969–1975), **Slobodan V. Ribnikar** (1975–1985), **Dragutin M. Dražić** (1986–2006).
Editor-in-Chief:	BRANISLAV Ž. **NIKOLIĆ**, Serbian Chemical Society (E-mail: jscs-ed@shd.org.rs)
Deputy Editor:	DUŠAN **SLADIĆ**, Faculty of Chemistry, University of Belgrade
Sub editors:	
Organic Chemistry	DEJAN **OPSENICA**, Institute of Chemistry, Technology and Metallurgy, University of Belgrade JÁNOS **CSANÁDI**, Faculty of Science, University of Novi Sad
Biochemistry and Biotechnology	OLGICA **NEDIĆ**, INEP – Institute for the Application of Nuclear Energy, University of Belgrade
Inorganic Chemistry	MILOŠ **ĐURAN**, Serbian Chemical Society
Theoretical Chemistry	IVAN **JURANIĆ**, Serbian Chemical Society
Physical Chemistry	LJILJANA **DAMJANOVIĆ-VASILIĆ**, Faculty of Physical Chemistry, University of Belgrade
Electrochemistry	SNEŽANA **GOJKOVIĆ**, Faculty of Technology and Metallurgy, University of Belgrade
Analytical Chemistry	SLAVICA **RAŽIĆ**, Faculty of Pharmacy, University of Belgrade
Polymers	BRANKO **DUNJIĆ**, Faculty of Technology and Metallurgy, University of Belgrade
Thermodynamics	MIRJANA **KIJEVČANIN**, Faculty of Technology and Metallurgy, University of Belgrade
Chemical Engineering	TATJANA **KALUĐEROVIĆ RADOIČIĆ**, Faculty of Technology and Metallurgy, University of Belgrade
Materials	RADA **PETROVIĆ**, Faculty of Technology and Metallurgy, University of Belgrade
Metallic Materials and Metallurgy	NENAD **RADOVIĆ**, Faculty of Technology and Metallurgy, University of Belgrade
Environmental and Geochemistry	VESNA **ANTIĆ**, Faculty of Agriculture, University of Belgrade
History of and Education in Chemistry	DRAGICA **TRIVIĆ**, Faculty of Chemistry, University of Belgrade
English Language Editors:	LYNNE **KATSIKAS**, Serbian Chemical Society VLATKA **VAJS**, Serbian Chemical Society JASMINA **NIKOLIĆ**, Faculty of Technology and Metallurgy, University of Belgrade
Technical Editors:	VLADIMIR **PANIĆ**, ALEKSANDAR **DEKANSKI**, VUK **FILIPOVIĆ**, Institute of Chemistry, Technology and Metallurgy, University of Belgrade
Journal Manager & Web Master:	ALEKSANDAR **DEKANSKI,** Institute of Chemistry, Technology and Metallurgy, University of Belgrade
Office:	VERA **ĆUŠIĆ**, Serbian Chemical Society

Editorial Board

From abroad: **R. Adžić**, Brookhaven National Laboratory (USA); **A. Casini**, University of Groningen (The Netherlands); **G. Cobb**, Baylor University (USA); **D. Douglas**, University of British Columbia (Canada); **G. Inzelt**, Etvos Lorand University (Hungary); **N. Katsaros**, NCSR "Demokritos", Institute of Physical Chemistry (Greece); **J. Kenny**, University of Perugia (Italy); **Ya. I. Korenman**, Voronezh Academy of Technology (Russian Federation); **M. D. Lechner**, University of Osnabrueck (Germany); **S. Macura**, Mayo Clinic (USA); **M. Spiteller**, INFU, Technical University Dortmund (Germany); **M. Stratakis**, University of Crete (Grecce); **M. Swart**, University de Girona (Cataluna, Spain); **G. Vunjak-Novaković**, Columbia University (USA); **P. Worsfold**, University of Plymouth (UK); **J. Zagal**, Universidad de Santiago de Chile (Chile).

From Serbia: **B. Abramović**, **V. Antić, V. Beškoski**, **J. Csanadi**, **Lj. Damjanović-Vasilić**, **A. Dekanski**, **V. Dondur**, **B. Dunjić**, **M. Đuran, S. Gojković**, **I. Gutman**, **B. Jovančićević**, **I. Juranić**, **L. Katsikas**, **M. Kijevčanin**, **V. Leovac**, **S. Milonjić**, **V.B. Mišković-Stanković, O. Nedić**, **B. Nikolić**, **J. Nikolić, D. Opsenica**, **V. Panić**, **M. Petkovska**, **R. Petrović**, **I. Popović**, **B. Radak**, T. **Kaluđerović Radiočić, N. Radović**, **S. Ražić**, **D. Sladić**, **S. Sovilj**, **S. Šerbanović**, **B. Šolaja**, **Ž. Tešić**, **D. Trivić, V. Vajs**.

Subscription: The annual subscription rate is **150.00 €** including postage (surface mail) and handling. For Society members from abroad rate is **50.00 €**. For the proforma invoice with the instruction for bank payment contact the Society Office (E-mail: shd@shd.org.rs) or see JSCS Web Site: http://www.shd.org.rs/JSCS/, option Subscription.

Godišnja pretplata: Za članove SHD: **2.500,00 RSD**, za penzionere i studente: **1000,00 RSD**, a za ostale: **3.500,00 RSD**:za organizacije i ustanove: **16.000,00 RSD**. Uplate se vrše na tekući račun Društva: **205-13815-62**, poziv na broj **320**, sa naznakom "pretplata za JSCS".

Nota: Radovi čiji su svi autori članovi SHD prioritetno se publikuju.

Odlukom Odbora za hemiju Republičkog fonda za nauku Srbije, br. 66788/1 od 22.11.1990. godine, koja je kasnije potvrđena odlukom Saveta Fonda, časopis je uvršten u kategoriju međunarodnih časopisa (**M-23**). Takođe, aktom Ministarstva za nauku i tehnologiju Republike Srbije, 413-00-247/2000-01 od 15.06.2000. godine, ovaj časopis je proglašen za publikaciju od posebnog interesa za nauku. **Impact Factor** časopisa objavljen 2020. godine iznosi **1,097**, a petogodišnji **Impact Factor 1,023**.

Publication of this issue is generously supported
by Ivanka Popović, who shared her
“Hemofarm Foundation Excellence Award 2020”
with the Serbian Chemical Society.

Impact Factor anounced 2020: **1.097**; **Five-Year Impact Factor**: **1.023**
Impakt faktor objavljen 2020 iznosi **1,097**, a **petogodišnji impakt faktor** 1,023

INSTRUCTIONS FOR AUTHORS (2021)

GENERAL

The *Journal of the Serbian Chemical Society* (the *Journal* in further text) is an international journal publishing papers from all fields of chemistry and related disciplines. Twelve issues are published annually. The Editorial Board expects the editors, reviewers, and authors to respect the well-known standard of professional ethics.

Types of Contributions

Original scientific papers	(up to 15 typewritten pages, including Figures, Tables and References) report original research which must not have been previously published.
Short communications	(up to 8 pages) report unpublished preliminary results of sufficient importance to merit rapid publication.
Notes	(up to 5 pages) report unpublished results of short, but complete, original research
Authors' reviews	(up to 40 pages) present an overview of the author's current research with comparison to data of other scientists working in the field
Reviews[a]	(up to 40 pages) present a concise and critical survey of a specific research area. Generally, these are prepared at the invitation of the Editor
Surveys	(about 25 pages) communicate a short review of a specific research area.
Book and Web site reviews	(1 - 2 pages)
Extended abstracts	(about 4 pages) of Lectures given at meetings of the Serbian Chemical Society Divisions
Letters to the Editor	report miscellaneous topics directed directly to the Editor

[a]Generally, Authors' reviews, Reviews and Surveys are prepared at the invitation of the Editor.

Submission of manuscripts

Manuscripts should be submitted using the **OnLine Submission Form**, available on the JSCS Web Site (**http://www.shd-pub.org.rs/index.php/JSCS**). The manuscript must be uploaded as a Word.doc or .rtf file, with tables and figures (including the corresponding captions – above Tables and below Figures), placed within the text to follow the paragraph in which they were mentioned for the first time.

Please note that **Full Names (**First Name, Last Name), **Full Affiliation** and **Country** (from drop down menu) of **ALL OF AUTHORS** (written in accordance with English spelling rules - the first letter capitalized) must be entered in the manuscript Submission Form (Step 3). Manuscript Title, authors' names and affiliations, as well as the Abstract, **WILL APPEAR** in the article listing, as well as in **BIBLIOGRAPHIC DATABASES (WoS, SCOPUS...)**, in the form and in the order entered in the author details

Graphical abstract

Graphical abstract is a one-image file containing the main depiction of the authors work and/or conclusion and must be supplied along with the manuscript. It must enable readers to quickly gain the main message of the paper and to encourage browsing, help readers identify which papers are most relevant to their research interests. Authors must provide an image that clearly represents the research described in the paper. The most relevant figure from the work, which summarizes the content, can also be submitted. The image should be submitted as a separate file in **Online Submission Form - Step 2**.

Specifications: The graphical abstract should have a clear start and end, reading from top to bottom or left to right. Please omit unnecessary distractions as much as possible.

- **Image size:** minimum of 500×800 pixels (W×H) and a minimum resolution of 300 dpi. If a larger image is sent, then please use the same ratio: 16 wide × 9 high. Please note that your image will be scaled proportionally to fit in the available window in TOC; a 150x240 pixel rectangle. Please be sure that the quality of an image cannot be increased by changing the resolution from lower to higher, but only by rescanning or exporting the image with a higher resolution, which can be set in usual "settings" option.
- **Font:** Please use Calibri and Symbol font with a large enough font size, so it is readable even from the image of a smaller size (150 × 240 px) in TOC.
- **File type:** JPG and PNG only.

No additional text, outline or synopsis should be included. Please do not use white space or any heading within the image.

Cover Letter

Manuscripts must be accompanied by a cover letter (strictly uploaded in **Online Submission Step 2**) in which the type of the submitted manuscript and a warranty as given below are given. The Author(s) has(have) to warranty that the manuscript submitted to the *Journal* for review is original, has been written by the stated author(s) and has not been published elsewhere; is currently not being considered for publication by any other journal and will not be submitted for such a review while under review by the *Journal*; the manuscript contains no libellous or other unlawful statements and does not contain any materials that violate any personal or proprietary rights of any other person or entity. All manuscripts will be acknowledged on receipt (by e-mail).

Illustrations

Illustrations (Figs, schemes, photos…) in TIF or EPS format (JPG format is acceptable for colour and greyscale photos, only), must be additionally uploaded (Online Submission Step 2) as a separate file or one archived (.zip, .rar or .arj) file. Figures and/or Schemes should be prepared according to the **Artwork Instructions -** http://www.shd.org.rs/JSCS/jscs-pdf/Artwork_Instructions.pdf!

For any difficulties and questions related to **OnLine Submission Form -** https://www.shd-pub.org.rs/index.php/JSCS/submission/wizard, please refer to **User Guide -** https://openjournal-systems.com/ojs-3-user-guide/ , Chapter **Submitting an Article -** https://openjournalsystems.com/ojs-3-user-guide/submitting-an-article/. If difficulties still persist, please contact JSCS Editorial Office at **JSCS@shd.org.rs**

A manuscript not prepared according to these instructions will be returned for resubmission without being assigned a reference number.

Conflict-of-Interest Statement*: Public trust in the peer review process and the credibility of published articles depend in part on how well a conflict of interest is handled during writing, peer review, and editorial decision making. A conflict of interest exists when an author (or the author's institution), reviewer, or editor has financial or personal relationships that inappropriately influence (bias) his or her actions (such relationships are also known as dual commitments, competing interests, or competing loyalties). These relationships vary from those with negligible potential to those with great potential to influence judgment, and not all relationships represent true conflict of interest. The potential for a conflict of interest can exist whether or not an individual believes that the relationship affects his or her scientific judgment. Financial relationships (such as employment, consultancies, stock ownership, honoraria, paid expert testimony) are the most easily identifiable conflicts of interest and the most likely to undermine the credibility of the journal, the authors, and of science itself. However, conflicts can occur for other reasons, such as personal relationships, academic competition, and intellectual passion.

Informed Consent Statement*: Patients have a right to privacy that should not be infringed without informed consent. Identifying information, including patients' names, initials, or hospital numbers, should not be published in written descriptions, photographs, and pedigrees unless the information is essential for scientific purposes and the patient (or parent or guardian) gives written informed consent for publication. Informed consent for this purpose requires that a patient who is identifiable be shown the manuscript to be published. Authors should identify Individuals who provide writing assistance and disclose the funding source for this assistance. Identifying details should be omitted if they are not essential. Complete anonymity is difficult to achieve, however, and informed consent should be obtained if there is any doubt. For example, masking the eye region in photographs of patients is inadequate protection of anonymity. If identifying characteristics are altered to protect anonymity, such as in genetic pedigrees, authors should provide assurance that alterations do not distort scientific meaning and editors should so note. The requirement for informed consent should be included in the journal's instructions for authors. When informed consent has been obtained it should be indicated in the published article.

Human and Animal Rights Statement* When reporting experiments on human subjects, authors should indicate whether the procedures followed were in accordance with the ethical standards of the responsible committee on human experimentation (institutional and national) and with the Helsinki Declaration of 1975, as revised in 2000 (5). If doubt exists whether the research was conducted in accordance with the Helsinki Declaration, the authors must explain the rationale for their approach, and demonstrate that the institutional review body explicitly approved the doubtful aspects of the study. When reporting experiments on animals, authors should be asked to indicate whether the institutional and national guide for the care and use of laboratory animals was followed.

---

*International Committee of Medical Journal Editors ("Uniform Requirements for Manuscripts Submitted to Biomedical Journals"), February 2006

PROCEDURE

All contributions will be peer reviewed and only those deemed worthy and suitable will be accepted for publication. The Editor has the final decision. To facilitate the reviewing process, authors are encouraged to suggest up to three persons competent to review their manuscript. Such suggestions will be taken into consideration but not always accepted. If authors would prefer a specific person not be a reviewer, this should be announced. The Cover Letter must be accompanied by these suggestions. Manuscripts requiring revision should be returned according to the requirement of the Editor, within 60 days upon reception of the reviewing comments by e-mail.

The *Journal* maintains its policy and takes the liberty of correcting the English as well as false content of manuscripts **provisionally accepted** for publication in the first stage of reviewing process. In this second stage of manuscript preparation by JSCS Editorial Office, the author(s) may be required to supply some **additional clarifications and corrections**. This procedure will be executed during copyediting actions, with a demand to author(s) to perform corrections of unclear parts before the manuscript would be published OnLine as **finally accepted manuscript (OLF Section of the JSCS website)**. Please note that the manuscript can receive the status of **final rejection** if the author's corrections would not be satisfactory.

When finally accepted manuscript is ready for printing, the corresponding author will receive a request for proof reading, which should be performed within 2 days. Failure to do so will be taken as the authors agree with any alteration which may have occurred during the preparation of the manuscript for printing.

Accepted manuscripts of active members of the Serbian Chemical Society (all authors) have publishing priority.

MANUSCRIPT PRESENTATION

Manuscripts should be typed in English (either standard British or American English, but consistent throughout) with 1.5 spacing (12 points Times New Roman; Greek letters in the character font Symbol) in A4 format leaving 2.5 cm for margins. For Regional specific, non-standard characters that may appear in the text, save documents with Embed fonts Word option: *Save as -> (Tools) -> Save Options… -> Embed fonts in the text.*

The authors are requested to seek the assistance of competent English language expert, if necessary, to ensure their English is of a reasonable standard. The Serbian Chemical Society can provide this service in advance of submission of the manuscript. If this service is required, please contact the office of the Society by e-mail (jscs-info@shd.org.rs).

Tables, figures and/or schemes must be embedded in the main text of the manuscript and should follow the paragraph in which they are mentioned for the first time. **Tables** must be prepared with the aid of the **WORD table function**, without vertical lines. The minimum size of the font in the tables should be **10 pt**. Table columns must not be formatted using multiple spaces. Table rows must not be formatted using any returns (enter key; ↵ key) and are **limited to 12 cm width**. Tables should not be incorporated as graphical objects. **Footnotes to Tables** should follow them and are to be indicated consequently (in a single line) in superscript letters and separated by semi-column.

Table caption must be placed above corresponding Table, while **Captions of the Illustrations** (Figs. Schemes...) must follow the corresponding item. **The captions, either for Tables or Illustrations**, should make the items comprehensible without reading of the main text (but clearly referenced in), must follow numerical order (Roman for Tables, Arabic for Illustrations), and should not be provided on separate sheets or as separate files.

High resolution Illustrations (named as Fig. 1, Fig. 2… and/or Scheme 1, Scheme 2…) in **TIF or EPS format** (JPG format is acceptable for photos, only) **must be additionally uploaded as a separate files or one archived (.zip, .rar) file.**

Illustrations should be prepared according to the ARTWORK INSTRUCTIONS - http://www.shd.org.rs/JSCS/jscs-pdf/Artwork_Instructions.pdf. **!**

All pages of the manuscript must be numbered continuously.

DESIGNATION OF PHYSICAL QUANTITIES AND UNITS

IUPAC recommendations for the naming of compounds should be followed. SI units, or other permissible units, should be employed. The designation of physical quantities must be in italic throughout the text (including figures, tables and equations), whereas the units and indexes (except for indexes having the meaning of physical quantities) are in upright letters. They should be in Times New Roman font. In graphs and tables, a slash should be used to separate the designation of a physical quantity from the unit

(example: p / kPa, j / mA cm^{-2}, t / °C, T_0 / K, τ / h, ln (j / mA cm^{-2})…). Designations such as: p (kPa), t [min]…, are not acceptable. However, if the full name of a physical quantity is unavoidable, it should be given in upright letters and separated from the unit by a comma (example: Pressure, kPa; Temperature, K; Current density, mA cm^{-2}…). Please do not use the axes of graphs for additional explanations; these should be mentioned in the figure captions and/or the manuscript (example: "pressure at the inlet of the system, kPa" should be avoided). The axis name should follow the direction of the axis (the name of y-axis should be rotated by 90°). Top and right axes should be avoided in diagrams, unless they are absolutely necessary.

Latin words, as well as the names of species, should be in *italic*, as for example: *i.e.*, *e.g.*, *in vivo*, *ibid*, *Calendula officinalis* L., *etc*. The branching of organic compound should also be indicated in *italic*, for example, *n*-butanol, *tert*-butanol, *etc*.

Decimal numbers must have decimal points and not commas in the text (except in the Serbian abstract), tables and axis labels in graphical presentations of results. Thousands are separated, if at all, by a comma and not a point.

Mathematical and chemical equations should be given in separate lines and must be numbered, Arabic numbers, consecutively in parenthesis at the end of the line. All equations should be embedded in the text Complex equations (fractions, integrals, matrix…) should be prepared with the aid of the **Microsoft Equation 3.0** (or higher) or **MathType** (Do not use them to create simple equations and labels). **Using the Insert -> Equation option, integrated in MS Office 2010 and MS Office 2013, as well as insertion of equation objects within paragraph text IS NOT ALLOWED.**

ARTICLE STRUCTURE

- TITLE PAGE;
- MAIN TEXT – including Tables and Illustrations with corresponding captions;
- SUPPLEMENTARY MATERIAL (optional**)**

Title page

- **Title** in bold letters, should be clear and concise, preferably 12 words or less. The use of non-standard abbreviations, symbols and formulae is discouraged.
- AUTHORS' NAMES in capital letters with the full first name, initials of further names separated by a space and surname. Commas should separate the author's names except for the last two names when 'and' is to be used. In multi-affiliation manuscripts, the author's affiliation should be indicated by an Arabic number placed in superscript after the name and before the affiliation. Use * to denote the corresponding author(s).
- *Affiliations* should be written in italic. The e-mail address of the corresponding author should be given after the affiliation(s).
- *Abstract:* A one-paragraph abstract written of 150 – 200 words in an impersonal form indicating the aims of the work, the main results and conclusions should be given and clearly set off from the text. Domestic authors should also submit, on a separate page, an Abstract - Izvod, the author's name(s) and affiliation(s) in Serbian (Cyrillic letters). (Домаћи аутори морају доставити Извод (укључујући имена аутора и афилијацију) на српском језику, исписане ћирилицом, иза Захвалнице, а пре списка референци.) For authors outside Serbia, the Editorial Board will provide a Serbian translation of their English abstract.
- *Keywords:* Up to 6 keywords should be given. Do not use words appearing in the manuscript title
- RUNNING TITLE: A one line (maximum five words) short title in capital letters should be provided.

Main text – should have the form:

- **INTRODUCTION,**
- **EXPERIMENTAL (RESULTS AND DISCUSSION),**
- **RESULTS AND DISCUSSION (EXPERIMENTAL),**
- **CONCLUSIONS,**
- **NOMENCLATURE (optional) and**
- ***Acknowledgements*: If any.**
- REFERENCES (Citation of recent papers published in chemistry journals that highlight the significance of work to the general readership is encouraged.)

The sections should be arranged in a sequence generally accepted for publication in the respective fields. They subtitles should be in capital letters, centred and NOT numbered.

- The INTRODUCTION should include the aim of the research and a concise description of background information and related studies directly connected to the paper.
- The EXPERIMENTAL section should give the purity and source of all employed materials, as well as details of the instruments used. The employed methods should be described in sufficient detail to enable experienced persons to repeat them. Standard procedures should be referenced and only modifications described in detail. On no account should results be included in the experimental section.

Chemistry

Detailed information about instruments and general experimental techniques should be given in all necessary details. If special treatment for solvents or chemical purification were applied that must be emphasized.

Example: Melting points were determined on a Boetius PMHK or a Mel-Temp apparatus and were not corrected. Optical rotations were measured on a Rudolph Research Analytical automatic polarimeter, Autopol IV in dichloromethane (DCM) or methanol (MeOH) as solvent. IR spectra were recorded on a Perkin-Elmer spectrophotometer FT-IR 1725X. ^{1}H and ^{13}C NMR spectra were recorded on a Varian Gemini-200 spectrometer (at 200 and 50 MHz, respectively), and on a Bruker Ultrashield Advance III spectrometer (at 500 and 125 MHz, respectively) employing indicated solvents (*vide infra*) using TMS as the internal standard. Chemical shifts are expressed in ppm (δ / ppm) values and coupling constants in Hz (J / Hz). ESI-MS spectra were recorded on Agilent Technologies 6210 Time-Of-Flight LC-MS instrument in positive ion mode with CH_3CN/H_2O 1/1 with 0.2 % HCOOH as the carrying solvent solution. Samples were dissolved in CH_3CN or MeOH (HPLC grade purity). The selected values were as follows: capillary voltage = 4 kV, gas temperature = 350 °C, drying gas flow 12 L min^{-1}, nebulizer pressure = 310 kPa, fragmentator voltage = 70 V.The elemental analysis was performed on the Vario EL III- C,H,N,S/O Elemental Analyzer (Elementar Analysensysteme GmbH, Hanau-Germany). Thin-layer chromatography (TLC) was performed on precoated Merck silica gel 60 F254 and RP-18 F254 plates. Column chromatography was performed on Lobar LichroPrep Si 60 (40-63 μm), RP-18 (40-63 μm) columns coupled to a Waters RI 401 detector, and on Biotage SP1 system with UV detector and FLASH 12+, FLASH 25+ or FLASH 40+ columns pre packed with KP-SIL [40-63 μm, pore diameter 6 nm (60 Å)], KP-C18-HS (40-63 μm, pore diameter 9 nm (90 Å) or KP-NH [40-63 μm, pore diameter 10 nm (100 Å)] as adsorbent. Compounds were analyzed for purity (HPLC) using a Waters 1525 HPLC dual pump system equipped with an Alltech, Select degasser system, and dual λ 2487 UV-VIS detector. For data processing, Empower software was used (methods A and B). Methods C and D: Agylent Technologies 1260 Liquid Chromatograph equipped with Quat Pump (G1311B), Injector (G1329B) 1260 ALS, TCC 1260 (G1316A) and Detector 1260 DAD VL+ (G1315C). For data processing, LC OpenLab CDS ChemStation software was used. For details, see Supporting Information.

1. Synthesis experiments

Each paragraph describing a synthesis experiment should begin with the name of the product and any structure number assigned to the compound in the Results and Discussions section. Thereafter, the compound should be identified by its structure number. Use of standard abbreviations or unambiguous molecular formulas for reagents and solvents, and of structure numbers rather than chemical names to identify starting materials and intermediates, is encouraged.

When a new or improved synthetic method is described, the yields reported in key experimental examples, and yields used for comparison with existing methods, should represent amounts of isolated and purified products, rather than chromategraphically or spectroscopically determined yields. Reactant quantities should be reported in weight and molar units and for product yields should be reported in weight units; percentage yields should only be reported for materials of demonstrated purity. When chromatography is used for product purification, both the support and solvent should be identified.

2. Microwave experiments

Reports of syntheses conducted in microwave reactors must clearly indicate whether sealed or open reaction vessels were used and must document the manufacturer and model of the reactor, the method of monitoring the reaction mixture temperature, and the temperature-time profile. Reporting a wattage rating or power setting is not an acceptable alternative to providing temperature data. Manuscripts describing work done with domestic (kitchen) microwave ovens will not be accepted except for studies where the unit is used for heating reaction mixtures at atmospheric pressure.

3. Compound characterization

The Journal upholds a high standard for compound characterization to ensure that substances being added to the chemical literature have been correctly identified and can be synthesized in known yield and purity by the reported preparation and isolation methods. For **all new** compounds, evidence adequate to establish both **identity** and **degree of purity** (homogeneity) must be provided.

Identity *- Melting point.* All homogeneous solid products (*e.g.* not mixtures of isomers) should be characterized by melting or decomposition points. The colors and morphologies of the products should also be noted.

Specific rotations. Specific rotations based on the equation $[\alpha]^t; D = (100\ \alpha) / (l\ c)$ should be reported as unitless numbers as in the following example: $[\alpha]^{20}$; D = -25.4 (c 1.93, $CHCl_3$), where c / g mL^{-1} is concentration and l / dm is path length. The units of the specific rotation, (deg mL) / (g dm), are implicit and are not included with the reported value.

Spectra/*Spectral Data.* Important IR adsorptions should be given.

For all new diamagnetic substances, NMR data should be reported (^1H, ^{13}C, and relevant heteronuclei). ^1H NMR chemical shifts should be given with two digits after the decimal point. Include the number of protons represented by the signal, signal multiplicity, and coupling constants as needed (J italicized, reported with up to one digit after the decimal). The number of bonds through which the coupling is operative, ^xJ, may be specified by the author if known with a high degree of certainty. ^{13}C NMR signal shifts should be rounded to the nearest 0.01 ppm unless greater precision is needed to distinguish closely spaced signals. Field strength should be noted for each spectrum, not as a comment in the general experimental section. Hydrogen multiplicity (C, CH, CH_2, CH_3) information obtained from routine DEPT spectra should be included. If detailed signal assignments are made, the type of NOESY or COSY methods used to establish atom connectivity and spatial relationships should be identified in the Supporting Information. Copies of spectra should also be included where structure assignments of complex molecules depend heavily on NMR interpretation. Numbering system used for assignments of signals should be given in the Supporting Information with corresponding general structural formula of named derivative.

HPLC/LCMS can be substituted for biochemistry papers where the main focus is not on compound synthesis.

HRMS/*elemental analysis.* To support the molecular formula assignment, HRMS data accurate within 5 ppm, or combustion elemental analysis [carbon and hydrogen (and nitrogen, if present)] data accurate within 0.5 %, should be reported for new compounds. HRMS data should be given in format as is usually given for combustion analysis: calculated mass for given formula following with observed mass: (+)ESI-HRMS *m*/*z*: [molecular formula + H]$^+$ calculated mass, observed mass. Example: (+)ESI-HRMS *m*/*z*: calculated for [$C_{13}H_8BrCl_2N$ + H^+] 327.92899, observed 327.92792.

NOTE: in certain cases, a crystal structure may be an acceptable substitute for HRMS/elemental analysis.

Biomacromolecules. The structures of biomacromolecules may be established by providing evidence about sequence and mass. Sequences may be inferred from the experimental order of amino acid, saccharide, or nucleotide coupling, from known sequences of templates in enzyme-mediated syntheses, or through standard sequencing techniques. Typically, a sequence will be accompanied by MS data that establish the molecular weight.

Example: Product was isolated upon column chromatography [dry flash (SiO_2, eluent EA, EA/MeOH gradient 95/5 → 9/1, EA/MeOH/NH_3 gradient 18/0.5/0.5 → 9/1/1, and flash chromatography (Biotage SP1, RP column, eluent MeOH/H_2O gradient 75/25 → 95/5, N-H column, eluent EA/Hex gradient 6/3 → EA). was obtained after flash column chromatography (Biotage SP NH column, eluent hexane/EA 4:6 → 2:6). Yield 968.4 mg (95 %). Colorless foam softens at 96-101 °C. $[\alpha]^{20}$; D = +0,163 (c =2.0×10^{-3} g/mL, CH_2Cl_2). IR (ATR): 3376w, 2949m, 2868w, 2802w, 1731s, 1611w, 1581s, 1528m, 1452m, 1374s, 1331w, 1246s, 1171m, 1063w, 1023m, 965w, 940w, 881w, 850w, 807w, cm^{-1}. ^1H NMR (500 MHz, $CDCl_3$, δ): 8.46 (*d*, 1H, J = 5.4, H-2'), 7.89 (*s*, 1H, J = 2.0, H-8'), 7.71 (*d*, 1H, J = 8.9, H-5'), 7.30 (*dd*, 1H, J_1 = 8.8, J_2 = 2.1, H-6'), 6.33 (*d*, 1H, J = 5.4, H-3'), 6.07 (*s*, HN-Boc, exchangeable with D_2O), 5.06 (*s*, 1H, H-12), 4.92-4.88 (*m*, 1H, H-7), 4.42 (*bs*, H-3), 3.45 (*s*,CH_3-N), 3.33 (*bs*, H-9'), 3.05-2.95 (*m*, 2H, H-11'), 2.70-2.43 (*m*, 2H, H-24) and HN, exchangeable with D_2O), 2.07 (*s*, CH_3COO), 2.04 (*s*, CH_3COO), 1.42 (*s*, 9H, $(CH_3)_3C$-N(Boc)), 0.88 (*s*, 3H, CH_3-10), 0.79 (*d*, 3H,J = 6.6, CH_3-20), 0.68 (*s*, 3H, CH_3-13). ^{13}C NMR (125 MHz, $CDCl_3$, δ): 170.34, 170.27, 151.80, 149.92, 148.87, 134.77, 128.36, 125.11, 121.43, 117.29, 99.98, 75.41, 70.82, 50.43, 49.66, 47.60, 47.33, 44.97, 43.30, 41.83, 41.48, 37.65, 36.35, 35.44, 34.89,

34.19, 33.23, 31.24, 28.79, 28.35, 27.25, 26.45, 25.45, 22.74, 22.63, 21.57, 21.31, 17.85, 12.15. (+)ESI-HRMS (*m/z*): calculated for $[C_{45}H_{67}ClN_4O_6 + H]^+$ 795.48219, observed 795.48185. Combustion analysis for $C_{45}H_{67}ClN_4O_6$: Calculated. C 67.94, H 8.49, N 7.04; found C 67.72, H 8.63, N 6.75. HPLC purity: method A: RT 1.994, area 99.12 %; method C: RT 9.936, area 98.20 %.

Purity **-** Evidence for documenting compound purity should include one or more of the following:

a) Well-resolved high field 1D ^{1}H NMR spectrum showing at most only trace peaks not attributable to the assigned structure and a standard 1D proton-decoupled ^{13}C NMR spectrum. Copies of the spectra should be included as figures in the Supporting Information.
b) Quantitative gas chromatographic analytical data for distilled or vacuum-transferred samples, or quantitative HPLC analytical data for materials isolated by column chromatography or separation from a solid support. HPLC analyses should be performed in two diverse systems. The stationary phase, solvents (HPLC), detector type, and percentage of total chromatogram integration should be reported; a copy of the chromatograms may be included as a figure in the Supporting Information.
c) Electrophoretic analytical data obtained under conditions that permit observing impurities present at the 5 % level.

HRMS data may be used to support a molecular formula assignment **but cannot be used as a criterion of purity**.

4. Biological Data

Quantitative biological data are required for all tested compounds. Biological test methods must be referenced or described in sufficient detail to permit the experiments to be repeated by others. Detailed descriptions of biological methods should be placed in the experimental section. Standard compounds or established drugs should be tested in the same system for comparison. Data may be presented as numerical expressions or in graphical form; biological data for extensive series of compounds should be presented in tabular form. Tables consisting primarily of negative data will not usually be accepted; however, for purposes of documentation they may be submitted as supporting information. Active compounds obtained from combinatorial syntheses should be resynthesized and retested to verify that the biology conforms to the initial observation.

Statistical limits (statistical significance) for the biological data are usually required. If statistical limits cannot be provided, the number of determinations and some indication of the variability and reliability of the results should be given. References to statistical methods of calculation should be included. Doses and concentrations should be expressed as molar quantities (*e.g.*, mol/kg, μmol/kg, M, mM). The routes of administration of test compounds and vehicles used should be indicated, and any salt forms used (hydrochlorides, sulfates, *etc.*) should be noted. The physical state of the compound dosed (crystalline, amorphous; solution, suspension) and the formulation for dosing (micronized, jet-milled, nanoparticles) should be indicated. For those compounds found to be inactive, the highest concentration (*in vitro*) or dose level (*in vivo*) tested should be indicated.

- The RESULTS AND DISCUSSION should include concisely presented results and there significance discussed and compared to relevant literature data. The results and discussion may be combined or kept separate.
- The inclusion of a CONCLUSION section, which briefly summarizes the principal conclusions, is recommended.
- NOMENCLATURE is optional but, if the authors wish, a list of employed symbols may be included.
- REFERENCES should be numbered sequentially as they appear in the text. Please note that any reference numbers appearing in the Illustrations and/or Tables and corresponding captions must follow the numbering sequence of the paragraph in which they appear for the first time. When cited, the reference number should be superscripted in Font 12, following any punctuation mark. In the reference list, they should be in normal position followed by a full stop. Reference entry must not be formatted using Carriage returns (enter key; ↵ key) or multiple space key. The formatting of references to published work should follow the *Journal'*s style as follows:

Journals[a]:	A. B. Surname1, C. D. Surname2, *J. Serb. Chem. Soc.* **Vol** (Year) first page Number (https://doi.org/doi)[b]
Books:	A. B. Surname1, C. D. Surname2, *Name of Book*, Publisher, City, Year, pp. 100-101 (https://doi.org/doi)[b]
Compilations:	A. B. Surname1, C. D. Surname2, in *Name of Compilation*, A. Editor1, C. Editor2, Ed(s)., Publisher, City, Year, p. 100 (https://doi.org/doi)[b]
Proceedings:	A. B. Surname1, C. D. Surname2, in *Proceedings of Name of the Conference or Symposium*, (Year), Place of the Conference, Country, *Title of the Proceeding*, Publisher, City, Year, p. or Abstract No. 100
Patents:	A. B. Inventor1, C. D. Inventor2, (Holder), Country Code and patent number (registration year)
Chemical Abstracts:	A. B. Surname1, C. D. Surname2, *Chem. Abstr*. CA 234 567a; For non-readily available literature, the Chemical Abstracts reference should be given in square brackets: [C.A. 139/2003 357348t] after the reference
Standards:	EN ISO 250: *Name of the Standard* (Year)
Websites:	Title of the website, URL in full (date accessed)

[a] When citing Journals, the International Library Journal abbreviation is required. Please consult, *e.g.*, https://images.webofknowledge.com/WOK46/help/WOS/A_abrvjt.html

[b] doi should be replaced by doi number of the Article, for example: http://dx.doi.org/10.2298/JSC161212085B (as active link). If doi do not exist, provide the link to the online version of the publication.

Only the last entry in the reference list should end with a full stop.

The names of all authors should be given in the list of references; the abbreviation *et al.* may only be used in the text. The original journal title is to be retained in the case of publications published in any language other than English (please denote the language in parenthesis after the reference). Titles of publications in non-Latin alphabets should be transliterated. Russian references are to be transliterated using the following transcriptions:

ж→zh, х→kh, ц→ts, ч→ch, ш→sh, щ→shch, ы→y, ю→yu, я→ya, э→e, й→i, ь→’.

Supplementary material

Authors are encouraged to presentthe information and results non-essential to the understanding of their paper as SUPPLEMENTARY MATERIAL (can be uploaded inStep 4 of Online Submission). This material may include as a rule, but is not limited to, the presentation of analytical and spectral data demonstrating the identity and purity of synthesized compounds, tables containing raw data on which calculations were based, series of figures where one example would remain in the main text, etc. The Editorial Board retain the right to assign such information and results to the Supplementary material when deemed fit. Supplementary material does not appear in printed form but can be downloaded from the web site of the JSCS.

Mathematical and chemical equations should be given in separate lines and must be numbered, Arabic numbers, consecutively in parenthesis at the end of the line. All equations should be embedded in the text Complex equations (fractions, integrals, matrix…) should be prepared with the aid of the Microsoft Equation 3.0 (or higher) or MathType (Do not use them to create simple equations and labels). Using the Insert -> Equation option, integrated in MS Office 2010 and MS Office 2013, as well as insertion of equation objects within paragraph text IS NOT ALLOWED.

Deposition of crystallographic data

Prior to submission, the crystallographic data included in a manuscript presenting such data should be deposited at the appropriate database. Crystallographic data associated with organic and metal-organic structures should be deposited at the Cambridge Crystallographic Data Centre (CCDC) by e-mail to **deposit@ccdc.cam.ac.uk**

Crystallographic data associated with inorganic structures should be deposited with the Fachinformationszentrum Karlsruhe (FIZ) by e-mail to **crysdata@fiz-karlsruhe.de**. A deposition number will then be provided, which should be added to the reference section of the manuscript.

For detailed instructions please visit the JSCS website:
https://www.shd-pub.org.rs/index.php/JSCS/Instructions

ARTWORK INSTRUCTIONS

JSCS accepts only **TIFF** or **EPS** formats, as well as **JPEG** format (only for colour and greyscale photographs) for electronic artwork and graphic files. **MS files** (Word, PowerPoint, Excel, Visio) **NOT acceptable**. Generally, scanned instrument data sheets should be avoided. Authors are responsible for the quality of their submitted artwork. Every single Figure or Scheme, as well as any part of the Figure (A, B, C…) should be prepared according to following instructions (every part of the figure, A, B, C…, must be submitted as an independent single graphic file):

TIFF

Virtually all common artwork and graphic creation software is capable of saving files in TIFF format. This 'option' can normally be found under 'the 'Save As...' or 'Export...' commands in the 'File' menu.

TIFF (Tagged Image File Format) is the recommended file format for bitmap, greyscale and colour images.

- Colour images should be in the RGB mode
- When supplying TIFF files, please ensure that the files are supplied at the correct resolution:
    1. Line artwork: minimum of 1000 dpi
    2. RGB image: minimum of 300 dpi
    3. Greyscale image: minimum of 300 dpi
    4. Combination artwork (line/greyscale/RGB): minimum of 500 dpi
- Images should be tightly cropped, without frame and any caption.
- If applicable please re-label artwork with a font supported by JSCS (Arial, Helvetica, Times, Symbol) and ensure it is of an appropriate font size.
- Save an image in TIFF format with LZW compression applied.
- It is recommended to remove Alpha channels before submitting TIFF files.
- It is recommended to flatten layers before submitting TIFF files.

Please be sure that quality of an image cannot be increased by changing the resolution from lower to higher, but only by rescanning or exporting the image with higher resolution, which can be set in usual "settings" facilities.

EPS

Virtually all common artwork creation software, such as Canvas, ChemDraw, CorelDraw, SigmaPlot, Origin Lab…, are capable of saving files in EPS format. This 'option' can normally be found under the 'Save As...' or 'Export...' commands in the 'File' menu.

For vector graphics, EPS (Encapsulated PostScript) files are the preferred format as long as they are provided in accordance with the following conditions:

- when they contain bitmap images, the bitmaps should be of good resolution (see instructions for TIFF files)
- when colour is involved, it should be encoded as RGB
- an 8-bit preview/header at a resolution of 72 dpi should always be included
- embed fonts should always included and only the following fonts should be used in artwork: Arial, Helvetica, Times, Symbol
- the vertical space between the parts of an illustration should be limited to the bare necessity for visual clarity
- no data should be present outside the actual illustration area
- line weights should range from 0.35 pt to 1.5 pt
- when using layers, they should be reduced to one layer before saving the image (Flatten Artwork)

JPEG

Virtually all common artwork and graphic creation software is capable of saving files in JPEG format. This 'option' can normally be found under 'the 'Save As...' or 'Export...' commands in the 'File' menu.

JPEG (Joint Photographic Experts Group) is the acceptable file format **only for colour and greyscale photographs**. JPEG can be created with respect to photo quality (low, medium, high; from 1 to 10), ensuring file sizes are kept to a minimum to aid easy file transfer. Images should have a minimum resolution of 300 dpi. Image width: minimum 3.0 cm; maximum 12.0 cm.

Please be sure that quality of an image cannot be increased by changing the resolution from lower to higher, but only by rescanning or exporting the image with higher resolution, which can be set in usual "settings" facilities.

SIZING OF ARTWORK

- JSCS aspires to have a uniform look for all artwork contained in a single article. Hence, it is important to be aware of the style of the journal.
- Figures should be submitted in black and white or, if required, colour (charged). If coloured figures or photographs are required, this must be stated in the cover letter and arrangements made for payment through the office of the Serbian Chemical Society.
- As a general rule, the lettering on an artwork should have a finished, printed size of 11 pt for normal text and no smaller than 7 pt for subscript and superscript characters. Smaller lettering will yield a text that is barely legible. This is a rule-of-thumb rather than a strict rule. There are instances where other factors in the artwork, (for example, tints and shadings) dictate a finished size of perhaps 10 pt. Lines should be of at least 1 pt thickness.
- When deciding on the size of a line art graphic, in addition to the lettering, there are several other factors to address. These all have a bearing on the reproducibility/readability of the final artwork. Tints and shadings have to be printable at the finished size. All relevant detail in the illustration, the graph symbols (squares, triangles, circles, *etc*.) and a key to the diagram (to explain the explanation of the graph symbols used) must be discernible.
- The sizing of halftones (photographs, micrographs,...) normally causes more problems than line art. It is sometimes difficult to know what an author is trying to emphasize on a photograph, so you can help us by identifying the important parts of the image, perhaps by highlighting the relevant areas on a photocopy. The best advice that can be given to graphics suppliers is not to over-reduce halftones. Attention should also be paid to magnification factors or scale bars on the artwork and they should be compared with the details inside. If a set of artwork contains more than one halftone, again please ensure that there is consistency in size between similar diagrams.

General sizing of illustrations which can be used for the Journal of the Serbian Chemical Society:

- Minimum fig. size: 30 mm width
- Small fig. size - 60 mm width
- Large fig. size - 90 mm width
- Maximum fig. size - 120 mm width

Pixel requirements (width) per print size and resolution for bitmap images:

	Image width	A	B	C
Minimal size	30 mm	**354**	**591**	**1181**
Small size	60 mm	**709**	**1181**	**2362**
Large size	90 mm	**1063**	**1772**	**3543**
Maximal size	120 mm	**1417**	**2362**	**4724**

A: 300 dpi > RGB or Greyscale image
B: 500 dpi > Combination artwork (line/greyscale/RGB)
C: 1000 dpi> Line artwork

The designation of physical quantities and graphs formatting

The designation of physical quantities on figures must be in italic, whereas the units are in upright letters. They should be in Times New Roman font. In graphs a slash should be used to separate the designation of a physical quantity from the unit (example: p / kPa, t °C, T_0 / K, τ / h, ln (j / mA cm^{-2})…). Designations such as: p (kPa), t [min]…, are not acceptable. However, if the full name of a physical quantity is unavoiable, it should be given in upright letters and separated from the unit by a comma (example: Pressure, kPa, Temperature, K…). Please do not use the axes of graphs for additional explanations; these should be mentioned in the figure captions and/or the manuscript (example: "pressure at the inlet of the system, kPa" should be avoided). The axis name should follow the direction of the axis (the name of y-axis should be rotated by 90°). Top and right axes should be avoided in diagrams, unless they are absolutely necessary. Decimal numbers must have decimal points and not commas in the axis labels in graphical presentations of results. Thousands are separated, if at all, by a comma and not a point.

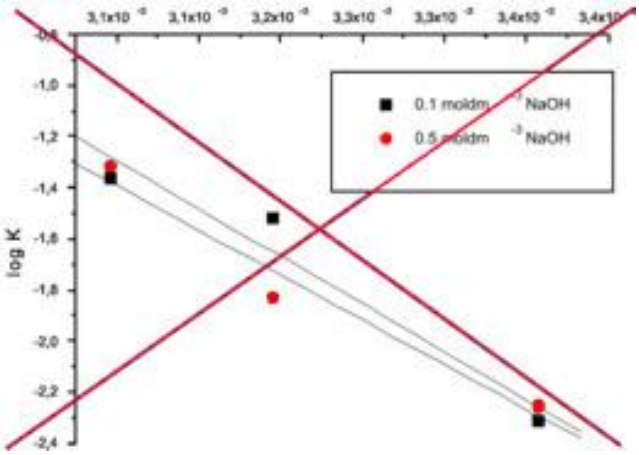

INCORRECT

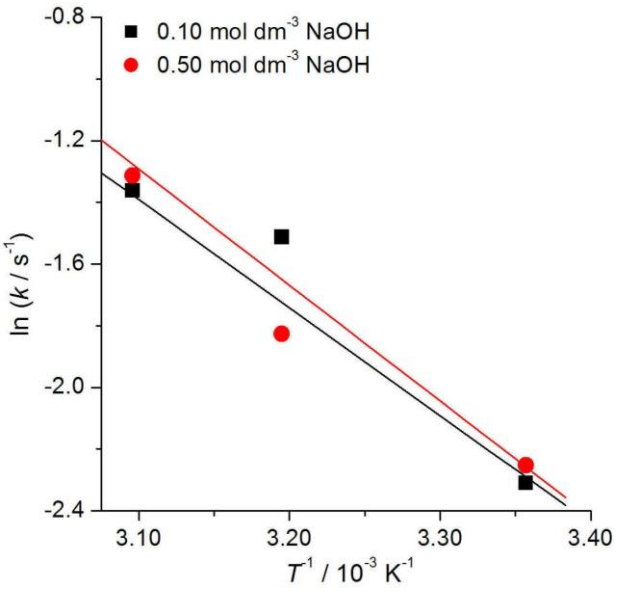

CORRECT

Journal of the Serbian Chemical Society
JSCS-info@shd.org.rs • www.shd.org.rs/JSCS

J. Serb. Chem. Soc. Vol. 86, No. 1 (2021)

CONTENTS*

Published by the Serbian Chemical Society
Karnegijeva 4/III, P.O. Box 36, 11120 Belgrade, Serbia
Printed by the Faculty of Technology and Metallurgy
Karnegijeva 4, P.O. Box 35-03, 11120 Belgrade, Serbia

* For colored figures in this issue please see electronic version at the Journal Home Page: http://www.shd.org.rs/JSCS/

Journal of the Serbian Chemical Society
JSCS-info@shd.org.rs • www.shd.org.rs/JSCS
J. Serb. Chem. Soc. *86* (1) 1–23 (2021)
JSCS–5400
Survey

Polymeric nanocomposites for innovative functional enhancement of electrodes and proton exchange membrane in microbial fuel cell

ABDUL AZEEZ OLAYIWOLA SIRAJUDEEN and M. SUFFIAN M. ANNUAR*

Institute of Biological Sciences, Faculty of Science, University of Malaya, 50603, Kuala Lumpur, Malaysia

(Received 2 April, revised 2 September, accepted 7 September 2020)

Abstract: Practical application of microbial fuel cell (MFC), a sustainable energy device, is hampered by low power output. Its principal components *i.e.*, anode, cathode and proton exchange membrane (PEM) are the focus of enhancement and modification in terms of their functional design and material. The anode surface conduciveness as electron sink is crucial to the power output magnitude, while the cathode electrode should be reactive for efficient oxygen reduction at tri-phase junction. PEM is solely responsible for unidirectional proton flow concomitantly completing the electrical circuit. Polymeric nanocomposites as electrode modifier improved significantly anode/cathode/PEM functions thus overall MFC performance. The review highlights the progress made in polymer-based modifications to anode, cathode and PEM material and function between year 2014 to 2019. The effects to biocompatibility, surface area, internal resistance, electrochemical activities, environmental sustainability and overall MFC performance are discussed.

Keywords: anode; cathode; proton exchange membrane; microbial fuel cell; polymeric nanocomposites.

CONTENT

* Corresponding author. E-mail: suffian_annuar@um.edu.my
https://doi.org/10.2298/JSC200402054S

1. INTRODUCTION

The increase in global energy demand due to expanding population and vigorous industrialization has resulted in the search for alternative energy sources that are renewable and ecologically friendly. Energy from fossil fuel are non--renewable, fast depleting and polluting from environmental perspectives. Alternative energy sources, which are green and renewable such as hydrogen fuel,[1] biodiesel,[2] bioethanol[3] and microbial fuel cell (MFC),[4] are among the focus of intensive research. One of the many possible solutions lies with non-combustion method such as microbial fuel cell. An MFC is a sustainable, promising and nascent energy generation device that combines electricity generation and wastewater treatment through metabolic activities of microorganisms such as *Escherichia coli*, *Geobacter sulfurreducens* and *Shewanella oneidensis*.[5,6] Its basic design is a two-chambered MFC consists of anode and cathode chambers, and a selective membrane designated as proton exchange membrane (PEM), Fig. 1. Typical anolyte compositions include wastewater, glucose, phosphate buffer, specifically-prepared anolyte containing appropriate amounts of K_2HPO_4, KH_2PO_4, $NaCl_2$, $NaHCO_3$, NH_4Cl, $MgSO_4{\cdot}7H_2O$, $CaCl_2{\cdot}2H_2O$ and trace element. Commonly utilized catholyte include phosphate buffer solution, ferricyanide solution, H_2O_2 amongst others. In anode compartment, electrons and hydrogen ions are liberated by the electrogens from biological oxidation of organic matters.[7] The electrons are transferred to the cathode chamber *via* electrical circuit and the protons pass through PEM for oxygen reduction reaction on the cathode surface, thus completing the redox mechanism.[7,8] By-products are also produced, *e.g.*, hydrogen peroxide (H_2O_2)[9] and caustic potash (KOH)[10,11] at the cathode chamber (Fig. 1).

The two known mechanisms utilized by electrogens for electron transfer to anode surface are direct electron transfer through conductive pili or cytochrome *c* (commonly used by *G. sulfurreducens* and *S. oneidensis*), and mediated electron transfer through secreted redox mediators (commonly used by *E. coli*). Modification of the anode electrode with polymeric nanocomposites has been reported to reduce internal resistance and improve overall MFC performance arising from more efficient extracellular transfer of electrons to the anode surface.[12–16] A detail review article addressing anode modifications for improved MFC perform-

ance has been presented by Hindatu *et al.*[12] Recent anode modifications with polymeric nanomaterials are discussed herewith.

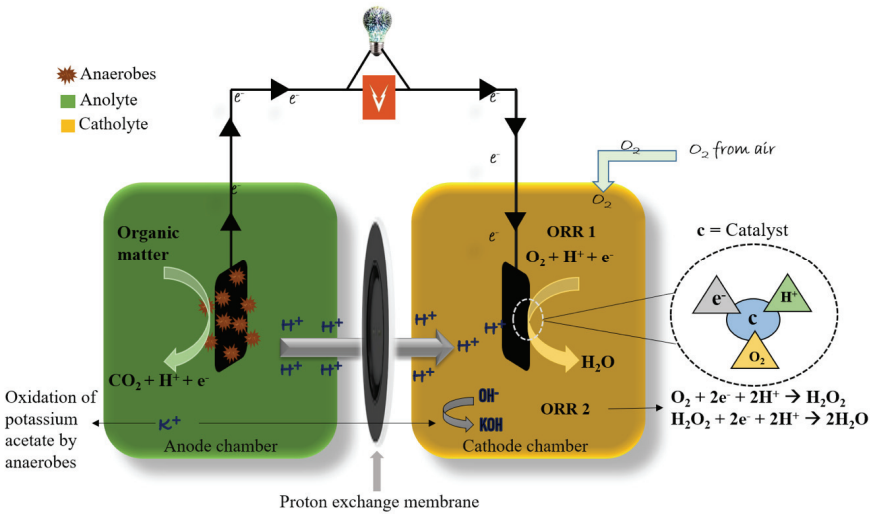

Fig. 1. Schematic overview of a double-chambered MFC.

2. ANODE MODIFICATION WITH POLYMERIC NANOMATERIALS

The anode chamber structure and function are a vital part of MFC set-up. Electrochemically-active bacteria oxidize organic matter liberating electrons and protons in the process. Efficient transfer of electrons to anode surface is crucial to the power output, hence generating overall MFC performance. An efficient anode electrode should support for maximum biofilm colonization and with high affinity as an electron sink. Electrical conductivity, durability and stability, large surface area and porosity amongst others are primary characteristics of a working anode electrode in MFC.[17–19] Carbon-based nanomaterials have been reported to satisfy these requirements to some extent. However, the hydrophobic nature of these materials strongly hinders maximum bacterial colonization of anode electrode.[20,21] As such, polymeric nanocomposites of polyesters, conducting polymers and polysaccharides have been studied as anode electrode modifier with some degree of success as discussed in the following sections.

3. NANOCOMPOSITES OF CONDUCTING POLYMERS

3.1. Polypyrrole (PPy)

One widely studied conducting polymer for MFC application is polypyrrole (PPy). Kaur *et al.*[22] modified the surface of carbon paper with both pristine and functionalized PPy. The PPy-modified electrode improves the voltage output, the start-up time and stability of maximum voltage generated. Further modification

of PPy with reduced graphene oxide (rGO) nanocomposites (Fig. 2) doubled the power density and recorded a maximum voltage of 400 mV for about 75 h attributed to superior biofilm growth on the modified electrode.[23]

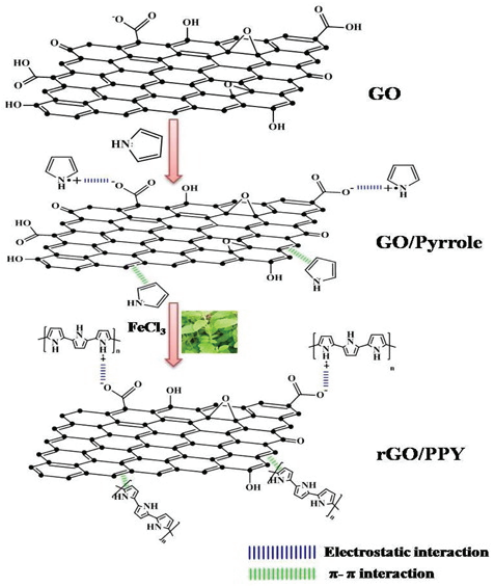

Fig. 2. Proposed mechanism for the preparation of the rGO/PPy composite (reproduced from[23] with permission from American Chemical Society).

One-step electrochemical method is recently employed by Li *et al.*[24] to synthesize PPy nanowires and composited it with graphene oxide (GO). The modified anode electrode exhibits functionally superior surface area, improved power density and higher open circuit voltage (OCV). The performance of stainless steel (SS) is significantly enhanced when layered with PPy.[25] It results in power density increase of 29-times higher than bare SS anode electrode and a maximum voltage of 547 mV compared to bare SS anode electrode (76 mV).[25]

3.2. Polyaniline (PANI)

PANI is another conducting polymer widely utilized as anode modifier. Cyclic voltammetry (CV) method has been employed in preparing PANI composited with multi-walled carbon nanotube (MWCNT) through electropolymerization.[26] Maximum voltage of almost one volt is recorded with power density of 286 mW/m^2. Bifunctional catalyst of graphene (G) and TiO_2 with PANI on carbon paper (CP) enhances the performance of MFC.[27] The modified electrode shows nearly triple higher power density than plain CP. The internal resistance is reduced by half with the modified electrode set-up. The superior performance is attributed to efficient extracellular electron transfer to anode from favorable colonization of the anode by the bacteria (Fig. 3). Recently, Li *et al.*[28] modified

carbon cloth (CC) electrode surface *in situ* using PANI composited with titanium suboxide (TS) and graphene nanoparticles.

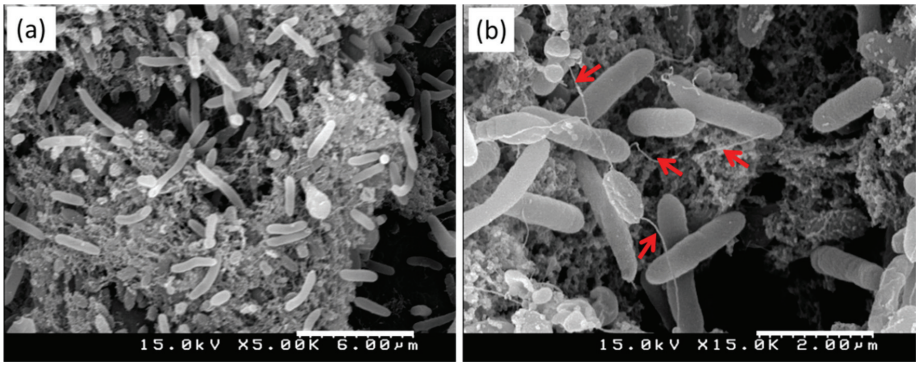

Fig. 3. *Shewanella oneidensis* MR1 morphology enclosed within the matrix of the PANI–TiO_2–GN catalyst at higher and lower magnifications. The red arrows indicate the nanowires of *Shewanella oneidensis* MR1 (reproduced from[27] with permission from *American Chemical Society*).

Longevity in maximum voltage output in modified electrode is evidenced with 13-fold increase in power density compared to bare CC. About 70 % decrease in internal resistance is recorded in PANI-TSG/CC electrode set-up. Similarly, Yellappa *et al.*[29] synthesized PANI and PANI/CNT nanoparticles through *in situ* oxidative chemical polymerization, and applied over stainless steel mesh (SSM) surface for wastewater treatment. PANI/CNT-SSM electrode yields 80 % chemical oxygen demand (COD) removal while 65 % is recorded for PANI–SSM and 58 % for bare SSM. Higher OCV is also recorded for polymeric modified electrodes compared to bare SSM. The superiority in PANI/CNT-SSM electrode is attributed to enhanced charge transfer due to incorporation of CNT, which subsequently promotes better conductivity between biocatalyst and anode surface. The studies of Yin *et al.*[30] have shown a synergistic effect between TiO_2 nanosheets (TiN) and PANI through electrochemical deposition of PANI onto TiN, at different CV cycles. Maximum power density up to 63.6 % increase is recorded for PANI deposited through 20 CV cycles. Lowest charge transfer resistance is also recorded by the modified electrode with 20 CV cycles.

3.3. Poly(3,4-ethylene dioxythiophene) (PEDOT)

PEDOT is a derivative of polythiophene with superior conductivity compared to PPy and PANI,[31] also has potential as excellent electrode modifier in MFC. Ma *et al.*[32] modified the surface of SS with PEDOT through electrochemical polymerization method. PEDOT/SS electrode recorded six-fold increase in power density compared to bare SS electrode. The current density recorded during MFC operation leveled off at 1150 mA/m^2 for PEDOT/SS compared to

210 mA/m^2 for SS electrode (Fig. 4). The efficiency of PEDOT/SS electrode is attributed to dense and conductive film formed on SS plate which not only prevent SS base from biogenic and chemical corrosion, but also improve the electron transport rate to anode.

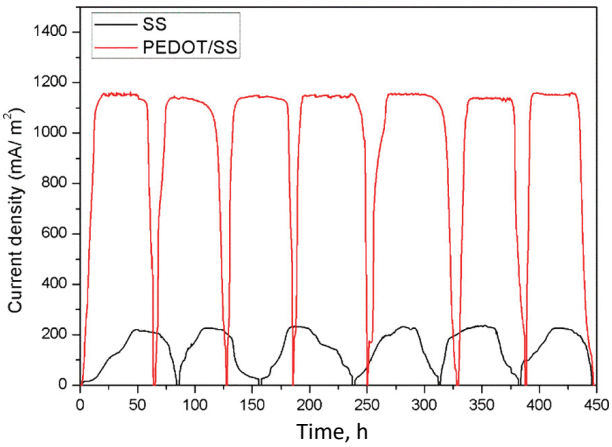

Fig. 4. Power generation in MFCs with an external resistance of 1000 Ω (reproduced from[32] with permission from *American Chemical Society*).

Recently, Senthikumar *et al.*[33] modified PEDOT with nickel ferrite nano-rod on biochar as a free-standing electrode. A maximum power density of 1200 mW/m^2 is recorded, *i.e.*, five times higher than control (ferric oxide on biochar). Further modification of PEDOT polymer matrix with nanoparticles of nickel and rGO (PEDOT/Ni/rGO) results in a power density up to 3200 mW/m^2 and improve internal resistance and OCV.[34] The improved performance of modified electrode is due to homogenous dispersion of the nanoparticles within PEDOT matrix and enhanced biocompatibility between biocatalyst, *i.e.*, *E. coli* and PEDOT/Ni/ /rGO electrode surface.

3.4. Nanocomposites of polyesters

Polymers with ester functional groups in their main chain are classified as polyesters. Due to their biocompatibility, biodegradability, piezoelectricity, elasticity, durability and resistivity to most chemicals, polyesters have been recently used as anode electrode modifier. Its first utilization in MFC is reported by Luckarift *et al.*[35] when 3-polyhydroxybutyrate-*co*-3-hydroxyvalerate (PHBV) is composed with carbon nanofiber by solvent casting method (Fig. 5). Superior biofilm colonization of the modified anode surface results in efficient bioelectrocatalysis, stability and reproducibility in electrolyte with significant power density generation compared to previously reported graphite felt electrode. Hindatu *et al.*[4] reported the utilization of flexible medium-chain-length polyhydroxyalkanoates

(mcl-PHA) composed of multi-walled carbon nanotube (MWCNT) as CC surface modifier. Maximum power density up to 53 % increase, internal resistance reduction of 31 % and improved maximum voltage of 50 % are recorded for mcl PHA-MWCNT composite modified electrode compared to pristine CC electrode. Interestingly, further modification of CC surface with amphiphilic mcl-PHA-*co*--polyethylene glycol methacrylate/MWCNT composite (mcl-PHA-*co*-PEGMA/ /MWCNT) further reduce the internal resistance by 97 %, improve the maximum voltage by 75 %, and 74 % enhancement in maximum power density.[13] It is hypothesized that the superiority in mcl-PHA-*co*-PEGMA/MWCNT electrode originates from its better biocompatibility and synergistic relationship between the *Escherichia coli* biocatalyst and the modified anode surface. Recently, Sirajudeen *et al.* [16] modified the surface of purified CC with amphiphilic mcl-PHA--*co*-methyl acrylate composed of functionalized MWCNT as electrode modifier. The modified anode electrode shows improved conductivity, superior redox peak, stable and elevated voltage and enhanced power and current densities, attributed to improved electron transfer rate on modified anode surface.[16] Polycaprolactone (PCL) nano- and micro-fibers have also been composed of gold particles and utilized as anode modifier.[36] While high activation loss and high internal resistance are reported, the modified electrode, nonetheless, shows an improved stability of maximum voltage at 600 mV up to 10 days MFC operation. Also, the micro-fiber composite exhibits two-fold increase in power and current densities compared to nano-fiber composite.

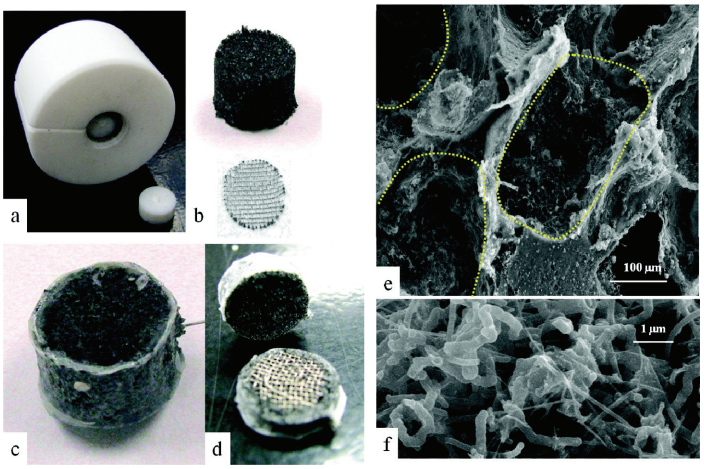

Fig. 5. Visual representation of polymeric nanocomposite fabrication (a). A mold used to: b) pack sucrose/CF around a nickel mesh, c) sucrose/CF scaffold inserted with polymer and d) dissected electrode to reveal the porous scaffold after sucrose removal; e) magnified scaffold with similar size to the original particle indicated by yellow lines; f) scaffold connected with carbon fibers (reproduced from[35] with permission from *American Chemical Society*).

3.5. Nanocomposites of polysaccharides

Polysaccharide nanocomposites have been reported as anode modifier. The effects of different nanocomposites *viz.* magnesium and graphite composed alongside chitin particles were investigated.[37] Maximum power density of 1872 mW/m^2 is recorded in magnesium/chitin composite. Chitin supplement is responsible for 121 % increase in magnesium anode, and 164 % increase in graphite anode. The improvement, by chitin-supplemented anode, is attributed to the active growth of bacterial communities on anode surface encouraged by the organic carbon source. A conductive carbon nanotube hydrogel, composed of chitosan, is layered onto carbon paper (CP) surface and applied as anode electrode (Fig. 6).[38] A current density peak of 500 mA/m^2 is recorded for hydrogel modified electrode at a power density of 132 mW/m^2, compared to raw CP electrode (150 mA/m^2 of current density). Coulombic efficiency (*CE*) of 32 % is reported for CNT-hydrogel modified electrode while 19 % *CE* for the control. It is suggested that the presence of oxygen-containing functional groups of C=O and C=OH are responsible for high conductivity of the modified electrode. Similarly, Mottet *et al.*[39] constructed a conductive composite hydrogel made up of alginate and carbon nanotube. The new electrode shows high compatibility with biocatalyst and better conductivity.

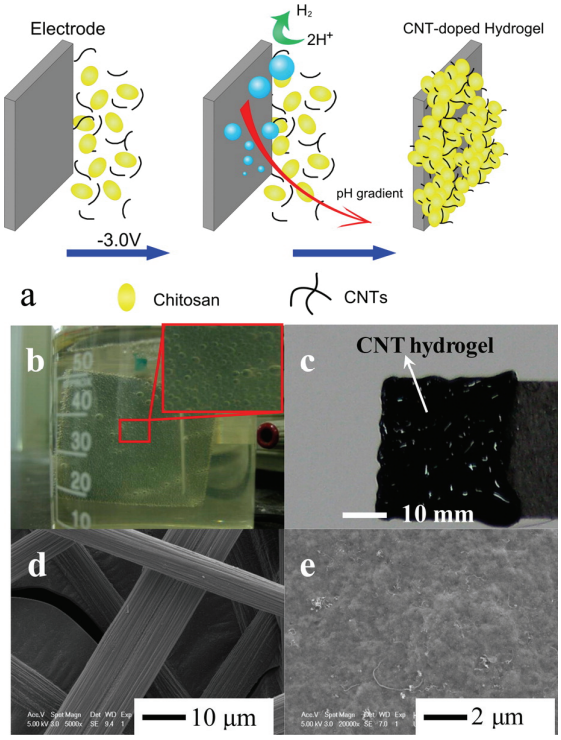

Fig. 6. Visual representations of: a) CNT-hydrogel electrode preparation, b) bubbles generated during the deposition process, c) CNT-hydrogel layered on carbon paper, d) SEM images of carbon paper and e) CNT-hydrogel/carbon paper composite (reproduced from[38] with permission from *American Chemical Society*).

3.6. Nanocomposites of other polymers

Temperature responsive polymer of poly-*N*-isopropylacrylamide (PNIPAM) has been investigated as anode modifier by Kumar *et al.*[40] PNIPAM prepared with CNT and GO nanoparticles is subsequently structured into hydrogel (Table I). Pristine PNIPAM electrode records a power density peak of 43 mW/m^2 at a current density of 453 mA/m^2. The incorporation of CNT into PNIPAM matrix results in six-fold increase of power density, *i.e.*, 264 mW/m^2 at a current density of 2502 mA/m^2. Further modification with GO nanoparticles results in significant increase in both power and current densities at 434 mW/m^2 and 3603 mA/m^2, respectively. The decrease in charge transfer resistance of PNIPAM is attributed to synergistic interaction between two highly conductive nanoparticles, *viz.* CNT and GO that concomitantly improve the MFC performance with a longevity of more than 300 h. Recently, Chen *et al.*[41] reported hydrogel formation of polyacrylamide (PAM) with rGO and graphite brush (GB) as current collector through *in situ* polymerization method, followed by reduction with ascorbic acid. The PAM/rGO/GB electrode records 34.8 % increase in maximum power density compared to GB anode. Superiority in CE is observed for PAM/rGO/GB electrode at 35.6 % compared to GB electrode (21.1 %). Close proximity of the biofilm to anode surface as well as large surface area afforded by modified electrode are suggested to be responsible for the enhanced MFC performance. Polymeric derived ceramics (PDC) route has been employed in making a highly conductive hydrophilic polymeric nanocomposite of polymethylsilsesquioxane and poly(methyl-phenylsilsesquioxane) composed of graphite and carbon black.[42] The

TABLE I. Typical anode materials, polymer and carbon loadings for anode modification

Anode material	Type of polymer loading	Type of C/metal loading	Reference
rGO	PPy	Graphite powder	Kumar *et al.*[23]
Nickel plate	PPy nanowires	GO	Li *et al.*[24]
CC	PANI	MWCNT	Wang *et al.*[26]
CP	PANI	Graphene/TiO_2	Han *et al.*[27]
CC	PANI	Graphene/Ti_4O_7	Li *et al.*[28]
SSM	PANI	CNT	Yellappa *et al.*[29]
CP	PANI	TiO_2 nanosheet	Yin *et al.*[30]
Biochar	PEDOT	Nickel ferrite nanorod	Senthilkumar *et al.*[33]
SS	PEDOT	Graphene/Nickel	Hernandez *et al.*[34]
CC	mcl-PHA	MWCNT	Hindatu *et al.*[4]
CC	mcl-PHA/PEGMA	MWCNT	Yusuf *et al.*[13]
CP	PCL	CNT/CNF/Gold	Fraiwan *et al.*[36]
CC	mcl-PHA/Methyl acrylate	MWCNT	Sirajudeen *et al.*[16]
CC	Chitin	Graphite/Magnesium	Jung *et al.*[37]
CP	Chitosan	CNT	Liu *et al.*[38]
CC	PNIPAM	Graphene/CNT	Kumar *et al.*[40]
Graphite brush	Polyacrylamide	rGO	Chen *et al.*[41]

novel anode material records two-fold increase in power density (211 mW/m^2) compared to carbon felt anode (111 mW/m^2). When the MFC system is applied for wastewater treatment, similar COD removal rate and CE are recorded for modified and pristine anode electrodes. The high specific surface area of the modified anode as well as its porous structure results in superior biocompatibility as evidenced by extensive biofilm growth on the electrode surface, and consequently improve electron transfer process.[42]

4. CATHODE MODIFICATION

Although MFC is a clean, sustainable, renewable and earth-friendly electricity generating device, low power output generated by the technology hampers its widespread practical applications.[12] To tackle this issue, the cathode electrode that determines catalytic activities of terminal electron acceptors, is a rational target to be modified accordingly. The primary challenge in fabricating an effective cathode electrode is keeping its surface highly conductive and catalytically-active for a prolonged period of MFC operation.[43] A practical cathode electrode should also be inexpensive and readily available,[44] easy to fabricate,[45,46] electrocatalytically efficient[47] and stable in catholyte.[48] Factors such as concentration of protons,[48–50] electrode spacing,[51] and electrode surface area[52] are known to affect electrocatalytic activities of the cathode electrode. Some commonly utilized materials and their respective loadings when applied as a component to improve electrocatalytic function of a cathode are carbon nanotube (5 mg/cm^2),[4] $KMnO_4$ (2 mg/cm^2), platinum (0.048 mg/cm^2)[20] amongst others. An extensive review on carbon-based polymer nanocomposites as cathode electrode material for MFC is provided by Jafary *et al.*[20] Significant improvements are evidenced in polymer-based modification of cathode electrodes compared to bare electrode materials. The development of a stable, efficient, polymer-based (modified) cathode electrode that enhances interfacial electrochemical reaction will significantly increase the power output of MFC, and a step closer towards its adoption in various applications.

4.1. Cathode modification with polymeric nanomaterials

Ahmad *et al.*[53] constructed MFC setup with PANI nanofibers prepared with carbon black. Higher electrochemical activities, with power density improvement up to 2.7-fold increase, is obtained with the composite cathode compared to pristine PANI (control). Although the power density is still lower than Pt-based electrode, the environmental-friendly polymeric composite is economically feasible when considering large-scale applications. Sulfonated PANI (SPANI), composed of highly efficient bimetallic nanocomposites of 1:1 nickel (Ni) and cobalt (Co), is investigated by Papiya *et al.*[54] for cathode electrode modifier. Spectroscopic analyses indicate the nanocomposites to be well distributed on the supporting matrix. When compared with the controls, the highest catalytic activity is obs-

erved in SPANI/Ni-Co electrode with a maximum power density at 659 mW/m^2 relative to Pt-based electrode at 483 mW/m^2. Incorporation of highly functional nanoparticles of graphene and TiO_2 into PANI matrix to enhance the reduction of oxygen at cathode has also been reported.[27] The ternary nanocomposite exhibited superior rate of oxygen reduction activity compared to controls (pristine PANI and PANI/TiO_2 electrodes).

Polypyrrole (PPy) is another conducting polymer that has been utilized as cathode modifier. A solvothermal method is employed to synthesize a novel composite of manganese, PPy and carbon nanotube.[55] The composite demonstrated efficiency and stability as cathode catalyst for oxygen reduction reaction. A power density peak of 213 mW/m^2 at a material loading rate of 2 mg/cm^2 is recorded, comparable to platinum/carbon black composite electrode. Further modification of PPy polymer matrix with MnO_2/CNT composite using cost--effective hydrothermal method results in an improved maximum power density of 721 mW/m^2.[56] Improved long-term stability of the composite electrode compared to Pt/C electrode is also reported, making the electrode an alternative to Pt/C electrode for sustainable energy generation.

A single-chambered MFC has been developed by coating the air-facing side with poly(dimethylsiloxane) prepared with nitrogen-doped nickel nanoparticles and carbon nanofibers. The polymer-metal-carbon nanocomposite shows high efficiency in oxygen reduction reaction in MFC, serving as an ideal alternative to potentially harmful Pt-based and Nafion electrode.[57] Ong *et al.*[58] recently have synthesized a polymeric cathode composed of polyvinylpyrrolidone/carbon nanotube/manganese oxide (P/MnO_2/CNT) for air cathode MFC. Electrochemical analyses reveal higher oxygen reduction reaction activities with low charge transfer resistance compared to control electrodes of MnO_2 and MnO_2/CNT. When utilized in MFC, a maximum power density of 91 mW/m^2 is recorded, which is significantly higher than MnO_2/CNT catalyst (72 mW/m^2), MnO_2 catalyst (36 mW/m^2) and CNT catalyst (29 mW/m^2). Also, relatively high COD removal percentage of 74 % is recorded for the P/MnO_2/CNT electrode.

One of the most recent modifications involving polymeric cathode nanocomposite utilizes polysaccharide-carbon composite. A bacterial cellulose doped with particles of phosphorus and copper is used as cathode catalyst in MFC[59] (Fig. 7). A three-dimensional structure with extensive large surface area is fabricated. Improvement in the catalytic activity of the polymeric nanocomposite is attributed to the increase in active sites from Cu and P doping.

A maximum power density of 1177 mW/m^2 at a current density of 6730 mA/m^2 is recorded, significantly higher than Pt-based electrode (1044 mW/m^2 at a current density of 6020 mA/m^2). A five-fold increase in power density is observed when a cathode electrode is modified with a dual-doped carbon derived from chitosan.[60] Improved internal resistance, high open circuit voltage as well

as large surface area of about 982 m^2/g, resulting in better oxygen mass transfer are attributed to better performance in the nitrogen- and phosphorus-doped electrodes.

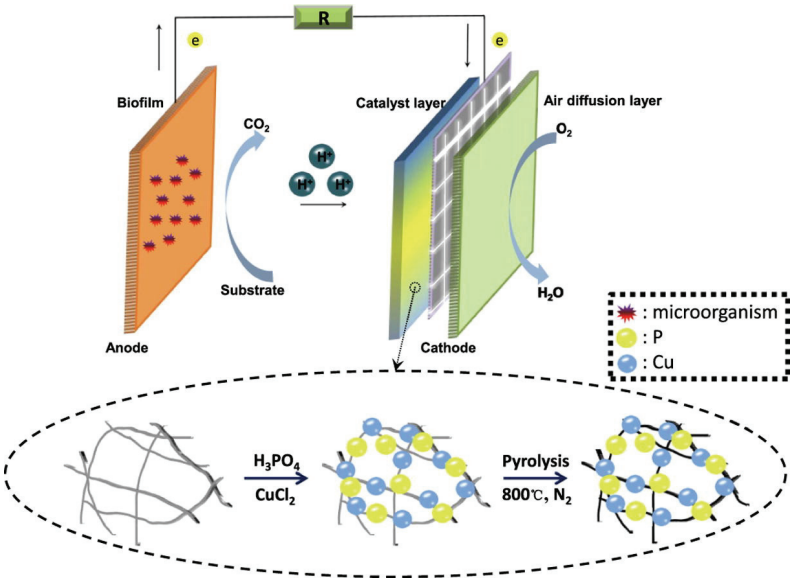

Fig. 7. Schematic diagram of bacterial cellulose doped with phosphorus and copper *via* freeze-drying and high-temperature pyrolysis (reproduced from[59] with permission from *Elsevier*).

5. PROTON EXCHANGE MEMBRANE (PEM)

The primary function of PEM in MFC is to separate the anode and cathode electrolytes, and simultaneously allow for maximum proton (H^+) passage from anode to cathode chamber. However, high cost and environmentally detrimental nature of some widely utilized PEM warrant for the development of alternative, efficient, readily available, economical, and environmental friendly PEMs. The recent advancements in PEM fabrication for MFC application are discussed in the following sections.

5.1. Polyether ether ketone (PEEK) nanocomposites as PEM

Quaternized PEEK (QPEEK) and sulfonated PEEK (SPEEK) are fabricated and utilized as anion and cation exchange membranes, respectively.[61] Superiority of QPEEK as exchange membrane is observed with maximum power density of 603 mW/m^2 and *CE* of 76 % compared to SPEEK (458 mW/m^2 and 61 %). SPEEK allows for more cation transport instead of protons, and exhibits high pH gradient. It results in the formation of chemical precipitate on cathode surface and subsequently, high internal resistance and MFC deterioration. SPEEK mem-

branes are fabricated with different degrees of sulfonation (DS) (20.8, 41, 63.6 and 76 %) for MFC application.[62] SPEEK with 63.3 % DS exhibits the highest power density (68.64 mW/m^2), COD removal (91 %) and *CE* (26 %). Although power density generation is still lower than Nafion membrane (74.8 mW/m^2), cost estimation suggests that the utilization of SPEEK with 63 % DS is a feasible alternative due to high power generation per cost. Further modification of the SPEEK membrane with hybridization of polysulfone (PS) at lower and higher DS for desalination and power generation has also been investigated.[63] The degree of porosity of the modified membrane is in direct proportion to DS as shown in Fig. 8. The amphiphilic hybrid membrane with 29 % DS exhibits the highest power density and significantly high NaCl (62 %) and $MgSO_4$ (68 %) rejection rate notwithstanding lower than PS/SPEEK (76 %) for NaCl (67 %) and $MgSO_4$ (81 %) rejection rate. Particles of silicotungstic acid are entrapped into the matrix of SPEEK through phase inversion method.[64] The hybrid composite membrane shows reduced oxygen gas crossover, which results in four-fold increase in the generation of maximum power density compared to Nafion membrane.

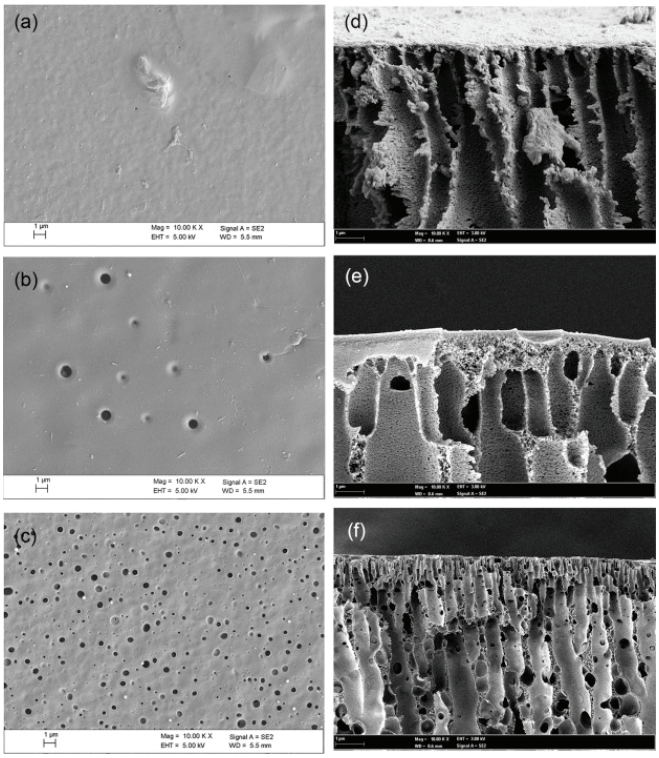

Fig. 8. SEM images of: a) surface of PS, b) surface of PS/SPEEK (29 %), c) surface of PS/SPEEK (76 %), d) cross section of PS, e) cross section of PS/SPEEK (29 %) and f) cross section of PS/SPEEK (76 %) (reproduced from[63] with permission from *Elsevier*).

5.2. Nafion nanocomposites as PEM

While neat Nafion is the most utilized PEM in MFC, enhancement of its performance through composites of nanoparticles has also been investigated. Angioni *et al.*[65] modified Nafion membrane with functionalized SB-15 silica. Functionalization is done with SO_3H group and applied as PEM in an extended MFC operation. Nafion-based SB-15 composite of 15 mass % is found to exhibit maximum power density, three times higher than neat Nafion after three months of MFC operation. The same membrane offers high resistivity to biofouling, high COD removal of 95 % after 14 days and also improve *CE* recovery of 34 %. The efficiency of the modified PEM is attributed to the presence of the silica-based SO_3H functionalized filler. Bajestani *et al.*[66] investigated the effects of different solvents in a process where Nafion is composited with TiO_2 through solvent casting method. Nafion composite with dimethylformamide (DMF) solvent yields the highest OCV, proton conductivity and the highest membrane porosity. Alumina nanoparticles (Al_2O_3) ranging 5–20 mass % are incorporated within the matrix of sulfonated poly-(vinylidene fluoride-hexafluoropropylene) (PVDF-*co*-HFP) blended with Nafion at different molar ratios.[67] Increase in water uptake is observed with increased incorporation of Al_2O_3 nanoparticles. Membrane with 5 mass % nano Al_2O_3 shows superior proton conductivity and improved maximum power and current densities of 48 and 11 %, respectively. Hernandez *et al.*[68] developed membranes of agar prepared with Nafion liquid and tested them against Nafion 117 membrane. Reduced internal resistance is observed in all modified membranes from incorporation of agar. Although the power densities are lower than the control, *i.e.*, Nafion 117 membrane, higher power/cost ratio is deemed to be an advantage in agar composite membranes than Nafion membrane.

5.3. Chitosan and polyester nanocomposites as PEM

A low-cost polyester cloth (PC) with varying layers are utilized as PEM in MFC and compared with Nafion membrane.[69] Higher mass transfer and reduced diffusion coefficient of oxygen are observed in PC membranes compared to Nafion. A comparable internal resistance, power and current densities are observed in PC membranes and Nafion membrane, indicating a possible alternative to health hazard Nafion. In another PEM investigation, Yusuf *et al.*[70] demonstrated for the first time the application of biodegradable microbial polyester, *i.e.*, medium-chain-length polyhydroxyalkanoates prepared with functionalized multi-walled carbon nanotubes (mcl-PHA/MWCNT) at varying amount (5–20 mass %), obtained through ultrasound dispersion blending method. Comparable power density to Nafion membrane is recorded. However, membrane with 10 % MWCNT is superior in COD removal percentage, *CE*, conductivity and reduced internal resistance over Nafion membrane. Recently, Sirajudeen *et al.*[71] incorporated different amount of polyhydroxybutyrate (PHB) crystal (5–15 mass %) into

mcl-PHA matrix through solvent blending method. The composite biopolymer was investigated as an alternative PEM to Nafion in a double-chambered MFC with real wastewater as substrate. Composite with 10 and 15 % PHB show superior maximum voltage at 988 and 1001 mV, respectively, compared to Nafion (594 mV). Better power density is also recorded for PHB15% (601 mW/m^2) compared to Nafion (520 mW/m^2). Superiority in overall MFC performance of composite membrane is attributed to better water uptake and wettability, as well as higher resistivity of the novel membrane to gas flux from cathode to anode compartment. Harewood *et al.*[72] investigated thermal condensation of malic and citric acid in 3:1 ratio and its blend with chitosan. The copolymer is utilized as PEM in MFC. The maximum power and current densities generated are comparable to Nafion 117 membrane. The copolymer is biodegradable, thus making it another environmental friendly alternative to Nafion membrane. Furthermore, the effects of applying different cross-linkers are investigated by Holder *et al.*[73] Graphene oxide nanoparticles are incorporated into the matrix of chitosan and cross--linked with either phosphoric- or sulfuric acid. Phosphoric acid cross-linked PEM shows 135 % increase in power density compared to sulfuric acid cross--linked PEM.

5.4. Ceramics and polyethersulfone (PES) nanocomposites

Polyethersulfone (PES) is sulfonated with chlorosulfonic acid (SPES) and finally blended with pristine PES (PES/SPES).[74] The PES/SPES as exchange membrane shows superiority in COD removal percentage, CE, oxygen permeability, biofouling and power generation compared to Nafion membrane. Di Palma *et al.*[75] recently developed a type of membrane where PES is prepared with different concentrations of Fe_3O_4 nanoparticles using melt-blend method. PES with 20 % Fe_3O_4 nanoparticles generated maximum power density of 9.59 mW/m^2 and current density of 38 mA/m^2. Incorporation of the nanoparticles of more than 20 mass % leads to fissuring of the membrane. Similar observation has also been reported by Yusuf *et al.*[70] In another study, ceramic membranes with different pore sizes (0.14 μm, 150 and 5 kDa) are investigated as PEM in MFC and compared with cation exchange membranes and Nafion membrane.[76] Ceramic membrane with the largest pore size, *i.e.*, 5 kDa shows improved power density, better *CE* and reduced internal resistance compared to other membranes. When the surface wall of ceramic is layered with films of chitosan and montmorillonite minerals,[77] membranes with six layers and above record a decrease of six-fold in the oxygen gas crossover, resulting in two-fold maximum power density in membrane with seven bi-layers compared to pristine ceramic membrane.

5.5. Nanocomposites of other materials as PEM

Hernandez *et al.*[78] developed a polymer inclusion membrane based on different weight percentage of ionic liquid as PEM in MFC application. Ionic liquid of 1-octyl-3-methylimidazolium hexafluorophosphate and methyl trioctyl ammonium chloride are utilized. Maximum power density of up to 30 mW/m^2 and COD removal efficiency of 80 % are recorded for membrane inclusion of 70 mass % ionic liquid supported with ammonium. The increase in ionic liquid concentration is followed by power density increase. In another study, synthetic fiber of polybenzimidazole (PBI) is fabricated with different amounts of polyvinylpyrrolidone (PVP) and utilized as PEM in MFC.[79] About 81 % increase in power output and superior COD removal percentage are observed in composite membrane with 70:30 PVP:PBI over pure PBI membrane, indicating the utility of PVP as composite membrane in MFC. Similarly, PBI has been fabricated with mesostructure of SB-15 silica as PEM in a long-term MFC operation for wastewater treatment.[80] The cost-efficient composite membrane shows an order of magnitude increase in maximum power density compared to Nafion, and about 31 % *CE* and 90 % COD removal are observed (Table II).

Blending of sulfonated SiO_2 (S-SiO_2) with sulfonated polystyrene ethylene butylene polystyrene (SSEBS) is investigated as yet another alternative to Nafion membrane. Various percentages of S-SiO_2 ranging 2.5–10 mass % are studied.[81] The modified membranes show superior power density over Nafion, with 7.5 % S-SiO_2 membrane exhibiting four-fold increase in power density (1209 mW/m^2) over Nafion (290 mW/m^2). S-SiO_2 incorporation is suggested to be responsible for enhanced proton conductivity. In a separate study, Li *et al.*[82] thermally grafted an ozone-pretreated poly(vinylidene fluoride) (PVDF) with sodium styrene sulfonate (SSS) as shown in Fig. 9. Better COD removal percentage (85 %) is observed using the cost-efficient copolymer compared to Nafion membrane (74 %). Although, higher power density is recorded for Nafion membrane (132.0 mW/m^2) compared to the modified membrane (106.7 mW/m^2), cost/power ratio of the modified membrane makes it an efficient alternative to Nafion.

TABLE II. Comparison of reported membranes in terms of thickness, water uptake, COD, *CE*, and power density

Membrane	Thickness mm	Water uptake, %	COD %	*CE* %	Power density mW m^{-2}	Reference
SPEEK	0.03	15	–	61	458	Elangovan & Dharmalingam[61]
QPEEK	0.03	23	–	76	603	
SPEEK + PS	–	22	86	22.4	97.47	Ghasemi *et al.*[63]
STA+ SPEEK	0.19	22	–	–	207	Venkatesan & Dharmalingam[64]
Mesoporous silica + Nafion 117	0.06	–	95	34	25.86	Angioni *et al.*[65]

TABLE II. Continued

Membrane	Thickness mm	Water uptake, %	COD %	*CE* %	Power density mW m^{-2}	Reference
Nano Al_2O_3 + PVDF-*co*-HFP + Nafion	0.02 – 0.021	24	86.62	3.3	541	Kumar *et al.*[67]
mcl-PHA + MWCNT	0.176	33	91	26	361	Yusuf *et al.*[70]
mcl-PHA + PHB	0.149	22	72.7	65.7	601	Sirajudeen *et al.*[71]
Chitosan + GO	–	60	89.52	–	1.11	Holder *et al.*[73]
PES + SPES	0.25	68.6	82	22	58.7	Zinadini *et al.*[74]
PES + Fe_3O_4	0.2 – 0.35	1.59	75	11.36	9.57	Di Palma *et al.*[75]
Ceramic membrane	24	–	89	41	1790	Daud *et al.*[76]
Polymer inclusion + Ionic liquid	0.25	–	80	12	30.6	Hernandez-Fernandez *et al.*[78]
PBI + PVP	–	35.4	84.36	–	231.38	Kumar *et al.*[79]
PBI + SBA-15	0.04	–	73	14	103.5	Angioni *et al.*[80]
SSEBS + SiO_2	0.18	210	–	85	1209	Sivasankaran *et al.*[81]
PVDF-g-SSS	0.1	25	85	5.96	106.7	Li *et al.*[82]

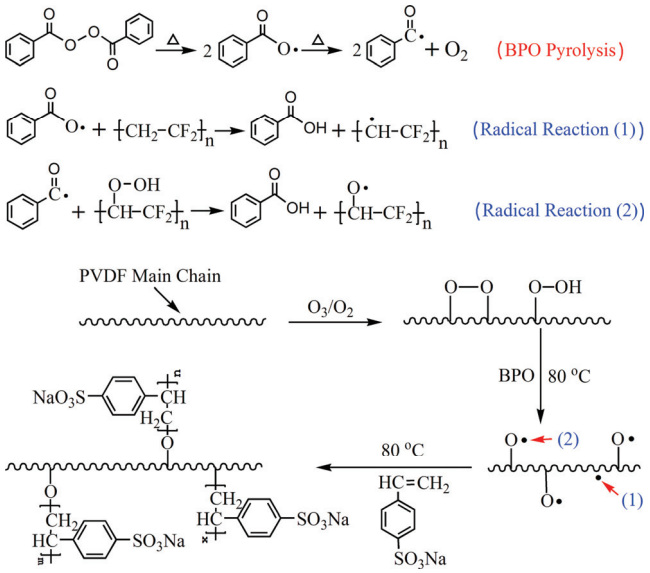

Fig. 9. Schematic representation of ozone pretreatment of PVDF and graft copolymerization of SSS (reproduced from[82] with permission from *Elsevier*).

6. CONCLUSION

Innovative technologies, such as microbial fuel cell (MFC), offer the conversion of chemical energy from waste into renewable energy. While the electrochemistry of the device is well-established, the next level progress towards its practical applications rests wholly within the material science aspect of the tech-

nology. In the current narrative of sustainable and zero detriment towards the environment, and with ever increasing demand and pressure to shift towards materials that fit such bill, biodegradable polymeric nano-composition approach is the most feasible and practical. It offers functional compatibilities with vast majority of electro-conductive nanomaterials, and the subsequent seamless integration of the composites as apparatus in the MFC device is extremely useful. Furthermore, natural bio-compatibility of the biopolymeric nanocomposites with electrogens when applied as anode surface modifier will significantly improve the electron transfer efficiency. Intensive research efforts to extensively explore novel formulation of bio-degradable polymeric nano-composition and its innovative integration as functional and structural components in the MFC device will be instrumental in advancing the technology to practical and sustainable wide applications.

ABBREVIATIONS

MFC	- Microbial fuel cell
PEM	- Proton exchange membrane
mcl-PHA	-Medium-chain-length polyhydroxyalkanoates
PEGMA	- Poly(ethylene glycol) methyl acrylate
MA	- Methyl acrylate
CV	- Cyclic voltammetry
CNT	- Carbon nanotube
MWCNT	- Multi-walled carbon nanotube
CNF	- Carbon nanofiber
CC	- Carbon cloth
CP	- Carbon paper
SS	- Stainless steel
SSM	- Stainless steel mesh
COD	- Chemical oxygen demand
CE	- Coulombic efficiency
PPy	- Polypyrrole
PANI	- Polyaniline
PEEK	- Polyether ether ketone
PEDOT	- Poly(3,4-ethylene dioxythiophene)
G	- Graphene
GO	- Graphene oxide
rGO	- Reduced graphene oxide
OCV	- Open circuit voltage
SPEEK	- Sulfonated polyether ether ketone
QPEEK	- Quaternized polyether ether ketone
PS	- Polysulfone
PVDF	- Poly(vinylidene fluoride)
PVDF-*co*-HFP	- Poly-(vinylidene fluoride-hexafluoropropylene)
PES	- Polyethersulfone
SPES	- Sulfonated polyethersulfone

PBI - Polybenzimidazole
PVP - Polyvinylpyrrolidone
SSEBS - Sulfonated polystyrene ethylene butylene polystyrene
SSS - Sodium styrene sulfonate

Acknowledgement. The authors acknowledged University of Malaya for research funding (Grant Nos. FG024-17AFR and IIRG017A-2019).

ИЗВОД

ПОЛИМЕРНИ НАНОКОМПООЗИТИ ЗА ИНОВАТИВНО ФУНКЦИОНАЛНО ПОБОЉШАЊЕ ЕЛЕКТРОДА И МЕМБРАНЕ ЗА РАЗМЕНУ ПРОТОНА У МИКРОБНОЈ ГОРИВНОЈ ЋЕЛИЈИ

ABDUL AZEEZ OLAYIWOLA SIRAJUDEEN и M. SUFFIAN M. ANNUAR

Institute of Biological Sciences, Faculty of Science, University of Malaya, 50603, Kuala Lumpur, Malaysia

Практичну примена микробних горивних ћелија (MFC), одрживог енергетског уређаја, ограничава мала излазна снага. Његове главне компоненте, тј. анода, катода и протонска мембрана за измену (PEM) представљају основни фокус унапређења и модификација у смислу њиховог функционалног дизајна и материјала. Површинска проводљивост аноде као понор електрона пресудна је за величину излазне снаге, док би катодна електрода требало да буде реактивна за ефикасну редукцију кисеоника на трифазном спајању. PEM је једини одговоран за једносмерни ток протона који истовремено прави струјно коло. Полимерни нанокомпозити као модификатор електрода значајно су побољшали функције аноде/катоде/PEM, чиме су остварили укупне перформансе MFC. Овај прегледни рад наглашава напредак у модификацијама аноде, катоде и PEM материјала полимерима од 2014. до 2019. године. Дискутује се о ефектима на биокомпатибилност, површину, унутрашњу отпорност, електрохемијску активност, одрживост и свеукупне перформансе MFC.

(Примљено 2. априла, ревидирано 2. септембра, прихваћено 7. септембра 2020)

REFERENCES

1. X. Jie, S. Gonzalez-Cortes, T. Xiao, J. Wang, B. Yao, D. R. Slocombe, P. P. Edwards, *Angew. Chem. Int. Ed. Engl.* **56** (2017) 10170 (https://doi.org/10.1002/anie.201703489)
2. S. Kanimozhi, K. Perinbam, in *Proceedings* of *the 3rd ISESCO International Workshop and Conference on Nanotechnology 2012 (IWCN2012), J. Phys: Conf. Ser.* (2012), Selangor, Malaysia, IOP Publishing LTD, Selangor, 2013, p. 431
3. A. Parmar, N. K. Singh, A. Pandey, E. Gnansounou, D. Madamwar, *Bioresour. Technol.* **102** (2011) 10163 (https://doi.org/10.1016/j.biortech.2011.08.030)
4. Y. Hindatu, M. Annuar, R. Subramaniam, A. Gumel, *Bioproc. Biosys. Eng.* **40** (2017) 919 (https://doi.org/10.1007/s00449-017-1756-4)
5. A. Almatouq, A. O. Babatunde, *Appl. Energy* **230** (2018) 122 (https://doi.org/10.1016/j.apenergy.2018.08.108)
6. F. Yu, C. Wang, J. Ma, *Materials* **9** (2016) 807 (https://doi.org/10.3390/ma9100807)
7. B. E. Logan, *Nat. Rev. Microbiol.* **7** (2009) 375 (https://doi.org/10.1038/nrmicro2113)
8. L. Xiao, Z. He, *Graphene-Based Energy Devices* **13** (2015) 355 (https://doi.org/10.1002/9783527690312.ch13)
9. L. Fu, S. J. You, F. L.Yang, M. M. Gao, X. H. Fang, G. Q. Zhang, *J. Chem. Technol. Biot.* **85** (2010) 715 (https://doi.org/10.1002/jctb.2367)
10. I. Gajda, J. Greenman, C. Melhuish, C. Santoro, I. Ieropoulos, *Bioresour. Technol.* **215** (2016) 285 (https://doi.org/10.1016/j.biortech.2016.04.004)

11. I. Gajda, J. Greenman, C. Melhuish, C. Santoro, B. Li, P. Cristiani I. Ieropoulos, *Water Res.* **86** (2015) 108 (https://doi.org/10.1016/j.watres.2015.08.014)
12. Y. Hindatu, M. Annuar, A. Gumel, *Renew. Sustain. Energy Rev.* **73** (2017) 236 (https://doi.org/10.1016/j.rser.2017.01.138)
13. H. Yusuf, M. S. M. Annuar, R. Subramaniam, A. M. Gumel, *Chem. Eng. Technol.* **42** (2018) 566 (https://doi.org/10.1002/ceat.201800023)
14. H. F. Cui, L. Du, P. B. Guo, B. Zhu, J. H. Luong, *J. Power Sources* **283** (2015) 46 (https://doi.org/10.1016/j.jpowsour.2015.02.088)
15. Y. L. Kang, S. Ibrahim, S. Pichiah, *Bioresour. Technol.* **189** (2015) 364 (https://doi.org/10.1016/j.biortech.2015.04.044)
16. A. A. O. Sirajudeen, M. S. M. Annuar, R. Subramaniam, *Biotechnol. Appl. Biochem.* **00** (2020) 1 (https://doi.org/10.1002/bab.1928)
17. A. Baudler, I. Schmidt, M. Langner, A. Greiner, U. Schröder, *Energy Environ. Sci.* **8** (2015) 2048 (https://doi.org/10.1039/c5ee00866b)
18. T. Huggins, H. Wang, J. Kearns, P. Jenkins, Z. J. Ren, *Bioresour. Technol.* **157** (2014) 114 (https://doi.org/10.1016/j.biortech.2014.01.058)
19. S. H. Lee, J. Y. Ban, C. H. Oh, H. K. Park, S. Choi, *Sci. Rep.* **6** (2016) 28588 (https://doi.org/10.1038/srep28588)
20. T. Jafary, M. Ghasemi, J. Alam, S. A. Aljlil, S. Yusup, in *Carbon-based polymer nanocomposites for environmental and energy applications*, A. F. Ismail, P. S. Goh (Eds.), Elsevier, Amsterdam, 2018, pp. 361–390 (https://doi.org/10.1016/B978-0-12-813574-7.00015-0)
21. S. Li, C. Cheng, A. Thomas *Adv. Mater.* **29** (2017) 1602547 (https://doi.org/10.1002/adma.201602547)
22. A. Kaur, S. Ibrahim, C. J. Pickett, I. S. Michie, R. M. Dinsdale, A. J. Guwy, G. C. Premier, *Sens. Actuators, B* **201** (2014) 266 (https://doi.org/10.1016/j.snb.2014.04.062)
23. G. G. Kumar, C. J. Kirubaharan, S. Udhayakumar, K. Ramachandran, C. Karthikeyan, R. Renganathan, K. S. Nahrn, *ACS Sustain. Chem. Eng.* **2** (2014) 2283 (https://doi.org/10.1021/sc500244f)
24. X. H. Li, J. S. Qian, X. G. Guo, L. W. Shi, *3 Biotech.* **8** (2018) 375 (https://doi.org/10.1007/s13205-018-1321-0)
25. K. B. Pu, Q. Ma, W. F. Cai, Q. Y. Chen, Y. H. Wang, F. J. Li, *Biochem. Eng. J.* **132** (2018) 255 (https://doi.org/10.1016/j.bej.2018.01.018)
26. X. Y. Wang, H. B. He, C. C. Zheng, Q. J. Guo, *Particle Sci. Eng.* **347** (2014) 62 (https://doi.org/10.1039/9781782627432-00062)
27. T. H. Han, N. Parveen, J. H. Shim, A. T. N. Nguyen, N. Mahato, M. H. Cho, *Ind. Eng. Chem. Res.* **57** (2018) 6705 (https://doi.org/10.1021/acs.iecr.7b05314)
28. Z. L. Li, S. K. Yang, Y. N. Song, H. Y. Xu, Z. Z. Wang, W. K. Wang, Y. Q. Zhao, *Int. J. Hydrogen Energy* **44** (2019) 6862 (https://doi.org/10.1016/j.ijhydene.2018.12.106)
29. M. Yellappa, J. S. Sravan, O. Sarkar, Y. V. R. Reddy, S. V. Mohan, *Bioresour. Technol.* **284** (2019) 148 (https://doi.org/10.1016/j.biortech.2019.03.085)
30. T. Yin, H. Zhang, G. Q. Yang, L. Wang, *Synth. Met.* **252** (2019) 8 (https://doi.org/10.1016/j.synthmet.2019.03.027)
31. S. N. J. S. Z. Abidin, M. S. Mamat, S. A. Rasyid, Z. Zainal, Y. Sulaiman, *Electrochim. Acta* **261** (2018) 548 (https://doi.org/10.1016/j.electacta.2017.12.168)
32. Q. Ma, K. B. Pu, W. F. Cai, Y. H. Wang, Q. Y. Chen, F. J. Li, *Ind. Eng. Chem. Res.* **57** (2018) 6633 (https://doi.org/10.1021/acs.iecr.8b00563)

33. N. Senthilkumar, M. Pannipara, A. G. Al-Sehemi, G. G. Kumar, *New J. Chem.* **43** (2019) 7743 (https://doi.org/10.1039/C9NJ00638A)
34. L. A. Hernandez, G. Riveros, D. M. Gonzalez, M. Gacitua, M. A. del Valle, *J. Mater. Sci. Mater. Electron.* **30** (2019) 12001 (https://doi.org/10.1007/s10854-019-01555-y)
35. H. R. Luckarift, S. R. Sizemore, K. E. Farrington, J. Roy, C. Lau, P. B. Atanassov, G. R. Johnson, *ACS Appl. Mater. Interfaces* **4** (2012) 2082 (https://doi.org/10.1021/am300048v)
36. A. Fraiwan, S. P. Adusumilli, D. Han, A. J. Steckl, D. F. Call, C. R. Westgate, S. Choi, *Fuel Cells* **14** (2014) 801 (https://doi.org/10.1002/fuce.201400041)
37. S. P. Jung, M. H. Yoon, S. M. Lee, S. E. Oh, H. Kang, J. K. Yang, *Int. J. Electrochem. Sci.* **9** (2014) 315
38. X. W. Liu, Y. X. Huang, X. F. Sun, G. P. Sheng, F. Zhao, S. G. Wang, H. Q. Yu, *ACS Appl. Mat. Interf.* **6** (2014) 8158 (https://doi.org/10.1021/am500624k)
39. L. Mottet, D. Le Cornec, J. M. Noel, F. Kanoufi, B. Delord, P. Poulin, N. Bremond, *Soft Matter* **14** (2018) 1434 (https://doi.org/10.1039/C7SM01929G)
40. G. G. Kumar, S. Hashmi, C. Karthikeyan, A. GhavamiNejad, M. Vatankhah-Varnoos-faderani, F. J. Stadler, *Macromol. Rapid Commun.* **35** (2014) 1861 (https://doi.org/10.1002/marc.201400332)
41. J. Y. Chen, P. Xie, Z.P. Zhang, *Chem. Eng. J.* **361** (2019) 615 (https://doi.org/10.1016/j.cej.2018.12.116)
42. T. C. D. E. Silva, G. D. Bhowmick, M. M. Ghangrekar, M. Wilhelm, K. Rezwan, *Biochem. Eng. J.* **148** (2019) 29 (https://doi.org/10.1016/j.bej.2019.04.004)
43. B. E. Logan, *Microbial fuel cells*, John Wiley & Sons Ltd., New York, 2008, pp. 1–199 (https://doi.org/10.1002/9780470258590)
44. V. M. Ortiz-Martínez, M. J. Salar-García, F. J. Hernández-Fernández, A. De los Ríos, *Energy* **93** (2015) 1748 (https://doi.org/10.1016/j.energy.2015.10.027)
45. J. R. Kim, G. C. Premier, F. R. Hawkes, R. M. Dinsdale, A. J. Guwy, *J. Power Sources* **187** (2009) 393 (https://doi.org/10.1016/j.jpowsour.2008.11.020)
46. H. Liu, B.E. Logan, *Environ. Sci. Technol.* **38** (2004) 4040 (https://doi.org/10.1021/es0499344)
47. I. Gajda, J. Greenman, C. Santoro, A. Serov, C. Melhuish, P. Atanassov, I. A. Ieropoulos, *Energy* **144** (2018) 1073 (https://doi.org/10.1016/j.energy.2017.11.135)
48. A. Dicks, D.A.J. Rand, *Fuel cell systems explained*, John Wiley & Sons Ltd., New York, 2018, pp. 1–460 (https://doi.org/10.1002/9781118706992)
49. P. Mani, T. Keshavarz, T. S. Chandra, G. Kyazze, *Enzyme Microb. Technol.* **96** (2017) 170 (https://doi.org/ 10.1016/j.enzmictec.2016.10.012)
50. F. Zhao, F. Harnisch, U. Schröder, F. Scholz, P. Bogdanoff, I. Herrmann, *Environ. Sci. Technol.* **40** (2006) 5193 (https://doi.org/10.1021/es060332p)
51. S. Cheng, H. Liu, B.E. Logan, *Environ. Sci. Technol.* **40** (2006) 2426 (https://doi.org/10.1021/es051652w)
52. S. E. Oh, B. E. Logan, *Appl. Microb. Biotechnol.* **70** (2006) 162 (https://doi.org/10.1007/s00253-005-0066-y)
53. J. Ahmed, H.J. Kim, S. Kim, *J. Electrochem. Soc.* **159** (2012) B497 (https://doi.org/10.1149/2.049205jes)
54. F. Papiya, P. Pattanayak, P. Kumar, V. Kumar, P. P. Kundu, *Electrochim. Acta* **282** (2018) 931 (https://doi.org/10.1016/j.electacta.2018.07.024)
55. M. Lu, L. Guo, S. Kharkwal, H. Y. Ng, S. F. Y. Li, *J. Power Sources* **221** (2013) 381 (https://doi.org/10.1016/j.jpowsour.2012.08.034)

56. H. Yuan, L. Deng, J. Tang, S. Zhou, Y. Chen, Y. Yuan, *ChemElectroChem* **2** (2015) 1152 (https://doi.org/10.1002/celc.201500109)
57. A. Modi, S. Singh, N. Verma, *Int. J. Hydrogen Energy* **42** (2017) 3271 (https://doi.org/10.1016/j.ijhydene.2016.10.041)
58. H. R. Ong, C. W. Woon, M. S. Ahmad, A. Yousuf, C. K. Cheng, M. M. R. Khan, *Int. J. Electrochem. Sci.* **13** (2018) 7789 (https://doi.org/ 10.20964/2018.08.05)
59. H. Y. Li, H. Z. Ma, T. Liu, J. Ni, Q. H. Wang, *Bioresour. Technol.* **289** (2019) 121661 (https://doi.org/10.1016/j.biortech.2019.121661)
60. B. L. Liang, K. X. Li, Y. Liu, X. W. Kang, *Chem. Eng. J.* **358** (2019) 1002 (https://doi.org/10.1016/j.cej.2018.09.217)
61. M. Elangovan, S. Dharmalingam, *J. Polym. Res*. **23** (2016) 250 (https://doi.org/10.1007/s10965-016-1136-9)
62. M. Ghasemi, W. R. W. Daud, J. Alam, Y. Jafari, M. Sedighi, S. A. Aljlil, H. Ilbeygi, *Int. J. Hydrogen Energy* **41** (2016) 4862 (https://doi.org/10.1016/j.ijhydene.2015.10.029)
63. M. Ghasemi, W. R. W. Daud, J. Alam, H. Ilbeygi, M. Sedighi, A. F. Ismail, S. A. Aljlil, *Energy* **96** (2016) 303 (https://doi.org/10.1016/j.energy.2015.12.053)
64. P. N. Venkatesan, S. Dharmalingam, *Renew. Energy* **102** (2017) 77 (https://doi.org/10.1016/j.renene.2016.10.027)
65. S. Angioni, L. Millia, G. Bruni, C. Tealdi, P. Mustarelli, E. Quartarone, *J. Power Sources* **334** (2016) 120 (https://doi.org/10.1016/j.jpowsour.2016.10.014)
66. M. B. Bajestani, S.A. Mousavi, *Int. J. Hydrogen Energy* **41** (2016) 476 (https://doi.org/10.1016/j.ijhydene.2015.11.036)
67. V. Kumar, P. Kumar, A. Nandy, P. P. Kundu, *RSC Adv.* **6** (2016) 23571 (https://doi.org/10.1039/C6RA03598A)
68. G. Hernandez-Flores, H.M. Poggi-Varaldo, O. Solorza-Feria, *Int. J. Hydrogen Energy* **41** (2016) 23354 (https://doi.org/10.1016/j.ijhydene.2016.08.206)
69. T. Kim, S. Kang, J. H. Sung, Y. K. Kang, Y. H. Kim, J. K. Jang, *J. Microbiol. Biotechnol.* **26** (2016) 2171 (https://doi.org/10.4014/jmb.1608.08040)
70. H. Yusuf, M. S. M. Annuar, S. M. D. Syed Mohamed, R. Subramaniam, *Chem. Eng. Commun.* **206** (2018) 731 (https://doi.org/10.1080/00986445.2018.1521392)
71. A. A. O. Sirajudeen, M. S. M. Annuar, K. A. Ishak, Y. Hindatu, R. Subramaniam, *J. Clean Prod.* **278** (2021) 123449 (https://doi.org/10.1016/j.jclepro.2020.123449)
72. A. J. T. Harewood, S. R. Popuri, E. I. Cadogan, C. H. Lee, C. C. Wang, *Int. J. Environ. Sci. Technol.* **14** (2017) 1535 (https://doi.org/10.1007/s13762-017-1258-6)
73. S. L. Holder, C.H. Lee, S.R. Popuri, *Environ. Sci. Pollut. Res.* **24** (2017) 13782 (https://doi.org/10.1007/s11356-017-8839-2)
74. S. Zinadini, A. A. Zinatizadeh, M. Rahimi, V. Vatanpour, Z. Rahimi, *Energy* **125** (2017) 427 (https://doi.org/10.1016/j.energy.2017.02.146)
75. L. Di Palma, I. Bavasso, F. Sarasini, J. Tirillo, D. Puglia, F. Dominici, L. Torre, *Eur. Polym. J.* **99** (2018) 222 (https://doi.org/10.1016/j.eurpolymj.2017.12.037)
76. S. M. Daud, W. R. W. Daud, B. H. Kim, M. R. Somalu, M. H. Abu Bakar, A. Muchtar, I. S. Chang, *Electrochim. Acta* **259** (2018) 365 (https://doi.org/10.1016/j.electacta.2017.10.118)
77. V. Yousefi, D. Mohebbi-Kalhori, A. Samimi, *Electrochim. Acta* **283** (2018) 234 (https://doi.org/10.1016/j.electacta.2018.06.173)
78. F. J. Hernandez-Fernandez, A. de los Rios, F. Mateo-Ramirez, M. D. Juarez, L. J. Lozano-Blanco, C. Godinez, *Sep. Purif. Technol.* **160** (2016) 51 (https://doi.org/10.1016/j.seppur.2015.12.047)

79. V. Kumar, S. Mondal, A. Nandy, P. P. Kundu, *Biochem. Eng. J.* **111** (2016) 34 (https://doi.org/10.1016/j.bej.2016.03.003)
80. S. Angioni, L. Millia, G. Bruni, D. Ravelli, P. Mustarelli, E. Quartarone, *J. Power Sources* **348** (2017) 57 (https://doi.org/10.1016/j.jpowsour.2017.02.084)
81. A. Sivasankaran, D. Sangeetha, Y.H. Ahn, *Chem. Eng. J.* **289** (2016) 442 (https://doi.org/10.1016/j.cej.2015.12.095)
82. C. Li, L. Wang, X. D. Wang, M. X. Kong, Q. Zhang, G. Y. Li, *J. Membrane Sci.* **527** (2017) 35 (https://doi.org/10.1016/j.memsci.2016.12.065).

Journal of the Serbian Chemical Society
JSCS-info@shd.org.rs • www.shd.org.rs/JSCS
J. Serb. Chem. Soc. *86* (1) 25–38 (2021)
JSCS–5401
Original scientific paper

The use of mucilage extracted from *Opuntia ficus indica* as a microencapsulating shell

HANEDI ELHLELI[1,2], FATEN MANNAI[1], RAMZI KHIARI[3–5] and YOUNES MOUSSAOUI[6,7]*

[1]*Materials, Environment and Energy Laboratory (UR14ES26), Faculty of Sciences of Gafsa, University of Gafsa, Tunisia,* [2]*Faculty of Sciences of Gabes, University of Gabes, Tunisia,* [3]*University of Monastir, Faculty of Sciences, UR13 ES 63 - Research Unity of Applied Chemistry & Environment, 5000 Monastir, Tunisia,* [4]*Higher Institute of Technological Studies of Ksar Hellal, Department of Textile, Tunisia,* [5]*University of Grenoble Alpes, CNRS, Grenoble INP, LGP2, F-38000 Grenoble, France,* [6]*Organic Chemistry Laboratory (LR17ES08), Faculty of Sciences of Sfax, University of Sfax, Tunisia and* [7]*Faculty of Sciences of Gafsa, University of Gafsa, Tunisia*

(Received 29 February, revised 17 April, accepted 19 May 2020)

Abstract: This study was aimed at investigating the micro-formulation of capsules using natural biopolymers, such as cactus mucilage (CM), carboxymethyl cellulose sodium salt (CMCNa) and chitosan (Chi) as the wall material, for the transport and supply of sunflower oil. CM samples were extracted from *Opuntia ficus indica* (OFI) by precipitation at different supernatant pH values (2, 4 and 12). The extracted natural polysaccharide and the resulting microcapsules were characterized by different experimental techniques. Fourier transform infrared spectroscopy analysis of the CM showed the presence of uronic acid units and sugars. Scanning electron microscopy revealed that most particles were adhered together, causing the formation of compact, linked agglomerates, which resulted in different microstructures with irregular shapes. All oil–core microcapsules were characterized, and the results showed that the different shell materials could be used to microencapsulate sunflower oil. Among them, the microcapsule crosslinked with CM and Chi was the most suitable, with the highest encapsulation efficiency (95 %). This coacervation led to the narrowest size distribution of the capsules, with diameters ranging from 1 to 5 μm. Optical microscopy confirmed the deposition of coacervate droplets around oil drops and clearly showed that the formation of coacervated particles and their deposition onto oil droplets were successive events.

Keywords: *Opuntia ficus indica*; extraction; microcapsules; mucilage cactus.

* Corresponding author. E-mail: y.moussaoui2@gmx.fr
https://doi.org/10.2298/JSC200229033E

INTRODUCTION

Encapsulation is a technique allowing the inclusion of solid, liquid or gaseous substances within a support material.[1] It leads to the formation of particles. This process appeared in the early 1950s in the food industry. Griffin patented a process for the preparation of oils in the form of solids.[2] In 1956, Green and Schleicher[3] prepared pressure-sensitive capsules for the production of carbonless paper by complex coacervation between gelatin and gum arabic. Thanks to this work, they are now considered to be the pioneers of microencapsulation. Among these, microencapsulation using coacervation methods has become one of the most attractive alternatives in the cosmetics industry, as well as in the pharmaceutical, agro-chemical and food industries.[4–9] This process may be either simple or complex. In the simple coacervation process, a single polymer is involved. However the interaction of two or more oppositely charged polyelectrolytes in aqueous form, usually proteins and polysaccharides, leads to complex coacervate formation and phase separation. Microencapsulation by coacervation is establish in three steps made under continuous agitation. The first step concerns the formation of three immiscible chemical stages namely, the assembly liquid, the core medium, and the coating material. The second one, consists of a coating deposition stage, when the core material is dispersed in a polymer coating solution. The last one is the coating rigidification, when the immiscible material becomes more rigid and strong, which generally concerns warm, cross-connect, or desolvation methods. In all cases, the size of the microcapsules could be in the region of 1–5000 μm. Each capsule has two phases, namely the core and the coating or matrix material. The release mechanism of active compounds could be as following: *i*) dissolution-controlled released dissolution of the matrix or encapsulated dissolution system; *ii*) diffusion-controlled monolithic system nonporous/microporous matrix; *iii*) diffusion-controlled reservoir system nonporous/microporous matrix; *iv*) ion-exchange-controlled release. Therefore, the choice of the appropriate wall material is an extremely important factor for a successful coacervation process. Indeed, the microcapsule wall material must protect the encapsulated substance from deterioration, must have the required mechanical strength, must allow controlled release, and it must have thermal properties compatible with the encapsulated substance.[6,10]

Polysaccharides, which are the most abundant biomolecules,[7,11–15] have been used as microencapsulation matrices due to their good solubility in water and their low viscosity, even at high concentrations.[10,11] Several researchers reported a large number of publications on microcapsules based on polysaccharides.[6,10] Chitosan (Scheme 1a) is the polysaccharide most widely used as a membrane for microcapsules due to its biocompatibility and biodegradability properties as well as its antimicrobial activity. It is a commercially available polysaccharide produced from crustacean waste. The main field of application of mic-

rocapsules based on natural polymer is biomedical, which explains the numerous studies on the salting-out properties of the active ingredients according to the characteristics of the capsule or the external environment. The most commonly used production process is layer-by-layer deposition (LbL) on a core that can be removed later. Given the large number of publications on this subject, we have chosen to highlight only systems with a certain particularity. Another polysaccharide namely, CMCNa, is cellulose derivative with good solubility in water. The derivative is obtained by substitution reaction of hydroxyalcohol groups by hydrophobic carboxymethyl groups at position 2, 3, and 6 (Scheme 1b). CMCNa presents a linear polymer chain containing 1,4-linked glycans and displays polyelectrolyte behavior due to weak acidic groups in the molecular backbone. The substitution degree (DS) is one of the major factors affecting the physicochemical behavior of CMCNa, which consequently leads to its many diversified applications, such as thickener, emulsion stabilizer, fat replacer in meat, binder, and film-forming properties.[16–18] Moreover, concerning the safety of human health and the environment, CMCNa is biocompatible, biodegradable, and nontoxic.

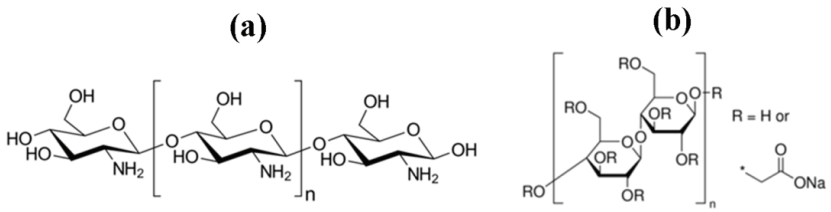

Scheme 1. a) Chitosan; b) CMCNa.

The mucilage extracted from the cladodes of OFI is a hetero-polysaccharide with a molecular weight varying from 2.3×10^4 to 3×10^6 g mol^{-1}, being a complex mixture of polysaccharides, L-arabinose (24.6–42 %), D-galactose (21–40.1 %), D-xylose (22–22.2 %), L-rhamnose (7–13.1 %) and D-galacturonic acid (8––12.7 %).[19,20] Moreover, the neutral mucilage polysaccharide extracted from OFI using ethanol as the extracting solvent is considered non-toxic and safe for human and animal consumption.[21–23]

The main advantage of natural polymers is their biocompatibility and biodegradability making them more easily usable for pharmaceutical or medical applications. In addition, due to the growing demand of biobased materials for future sustainability, chitosan and carboxymethyl cellulose based material and their applications will bring good future perspective in fundamental and applied aspects of new product formulations. Both chitosan and carboxymethyl cellulose present several properties which are affected by a change in pH, such as swelling behavior, which allows increasing the matrix volume of polyelectrolyte and polyelectrolyte complex upon changing the pH from acidic to basic conditions. In this

context, the present study was conducted to evaluate the viability of the formation of microcapsules using different shell materials (CM extracted from OFI, carboxymethyl cellulose sodium salt (CMCNa), and chitosan (Chi)). Microencapsulation was performed using a segregative coacervation method.[20] The interactions and the stoichiometry between the biopolymers used in complex coacervation, as well as the ratio between wall materials, are important parameters in the encapsulation process. Another goal of this study was to evaluate the effect of cross-linking on the morphological characteristics, particle sizes, and encapsulation efficiency.

EXPERIMENTAL

Materials

Mucilage powders extracted from OFI were used as wall materials to prepare oil microcapsules. The cladodes were harvested from the oasis of El-Metkides-Gafsa, southwest of Tunisia. The epidermal cells of the OFI were removed and washed several times with distilled water to remove sand and hydrophilic impurities. The cleaned OFI was cut into chips (1×1×1 cm^3).[24]

Sunflower oil (palmitic acid: 5–7.6 %; stearic acid: 2.7–6.5 %; oleic acid:14–39.4 %; linoleic acid 48.3–74 %) was kindly donated by the SAS PIVERT (Compiègne, France). All other chemicals used (sodium hydroxide (NaOH, 98 %), hydrochloric acid (HCl, 37 %), carboxymethyl cellulose sodium salt (CMCNa), chitosan (degree of deacetylation: 75 %) and a cationic surfactant (tetradecyltrimethylammonium bromide, TTAB, 99 %, CMC = 4–5 mmol L^{-1})) were obtained from Sigma–Aldrich and used without further purification.

Mucilage extraction

The obtained chips were homogenized using 1 L of distilled water per 1 kg of material. Subsequently, the mixture was mechanically stirred at 80 °C for 20 min to inactivate enzymes and left to cool to ambient temperature. After cooling, the suspension was filtered to separate the liquid from the solids, and the obtained suspensions were centrifuged. The pH of the obtained filtrate was fixed at the desired pH value by the addition of a solution of hydrochloric acid or sodium hydroxide. Then, the mucilage was recuperated by precipitating the filtrate with ethanol. Then, in order to accelerate the precipitation, the obtained solution was centrifuged, and, finally, the mucilage was dried at room temperature for 3 days to obtain a powder, which was stored at 4 °C until further use. All the experiments were performed in triplicate.

Microcapsule formation

Oil–core microcapsules were prepared by simple and complex coacervation methods. The first step of the microencapsulation process consisted of forming an oil-in-water emulsion. This emulsion was prepared from a continuous aqueous phase and a dispersed oil phase. The continuous phase was obtained by dissolution of TTAB in 100 mL of water under magnetic stirring at 600 rpm. Both phases were then vigorously dispersed with an ultra turrax high speed homogenizer (Ika T 25 basic, France) at room temperature (≈20 °C) and 11000 rpm for 15 min to create an oil in water emulsion. During the formation of surfactant stabilized emulsion, the oil–water interfaces must be covered with an adequate number of particles to stabilize the droplets by providing repulsive interactions between drops and lowering the interfacial tension. The final surfactant concentration is therefore at their corresponding *CMC* (about four times the *CMC* value).

For simple coacervation, particles were obtained by the dropwise addition of an aqueous solution CM into the prepared emulsion. The pH of the premix was then adjusted to 4.0 by adding hydrochloric acid, 0.1 mol L^{-1}, in order to cross-link the capsules. Finally, the mixture was stirred mechanically at room temperature for over 2 h. The upper aqueous-rich phase was removed and the coacervated rich phase was recovered and stored for further analyses.

The complex coacervation was basically the same as the simple coacervation except that the CM and CMCNa solutions were added to the pre-emulsion vessel.

In order to crosslink the capsules prepared with cactus mucilage and chitosan (CM/Chi), a Chi solution was prepared by dissolving 5 mg of polymer in 100 mL of 2 % aqueous acetic acid solution at pH 4. CM/Chi coacervation was obtained by the dropwise addition of CM and Chi solutions (pH 3.6) in the required proportions. Then, the CM solution was added, and coacervation between the oppositely charged Chi and carboxylic groups of the CM started to form a thin coating layer around the core material. After 30 min, a 1 mol L^{-1} sodium hydroxide solution was added and the pH was adjusted to 8 to complete the coacervation reaction. All the experiments were performed in triplicate.

Characterization

Fourier transform infrared spectroscopy (FTIR) was used in this study to identify functional groups of the prepared CM powder. The spectra of the samples were recorded in the range of 4000–500 cm^{-1} in KBr pellets using a Shimadzu 8400S spectrometer (France) with a resolution of 4 cm^{-1}.

The particle size distribution of the powdered CM, the emulsions, and the suspensions of microcapsules was investigated by laser diffraction using a Mastersizer X Malvern (laser Cilas 1190, France). The sample was dispersed in aqueous medium under mechanical stirring for 2 min. The technique is based on measurement of the intensity of light scattered as a laser beam passes through a dispersed particulate sample. The test was repeated at least in triplicate and the difference between the various values obtained was within an experimental error of 5 %.

Scanning electron microscopy (SEM) was used to investigate the morphology of the different power microcapsules. The micrographs were recorded with a Zeiss-Ultra 55 SEM device, operating at 10 kV. The dried samples were fixed on SEM stubs using a double sided tape and coated with gold metal under high-vacuum evaporator.

The particle shape and surface morphology of the obtained particles were examined using optical microscopy (Axio Imager, Zeiss, Marly-le-Roi, France).

Carboxylic groups in the CM powder obtained at different supernatant pH values were quantified by conductometric titration. The CM sample (30 mg) was added to a beaker. and 200 mL of distilled water was added. The obtained solution was stirred for 10 min and ultrasonicated in order to obtain a well-dispersed suspension. Conductometric titration was performed using a 0.01 mol L^{-1} NaOH or HCl solutions. The number of functional groups is given by the following equation:

$$X = \frac{C(V_2 - V_1)}{w} \quad (1)$$

where X / μmol g^{-1} is the total acidic group content, C / μmol L^{-1} is the concentration of the sodium hydroxide solution, V_1 and V_2 in L are the amounts of NaOH or HCl, and w / g is the oven-dried weight of the sample. The test was repeated at least in triplicate and the difference between the various values obtained was within an experimental error of 5 %.

The encapsulation efficiency (*EE*) was evaluated according the procedure reported by Bae and Lee,[25] and Carneiro *et al.*[26] Fifteen milliliters of hexane were added to 1.5 g of pow-

der in a glass jar with a lid, which was shaken by hand for the extraction of free oil, during 2 min, at room temperature. The solvent mixture was filtered through a Whatman filter paper No. 1 and the powder collected on the filter was rinsed three times with 20 mL of hexane. Then, the solvent was left to evaporate until constant weight. The non-encapsulated oil (surface oil) was measured by weight difference between the initial clean flask and that contained the extracted oil residue. The total oil was assumed to be equal to the initial oil, since preliminary tests revealed that all the initial oil was retained, which was expected, since flax seed oil is not volatile. *EE* was calculated from the following equation:

$$EE, \% = 100\frac{\text{Total amount of oil} - \text{Surface oil}}{\text{Initial amount of oil}} \quad (2)$$

The test was repeated at least in triplicate and the difference between the various values obtained was within an experimental error of 5 %.

RESULTS AND DISCUSSION

Physicochemical characterization of mucilage powder

The FTIR spectrums of CM samples (Fig. 1) revealed typical absorption bands of polysaccharide between 800 and 1200 cm^{-1}, which is overpowered by ring vibrations overlapped with the characteristic vibrational modes of the pyranose ring.[27–29]

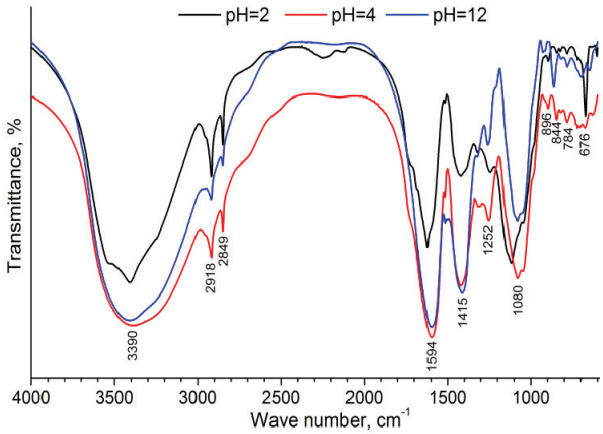

Fig. 1. FTIR spectra of different CM samples.

The absorption bands at 896 and 844 cm^{-1} indicate that the two configuration (α- and β-D-glucose) exist and that α-D-glucose was the major linkage.[27,30] The bands at 784 and 676 cm^{-1} are attributed to out-of-plane N–H and O–H vibrations, respectively.[31] The adsorption bands at 1252 and 1080 cm^{-1} result from vibration bonds C–O, C–C, O–H and C–O–C of the mucilage molecules.[32–34] Indeed, the wave numbers at 1594 and 1415 cm^{-1} are attributed to asymmetric and symmetric stretching vibration of deprotonated carboxylic acid groups (COO^-), probably due to the presence of uronic acid in CM samples.[31–36] In

addition, the band around 3390 cm^{-1} reflects the stretching vibration of the hydroxyl groups (–OH) and amine groups. While, the absorption bands around 2918 and 2849 cm^{-1} were assigned to asymmetric vibrations of C–H and methoxyl groups (CH_3O) in the CM samples.[32,33,37]

A wide distribution of particle size, as well as irregular morphology and different heterogeneous microstructures of the CM were observed by SEM (Fig. 2).

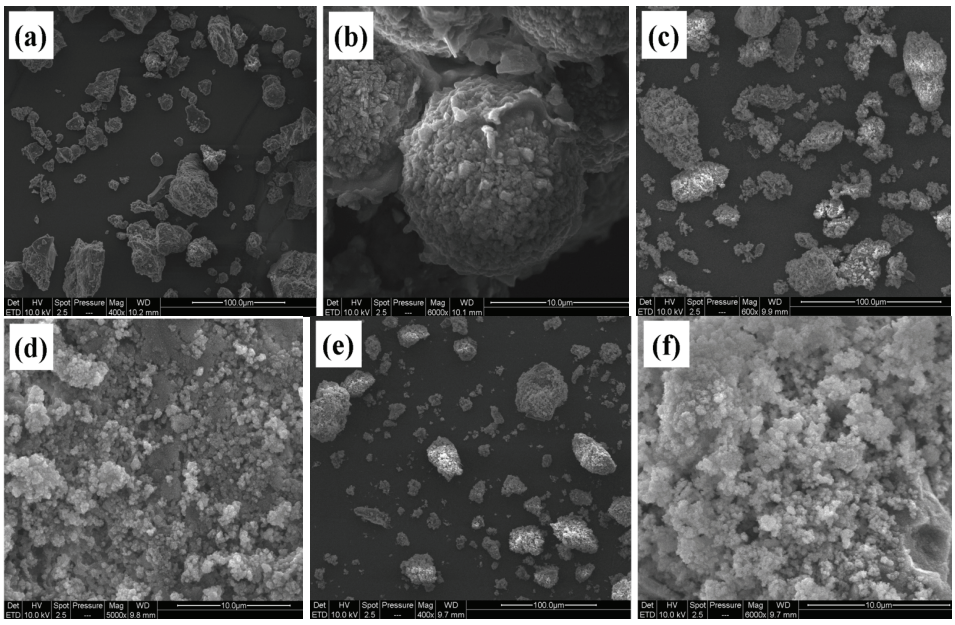

Fig. 2. Micrographics of CM powder ethanol extracted and precipitated at different pH values, 2 (a, b), 4 (c, d) and 12 (e, f).

The strong aggregation observed in the mucilaginous extracts obtained from OFI can lead to the formation of compact, bound agglomerates. Mucilaginous extracts obtained at pH 4 and 12 included various microstructures. The particles were interpenetrated at random in the entangled matrix of the polysaccharide chains. The agglomeration could be attributed to the effects of ionic crosslinking by calcium ions initially present in the sample. Indeed, Ca^{2+} and other metal ions naturally present in the CM[38] can enhance the ionic interactions between the dissociated carboxyl groups. The strong aggregation observed in the CM obtained from OFI agrees with that reported by Du Toit *et al.*[39] However, an obvious difference and incomplete crosslinking was observed in the microstructure of the CM obtained at pH 2. This CM had a spongy structure of spherical aggregates of irregular shape at different sizes, formed by the adhesion and superposition of polymeric chains. These observations suggest that chelation has a significant

effect on morphology and that metal ions can contribute to the formation of compact, bound agglomerates with sufficient dissociated carboxyl groups.[40]

The average particle size, as determined by laser diffraction analysis, was established and the results are shown in Fig. 3. The dried CM powder had almost the same particle size distribution and consisted of fine particles within the range 46 to 595 μm. The presence of very small particles facilitated a greater number of particle-to-particle interactions and, subsequently, the formation of agglomerates. The polysaccharides obtained at basic pH contained the highest number of carboxyl groups, and the number of carboxylic groups depended on the pH. Thus, the concentrations of carboxylic groups were 0.733, 0.870 and 3.033 μmol g^{-1} for the CM obtained at pH 2, 4 and 12, respectively.

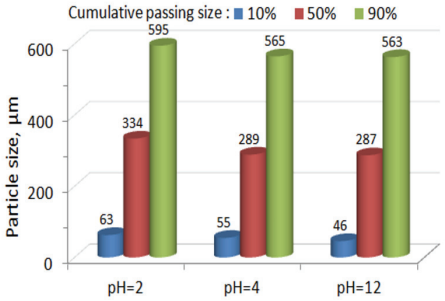

Fig. 3. Particle size distribution of the CM samples.

Physicochemical characterization of the emulsion and microcapsules

Particle size is an important parameter in microencapsulation because it influences the texture and sensory aspects of particles and it defines their applications. The stable, primary emulsions of oil were used for the preparation of the microcapsules by different coacervation methods. After addition of surfactants, stable oil-in-water emulsions were successfully prepared using CMC concentrations. The average particle sizes of the emulsions ranged from 0.45 to 4 μm (Fig. S-1 of the Supplementary material to this paper). The size distribution curves (Fig. S-1) showed unimodal and homogenous distributions (the diameters were distributed in a single peak). An image of these emulsion drops is shown in Fig. S-1 showing bleaching of the aqueous phase caused by displacement of the particles from the drops to the continuous phase. These emulsion drops remained stable for at least 6 months with no measurable change in the size distribution of the drop. This due to the ability of TTAB surfactant to minimize the energy required for emulsion formation by reducing the liquid–liquid interfacial tension and the formation of electrostatic or steric barriers around the droplet surfaces.

The average diameters of the microcapsules obtained by simple coacervation ranged from 50 to 400 μm (Fig. 4), which confirms that there was flocculation on the surface, with a hard and difficult to break shell. This could be associated with

the process conditions, including emulsion preparation, the cooling rate, and the characteristics of the wall and core materials.

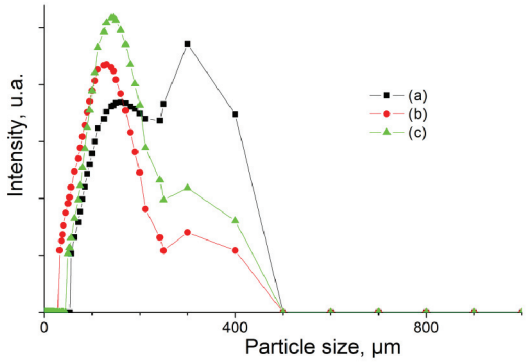

Fig. 4. Particle size distribution of microcapsule suspensions *via* simple coacervation at pH 4 crosslinked by CM precipitated at pH: 12 (a), 4 (b) and 2 (c).

Likewise, increasing the core-to-wall ratio increases the size of the microcapsules and their distribution. Increasing the proportion of encapsulating polymer or reducing the velocity of stirring resulted in increasing microcapsule size.

However, despite the small difference observed in the particle size distribution of the emulsions and the corresponding suspensions of microcapsules prepared using CM/CMCNa and CM/Chi by complex coacervation (Figs. 5 and 6), the microcapsules were successfully prepared, and were stable. This is probably related to the increase in the number of crosslinks, leading to strengthening of the walls of the microparticles.[41] Thus, the addition of the anionic polymer CMCNa with the CM solution to the prepared emulsion results in electrostatic repulsion between the biopolymers, leading to phase separation and coacervate formation. Subsequently, these coacervates form deposits around the sunflower oil droplets.

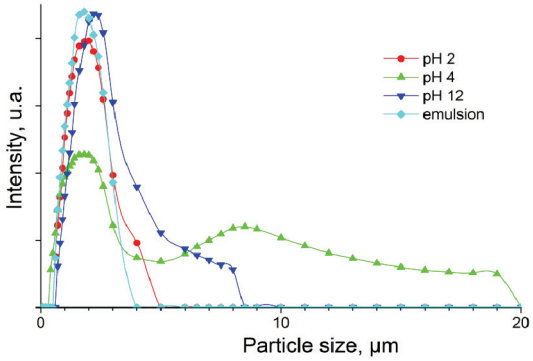

Fig. 5. Particle size distribution of emulsions and microcapsule suspensions *via* complex coacervation at pH 4 crosslinked with CMCNa and CM precipitated at different pH values.

A slight variation was observed between the emulsions and the corresponding suspensions of microcapsules, especially with the use of Chi. This lead to a much narrower size distribution, with diameters that ranged from 1 to 5 μm. The

ability of Chi and CM to form a very thin coating layer can be explained by the electrostatic attractions between oppositely charged biopolymers. These interactions induce the formation of complexes, which can be insoluble, and they are closely related to the pH of the two solutions, as well as the weight ratio of the CM/Chi mixtures. Chi developed a positively charged surface in the acidic aqueous medium due to the presence of amino groups, and CM displayed a net negative charge.[42]

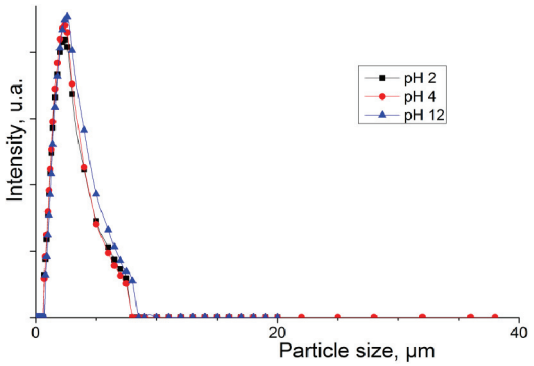

Fig. 6. Particle size distribution of microcapsule suspensions *via* complex coacervation precipitated at pH 8 and crosslinked with Chi and CM obtained at different pH values.

The electrostatic interactions in the aqueous system between the protonated Chi amino groups and the negatively charged COO– groups of CM were due to the formation of a stable polyelectrolyte complex at pH 8. Therefore, a barrier was built around the sunflower oil by the formation of additional functional groups, primarily azomethin linkage groups (>C=N<) and, secondly, acetal linkages (–C–O–C–O–C–).[43] The particle size of the obtained microcapsules was confirmed by optical observation. Thus, microcapsules were prepared by simple and complex coacervation *via* mucilaginous cactus extracts. It is clear that the active ingredient was well surrounded and protected by the coacervate deposits (Fig. S-2 of the Supplementary material).

Optical observation analysis revealed that the microparticles obtained by complex coacervation were round, with various sizes and a polynuclear distribution of the core material (Figs. S-3 and S-4 of the Supplementary material). These results were related to the different cactus extract compositions and their influences on the diffusivity and film formation properties of these extracts.

The effect of wall material on encapsulation efficiency (EE) of sunflower oil is recapitulated in Fig. 7. It could be observed that the encapsulation efficiencies of the microcapsules obtained by complex coacervation and crosslinked with Chi and CM are different than those of the system CM/CMCNa. For the former system. CM/Chi, the EE values ranged from 87 to 95 %. Whereas, the encapsulation efficiencies for the latter system, CM/CMCNa, varied from 65 to 72 %. It could be concluded that it is possible to use the different cactus extracts as carrier mat-

erials to protect sensitive compounds. The results also showed that the suggest methodology (complex coacervation *via* CM/Chi) and the chosen encapsulation polymers were adequate and very effective for the proposed goal.

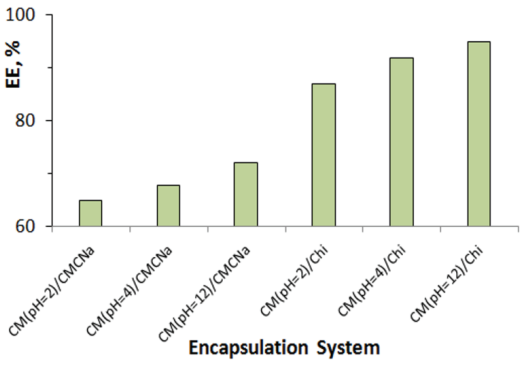

Fig. 7. Effect of wall material on encapsulation efficiency (*EE*) of sunflower oil.

CONCLUSIONS

This work consisted of developing bio-based microcapsules using CM and CMCNa as well as chitosan. which are the polysaccharides most commonly used in virtually all the reported microencapsulation methods. It can be highlighted from the results that CM is a promising agent for the microencapsulation of bioactive molecules. The microcapsules crosslinked with Chi and different cactus extracts had sufficient stabilities needed to maintain their structures, with good entrapment efficiency (87 to 95%) compared to those crosslinked with CMCNa or only with CM. The morphologies and particle sizes of the resultant microcapsules were influenced by the polymer type. Optical observation confirmed that core–shell morphology existed in all types of capsules, with spherical morphologies and smooth surfaces. The integrated data indicated that the sunflower oil was successfully encapsulated by complex coacervation using the cactus extract as the carrier material. Moreover, CM could be used as a potentially effective shell material, especially with a cationic polymer, for protection of bioactive compounds from oxidative deterioration and for drug delivery.

SUPPLEMENTARY MATERIAL

Additional data are available electronically at the pages of journal website: https://www.shd-pub.org.rs/index.php/JSCS/index, or from the corresponding author on request.

Acknowledgements. The authors would like to express their deep gratitude to Mohamed Naceur Belgacem, Professor and Director of the Grenoble INP-Pagora, for his valuable advice and assistance, as well as to the Tunisian Ministry of Higher Education for the financial support.

И З В О Д

ПРИМЕНА СЛУЗИ ИЗОЛОВАНЕ ИЗ КАКТУСА *Opuntia ficus indica* као ОПНЕ ЗА МИКРОИНКАПСУЛАЦИЈУ

HANEDI ELHLELI[1,2], FATEN MANNAI[1], RAMZI KHIARI[3-5] и YOUNES MOUSSAOUI[6,7]

[1]Materials, Environment and Energy Laboratory (UR14ES26), Faculty of Sciences of Gafsa, University of Gafsa, Tunisia, [2]Faculty of Sciences of Gabes, University of Gabes, Tunisia, [3]University of Monastir, Faculty of Sciences, UR13 ES 63 - Research Unity of Applied Chemistry & Environment, 5000 Monastir, Tunisia, [4]Higher Institute of Technological Studies of Ksar Hellal, Department of Textile, Tunisia, [5]University of Grenoble Alpes, CNRS, Grenoble INP, LGP2, F-38000 Grenoble, France, [6]Organic Chemistry Laboratory (LR17ES08), Faculty of Sciences of Sfax, University of Sfax, Tunisia и [7]Faculty of Sciences of Gafsa, University of Gafsa, Tunisia

У раду је испитано стварање микрокапсула користећи природне биополимере, као што су слуз кактуса (CM), натријумова со карбоксиметил целулозе (CMCNa) и хитозан (Chi), за транспорт и доставу уља сунцокрета. CM узорци су екстраховани из *Opuntia ficus indica* (OFI) таложењем супернатанта на различитим pH (2, 4 и 12). Екстраховани природни полисахарид и формиране микрокапсуле су окарактерисане различитим методама. Инфрацрвена спектроскопија са Фуријеовом трансформацијом (FTIR) CM је указала на присуство јединица уронске киселине и шећера. Скенирајућа електронска микроскопија (SEM) је показала да је већина честица атхерирала стварајући компактне агломерате, дајући различите микроструктуре неправилних облика. Резултати су показали да се могу користити опне од различитог материјала за инкапсулацију уља сунцокрета. Највећу ефикасност су исказале микрокапсуле са умреженим CM и Chi (95 %). Ови коацервати су имали најмањи опсег величине капсула, пречника од 1 до 5 μm. Оптичком микроскопијом је потврђено окруживање капи уља капима коацервата.

(Примљено 29. фебруара, ревидирано 17. априла, прихваћено 19. маја 2020)

REFERENCES

1. C. Thies, in *Encyclopiedia of Polymer Science Engineering*, H. F. Mark, N. M. Bikales, C. G. Overberger, G. Menges (Eds.), 2nd ed., Vol. 9, Wiley, 1987. pp. 724–745 (ISBN: 9780471809418)
2. W. C. Griffin, *Solid essential oil concentrate and process of preparing the same* (1951), U. S. Patent No. 2,556,410
3. B. K. Green, L. Scheleicher, *Manifold record material* (1956), U. S. Patent No. 2,730,456
4. A. Gharsallaoui, *Food Res. Int.* **40** (2007) 1107 (https://doi. org/10. 1016/j. foodres. 2007. 07. 004)
5. R. R. Esfahani, H. Jun, S. Rahmani, A. Miller, J. Lahann, *ACS Omega* **30** (2017) 2839 (https://doi. org/10. 1021/acsomega. 7b00570)
6. B. Gomez, F. J. Barba, R. Domínguez, P. Putnik, D. B. Kovacevic, M. Pateiro, F. Toldra, J. M. Lorenzo, *Trends Food Sci. Tech.* **82** (2018) 135 (https://doi. org/10. 1016/j. tifs. 2018. 10. 006)
7. G. Ozkan, P. Franco, I. De Marco, J. Xiao, E. Capanoglu, *Food Chem.* **272** (2019) 494 (https://doi. org/10. 1016/j. foodchem. 2018. 07. 205)
8. G. Orive, E. Santos, J. L. Pedraz, R. M. Hernandez, *Adv. Drug Deliver Rev.* **67**–**68** (2014) 3 (https://doi. org/10. 1016/j. addr. 2013. 07. 009)
9. L. Zhao, J. Luo, H. Wang, G. Song, G. Tang, *Appl. Therm. Eng.* **99** (2016) 495 (http://dx. doi. org/10. 1016%2Fj. applthermaleng. 2015. 12. 111)
10. A. Nesterenko, I. Alric, F. Silvestre, V. Durrieu, *Ind. Crop. Prod.* **42** (2013) 469 (https://doi. org/10. 1016/j. indcrop. 2012. 06. 035)

11. B. N. Estevinho, F. Rocha, *Application of Biopolymers in Microencapsulation Processes, Biopolymers for Food Design*, *Handbook of Food Bioengineering*, Elsevier, 2018, p. 191 (ISBN: 9780128115015)
12. T. A. Comunian, C. S. Favaro-Trindade, *Food Hydrocolloids* **61** (2016) 442 (https://doi. org/10. 1016/j. foodhyd. 2016. 06. 003)
13. I. J. Joye, D. J. McClements, *Curr. Opin. Colloid Interface Sci.* **19** (2014) 417 (https://doi. org/10. 1016/j. cocis. 2014. 07. 002)
14. G. K. Kouassi, V. Gogineni, T. Ahmad, N. M. Gowda, M. S. Boley, N. Koissi, in *Advances in Applied Nanotechnology for Agriculture*; Б. Park, M. Appell (Eds.), A*CS Symposium Series* **1143** (2013) pp. 221–234
15. C. Schmitt, C. Sanchez, S. Desobry-Banon, J. Hardy, *Crit. Rev. Food Sci.* **38** (1998) 689 (https://doi. org/10. 1080/10408699891274354)
16. R. Khiari, N. Meksi, M. F. Mhenni, M. N. Belgacem, E. Mauret, *Fiber Polym.* **12** (2011) 587 (https://doi. org/10. 1007/s12221-011-0587-1)
17. S. Mansouri, R. Khiari, F. Bettaieb, A. El-Gendy, M. F. Mhenni, *J. Polym. Environ.* **23** (2015) 190 (https://doi. org/10. 1007/s10924-014-0691-6)
18. I. Moussa, R. Khiari, A. Moussa, M. N. Belgacem, M. F. Mhenni, *Fiber. Polym.* **20** (2019) 933 (https://doi. org/10. 1007/s12221-019-8665-x)
19. L. Medina-Torres, E. Brito-De La Fuente, B. Torrestiana-Sanchez, R. Katthain, *Food Hydrocolloids* **14** (2000) 417 (https://doi. org/10. 1016/S0268-005X(00)00015-1)
20. C. Sáenz, E. Sepúlveda, B. Matsuhiro, *J. Arid Environ.* **57** (2004) 275 (https://doi. org/10. 1016/S0140-1963(03)00106-X)
21. I. Sanchez-Ortega, B. E. Garcia-Almendarez, E. M. Santos-Lopez, L. R. Reyes-Gonzalez, C. Regalado, *Food Hydrocolloids* **52** (2016) 906 (https://doi. org/10. 1016/j. foodhyd. 2015. 09. 004)
22. A. Bernardino-Nicanor, E. N. Hinojosa-Hernandez, J. M. S. Juarez-Goiz, J. L. Montanez-Soto, M. E. Ramirez-Ortiz, L. Gonzalez-Cruz, *J. Food Sci. Tech.* **52** (2015) 343 (https://doi. org/10. 1007/s13197-013-0989-8)
23. A. K. Nayak, D. Pal, D. R. Pany, B. Mohanty, *J. Adv. Pharm. Technol. Res.* **1** (2010) 338 (https://dx. doi. org/10. 4103%2F0110-5558. 72430)
24. F. Mannai, M. Ammar, J. G. Yanez, E. Elaloui, Y. Moussaoui, *J. Polym. Environ.* **26** (2018) 798 (https://doi. org/10. 1007/s10924-017-0968-7)
25. E. K. Bae, S. J. Lee, *J. Microencapsul.* **25** (2008) 549 (https://doi. org/10. 1080/02652040802075682)
26. H. C. F. Carneiro, R. V. Tonon, C. R. F. Grosso, M. D. Hubinger, *J. Food Eng.* **115** (2013) 443 (https://doi. org/10. 1016/j. jfoodeng. 2012. 03. 033)
27. N. Bayar, M. Kriaa, R. Kammoun, *Int. J. Biol. Macromol.* **92** (2016) 441 (https://doi. org/10. 1016/j. ijbiomac. 2016. 07. 042)
28. N. Bayar, T. Bouallegue, M. Achour, M. Kriaa, R. Kammoun, A. Bougatef, *Food Chem.* **235** (2017) 275 (https://doi. org/10. 1016/j. foodchem. 2017. 05. 029)
29. O. Ishurd, F. Zgheel, M. Elghazoun, M. Elmabruk, A. Kermagi, J. F. Kennedy, C. J. Knill, *Carbohyd. Polym.* **82** (2010) 848 (https://doi. org/10. 1016/j. carbpol. 2010. 06. 006)
30. H. Zeng, S. Miao, Y. Zhang, S. Lin, Y. Jian, Y. Tian, B. Zheng, *Food Hydrocolloids* **52** (2016) 126 (https://doi. org/10. 1016/j. foodhyd. 2015. 05. 028)
31. M. M. Zhao, N. Yang, B. Yang, Y. Jiang, G. Zhang, *Food Chem.* **105** (2007) 1480 (https://doi. org/10. 1016/j. foodchem. 2007. 05. 031)

32. J. L. Rivera-Corona, F. Rodríguez-Gonzalez, R. Rendon-Villalobos, E. García-Hernandez, J. Solorza-Feria, *LWT - Food Sci. Technol.* **59** (2014) 806 (https://doi. org/10. 1016/j. lwt. 2014. 06. 011)
33. M. C. Otálora, J. A. G. Castaño, A. Wilches-Torres, *LWT - Food Sci. Technol.* **112** (2019) 108234 (https://doi. org/10. 1016/j. lwt. 2019. 06. 001)
34. V. E. Manhivi, S. Venter, E. O. Amonsou, T. Kudanga, *Carbohyd. Polym.* **195** (2018) 163 (https://doi. org/10. 1016/j. carbpol. 2018. 04. 062)
35. R. Gheribi, L. Puchot, P. Verge, N. Jaoued-Grayaa, M. Mezni, Y. Habibi, K. Khwaldia, *Carbohyd. Polym.* **190** (2018) 204 (https://doi. org/10. 1016/j. carbpol. 2018. 02. 085)
36. Q. Guo, S. W. Cui, Q. Wang, X. Hu, Q. Guo, K. Ji, R. Yada, *Carbohyd. Polym.* **86** (2011) 831 (https://doi. org/10. 1016/j. carbpol. 2011. 05. 034)
37. Y. L. Han, J. Gao, Y. Y. Yin, Z. Y. Jin, X. M. Xu, H. Q. Chen, *Carbohyd. Polym.* **151** (2016) 381 (https://doi. org/10. 1016/j. carbpol. 2016. 05. 085)
38. F. Mannai, M. Ammar, J. G. Yanez, E. Elaloui, Y. Moussaoui, *Cellulose* **23** (2016) 2061 (https://doi. org/10. 1007/s10570-016-0899-9)
39. A. Du Toit, M. De Wit, A. Hugo, *Molecules* **23** (2018) 916 (https://doi. org/10. 3390/molecules23040916)
40. J. Y. Yin, S. P. Nie, J. Li, C. Li, S. W. Cui, M. Y. Xie, *J. Agr. Food Chem.* **60** (2012) 7981 (https://doi. org/10. 1021/jf302052t)
41. H. Guo, X. Zhao, *J. Microencapsul.* **25** (2008) 221m (https://doi. org/10. 1080/02652040701861828)
42. J. C. Roy, F. Salaün, S. Giraud, A. Ferri, J. Guan, *Carbohyd. Polym.* **173** (2017) 202 (https://doi. org/10. 1016/j. carbpol. 2017. 06. 001)
43. H. Zhang, X. Wang, *Sol. Energy Mat. Sol. Cells* **93** (2009) 1366 (https://doi. org/10. 1016/j. solmat. 2009. 02. 021).

Journal of the Serbian Chemical Society
JSCS-info@shd.org.rs • www.shd.org.rs/JSCS
J. Serb. Chem. Soc. 86 (1) S1–S4 (2021) *Supplementary material*

SUPPLEMENTARY MATERIAL TO

The use of mucilage extracted from *Opuntia ficus indica* as a microencapsulating shell

HANEDI ELHLELI[1,2], FATEN MANNAI[1], RAMZI KHIARI[3–5] and YOUNES MOUSSAOUI[6,7]*

[1]*Materials, Environment and Energy Laboratory (UR14ES26), Faculty of Sciences of Gafsa, University of Gafsa, Tunisia,* [2]*Faculty of Sciences of Gabes, University of Gabes, Tunisia,* [3]*University of Monastir, Faculty of Sciences, UR13 ES 63 - Research Unity of Applied Chemistry & Environment, 5000 Monastir, Tunisia,* [4]*Higher Institute of Technological Studies of Ksar Hellal, Department of Textile, Tunisia,* [5]*University of Grenoble Alpes, CNRS, Grenoble INP, LGP2, F-38000 Grenoble, France,* [6]*Organic Chemistry Laboratory (LR17ES08), Faculty of Sciences of Sfax, University of Sfax, Tunisia and* [7]*Faculty of Sciences of Gafsa, University of Gafsa, Tunisia*

J. Serb. Chem. Soc. 86 (1) (2021) 25–38

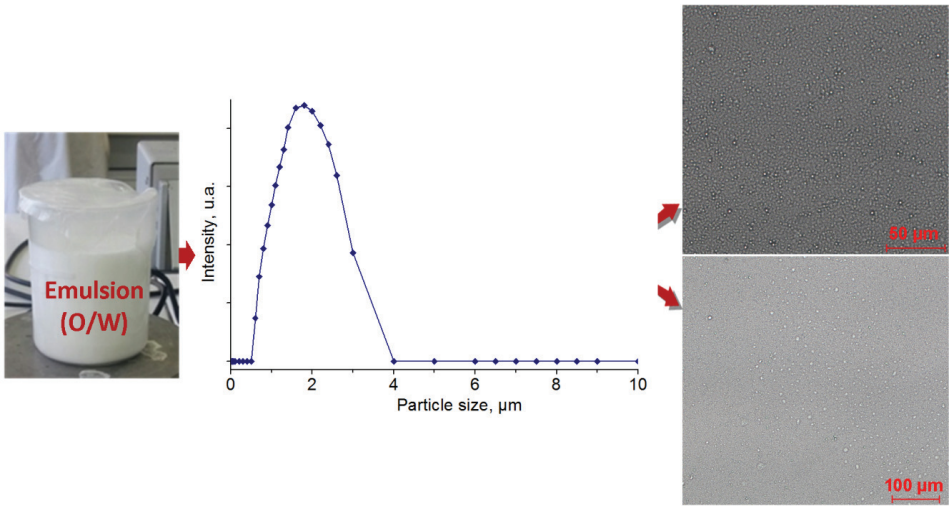

Fig. S-1. Optical observation and particle size distribution of sunflower oil emulsion.

* Corresponding author. E-mail: y.moussaoui2@gmx.fr

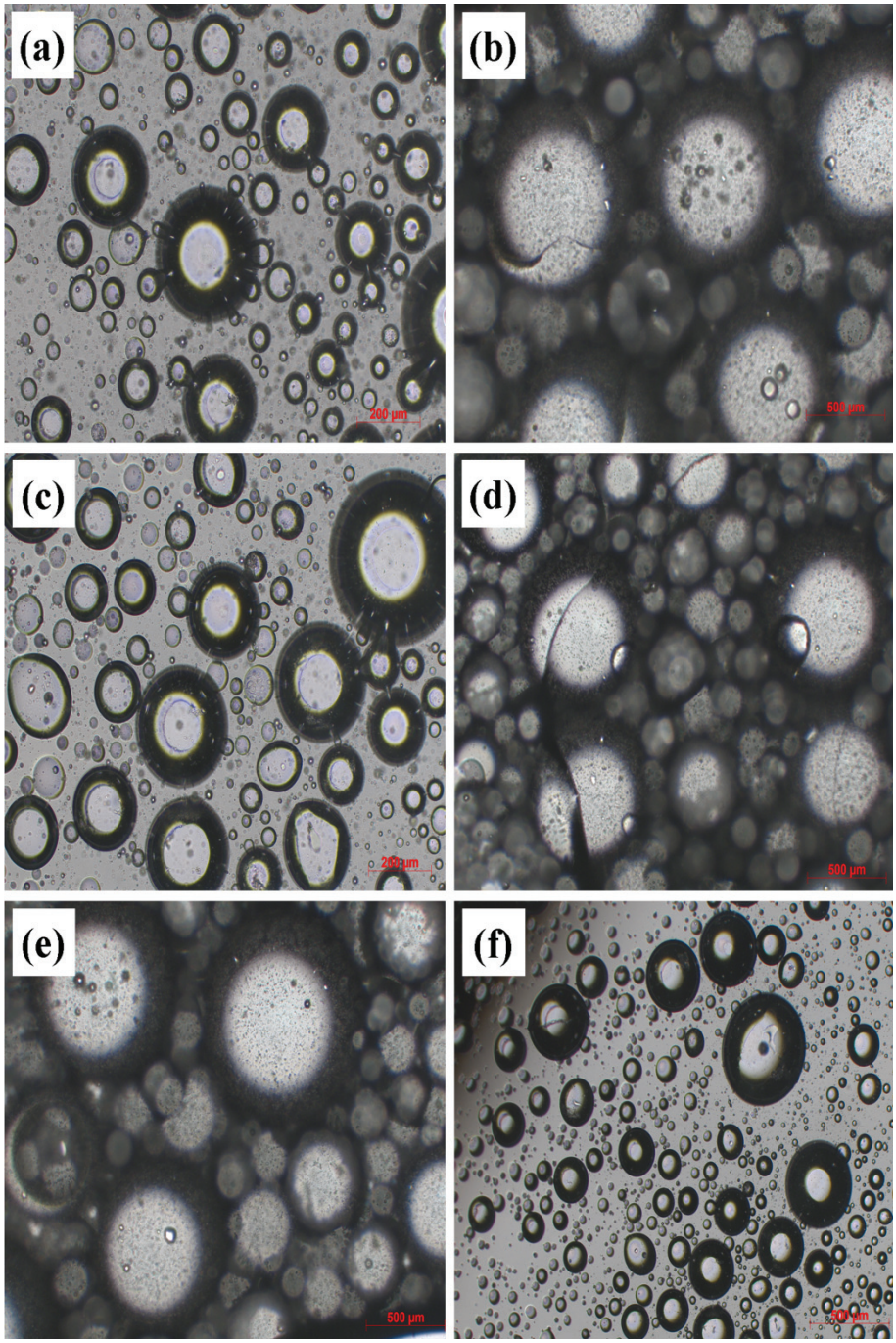

Fig. S-2. Microphotographs of microcapsules prepared by simple coacervation using CM obtained at pH 2 (a, b), pH 4 (c, d) and pH 12 (e, f).

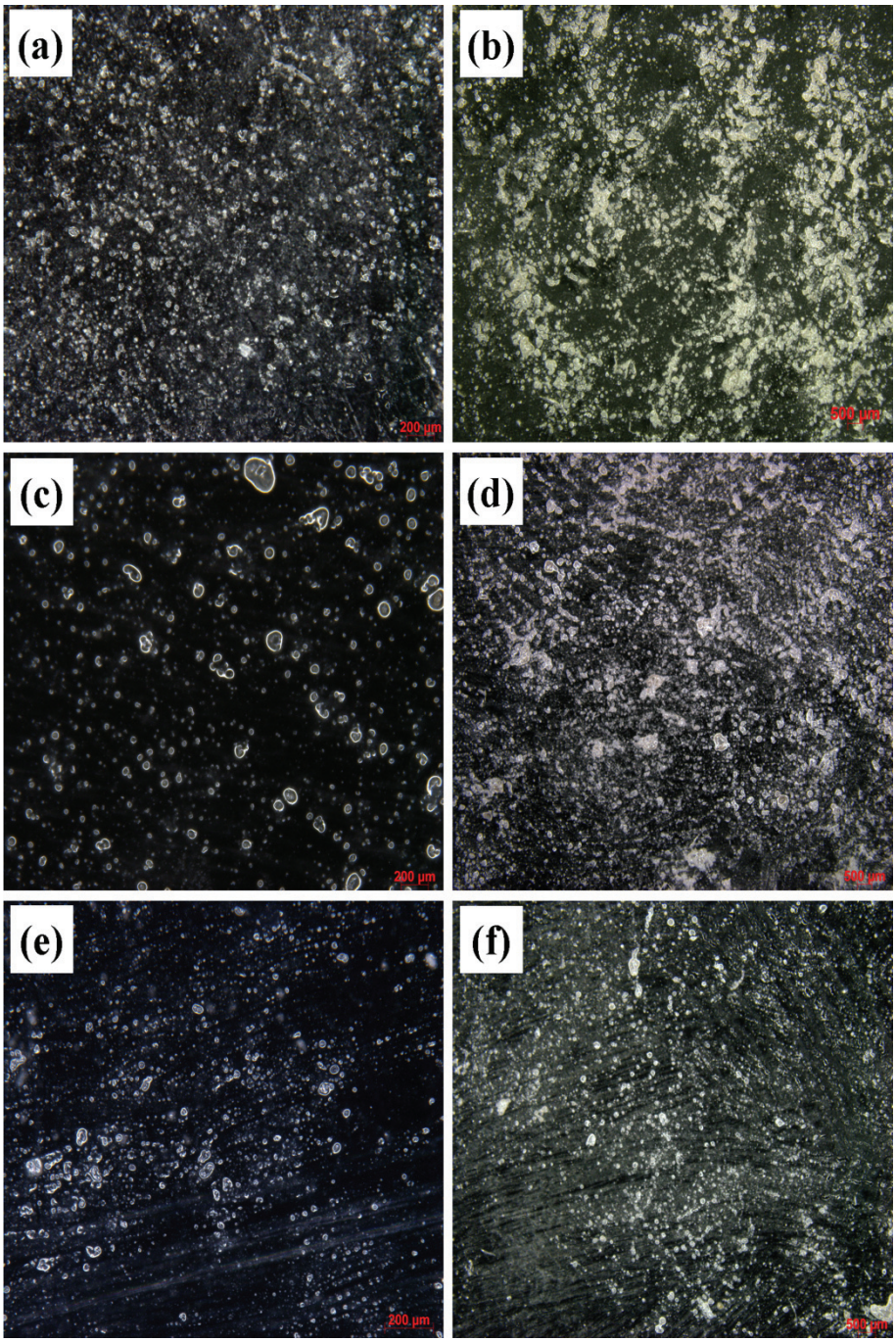

Fig. S-3. Microphotographs of microcapsules obtained by complex coacervation *via* CMCNa and different CM precipitated at pH 2 (a, b), pH 4 (c, d) and pH 12 (e, f).

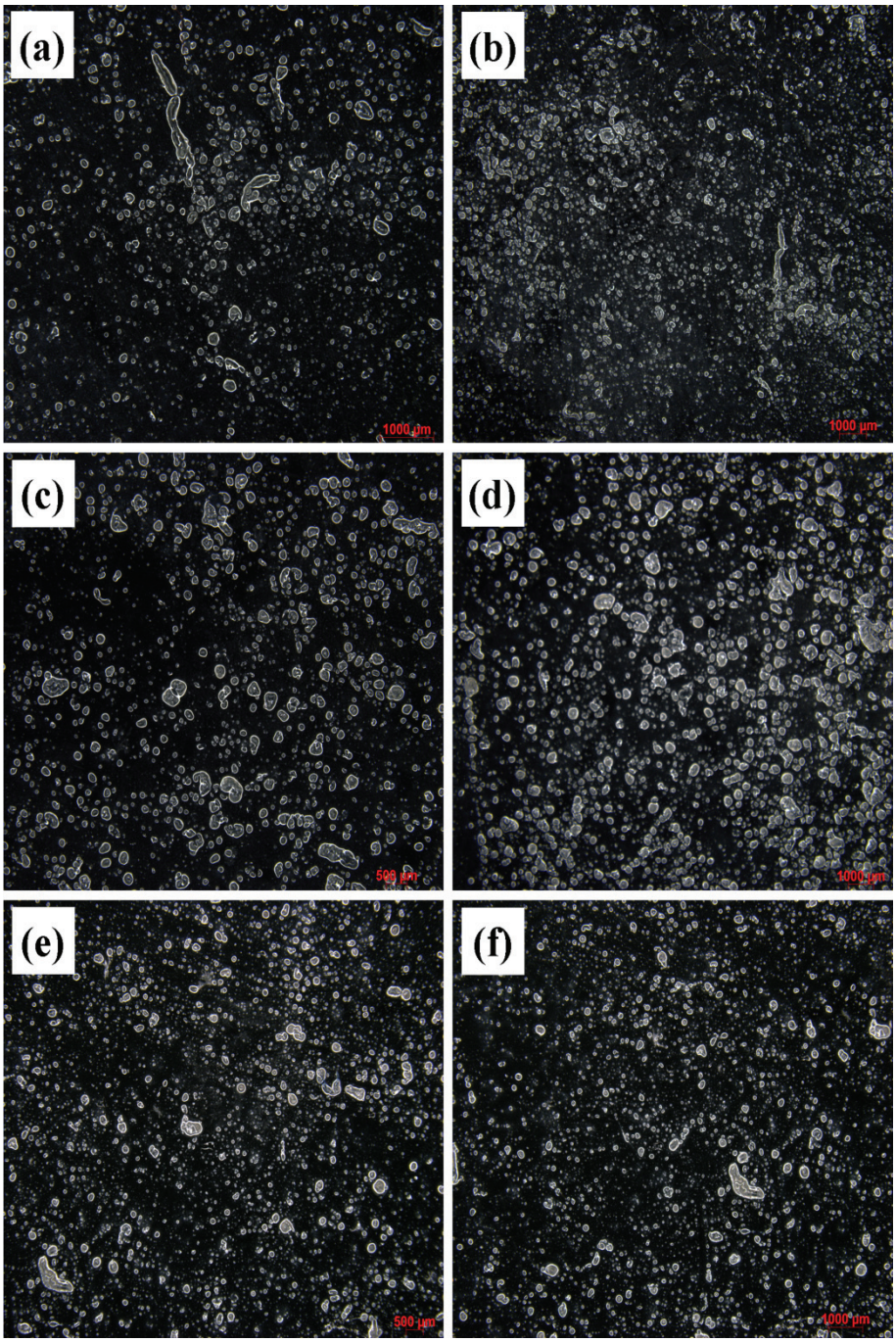

Fig. S-4. Microphotographs of microcapsules obtained by complex coacervation *via* chitosan and CM precipitated at pH 2 (a, b), pH 4 (c, d) and pH 12 (e, f).

Journal of the Serbian Chemical Society
JSCS-info@shd.org.rs • www.shd.org.rs/JSCS
J. Serb. Chem. Soc. *86* (1) 39–49 (2021)
JSCS–5402
Original scientific paper

Schiff bases of 1,5-diarylpent-4-ene-1,3-diones and their metal complexes: Synthesis, characterization and fluorescent studies

MUHAMMED BASHEER UMMATHUR[1]*, RADHIKA PALLIKKAVIL[2] and KRISHNANNAIR KRISHNANKUTTY[2]

[1]*Department of Chemistry, KAHM Unity Women's College, Manjeri, Kerala-676122, India and* [2]*Department of Chemistry, University of Calicut, Kerala-673635, India*

(Received 20 May, revised 27 September, accepted 28 September 2020)

Abstract: Four Schiff bases (H_2L^1 to H_2L^4) were synthesized by the condensation of *o*-aminophenol and unsaturated diketones (1,5-diarylpent-4-ene-1,3--diones). Analytical, IR, ^{1}H-NMR and mass spectral data revealed their existence in the imine–enamine form. Dibasic tetradentate coordination of the Schiff bases in their ML complexes (M = Cu(II), Ni(II), Co(II), Zn(II), Cd(II), and Hg(II)) was established based on physical, analytical and spectral data. The fluorescent studies of H_2L^4 showed that the fluorescence emission maxima shifted with increasing polarity and hydrogen bonding ability of the solvent. Paramagnetic Cu(II), Ni(II) and Co(II) ions decrease the fluorescence intensity with increasing concentration of the metal ion while diamagnetic Zn(II), Cd(II) and Hg(II) ions have very little influence on the fluorescence intensity of the Schiff base H_2L^4.

Keywords: *o*-aminophenol; imine–enamine form; tetradentate coordination; spectral data.

INTRODUCTION

In polycarbonyl compounds, Schiff base condensation can occur with more than one carbonyl function that normally results in the formation of polydentate chelating ligand systems having interesting properties.[1,2] Metal complex formation of these Schiff's bases depends on the type and nature of functional groups present in the vicinity of the azomethine group.[3,4] Most of the reported Schiff's bases of 1,3-diketones are based on compounds in which the diketo function is directly attached to alkyl/aryl functions.[5–7] Only very few reports are available on Schiff's bases of unsaturated 1,3-diketones.[8–10] Many naturally occurring and synthetic unsaturated 1,3-diketones and their metal complexes are known to exhi-

* Corresponding author. E-mail: mbummathur@gmail.com
https://doi.org/10.2298/JSC200520062U

bit anticancer, antitumor, antioxidant, anti-inflammatory, antiviral and immunomodulatory activities.[11–14]

The photochemical properties of various unsaturated 1,3-diketones have been well studied by many research groups and the behaviour of these molecules in the excited states explained.[15] Curcuminoids, a group of unsaturated 1,3-diketones, are generally less stable to UV radiation and hence the yellow colour of turmeric products fades considerably when exposed to light. The formation of cyclic products on exposure to light has been reported.[16] The reaction mechanism and kinetics of the overall photochemical degradation of curcuminoids suggest that they act as photosensitizer of singlet oxygen. The possibility that curcumin itself could act as a photosensitizing agent is an interesting aspect in many drug formulations.[17] Studies have shown that the antibacterial activity of curcumin is generally enhanced by visible radiation.[18] The photophysical properties of curcumin were studied using time resolved fluorescence spectra.[19] Studies on the steady state absorption and fluorescence of curcumin showed that absorption/ /emission maxima are solvent dependent.[20]

In the present investigation, four Schiff bases derived from unsaturated 1,3- -diketones (1,5-diarylpent-4-ene-1,3-diones) and *o*-aminophenol were synthesized and characterized. Typical metal complexes of these polydentate ligand systems were also studied. The effects of different solvents, water and various metal ions on the fluorescence behaviour of a typical Schiff's base (H_2L^4) were also investigated.

EXPERIMENTAL

Instruments, materials and methods

The carbon, hydrogen and nitrogen contents were determined by microanalyses (Heraeus elemental analyzer) and the metal contents of the complexes by AAS (Perkin Elmer 2380). The electronic spectra of the compounds in methanol (10^{-6} M) were recorded on a JASCO V-550 UV–Vis spectrophotometer, IR spectra (KBr disks) on a JASCO FT/IR 4100 instrument, ^{1}H-NMR spectra ($CDCl_3$ or DMSO-d_6) on a JEOL 400 NMR spectrometer and mass spectra on a JEOL-JMS 600H FAB mass spectrometer. Fluorescence spectra were recorded using solutions of 10^{-3} to 10^{-6} M concentration on an Elico SL 174 spectrophotofluorometer. Ground state absorption measurements were realised with a Systronics UV–Vis double beam spectrophotometer. Molar conductance of the complexes was determined in DMF ($\approx 10^{-3}$ mol L^{-1}) at 28±1 °C. Magnetic susceptibilities were determined at room temperature on a Sherwood Scientific magnetic susceptibility balance at room temperature (28±1 °C) using $Hg[Co(NCS)_4]$ as the standard. The chemicals used were from Merck and Aldrich or of chemically pure grade. The metal salts used for the synthesis of metal chelates were $Cu(OAc)_2 \cdot H_2O$, $Ni(OAc)_2 \cdot 4H_2O$, $Co(OAc)_2.4H_2O$, $Zn(OAc)_2$, $Cd(OAc)_2$ and $Hg(OAc)_2$.

Synthesis

Synthesis of unsaturated 1,3-diketones. The unsaturated 1,3-diketones were synthesized by the reaction of aromatic aldehydes with benzoyl acetone in presence of boric oxide and tri(*sec*-butyl)borate using *n*-butylamine as the condensing agent as reported earlier.[21-23] The

aldehydes used for the condensation reaction were benzaldehyde, *p*-anisaldehyde, cinnamaldehyde and vanillin.

Synthesis of Schiff bases (H_2L). A methanolic solution of *o*-aminophenol (0.02 mol, 2.18 g) was mixed with a methanolic solution of an unsaturated 1,3-diketone (0.01 mol) and refluxed for ≈5 h. The resulting solution was poured into ice-cold water under vigorous stirring. The dark brown coloured precipitate formed was filtered and recrystallized from methanol.

Synthesis of metal complexes. Cu(II), Ni(II), Co(II), Zn(II), Cd(II) and Hg(II) complexes were prepared by the following method. To a refluxing ethanolic solution of the ligand (0.01 mol, 30 mL), an ethanolic solution of the metal(II)acetate (0.01 mol, 30 mL) was added. A pinch of sodium acetate was also added to maintain the pH of the solution at around 6. The mixture was refluxed for ≈5 h on a boiling water bath. The complex that precipitated on cooling to room temperature was filtered, washed with ethanol, and then with water and dried under vacuum. The complexes were recrystallized from hot benzene.

Absorption and fluorescence spectroscopy

Effect of solvents on the maxima. Solutions (1 μM of the Schiff base, H_2L^4, in different solvents (methanol, ethanol, acetone and DMSO) were prepared. The absorption and fluorescence spectra were recorded. The fluorescent emission was measured at 400 V.

Effect of water on fluorescence. The effect of various concentrations of water on fluorescence was studied by measuring the fluorescence intensity of the compound in different ratio of methanol and water. For this, a different volume of water was added to a methanolic solution of the compound (2 μM) and in each case fluorescence intensity was measured at 500 V. The intensity of fluorescence of the compound in pure anhydrous methanol was also determined.

Effect of metal ions on fluorescence. Different concentrations of methanolic solutions of metal salts were added to 1 mL of 1 μM solution of the Schiff base in methanol. The total volume was then made up to 10 mL and the spectra were recorded. The excitation wavelength was 402 nm.

Emission max*ima of the metal complexes.* Solutions of the metal chelates (1 μM) in DMSO were prepared. The absorption and emission spectra were recorded. The fluorescent emission was measured at 550 V.

Selection of the standard. A solution (10 ppm) of quinine sulphate in 0.1 M H_2SO_4 was taken as the standard, the quantum yield of which is 0.54. Standard 10 mm path length fluorescence cuvettes were used for the fluorescence measurements.

The spectral data of the synthesized Schiff bases (H_2L) and the synthesized metal complexes are given in the Supplementary material to this paper.

RESULTS AND DISCUSSION

Characterization of Schiff bases and their metal complexes

The elemental analytical data of the Schiff bases indicated that the reaction between unsaturated 1,3-diketone and *o*-aminophenol occurred in 1:2 ratio. All the compounds (H_2L) were crystalline in nature and soluble in common organic solvents. Attempts to prepare a single crystal of the ligands failed. The Schiff bases formed stable complexes with Cu(II), Ni(II), Co(II), Zn(II), Cd(II) and Hg(II) ions. The analytical data together with their non-electrolytic nature in DMF (specific conductance < 10 Ω^{-1} cm^{-1}; 10^{-3} M solution) suggested ML

stoichiometry. The Zn(II), Cd(II), and Hg(II) chelates were diamagnetic while the Cu(II), Ni(II), and Co(II) complexes showed normal paramagnetic moment. The observed UV, IR, ^{1}H-NMR and mass spectral data were in conformity with the proposed structural formulas of the Schiff bases and their metal complexes given in Fig. 1.

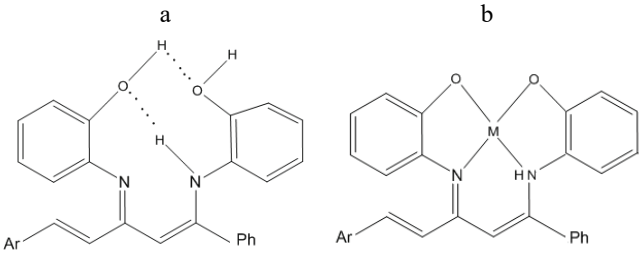

Fig. 1. The proposed structural formulas of: a) the Schiff bases, H_2L and b) their metal complexes, ML; Ar = phenyl (H_2L^1 and ML^1); 4-methoxyphenyl (H_2L^2 and ML^2); styryl (H_2L^3 and ML^3); 4-hydroxy-3-methoxyphenyl (H_2L^4 and ML^4); M = Cu(II), Ni(II), Co(II), Zn(II), Cd(II) and Hg(II); Co(II) and Ni(II) complexes also contain two coordinated H_2O molecules.

Infrared spectra. The two important functional groups present in the unsaturated 1,3-diketones considered in this investigation are the benzoyl and cinnamoyl carbonyls. The stretching frequency of the former appears[21–24] at ≈1650 cm^{-1} and the later at ≈1630 cm^{-1}. The IR spectra of the Schiff bases are characterized by the absence of both bands in these regions. Thus, it could be concluded that the compounds do not contain free benzoyl or cinnamoyl functions and both the carbonyl groups were involved in the condensation of the Schiff's bases.

The IR spectra of all the Schiff bases exhibited two strong bands at ≈1610 and ≈1580 cm^{-1} due to the stretching of the highly conjugated $\nu_{C=N}$ and $\nu_{C=C}$ functions,[9,24] respectively, seen in Fig. 1. The IR spectra of the compounds showed prominent bands at ≈1540 and ≈1280 cm^{-1} due to NH deformation vibrations and $\nu_{C–N}$. These, together with the $\nu_{C=N}$ band, suggested the existence of the compounds in the imine–enamine form rather than in the di-imine or di-enamine form. The broad band observed in the range 3000–3500 cm^{-1} in the spectra are due to the intramolecularly hydrogen bonded phenolic and NH groups,[24] seen in Fig. 1.

The most important feature of the IR spectra of all the metal complexes was the disappearance of the free ligand band at ≈1610 cm^{-1} due to $\nu_{C=N}$. Instead, a prominent band appeared at ≈1550 cm^{-1} assignable to the stretching of the metal bonded C=N function,[9,25] seen in Fig. 1. The prominent band observed in the ligands at ≈1540 cm^{-1} due to NH deformation vibrations remained almost unaffected and the band at ≈1280 cm^{-1} due to $\nu_{C–N}$ shifted to lower wave numbers in

the spectra. These indicate that the NH proton was not replaced by a metal ion during coordination involving nitrogen.[25] The broad band in the region 3000–3500 cm^{-1} of the ligands was absent in the spectra of all the metal complexes, indicating deprotonation of phenolic oxygen atoms prior to complexation.[25] The spectra of the Ni(II) and Co(II) complexes showed bands due to coordinated water at ≈3450 cm^{-1}. That the two phenolic oxygens along with the imino and amino nitrogens were involved in complexation is further supported by the appearance of additional medium intensity bands in the range 520–580 cm^{-1} and 420–480 cm^{-1} due to the stretching of ν_{M-N} and ν_{M-O}, respectively.[25]

^{1}H-NMR spectra. The ^{1}H-NMR spectra of all the Schiff bases displayed three low field one proton signals at $\delta \approx$ 8.6, 9.5 and 10.7 ppm due to amino and intramolecularly hydrogen bonded phenolic protons.[26] Since the two phenolic protons are in different electronic environments, the signal at $\delta \approx$ 10.7 ppm can be assigned to phenolic proton associated with the olefinic group. The methine proton signal was located at $\delta \approx$ 5.8 ppm. The trans orientation of the –CH=CH– group is evident[13] from their observed *J* values (≈16 Hz). The integrated intensities of all the protons agree well with the formulation of the compounds as in Fig. 1.

In the ^{1}H-NMR spectra of the diamagnetic Zn(II) complexes, the phenolic proton signals of the ligands disappeared, indicating the replacement of these protons with a metal ion during complexation.[23] The N–H proton signal of the ligands remain unaltered, which indicated that this proton was not replaced during coordination. The methine proton signal shifted appreciably to a lower field compared to the shift in the olefinic and aromatic protons. This may be due to the aromatic character imparted to the C_3N_2M ring system of the chelates by the attachment of highly conjugated groups. That the aryl substituents of H_2L^2 and H_2L^4 were not involved in bonding with the metal ion was clearly indicated in the spectra of the complexes in which the signals remain unaltered.[23] Aryl protons appeared in the δ range 6.8–7.5 ppm as a complex multiplet. The integrated intensities of the various signals agree well with the proposed ML stoichiometry of the complexes as shown in Fig. 1.

Mass spectra. The mass spectra of all the Schiff bases displayed intense parent ion peak, $P^+/(P+1)^+$, thereby confirming the formulation of the compounds.[27] Other prominent peaks were due to the elimination of aryl substituents, Ar–CH=CH, Ph, Ar, *etc.* from the parent ion. The FAB mass spectra of the Cu(II) complexes showed a molecular ion peaks, $P^+/(P+1)^+$, corresponding to CuL stoichiometry. Peaks correspond to L^+ and fragments of L^+ were also present in the spectra. The spectra of all the chelates contained a number of fragments containing copper in the 3:1 natural abundance of ^{63}Cu and ^{65}Cu isotopes.[9,12]

Electronic spectra. The UV spectra of the Schiff bases showed two broad bands with maxima at ≈360 and 260 nm due to various $n \rightarrow \pi^*$ and $\pi \rightarrow \pi^*$ transitions. The absorption maxima of the metal chelates bear close resemblance with

the free ligands, which indicates that no structural alteration of the ligand occurred during complexation. However, the values shifted to longer wavelength. The shift was more prominent for the band at ≈360 nm of the free ligand due to the n→π* transition of the azomethine function;[28] This clearly indicated the involvement of the group in metal coordination as shown in Fig. 1.

The Cu(II) complexes showed a broad visible band with λ_{max} at ≈14,800 cm^{-1}. This, together with the measured μ_{eff} values (≈1.75 BM), suggests their square-planar geometry.[4] The spectra of the paramagnetic Ni(II) chelates (μ_{eff} ≈2.80 BM) showed three bands at λ_{max} ≈8,500, ≈14,000 and ≈24,500 cm^{-1}, corresponding to the transitions $^3A_{2g} \rightarrow {}^3T_{2g}(F)$; $^3A_{2g} \rightarrow {}^3T_{1g}(F)$ and $^3A_{2g} \rightarrow$ $\rightarrow {}^3T_{1g}(P)$, respectively, confirming their octahedral geometry along with two coordinated water molecules.[29] The spectra of the Co(II) chelates showed three bands at λ_{max} ≈9,500, ≈12,000 and ≈20,000 cm^{-1}, corresponding to the transitions $^4T_{1g}(F) \rightarrow {}^4T_{2g}$; $^4T_{1g}(F) \rightarrow {}^4A_{2g}$; $^4T_{1g}(F) \rightarrow {}^4T_{1g}(P)$, respectively. The transition to $^4A_{2g}$ is very weak and appears as a shoulder. This, together with the measured μ_{eff} values (≈4.80 BM), suggest their octahedral geometry with two coordinated water molecules.[30] In most of the cases, interpretation was difficult as the d–d bands were masked by intense charge transfer transitions.

Studies on the fluorescence characteristics of the Schiff base (H_2L^4)

Effect of solvents. The unsaturated 1,3-diketones are insoluble in water but soluble in many organic solvents and are readily soluble in polar organic solvents.[12,14] The absorption and emission spectra are highly dependent on the nature of the solvent. Absorption maxima of H_2L^4 showed a red shift with increasing solvent polarity (Table I). The absorption band was very broad and consisted of a shoulder. All these features indicated the presence of more than one species of the compound in solution.

TABLE I. Absorption and emission maxima of H_2L^4 in different organic solvents

Solvent	λ_{ab} / nm	λ_{fl} / nm
Acetone	392	773
Ethanol	400	792
Methanol	402	795
DMSO	498	822

The fluorescence maxima also showed solvent dependence. A large red shift from 773 nm in acetone to 822 nm in DMSO, the most polar among the solvents used. As the polarity of the solvent increased, the broadening of the spectral band also increased. This suggests that the excited singlet state has a large intramolecular charge transfer character.[31] This is possible in these types of molecules in which a reasonable amount of energy from the aromatic ring can be transferred to the enamine tautomer of the Schiff base. Similarly, hydrogen bonding with the solvent may also be involved in this process. Thus, it appears that polarity and

hydrogen bonding ability of the solvents have significant influence on the absorption and emission spectra of the compound.

Effect of water. Earlier reports showed that water quenches the fluorescence intensity of curcuminoids.[32] The results obtained for H_2L^4 also agreed with this observation. The effect of water on the fluorescence intensity of the compound is given in Table II. The fluorescence intensity decreased with increasing water content.

TABLE II. Effect of various concentrations of water on the fluorescence of H_2L^4 in methanol

c_{H_2O} / %	Emission maxima, nm	Fluorescence intensity	η^o/η	I^o_{fl}/I_{fl}	$(\eta^o/\eta)\times(I^o_{fl}/I_{fl})$
0	796	369	1.00	1.00	1.00
3	796	326	0.99	1.1366	1.1252
5	796	286	0.96	1.2991	1.2871
7	795	273	0.95	1.3696	1.3011
10	797	241	0.92	1.5435	1.4200
20	796	215	0.85	1.7317	1.4719
30	795	207	0.79	1.7842	1.799
40	797	173	0.66	2.1462	1.986

It was reported that the fluorescence quenching could be attributed to the interaction of the lone pair electrons of H_2O with the excited state of the compound, resulting in the formation of a non-fluorescent associated species.[33] The effect of water could be studied with the help of a modified Stern–Volmer equation:[34]

$$I^o_{fl}/I_{fl} = (1 + K_q\tau c_{H_2O})/(\eta^o/\eta)$$

where K_q is the rate constant for quenching, τ is the life time of the excited singlet state, and I^o_{fl} is the fluorescence intensity in the absence of water, η^o and η are the viscosity of pure methanol and methanol–water mixture, respectively.

From the modified Stern–Volmer plot of $(I^o_{fl}/I_{fl})\times(\eta^o/\eta)$ *vs.* c_{H_2O} on the fluorescence quenching, it is clear that fluorescence quenching by water is dependent on the viscosity of the solvent. The slope of the plot is 1.29×10^{-2} M^{-1}. However, the reported value for curcumin[34] is 1.38×10^{-2} M^{-1}, which indicates that the effect of water quenching on the fluorescence of H_2L^4 is slightly less than that of curcumin.

Effect of metal ions. Metal ions generally influence the fluorescent intensity and fluorescent maxima of organic molecules. In the present study, the effect of Cu(II), Ni(II), Co(II), Zn(II), Cd(II) and Hg(II) ions on the fluorescent intensity and fluorescent maxima of H_2L^4 were measured. The results are summarized in Tables III and IV. The observed data revealed that in all the cases, the fluorescent maxima showed only marginal shift (±5 nm) with increasing concentration of metal ions, whereas the fluorescent intensity was highly dependent on the metal ion concentration. Thus the presence of Cu(II), Ni(II) and Co(II) ions decreased

the fluorescent intensity of the Schiff base. In the case of Zn(II), Cd(II) and Hg(II) ions, the decrease in the intensity was very small.

TABLE III. Effect of Cu(II), Ni(II) and Co(II) ions on the fluorescence intensity of H_2L^4; concentration of H_2L^4 was 1 μM

Concentration of metal(II) solution, μM	Cu(II)		Ni(II)		Co(II)	
	$\lambda_{fl\ max}$ nm	Fluorescence intensity	$\lambda_{fl\ max}$ nm	Fluorescence intensity	$\lambda_{fl\ max}$ nm	Fluorescence intensity
0	792	322	800	174	796	491
1	792	298	802	139	796	457
2	791	270	805	135	795	415
3	796	195	803	128	796	364
4	792	141	804	120	797	352
5	797	120	801	93	796	308
6	796	100	802	86	795	276
7	796	88	801	76	795	247
8	799	66	801	55	794	221

From the measurements, it is clear that whether or not the metal ion form a complex with the organic molecule in its ground state, they have significant influence on the fluorescence.

Table IV. Effect of Zn(II), Cd(II) and Hg(II) ions on the fluorescence intensity of H_2L^4; concentration of H_2L^4 was 1 μM

Concentration of metal(II) solution, μM	Zn(II)		Cd(II)		Hg(II)	
	$\lambda_{fl\ max}$ nm	Fluorescence intensity	$\lambda_{fl\ max}$ nm	Fluorescence intensity	$\lambda_{fl\ max}$ nm	Fluorescence intensity
0	795	372	799	258	798	243
1	795	369	798	243	797	242
2	795	366	797	239	797	240
3	794	364	797	238	797	229
4	796	368	797	238	796	228
5	795	361	797	237	798	222
6	795	368	799	232	798	222
7	794	363	797	233	797	209
8	795	362	797	230	797	205

Generally, paramagnetic metal ions influence the intensity of fluorescence because paramagnetic spectrum enhances the rate of intersystem crossing in organic molecules.[35] This may be due to the influence of the unpaired electron on the excited state of the ligand.

In the presence of metal ions, the changes in the fluorescent intensity of an organic metal chelating ligand molecule may be due to several factors. The metal ion form complexes with the ligand. Then the complex may be fluorescent or non-fluorescent. If the complex is fluorescent, it may emit at different wave-

lengths. When the complex is non-fluorescent, the emission profile depends only on the ligand concentration. Another factor that may affect the fluorescence intensity is the magnetic properties of the metal ion. Most of the paramagnetic metal ions are effective quenchers of fluorescence and cause a reduction in the fluorescence intensity. An excited state charge transfer process occurs between the fluorescent molecule and the metal ion. Spin–orbit coupling between the unpaired electron on the metal ion and the excited state of the molecule also increases the rate of intersystem crossing.[35] Hence, the decrease in the fluorescence intensity in the presence of Cu(II), Ni(II), and Co(II) ion was due to the formation of non-fluorescent complexes. The emission profile was due to the free ligand molecules that were not involved in the chelation process.[35]

CONCLUSIONS

Four new Schiff bases (H_2L^1 to H_2L^4) were synthesized by condensing both the carbonyl groups of four unsaturated 1,3-diketones (1,5-diarylpent-4-ene-1,3--diones) with the amino group of *o*-aminophenol. The existence of these Schiff bases in the intramolecularly hydrogen bonded imine–enamine form has been well demonstrated from their physical, analytical and various spectral data. Spectral and analytical data of the metal complexes are in agreement with the dibasic tetradentate coordination of the Schiff bases with ML stoichiometry (M = Cu(II), Ni(II), Co(II), Zn(II), Cd(II), and Hg(II)) in which both the phenolic protons of the ligand are replaced by the divalent metal cations. The fluorescent studies of the typical Schiff base H_2L^4 showed that fluorescence emission maxima shift with increasing polarity and hydrogen bonding ability of the solvent. As the concentration of metal ion increases, a decrease in fluorescence intensity was observed for paramagnetic Cu(II), Ni(II) and Co(II) ions. The results revealed that the intensity of fluorescence of the Schiff base H_2L^4 is not significantly affected by diamagnetic Zn(II), Cd(II) and Hg(II) ions.

SUPPLEMENTARY MATERIAL

Spectral data of the synthesized Schiff bases (H_2L) are available electronically at the pages of journal website: https://www.shd-pub.org.rs/index.php/JSCS/index, or from the corresponding author on request.

Acknowledgment. The author, Dr. Muhammed Basheer Ummathur, is thankful to University Grants Commission, New Delhi, India, for financial assistance (Research Project No. MRP(S)-865/10-11/KLCA045/UGC-SWRO).

ИЗВОД

1,5-ДИАРИЛПЕНТ-4-ЕН-1,3-ДИОН ШИФОВЕ БАЗЕ И ЊИХОВИ КОМПЛЕКСИ МЕТАЛА: СИНТЕЗА, КАРАКТЕРИЗАЦИЈА И ФЛУОРЕСЦЕНТНА ИСПИТИВАЊА

MUHAMMED BASHEER UMMATHUR[1], RADHIKA PALLIKKAVIL[2] и KRISHNANNAIR KRISHNANKUTTY[2]

[1]*Department of Chemistry, KAHM Unity Women's College, Manjeri, Kerala-676122, India и* [2]*Department of Chemistry, University of Calicut, Kerala-673635, India*

Кондензационом реакцијом између *o*-аминофенола и незасићених дикетона (1,5--диарилпент-4-ен-1,3-дион) синтетисана су четири лиганда типа Шифових база (H_2L^1–H_2L^4). На основу IR и ^{1}H-NMR спектроскопских и масених спектрометријских мерења потврђено је да све синтетисане Шифове базе садрже имин–енаминску структурну јединицу. Тетрадентатна координација ових Шифових база (L) у одговарајућим ML комплексима)M = Cu(II), Ni(II), Co(II), Zn(II), Cd(II) и Hg(II)= потврђена је на основу физичкохемијских, аналитичких и спектроскопских испитивања. Флуоресцентна испитивања H_2L^4 Шифове базе су показала да се емисиони максимум помера са повећањем поларности растварача и његове способности за формирање водоничних веза. Парамагнетични Cu(II), Ni(II) и Co(II) јони смањују флуоресцентни интензитет са повећањем концентрације ових јона метала, док дијамагнетични Zn(II), Cd(II) и Hg(II) јони имају врло мали утицај на интензитет флоресценције H_2L^4 Шифове базе.

(Примљено 20. маја, ревидирано 27. септембра, прихваћено 28. септембра 2020)

REFERENCES

1. N. E. Borisova, V. V. Roznyatovskii, M. D. Reshetova, Y. A. Ustynyuk, *Russian J. Org. Chem.* **41** (2005) 1005 (https://doi.org/10.1007/s11178-005-0285-9)
2. R. Pallikkavil, M. B. Ummathur, K. Krishnankutty, *Arch. Appl. Sci. Res.* **4** (2012) 2223
3. G. G. Mohamed, M. M. Omar, A. M. Hindy, *Turk. J. Chem.* **30** (2006) 361
4. K. Krishnankutty, P. Sayudevi, M. B. Ummathur, *J. Serb. Chem. Soc.* **72** (2007) 1075 (https://doi.org/10.2298/JSC0711075K)
5. P. D. Benny, J. L. Green, H. P. Engelbrecht, C. L. Barnes, S. S. Jurisson, *Inorg. Chem.* **44** (2005) 2381 (https://doi.org/10.1021/ic048670j)
6. T. D. Thangadurai, K. Natarajan, *Synth. React. Inorg. Met.-Org. Chem.* **31** (2000) 549 (https://doi.org/10.1081/SIM-100104786)
7. N. Raman, Y. Pitchaikaniraja, A. Kulandaisami, *Proc. Ind. Acad. Sci. (Chem. Sci).* **113** (2001) 183
8. K. Krishnankutty, M. B. Ummathur, P. Sayudevi, *J. Argent. Chem. Soc.* **96** (2008) 13
9. T. J. Saritha, P. Metilda, *Int. J. Eng. Trends Appl.* **5** (2018) 1
10. M. Ahmed, M. A. Qadir, M. I. Shafiq, M. Muddassar, Z. Q. Samra, A. Hameed, *Arab. J. Chem.* **12** (2019) 41 (https://dx.doi.org/10.1016/j.arabjc.2016.11.017)
11. K. Krishnankutty, V. D. John, *Synth. React. Inorg. Met.-Org. Chem.* **33** (2003) 343 (https://doi.org/10.1081/SIM-120017791)
12. J. L. Funk, J. B. Frye, J. N. Oyarzo, H. Zhang, B. N. Timmermann, *J. Agric. Food Chem.* **58** (2010) 842 (https://doi.org/10.1021/jf9027206)
13. V. D. John, M. B. Ummathur, K. Krishnankutty, *J. Coord. Chem.* **66** (2013) 1508 (https://doi.org/10.1080/00958972.2013.784281)
14. R. Pallikkavil, M. B. Ummathur, K. Krishnankutty, *Res. J. Chem. Sci.* **5** (2015) 40
15. C. F. Chignell, P. Bilski, K. J. Reszka, A. G. Motten, R. H. Sik, T. A. Dahl, *Photochem. Photobiol. Sci.* **59** (1994) 295 (https://doi.org/10.1111/j.1751-1097.1994.tb05037.x)

16. M. Griesser, V. Pistis, T. Suzuki, N. Tejera, D. A. Pratt, C. Schneider, *J. Biol. Chem.* **286** (2011) 1114 (https://doi.org/10.1074/jbc.M110.178806)
17. K.T. Kazantzis, K. Koutsonikoli, B. Mavroidi, M. Zachariadis, P. Alexiou, M. Pelecanou, K. Politopoulos, E. Alexandratou, M. Sagnou, *Photochem. Photobiol. Sci.* **19** (2020) 193 (https://doi.org/10.1039/C9PP00375D)
18. E. F. Oliveira, J. V. Tosati, R. Tikekar, A. R. Monteiro, N. Nitin, *Postharvest Biol. Tec.* **137** (2018) 86 (http://doi.org/10.1016/j.postharvbio.2017.11.014).
19. L. Nardo, A. Andreoni, M. Masson, T. Haukvik, H. H. Tonnesen, *J. Fluoresc.* **21** (2011) 627 (https://doi.org/10.1007/s10895-010-0750-x)
20. R. Ghosh, D. K. Palit, *Photochem. Photobiol. Sci.* **12** (2013) 987 (https://doi.org/10.1039/C3PP25429A)
21. M. Paul, P. Venugopalan, K. Krishnankutty, *Asian J. Chem.* **14** (2002) 1335
22. M. B. Ummathur, A. Krishnan, M. P. Ukken, *J. Iran. Chem. Res.* **3** (2010) 71 (http://jicr.iau-arak.ac.ir/article_517487_00fd978bde4e478354207cffc21a5c24.pdf)
23. M. P. Ukken, M. B. Ummathur, *Arch. Appl. Sci. Res.* **5** (2013) 247 (https://www.scholarsresearchlibrary.com/articles/synthesis-and-characterization-of-two-conjugated-bdiketones-and-their-metal-complexes.pdf)
24. L. J. Bellamy, *The Infrared Spectra of Complex Molecule*s, Chapman and Hall, London, 1980
25. K. Nakamoto, *Infrared Spectra of Inorganic and Coordination Compounds,* Wiley, New York, 1970
26. A. Lycka, J. Jirman, A. Cee, *Mag. Res. Chem.* **28** (1990) 408 (https://doi.org/10.1002/mrc.1260280505)
27. H. Budzikiewicz, C. Djerassi, D. H. Williams, *Mass Spectrometry of Organic Compounds,* Holden Day, San Francisco, CA, 1967
28. K. Ray, T. Weyhermüller, F. Neese, K. Wieghardt, *Inorg. Chem.* **44** (2005) 5345 (https://doi.org/10.1021/ic0507565)
29. Y. Sasaki, *Bull. Inst. Chem. Res., Kyoto Univ.* **8** (1980) 187 (http://hdl.handle.net/2433/76881)
30. K. S. Melha, *J. Coord. Chem.* **61** (2008) 2053 (https://doi.org/10.1080/00958970701862167)
31. M. M. Enriquez, M. Fuciman, A. M. LaFountain, N. L. Wagner, R. R. Birge, H. A. Frank, *J. Phys. Chem., B* **114** (2010) 12416 (https://doi.org/10.1021/jp106113h)
32. P. H. Bong, *Bull. Korean Chem. Soc.* **21** (2000) 81
33. J. H. Chang, Y. M. Choi, Y. K. Shin, *Bull. Korean Chem. Soc.* **22** (2001) 527
34. M. C. DeRosa, R. J. Crutchley, *Coord. Chem. Rev.* **233** (2002) 351 (https://doi.org/10.1016/S0010-8545(02)00034-6)
35. R. Pallikkavil, M. B. Ummathur, K. Krishnankutty, *Turk. J. Chem.* **37** (2013) 889 (https://doi.org/10.3906/kim-1301-19).

Journal of the Serbian Chemical Society
JSCS-info@shd.org.rs • www.shd.org.rs/JSCS
J. Serb. Chem. Soc. 86 (1) S5–S7 (2021) *Supplementary material*

SUPPLEMENTARY MATERIAL TO

Schiff bases of 1,5-diarylpent-4-ene-1,3-diones and their metal complexes: Synthesis, characterization and fluorescent studies

MUHAMMED BASHEER UMMATHUR[1]*, RADHIKA PALLIKKAVIL[2] and KRISHNANNAIR KRISHNANKUTTY[2]

[1]*Department of Chemistry, KAHM Unity Women's College, Manjeri, Kerala-676122, India and* [2]*Department of Chemistry, University of Calicut, Kerala-673635, India*

J. Serb. Chem. Soc. 86 (1) (2021) 39–49

Synthesized Schiff bases (H_2L)

H_2L^1 *($C_{29}H_{24}N_2O_2$)*. IR (cm^{-1}):_ 1610*s* (C=N), 1580*s* (C=C), 1280*m* (C–N), 1540*m* (N–H); ^{1}H-NMR (δ / ppm): 8.62 (1H, NH), 10.10 (1H, phenolic OH), 9.50 (1H, methine), 5.88 (1H, alkenyl), 8.06 (1H), 7.90 (1H); mass spectrum (*m*/*z*): 433, 357, 321, 255, 181, 103; UV (λ_{max} / nm): 364, 265.

H_2L^2 *($C_{30}H_{26}N_2O_3$)*. IR (cm^{-1}): 1614s (C=N), 1586s (C=C), 1278m (C–N), 1542m (N–H); ^{1}H-NMR (δ / ppm): 8.60 (1H, NH), 10.74 (1H, phenolic OH), 9.52 (1H, methine), 5.81 (1H, alkenyl) 8.04 (1H) 7.86 (1H), 3.92 (3H, OCH_3); mass spectrum (*m*/*z*): 462, 385, 355, 329, 252, 133, 107; UV (λ_{max} / nm): 366, 258.

H_2L^3 ($C_{31}H_{26}N_2O_2$). IR (cm^{-1}): 1610*s* (C=N), 1578*s* (C=C), 1280*m* (C–N), 1544*m* (N–H); ^{1}H-NMR (δ / ppm): 8.58 (1H, NH), 10.66 (1H, phenolic OH), 9.60 (1H, methine), 5.78 (1H, alkenyl), 7.98–8.10 (4H); mass spectrum (*m*/*z*): 433, 355, 329, 278, 175, 129, 103; UV (λ_{max} / nm): 360, 262.

H_2L^4 ($C_{30}H_{26}N_2O_4$). IR (cm^{-1}): 1608*s* (C=N), 1576*s* (C=C), 1276*m* (C–N), 1540*m* (N–H); ^{1}H-NMR (δ / ppm): 8.62 (1H, NH), 10.72 (1H, phenolic OH), 10.15 (1H, phenolic OH), 9.56 (1H, methine) 5.82 (1H, alkenyl), 8.06 (1H) 7.90 (1H), 3.88 (3H, OCH_3); mass spectrum (*m*/*z*): 478, 355, 401, 329, 252, 149, 123; UV (λ_{max} / nm): 358, 265.

Synthesized metal complexes

CuL^1 ($C_{29}H_{22}CuN_2O_2$). IR (cm^{-1}): 1552*s* (C=N), 1582*s* (C=C), 1260*m* (C–N), 1536*m* (N–H), 580*m* & 520*m* (M–N), 472*m* & 423*m* (M–O); mass spectrum (*m*/*z*): 495, 493, 432, 418, 416, 392, 390, 355, 341, 339, 315, 313, 252; UV (λ_{max} / nm): 384, 275.

* Corresponding author. E-mail: mbummathur@gmail.com

NiL¹(H₂O)₂ *($C_{29}H_{26}N_2NiO_4$)*. IR: (cm^{-1}): 1550*s* (C=N), 1576*s* (C=C), 1256*m* (C–N), 1538*m* (N–H), 580*m* & 528*m* (M–N), 470*m* & 420*m* (M–O); UV (λ_{max} / nm): 390, 278.

CoL¹(H₂O)₂ *($C_{29}H_{26}CoN_2O_4$)*. IR (cm^{-1}): 1558*s* (C=N), 1578*s* (C=C), 1258*m* (C–N), 1539*m* (N–H), 577*m* & 520*m* (M–N), 467*m* & 425*m* (M–O); UV (λ_{max} / nm): 386, 272.

ZnL¹ *($C_{29}H_{22}N_2O_2Zn$)*. IR (cm^{-1}): 1556*s* (C=N), 1580*s* (C=C), 1258*m* (C–N), 1540*m* (N–H), 576*m* and 522*m* (M–N), 468*m* and 422*m* (M–O); ^{1}H-NMR (δ / ppm): 8.60 (1H, NH), 6.34 (1H, methine) 8.13 (1H, alkenyl), 7.98 (1H, alkenyl); UV (λ_{max} / nm): 380, 268.

CdL¹ *($C_{29}H_{22}CdN_2O_2$)*. IR (cm^{-1}): 1558s (C=N), 1584s (C=C), 1262m (C–N), 1538m (N–H), 574m & 520m (M–N), 472m & 425m (M–O); UV (λ_{max} / nm): 392, 272.

HgL¹ *($C_{29}H_{22}HgN_2O_2$)*. IR (cm^{-1}): 1560*s* (C=N), 1582*s* (C=C), 1266*m* (C–N), 1542*m* (N–H), 578*m* & 526*m* (M–N), 474*m* & 426*m* (M–O); UV,(λ_{max} / nm): 392, 272.

CuL² *($C_{30}H_{24}CuN_2O_3$)*. IR (cm^{-1}): 1550*s* (C=N), 1580*s* (C=C), 1266*m* (C–N), 1540*m* (N–H), 580*m* & 522*m* (M–N), 470*m* & 424*m* (M–O); mass spectrum (*m*/*z*): 525, 523, 462, 448, 446, 418, 416, 392, 390, 385, 315, 313, 252; UV (λ_{max} / nm): 396, 278.

NiL²(H₂O)₂ ($C_{30}H_{28}N_2NiO_5$). IR (cm^{-1}): 1550*s* (C=N), 1582*s* (C=C), 1258*m* (C–N), 1536*m* (N–H), 580*m* & 528*m* (M–N), 467*m* & 420*m* (M–O); UV (λ_{max} / nm): 390, 268.

CoL²(H₂O)₂ *($C_{30}H_{28}CoN_2O_5$)*. IR (cm^{-1}): 1552*s* (C=N), 1584*s* (C=C), 1259*m* (C–N), 1534*m* (N–H), 580*m* & 523*m* (M–N), 469*m* & 427*m* (M–O); UV (λ_{max} / nm): 396, 278.

ZnL² *($C_{30}H_{24}N_2O_3Zn$)*. IR (cm^{-1}): 1547*s* (C=N), 1580*s* (C=C), 1260*m* (C–N), 1540*m* (N–H), 574*m* & 520*m* (M–N), 472*m* & 423*m* (M–O); ^{1}H-NMR (δ / ppm): 8.59 (1H, NH), 6.26 (1H, methine), 8.10 (1H, alkenyl) 7.92 (1H, alkenyl), 3.92 (3H, OCH_3); UV (λ_{max} / nm): 386, 272.

CdL² *($C_{30}H_{24}CdN_2O_3$)*. IR (cm^{-1}): 1552s (C=N), 1576s (C=C), 1262m (C–N), 1542m (N–H), 580m & 522m (M–N), 474m & 426m (M–O); UV (λ_{max} / nm): 392, 274.

HgL² *($C_{30}H_{24}HgN_2O_3$)*: IR (cm^{-1}): 1553*s* (C=N), 1578*s* (C=C), 1260*m* (C–N), 1538*m* (N–H), 582*m* & 520*m* (M–N), 462*m* & 420*m* (M–O), UV (λ_{max} / / nm): 390, 269.

CuL³ *($C_{31}H_{24}CuN_2O_2$)*. IR (cm^{-1}): 1558*s* (C=N), 1578*s* (C=C), 1260*m* (C–N), 1540*m* (N–H), 580*m* & 520*m* (M–N), 472*m* & 420*m* (M–O); mass spectrum (*m*/*z*): 521, 519, 444, 442, 433, 418, 416, 392, 390, 355, 341, 339, 329, 278, 175, 103; UV (λ_{max} / nm): 388, 272.

NiL³(H₂O)₂ *($C_{31}H_{28}N_2NiO_4$)*. IR (cm^{-1}): 1543*s* (C=N), 1580*s* (C=C), 1256*m* (C–N), 1540*m* (N–H), 578*m* & 522*m* (M–N), 462*m* & 423*m* (M–O); UV (λ_{max} / nm): 390, 282.

CoL³(H₂O)₂ *($C_{31}H_{28}CoN_2O_4$)*. IR (cm^{-1}): 1549*s* (C=N), 1589*s* (C=C), 1258*m* (C–N), 1545*m* (N–H), 576*m* & 523*m* (M–N), 465*m* & 427*m* (M–O); UV (λ_{max} / nm): 392, 280.

ZnL³ *($C_{31}H_{24}N_2O_2Zn$)*. IR (cm^{-1}): 1551*s* (C=N), 1577*s* (C=C), 1263*m* (C–N), 1538*m* (N–H), 576*m* & 526*m* (M–N), 482*m* & 422*m* (M–O); ^{1}H-NMR (δ / ppm): 8.60 (1H, NH), 6.26 (1H, methine), 8.06–8.22 (4H, alkenyl); UV (λ_{max} / nm): 394, 272.

CdL³ *($C_{31}H_{24}CdN_2O_2$)*. IR (cm^{-1}): 1550*s* (C=N), 1575*s* (C=C), 1265*m* (C–N), 1543*m* (N–H), 580*m* & 522*m* (M–N), 470*m* & 423*m* (M–O); UV (λ_{max} / / nm): 396, 287.

HgL³ *($C_{31}H_{24}HgN_2O_2$)*. IR (cm^{-1}): 1563*s* (C=N), 1580*s* (C=C), 1259*m* (C–N), 1536*m* (N–H), 572*m* & 526*m* (M–N), 472*m* & 426*m* (M–O); UV (λ_{max} / / nm): 390, 280.

CuL⁴ *($C_{30}H_{24}CuN_2O_4$)*. IR (cm^{-1}): 1553*s* (C=N), 1576*s* (C=C), 1256*m* (C–N), 1534*m* (N–H), 579*m* & 520*m* (M–N), 472*m* & 423*m* (M–O); mass spectrum (*m*/*z*): 480, 478, 403, 401, 357, 355, 331, 329, 254, 252, 478, 355, 123; UV (λ_{max} / nm): 389, 277.

NiL⁴(H₂O)₂ *($C_{30}H_{28}N_2NiO_6$)*. IR (cm^{-1}): 1550*s* (C=N), 1578*s* (C=C), 1250*m* (C–N), 1540*m* (N–H), 580*m* & 522*m* (M–N), 470*m* & 426*m* (M–O); UV (λ_{max} / nm): 394, 285.

$CoL^4(H_2O)_2$ *($C_{30}H_{28}CoN_2O_6$)*. IR (cm^{-1}): 1556s (C=N), 1576s (C=C), 1256m (C–N), 1544m (N–H), 570m & 528m (M–N), 460m & 427m (M–O); UV, (λ_{max} / nm): 396 280.

ZnL⁴₂ *($C_{30}H_{24}N_2O_4Zn$)*. UV, IR (cm^{-1}): 1560*s* (C=N), 1580*s* (C=C), 1262*m* (C–N), 1542*m* (N–H), 580*m* & 522*m* (M–N), 470*m* & 424*m* (M–O); ^{1}H-NMR (δ / ppm): 8.56, (1H, NH); 6.22 (1H, methine); 8.13 (1H, alkenyl); 7.98 (1H); 3.92 (3H, OCH_3); 3.86 (3H, OCH_3), 10.16 (1H, phenolic OH); UV (λ_{max}, nm): 386, 285.

CdL⁴₂ *($C_{30}H_{24}CdN_2O_4$)*: IR (cm^{-1}): 1551*s* (C=N), 1576*s* (C=C), 1256*m* (C–N), 1540*m* (N–H), 570*m* & 528*m* (M–N), 472*m* & 420*m* (M–O); UV (λ_{max} / / nm): 393, 279.

HgL⁴₂ *($C_{30}H_{24}HgN_2O_4$)*: IR (cm^{-1}): 1547*s* (C=N), 1578*s* (C=C), 1253*m* (C–N), 1538*m* (N–H), 576*m* & 520*m* (M–N), 480*m* & 422*m* (M–O); UV (λ_{max} / / nm): 388, 276.

Journal of the Serbian Chemical Society
JSCS-info@shd.org.rs • www.shd.org.rs/JSCS
J. Serb. Chem. Soc. *86* (1) 51–61 (2021)
JSCS–5403
Original scientific paper

Crystal products of lamotrigine–citric acid for improvement of *in vitro* drug release in simulated gastric fluid

BHABANI SANKAR SATAPATHY, ASUPRITA PATEL, RUDRA NARAYAN SAHOO and SUBRATA MALLICK*

Department of Pharmaceutics, School of Pharmaceutical Sciences, Siksha 'O' Anusandhan (Deemed to be University), Kalinganagar, Bhubaneswar-751003, Odisha, India

(Received 5 July, revised 8 August, accepted 20 August 2020)

Abstract: Crystal engineering is an integral part of the drug development research. Crystal forms can modify the physicochemical properties of the parent drug molecule. The present work was aimed at the synthesis and characterization of crystalline product of lamotrigine (LT), an U.S. Food and Drug Administration approved anti-epileptic drug, with citric acid (CA) to improve its release in gastric region and oral absorption. The crystalline products of LT–CA were developed by solvent evaporation method using ethanol-water as the solvent system. Appearance of new characteristic peaks in the FTIR spectra for the crystal products indicated formation of new crystal state. In DSC thermogram, melting point of the experimental crystal products was different than that of the pure drug. Further, formation of new crystalline phase was confirmed from XRD data through the identification of new sharp peaks for the selected crystal products. A higher cumulative percentage of drug release was observed for the crystal products than for the free drug within 60 min of drug release in simulated gastric fluid. However, *in vivo* studies are warranted for the future technology transfer of the product at industrial scale.

Keywords: anti-epileptic; onset of action; BCS class II; solvent evaporation method; lattice strain.

INTRODUCTION

Crystal engineering has been emerged as an important tool in pharmaceutical industry to improve the dissolution and absorption rate of poorly soluble drugs.[1] Poor dissolution rate directly influences the therapeutic efficacy of pharmaceuticals, and significantly lowers the market value of a drug.[2] Especially, in the case of neurological disorders like epilepsy, timely absorption of drugs is very crucial to elicit prompt therapeutic action. However, many pharmaceutical agents have low aqueous solubility, which delays their absorption and consequently leads to

* Corresponding author. E-mails: subratamallick@soa.ac.in; profsmallick@gmail.com
https://doi.org/10.2298/JSC200705049S

delayed onset of action.[3] Thus, enhancing the dissolution rate of poorly soluble drugs without compromising their therapeutic potential or stability has been a major challenge in pharmaceutical industry during crystal product development. Crystals may be described as orderly arrangement of molecules in a geometrical pattern in three-dimensional space, where the molecules are connected through intermolecular bonds.[4] Suitable crystalline product of active pharmaceutical ingredients (APIs) can enhance important physicochemical properties like melting point, solubility, dissolution rate, refractive index, stability etc. without affecting their intrinsic therapeutic property and thus improves the industrial feasibility and patient compliance.[5]

Lamotrigine (LT), a widely used anti-epileptic drug, has poor aqueous solubility with low absorption rate.[6] It has been recommended for the treatment of both partial and generalized seizures (primary tonic/clonic seizure).[6] LT has the advantages of fewer side effects associated with a higher therapeutic index unlike other anti-epileptic drugs, thus it does not require regular blood monitoring after administration. However, LT belongs to class II of Biopharmaceutical System of Classification (BSC). Being a BCS class II drug (low solubility and high permeability), it has poor solubility in aqueous medium (0.17 mg/ml at 25 °C) and also is slightly soluble in 0.1 M. HCl (4.1 mg/mL at 25 °C). It is a weak base having dissociation constant (pK_a)[7] 5.7 with *n*-octanol: water partition coefficient of 1.19 (log *P*) at physiological pH.[8] Thus, absorption of LT after oral administration is dependent on the rate of dissolution and release under physiological conditions. Peak plasma concentrations are achieved after 2.5 h after oral administration. Low aqueous solubility linked with poor dissolution rate delays its absorption and onset of action. Hence improvement in dissolution rate is expected to elicit a faster absorption of the drug leading to a quicker onset of action, which is highly essential to control the seizure episodes in epileptic patients. For quicker onset of action lamotrigine orally disintegrating tablet has been formulated by Patil *et al.*[9] Though, several crystal products of LT has been reported over past years for the improvement of solubility and dissolution rate, however an optimized crystalline product of LT with citric acid (CA) is yet to be reported.[10–12] The present work aimed for the development and characterization of a novel crystalline product of LT with CA to improve its dissolution rate and oral absorption for enhanced clinical outcome. The study involved characterization of the LT–CA crystal products by different analytical techniques along with *in vitro* dissolution studies to report the optimized crystal product for future *in vivo* studies.

EXPERIMENTAL

Chemicals

LT was received as gift sample from Unichem Pvt. Ltd., MP, India. CA was purchased from Sisco Research Laboratories, Maharastra, India. Ethanol was received from Merck Specialties Pvt. Ltd., India. All other chemicals used in the experiment were of analytical grade.

Synthesis of experimental crystal products

The LT–CA crystal products were prepared by the conventional solvent evaporation method with required modifications. Briefly, accurately weighed amount of LT was mixed with accurately weighed amount of CA in a beaker. The mixtures were then dissolved in 50 vol. % ethanol followed by slow drying at 40–50 °C for 72 h.[13] Slow evaporation of the solvent under controlled conditions induced crystallization. The crystal products were formulated at three different molar ratio of LT with CA, *i.e.*, 1:1, 2:1 and 3:1. After complete removal of organic solvent, the dried crystal products were collected, weighed and stored until further use.

In vitro *characterization*

Fourier transform infrared (FTIR) spectroscopy. FTIR study was carried out with the help of a FTIR spectrophotometer (JASCO, FT/IR-4100). For the study, LT, CA along with selected crystal products, were mixed separately with IR grade potassium bromide (at 100:1 ratio) to prepare thin pellets.[14] A pressure of 5 t was applied in a hydraulic press for 5 min to prepare the pellets. Those were then scanned in the FTIR spectrophotometer over a wave number range of 400 to 4000 cm^{-1}. The spectra manager software (version 2.0) was employed to analyze the peaks.

Differential scanning calorimetry (DSC). For the DSC experiment, required quantity of samples of pure drug (LT), CA and all the selected crystal products were taken in crimped aluminum pans with pin-hole.[15] Calibration of the instrument about heat flow and temperature was done by Indium (m.p. 156.6 °C). Heating rate of 10 °C per min was used within a temperature range of 30–300 °C along with an inert (N_2) atmosphere. The study was carried out by using a DSC-1 (Mettler Toledo DSC) with STAR^e software.

X-ray diffractometry. X-ray diffractometry of free drug along with the synthesized crystal powder products was carried out to obtain idea on the crystallinity, crystal orientations along with other structural parameters. Briefly, dry powdered sample was placed on the glass slide and analyzed with the help of a powder X-ray diffractometer (Ultima, IV, Japan). For the experiment, an X-ray of 40 kV/40 mA was applied on the tested samples at a detection angle (2θ) for 120 s.[16,17]

In vitro drug release study

The release profile of the drug from different crystal products was estimated in a USP XXIII dissolution testing apparatus (Dissolution tester (USP) TDT06L, Electrolab) using rotating paddle method.[10,18] For the experiment, a weighed amount of powder sample of LT (100 mg) and selected crystal products (100 mg equivalent LT) were placed in a dissolution vessel rotated at 50 rpm at 37±0.5 °C. Simulated gastric fluid (900 ml of 0.1 M HCl at pH 1.2) was taken as the release medium. The study was conducted for 60 min duration. During the study, at time intervals of 5, 10, 20, 30 and 60 min, 10 ml of samples were withdrawn from the dissolution chamber through a syringe with simultaneous replenishment of fresh release medium to maintain the sink condition. After collection, the samples were filtered using a membrane filter (0.25 μm). The filtered aliquots following required dilutions were analyzed at 267 nm using a UV–Vis spectrophotometer (JASCO V-630, Japan) against 0.1 N HCl as blank.

Statistical analysis

The experiments were carried out in triplicate for accuracy and reproducibility. Data was expressed as the mean ± standard deviation (*SD*). Model independent statistical methods such as the difference factor f_1 and the similarity factor f_2 were applied for comparison of two dissolution profiles.

RESULTS AND DISCUSSION

Crystal product development

The experimental crystals were synthesized in three different mole ratios of LT and CA such as 1:1, 2:1 and 3:1. In all the crystal products, amount of CA was kept constant, whereas amount of the drug was varied under identical experimental conditions. Out of several crystal product batches, here we have reported three sets of crystal products, *i.e.*, L1S1, L2S1 and L3S1. The composition of various crystal products was depicted in Table I. Simultaneously we have provided a schematic representation of LT–CA crystals (Fig. 1**)** to depict the possible mechanism of development of crystal structure by the formation of strong covalent bond (peptide) between the functional group of LT and CA.

TABLE I. Crystal products of lamotrigine–citric acid by solvent evaporation method in ethanol–water as solvent system

Crystal product code	Mole ratio (LT:CA)	m_{LT} / g	m_{CA} / g
L1C1	1:1	1.87	1
L2C1	2:1	3.75	1
L3C1	3:1	5.62	1

In the schematic diagram, three possible mechanism of crystal formation has been depicted *via* three line diagrams (A, B and C). Considering three numbers of acidic (–COOH) groups present in one molecule of citric acid, there arise three probable types of stoichiometric ratio between the LT and CA molecules, *viz*. 1:1, 2:2 and 3:1 during the formation of crystal structure. Thus, all the three types of possible molecular arrangement in the crystal lattice at different ratio have been schematically represented. The resultant peptide bond formed between the components would make the crystal product more stable and also it would help to improve solubility property. This form of peptide bond will remain stable in hydrolysis, however under acidic conditions (pH 2–4); it can be readily broken into individual components.

FTIR study

FTIR is an important analytical technique, which is often used as a pre-crystal product study to assess any incompatibility between the drug and excipient. Any significant shifting in the characteristic peaks of the drug or excipient or appearance of new peaks in the crystal product justifies intermolecular interaction and formation of new products. In the FTIR spectra, major functional groups of LT that is at 3448 (N–H aromatic stretching), 3210 (C–H aromatic stretching) 1645 (C=N),[9] 1292 and 1319 cm^{-1} (two weak intensity sharp peaks for C–N bending vibration), 1405–1458 cm^{-1} (four peaks in pairs for aromatic C=C stretch benzene ring), 1051 (C–Cl), 716 (ortho-substituted benzene), 790 cm^{-1} (meta substituted benzene), etc. were all present in the spectrum of pure LT.

However, few changes in the characteristic peaks of experimental crystal products as compared to free drug (LT) were observed, which indicate formation of new crystalline phases (Fig. 2). The sharp peak observed for LT at 3448.21 cm^{-1} (due to N–H aromatic stretching) was found to be shifted at 3360.35 (L1C1), 3329.5 (L2C1) and 3332.39 cm^{-1} (L3C1), respectively. Similarly, the strong peaks observed in the FTIR spectra of the crystal products due to C–N stretching vibration (for aromatic amine), *i.e.*, 1284.36 (L1C1), 1291.11 (L2C1), and 1297.86 cm^{-1} (L3C1) were absent in the FTIR spectrum of the pure LT. Further, the strong peaks at 1754.9 and 1684.55 cm^{-1} (C=O stretching of the COOH group) along with 3364 and 3011 cm^{-1} (O–H stretching) for CA were absent in the crystal products. Particularly, in the crystal product L3C1 (3:1 mole ratio of LT and CA), much changes of the peaks for COOH group was observed, signifying stoichiometric formation of C–N bonds between NH_2 groups (three molecules of LT) with three COOH groups (one molecule of CA). In a nutshell, such type of changes in the peaks justified successful formation of intermolecular bonds in between the components to develop the new crystal state.

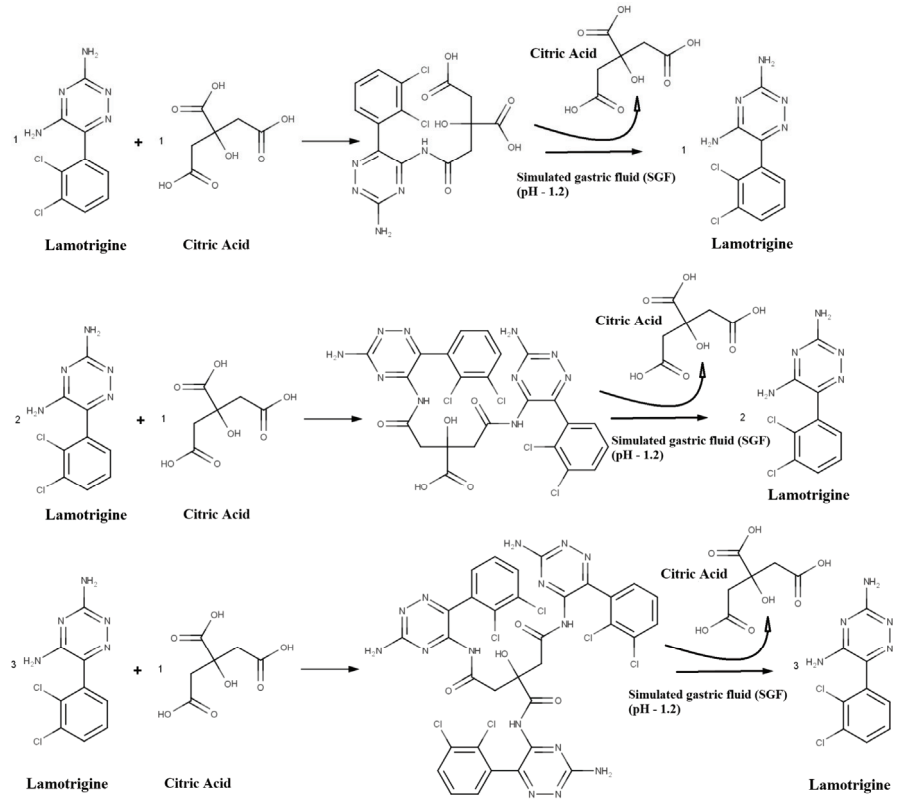

Fig. 1. Schematic representation of LT–CA crystal formation.

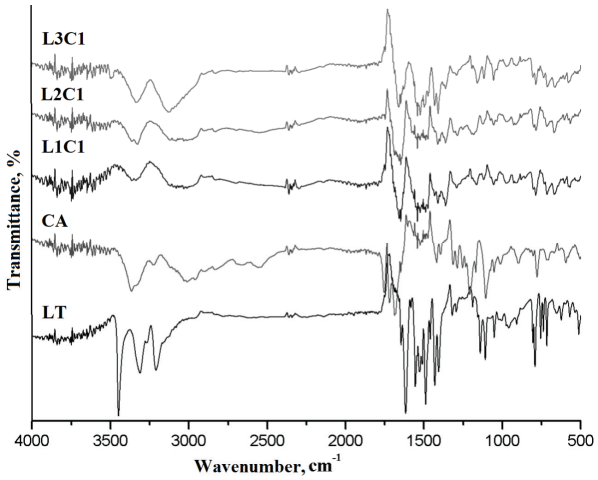

Fig. 2. FTIR spectra of pure drug (LT), excipient (CA) and crystal products (L1C1, L2C and L3C1).

DSC study

Differential scanning calorimetry helps to study the thermal behavior of the crystal form relative to the individual components along with any possible chemical interactions between the drug and excipient.[19] DSC thermogram of LT and experimental crystal products (L1C1, L2C1 and L3C1) were presented in Fig. 3.

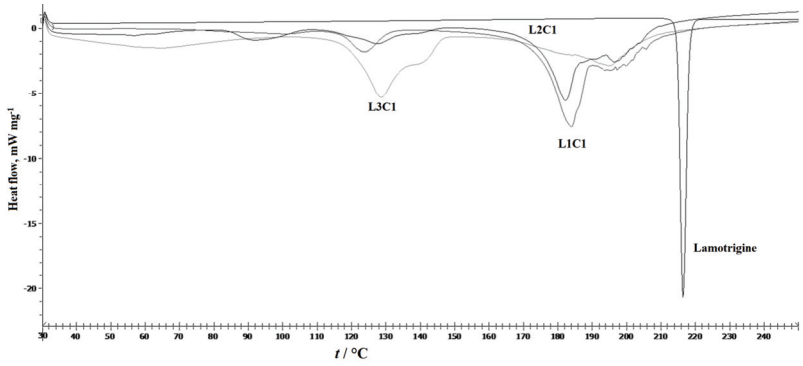

Fig. 3. DSC thermograms of pure drug, excipient (SA) and the crystal products (L1C1, L2C1 and L3C1).

DSC study of the pure drug showed sharp endothermic peak at 215 °C, whereas the experimental crystal products showed sharp peaks at 183 and 125 °C, respectively. From the DSC study, thermal profile of formed crystalline product was found to be different from that of the pure drug, which overall signified formation of new crystalline state. Further, there was no sign of chemical incom-

patibility found in the DSC thermogram, which is another important criterion for successful crystal product development.

PXRD study

To depict the phase identification of a crystalline material and to provide information on unit cell dimensions, XRD study has been used as an important analytical tool.[20] In XRD, a monochromatic beam of X-ray is actually allowed to fall on the powdered sample. Reflected X-rays are then detected by a detector fitted with the machine. Usually, amorphous regions of the samples produce broad peaks in contrast to crystalline regions, which produce relatively sharper peaks. From the experiment, XRD patterns of the experimental crystal products were different from that of the pure drug. For the pure drug, the characteristic crystalline peaks have been identified at 2θ 12.39, 17.35, 25.44, 27.78 and 28.33° (Fig. 4). However, some new peaks were observed in the crystal products. From the XRD data it was clearly found that L3C1 show sharp peak, which was different from that of L1C1 and L2C1, which confirmed the formation of novel crystalline phase. The relatively smaller peaks in case of L1C1 and L2C1 might be due to the phenomenon of amorphization in the product.

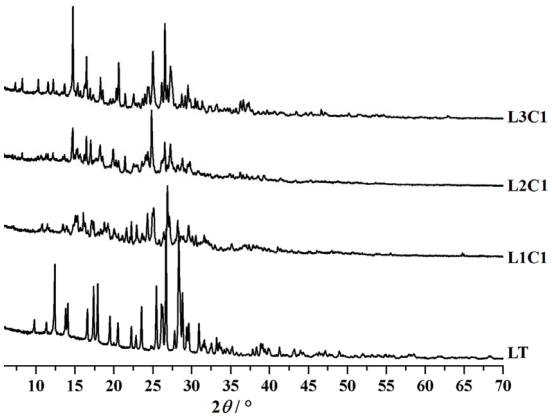

Fig. 4. PXRD data of the pure drug and the crystal products (L1C1, L2C1 and L3C1).

Debye–Scherrer formula was employed to find out other characteristic properties like particle size, strain and dislocation density in the formed crystal products (Table II).

Crystal size was calculated using following equation:

$$D = 0.9\lambda/\beta\cos\theta \quad (1)$$

The particle strain in lattice was determined from the equation:

$$\varepsilon = \beta/\tan\theta \quad (2)$$

where, e = strain, b = full width half maxima (FWHM), D = crystallite size, l = wavelength.

TABLE II. Crystal lattice dislocation and strain arising from crystal imperfections

Crystal product	Particle size, nm	Dislocation density×10^{15}, m^{-2}	Strain
LT	69.54	20.68	0.3528
L1C1	38.90	90.30	0.3455
L2C1	46.68	66.50	0.6338
L3C1	53.55	50.72	0.3518

The dislocation density (δ), which represents the amount of defects in the sample and can be defined as the length of dislocation lines per unit volume of the crystal was calculated:

$$\delta = 1/D^2 \quad (3)$$

The particle size was found lowest in case of L1C1 as compare to the pure drug and other crystal products. The changes in the strain and dislocation value between the pure drug and the crystal products may be due to the bond formation between LT and CA.

In vitro *drug release study*

In vitro drug release study of the experimental crystal products along with the free drug was carried out in simulated gastric fluid (pH 1.2). *In vitro* drug release remains an inevitable piece of study for all solid oral dosage forms, which actually signifies the rate and extent that an API is extracted from the crystal product. Data generated out of *in vitro* release experiments play a crucial role in designing *in vivo* test conditions.[21] In our study, all the selected crystal products showed higher dissolution profile than that of pure LT (Fig. 5). Among the crystal products, L3C1 showed higher percentage of cumulative drug release (97.11 %) within 10 min of experimental release period. The difference factor f_1 and the similarity factor f_2 as the model independent statistical methods were applied for comparison of two dissolution profiles.[3,22] Equivalence or similarity between two dissolution profiles is based on $f_1 \leq 15$ and $f_2 \geq 50$ and so on. f_1 and f_2 factor between LT and L3C1 were found to be 17.807 and 30.964, respectively. Hence, L3C1 may be reported as the optimized crystal product in our study as per *in*

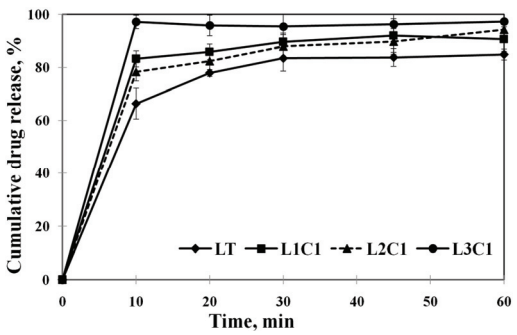

Fig. 5. *In vitro* dissolution data of pure drug (LT), and crystal products (L1C1, L2C1, and L3C1) in simulated gastric fluid (0.1 M HCl, pH 1.2) for 60 min. All set of experiments were performed in triplicate. Data show mean ± *SD* (n = 3). Error bars indicate standard deviation values.

vitro release profile based on the f_1 and f_2 factor. The higher drug release property of the reported crystal product might be due to the well formation of crystal lattice with supramolecular arrangement of molecules in a three-dimensional space.

The uniqueness of the study lies in the formation of strong peptide bond between LT and CA during crystal formation. Such strong covalent bond would help the crystal product to remain stable under normal experimental conditions including hydrolysis, but would readily break under low pH conditions. In the presence of acids or at low pH, peptide bond can be broken easily to free the entrapped drug molecule. As the peptides shorter than five residues are usually soluble in water, thus formation of the peptide bond between the components in our crystal product would increase the solubility of LT, which was the main aim of the work.

The work is highly expected to have interesting clinical implications in future days. These novel crystal products of LT-CA with higher dissolution rate may be formulated in tablet dosage forms and can be compared with marketed LT tablet crystal products to establish its superiority over other such crystal products. Though, LT tablets are widely available in the market in various doses, the extent of variations in LT serum concentration between the marketed tablets and tablets formed out of LT–CA crystals are yet to be investigated. By dint of its unique developmental feature (*i.e.*, formation of peptide bond, exceptionally stable under normal condition, highly sensitive under acidic condition), the experimental crystal product in suitable dosage forms would certainly provide much faster absorption of the drug with quicker onset of action, which undoubtedly improve its therapeutic efficacy and patient acceptability. A prompt onset of action is highly crucial to control the occurrence of epileptic seizures and is the present need of the hour.

However, our work also has some limitations. As we discussed above, the experimental crystal product has not been compared with any marketed LT tablet crystal products for the *in vitro* drug release study. Further, the crystal geometry or arrangement pattern of molecules/atoms during development of the crystal structure could have been investigated. Moreover, our work is totally restricted to *in vitro* studies; however, to get a clear idea on the therapeutic implications *in vivo* studies, in suitable experimental epileptic animal models, are also required. The data on the *in vitro*-*in vivo* correlation is also highly needed for its successful clinical transfer. All such experiments are planned to be included in the future course of our work.

CONCLUSIONS

Crystalline products of LT with CA have been developed for the improvement of dissolution rate and oral absorption of the drug. FTIR and DSC studies confirmed absence of any incompatibility between drug and excipient, however,

minor shifting of some characteristic peaks as well as appearance of newer peaks in the crystal product justified the formation of covalent bond (peptide) during the formation of crystal structure. In FTIR spectra, strong peaks observed for the crystal products, *i.e.*, 1284.36 (L1C1), 1291.11 (L2C1) and 1297.86 cm^{-1} (L3C1) due to C–N stretching vibration (for aromatic amine) were clearly absent in the FTIR spectrum of the pure LT. XRD data further confirmed formation of novel crystalline phase. In XRD analysis, L3C1 showed much sharper peaks among all the tested crystal products and pure LT justifying successful formation of crystal phase. *In vitro* drug release study depicted higher dissolution rate for the crystal products than the free LT under the identical experimental conditions. Further, among all the crystal products, L3C1 showed the highest dissolution rate (97.11 % within 10 min) as compared to the pure drug (60.32 % within 10 min) and thus reported as the optimized crystal product in our study. The production steps were kept very simple with optimization of all critical processing parameters, which would help for future technology transfer of the product at industrial scale. Further *in vivo* studies are warranted to establish the crystal product in clinics.

Acknowledgement. We are very much thankful to Prof. Manoj Ranjan Nayak, President, Siksha O Anusandhan (Deemed to be University) for giving necessary research facilities.

ИЗВОД

ЕФЕКАТ КРИСТАЛИСАНИХ ПРОИЗВОДА ЛАМОТРИГИНА ИЗ СИСТЕМА ЛАМОТРИГИН–ЛИМУНСКА КИСЕЛИНА НА ПОВЕЋАНО ОСЛОБАЂАЊЕ ЛЕКА У *IN VITRO* СИМУЛИРАНОЈ ЖЕЛУДАЧНОЈ СРЕДИНИ

BHABANI SANKAR SATAPATHY, ASUPRITA PATEL, RUDRA NARAYAN SAHOO и SUBRATA MALLICK

Department of Pharmaceutics, School of Pharmaceutical Sciences, Siksha 'O' Anusandhan (Deemed to be University), Kalinganagar, Bhubaneswar-751003, Odisha, India

Кристал-инжењеринг је саставни део истраживања у области развоја нових лекова. Различите кристалне форме неког лека могу значајно модификовати његова физичко-хемијска својства. Циљ овог рада је синтеза и карактеризација нових кристалних форми ламотригина (LT, од *U.S. Food and Drug Administration* одобреног антилептичког лека) у присуству лимунске киселине (CA) у циљу његовог већег отпуштања у симулираној желудачној средини и боље оралне апсорпције. Нове кристалне форме продуката из система ламотригин–лимунска киселина су добијене применом методе упаравања смеше растварача етанол–вода. Постојање нових форми кристала лека утврђено је на основу карактеристичних сигнала у FTIR спектру. Експериментално одређене тачке топљења добијених кристалних форми ламотригина су биле различите од тачке топљења чистог лека. Такође, формирање кристалних форми лека потврђено на основу постојања нових оштрих сигнала у XRD спектру. Нађен је већи проценат отпуштања лека у симулираној желудачној средини у току 60 min за експериментално добијене кристалне форме лека у односу на чист лек. Међутим, у циљу развоја технолошког процеса за индустријску производњу лека неопходно је урадити одговарајућа *in vivo* испитивања.

(Примљено 5. јула, ревидирано 8. августа, прихваћено 20. августа 2020)

REFERENCES

1. A. K. El-Yafi, H. El-Zein, *Asian J. Pharm. Sci.* **10** (2015) 283 (https://doi.org/10.1016/j.ajps.2015.03.003)
2. N. Blagden, M. De Matas, P. T. Cavan, *Adv. Drug Deliv. Rev.* **59** (2007) 617 (https://doi.org/10.1016/j.addr.2007.05.011)
3. R. N. Sahoo, A. De, V. Kataria, S. Mallick, *Indian J. Pharm. Edu. Res.* **53 (**2019) s554 (https://doi.org/10.5530/ijper.53.4s.150)
4. P. Jiaxin, W. Shuya, L. Wen, K. Dereje, Z. Ying, Z. Bing, Q. Dongli, G. Pan, L. Nan, L. Zhidong, *Asian J. Pharm. Sci.* **14** (2019) 154 (https://doi.org/10.1016/j.ajps.2018.04.009)
5. S. Indumathi, D. Sameer, *Pharmaceutics* **10** (2018) 1 (https://doi.org/10.1021/acs.cgd.7b00599)
6. G. Péter, C. Pallagigábor, K. Orsolya, J. Piroska, S. Ambrus, *Drug Des. Dev. Ther.* **11** (2017) 2453 (https://doi.org/10.2147/DDDT.S138559)
7. M. L. Cheney, N. Shan, E. R. Healey, M. Hanna, L. Wojtas, M. J. Zaworotko, V. Sava, S. Song, J. R. Sanchez-Ramos, *Cryst. Growth Des.* 10 (2010) 394 (https://doi.org/10.1021/cg901010v)
8. M. Lalic, A. Pilipovic,S. Golocorbin-Kon, K. Gebauer-Bukurov, K. Bozic, M. Mikov, J. Cvejic, *Drugs R&D* **11** (2011) 53 (https://doi.org/10.2165/11588260-000000000-00000)
9. C. Patil, S. Das, *Afr. J. Pharm. Pharmacol.* 5 (2009)76 (https://doi.org/10.5897/AJPP10.279)
10. P. Chappa, A. Maruthapillai, M. Tamilselvi, S. Devikala, J. A Selvi, *Mater. Today: Proceedings* **14** (2019) 504 (https://doi.org/10.1016/j.matpr.2019.04.173)
11. K. Nigam, A. Kaur, A. Tyagi, M. Nematullah, F. Khan, R. Gabrani, *Drug Deliv. Translat. Res*. **18** (2019) 1 (https://doi.org/10.1007/s13346-019-00622-5)
12. K. Wen, J. Shao, X. Shen, L. Ping, L. A. Ping, Z. Juying, Z. Jin, *Cryst. Growth Des.* **10** (2019) 1 (https://doi.org/10.1021/acs.cgd.9b01028)
13. Z. Rahman, C. Agarabi, A. S. Zidan, S. R. Khan, M. A. Khan, *AAPS PharmSciTech.* **12** (2011) 693 (https://doi.org/10.1208/s12249-011-9603-4)
14. A. Merdoud, M. Mouffok, A. Mesli, N. Chafi, M. Chaib, *J. Serb. Chem. Soc.* **85** (2020) 531 (https://doi.org/10.2298/JSC190326132M)
15. S. Mallick, S. K. Pradhan, M. Chandran, M. Acharya, T. Digdarsini, R. Mohapatra, *Results Pharm. Sci.* **1** (2011) 1 (https://doi.org/10.1016/j.rinphs.2011.05.003)
16. S. Mallick, P. K. Dey, S. Sannigrahi, A. Mitra, *Acta Pol. Pharm.* **61** (2004) 447 (https://www.ptfarm.pl/pub/File/Acta_Poloniae/2004/6/447.pdf)
17. R. Mohapatra, S. Mallick, *Asian J. Chem.* **28** (2016) 1149 (https://doi.org/10.14233/ajchem.2016.19614)
18. O. C. Larbi, H. Merine, Y. Ramli, F. B. Toumi, K. Guemra, A. Dehbi, *J. Serb. Chem. Soc.* **83** (2018) 1243 (https://doi.org/10.2298/JSC171112065L)
19. S. Patrycja, W. Marek, *J. Therm. Anal. Calorim.* **133** (2018) 785 (https://doi.org/10.1007/s10973-017-6858-30)
20. T. S. Latha, M. C. Reddy, V. D. Prasad, S. V. Muthukonda, D. Lomada, *Indian J. Pharmacol.* **49** (2017) 458 (https://doi.org/10.4103/ijp.IJP_536_16)
21. H. Muhammad, S. Muhammad, R. Yousuf, F. Zafar, *Plos One* **13** (2018) 1 (https://doi.org/10.1371/journal.pone.0203123)
22. A. Pramanik, R. N. Sahoo, A. Nanda, R. Mohapatra, R. Singh, S. Mallick, *Curr. Eye Res.* **43** (2018) 828 (https://doi.org/10.1080/02713683.2018.1446534).

Journal of the Serbian Chemical Society
JSCS-info@shd.org.rs • www.shd.org.rs/JSCS
J. Serb. Chem. Soc. *86* (1) 63–75 (2021)
JSCS–5404
Original scientific paper

Predicting retention indices of PAHs in reversed-phase liquid chromatography: Quantitative structure retention relationship approach

NABIL BOUARRA[1,2]*, NAWEL NADJI[1], LOUBNA NOURI[1], AMEL BOUDJEMAA[1], KHALDOUN BACHARI[1] and DEJLLOUL MESSADI[2]

[1]*Centre de Recherche Scientifique et Technique en Analyses Physico–Chimiques, BP 384, Zone Industrielle Bou-Ismail, 42004 Tipaza, Algeria and* [2]*Laboratory of Environmental and Food Safety, Department of Chemistry, Badji Mokhtar– Annaba University, PB 12, 23000, Annaba, Algeria*

(Received 19 February, revised 24 March, accepted 16 April 2020)

Abstract: In this work, the liquid chromatography retention time in monomeric and polymeric stationary phases of PAHs was investigated. Quantitative structure retention relationship approach has been successfully performed. At first, 3224 molecular descriptors were calculated for the optimized PAHs structure using Dragon software. Afterwards, the modelled dataset was divided using the CADEX algorithm into two subsets for internal and external validation. The genetic algorithm-based on a multiple linear regression was used for feature selection of the most significant descriptors and the model development. The selected models with five descriptors: *nCIR*, *GGI3*, *GGI4*, *JGT* and *DP14* were used for the monomeric column and *nR10*, *EEig01x*, *L1m*, *H5v* and *HATS6v* were introduced for the polymeric column. Robustness and predictive performance of the suggested models were verified by both internal and external statistical validation. The good quality of the statistical parameters indicates the stability and predictive power of the suggested models. This study demonstrated the suitability of the established models in the prediction of liquid chromatographic retention indices of PAHs.

Keywords: molecular descriptors; genetic algorithm; multiple linear regression; prediction.

INTRODUCTION

Polycyclic aromatic hydrocarbons (PAHs) establish a huge family of neutral and stable organic compounds, composed of carbon and hydrogen, containing from 2 to 6 fused aromatic rings.[1] PAHs are found in our environment as ubiquitous, persistent and toxic molecules.

* Corresponding author. E-mail: bouarranabil@yahoo.com
https://doi.org/10.2298/JSC200219019B

Indeed, the pyrolysis or the carbonization of organic compounds as coal, oil, and wood is the major source of PAHs.[2] Generally, PAHs are applied as intermediate compounds in pharmaceuticals, photographic products, lubricating materials, agricultural foodstuffs, thermosetting plastics, and other industrial products.[3,1] The emissions of PAHs during the incomplete combustion pose a serious disquiet for the environment.[2] The reversed-phase liquid chromatography (RPLC) is one of the important methods most used, versatile analytical techniques.[4] Usually, the C18 phase is used in RPLC and LC[5] as a stationary phase due to its excellent detection, separation and selectivity to PAHs and their isomers.[6]

The experimental determination of LC retention indices (*RI*) for all possible PAHs compounds is labor-intensive, and thus time-consuming and expensive. Recently, alternative approaches have been extensively investigated in an attempt to enhance the performance of substitute ways to obtain theoretical *RI*.[4]

Nowadays, quantitative structure retention relationship (QSRR) has gained much interest from researchers in the area of separation science. The QSRR is a powerful tool that provides promising methods for the valuation of *RI* based on structural descriptors calculated from the molecular structure.[7] The advantage of the QSRR approach is that the built model permits the estimation of *RI* for an unknown, unmeasured or novel compounds which have a similar structure to those used to build up the model.[8] Moreover, the use of QSRR allows for the fast and easily done input of the compounds' structures that are usually studied. Also, QSRR is used for the calculation, the analysis of descriptors and for the generation and validation of the model equation. Several estimation methods to understand the specific molecular interactions that govern PAHs chromatographic separation have been investigated[9-12] using topology of the molecule and/or quantum chemistry parameters calculated for the optimized molecular structure.

The main purpose of the present work is to establish robust and accurate models, which are capable to estimate the RI for the PAHs using combined method genetic algorithm-multiple linear regression (GA-MLR). The predictive power of the obtained models was validated by a prediction set. Moreover, the applicability domain of the developed models was checked graphically based on Williams plot. In addition, the developed models can help to understand and describe the retention behavior by highlighting the necessary factors to represent the relationship between the *RI* of PAHs and their molecular structure.

EXPERIMENTAL

Dataset

The experimental *RI* were taken from the study of Sander and Wise.[13] The reported values are between 2 and 6 for both polymeric and monomeric columns. The retention data are expressed as logarithms of *RI* (log *I*, Table S-I of the Supplementary material to this paper).

RI of the liquid chromatography of both monomeric and polymeric C18 reversed-phase column were determinated using Vydac 201TP 10μ (polymeric) 4.6 mm×25 cm (the separation group, Hesperia, CA, USA) and Zobrax ODS 6μ(monomeric), 6.4 mm×25 cm (Dupon, Wilington, DE, USA). The mobile phase used was composed of 85 % acetonitrile in water for both columns. Pop *et al.*[14] illustrated that *RI* was similar to Kováts indices in the gas chromatography (GC). The equation used was expressed as:

$$\log I_x = \log I_n + \frac{\log R_x - \log R_n}{\log R_{(n+1)} - \log R_n} \quad (1)$$

where x, n and (n+1) and R represents the solute, the lower, the higher standard and the values are the corresponding corrected retention volumes, respectively.

Descriptors generation

The chemical structures of the studied molecules were downloaded from the WebBook database[15] as SD-file format. The final geometry of the minimum energy conformation was obtained by the B3LYP functional approach[6] in combination with the 6-31G (d) basis set. For more information, the technical details of the geometric optimization of molecules are available at the NIST website.[15] Afterwards, Dragon software V5.5[17] was used for the calculation of 3224 molecular descriptors to describe the chemical's structural diversity. Then, constant descriptors, near-constant descriptors and highly correlation descriptors (R > 0.95) were excluded by using built-in variable exclusion procedure in Dragon to reduce the initial pool of descriptors and eliminate the redundant information that was not used. In the end, 398 molecular descriptors were retained.

Dataset division

In order to generate a strong QSRR model that could estimate the *RI* of PAHs, based on the algorithm of Kennard and Stone (Cadex),[18] the data set was divided into the training and the prediction set. The training set made up of 92 compounds was investigated to make the final model while the remaining 40 compounds (prediction set) were used to validate the built model (see Table S-II of the Supplementary material).

Model development and validation

QSARINS software[19] was used to construct the QSRR model. In order to select the best modelling descriptors, the statistical quality of all combinations of the whole descriptors was explored by using multiple linear regression and the genetic algorithm-variable subset selection (GA/VSS) methods based on ordinary least squares (OLS). The variable subset selection procedure generates a 'population' of models, ranked according to decreasing R^2 values. The optimal models were chosen according to Q^2Leave-One-Out (Q^2_{LOO}) as the optimization value and take into consideration the parsimony principle regarding the complexity of the models, which should be as small as possible. Moreover, the correlation between the descriptors and the response was verified by the Q under influence of K rule[20] to remove models with high predictor collinearity and exclude chance correlation.

A key step in QSRR studies is the validation of the built models, aims to guarantee their goodness of fit, reliability, robustness and ability to provide good predictions for new compounds.[21]

The coefficient (R^2) was calculated to evaluate the goodness-of-fit and to estimate the degrees of overall correlation. A robust model should have an R^2 values greater than 0.7.[22] The R^2 was calculated using:

$$R^2 = 1 - \frac{\sum_{i=1}^{n}\left(\hat{y}_i - y_i\right)^2}{\sum_{i=1}^{n}\left(y_i - \bar{y}\right)^2} \quad (2)$$

where y_i, $\hat{y}_i$, $\bar{y}$, and n represents the experimental, the calculated, the mean value of the experimental *RI* and the number of samples in the training set; respectively.

The reliability and consistency of a model can be investigated via the cross-validation technique (CV).[23] Leave-one-out (LOO) and leave-many-out (LMO) strategies can be carried out by calculating the cross-validation coefficient (Q^2_{LOO}) and (Q^2_{LMO}). In the LOO technique, each time one sample from the training set would be removed, consequently, several models will be generated. Whereas, in LMO technique M represents a group of compounds randomly selected that would be removed at the beginning and be predicted by the model, which was developed using the remaining compounds.

According to Chirico and Gramatica,[22,24] a model is statistically reliable if the Q^2_{LOO} value is greater than 0.6. Q^2_{LOO} values close to the Q^2_{LMO} indicated that the model is robust.[25] The Q^2_{LOO} is defined as follows:

$$Q^2_{LOO} = 1 - \frac{\sum_{i=1}^{n}\left(\hat{y}_{i/i} - y_i\right)^2}{\sum_{i=1}^{n}\left(y_i - \bar{y}\right)^2} \quad (3)$$

where, $\hat{y}_{i/i}$ is the value of log *I* predicted by the model built without the compound *i* according to LOO method.

The predictive power of the built models was evaluated by calculating several external validation metrics such as R^2_{ext}, Q^2_{F1},[26] Q^2_{F2},[27] Q^2_{F3},[28,29] and the concordance correlation coefficient (*CCC*).[22,24,30] For the predictive power of a model to be considered adequate, the values of Q^2_{F1}, Q^2_{F2} and Q^2_{F3} should be greater than 0.7, and the CCC_{ext} value must be greater than 0.85.[22,24] The equations defined the external validation metrics are regrouped in Table S-III of the Supplementary material.

Besides, the root mean square error (*RMSE*)[31] is calculated by squaring individual errors, summing them, dividing the sum by their total number, and then taking the square root of this quantity. Therefore, the *RMSE* summarizes the global error of the model used to measure and compare the accuracy of the predictions in training and prediction set, *i.e.*, the precision of the QSRR and can be applied to predictions (*i.e.*, $RMSE_{Pr}$):

$$RMSE_{tr(pr)} = \sqrt{\frac{1}{n_{tr(pr)}}\sum_{i=1}^{n_{tr(pr)}}\left(y_i - \hat{y}_i\right)^2} \quad (4)$$

Applicability domain (AD)

The applicability domain (AD)[32] of constructed model is a theoretical region in chemical space, defined by the modeled response and model descriptors. In this region, compounds possess similar structure, biological or physicochemical properties to the ones of the training compounds. Williams plot is the typical graphical description of the AD, which represents the standardized residuals versus leverages values (h_i). Leverage values are calculated as the diagonal of the Hat matrix:

$$h_i = x_i^T\left(X^T X\right)^{-1} x_i, \ (i = 1,...,n) \quad (1)$$

where x_i is the descriptor vector of the compound and X is the **n**×**p** matrix containing **p** descriptor values and **n** training compounds. Generally, the warning leverage[33] is defined as follows:

$$h^* = \frac{3(k+1)}{m} \tag{2}$$

where m is the number of compounds in the training set and k is the number of descriptors in the developed model.

Williams plot utilized as a graphical detection of both the outliers responses (*i.e.*, chemicals with absolute standardized residuals greater than 3 standard deviation units) and the structurally influential chemicals (*i.e.*, chemicals with leverage values greater than the threshold value $h_i > h^*$).[34]

To ensure that the established model is reliable and robust, the Y-scrambling is one of the most widely used techniques.[34] Indeed, it is not uncommon to obtain fortuitous correlations, *i.e.*, a model with good statistical results (R^2, Q^2) for training, but involving descriptors that in reality are not related to the modeled property. These random models can be detected by the Y-scrambling procedure. It consists of randomly mixing the experimental property for the training set and using the same descriptors, re-training the learning algorithm to try to obtain a model. Normally, the obtained models should have very low performance.[19]

RESULTS AND DISCUSSION

In order to develop the models, each column was treated separately by using the same pool of available descriptor to the regression analysis procedure. For each column type, it was a very important to see which of the descriptors were considered significant in predicting the RI values. The regression analysis procedure generated several reasonable models. The choice of the best model was made by using many criteria such as the size of the model, the multiple correlation coefficients (R^2), leave one out cross-validation coefficient (Q^2_{LOO}), the external validation metrics, *etc*. The best model is one that has a high value of the coefficients cited above. The optimal selected models for each column were deduced to be:

Monomeric column:

$$\log I = 1.40 + 0.0176nCIR + 0.442GGI3 + 0.733 + 1.36JGT + 0.130DP14 \tag{7}$$

$R^2 = 0.9799$, $Q^2_{LOO} = 0.9771$, $Q^2_{LMO} = 0.9770$, $RMSE_{cv} = 0.1155$, $RMSE_{tr} = 0.1083$, $CCC_{tr} = 0.9898$, $RMSE_{ext} = 0.1313$, $R^2_{ext} = 0.9721$, $Q^2_{F1} = 0.9714$, $Q^2_{F2} = 0.9706$, $Q^2_{F3} = 0.9705$, $CCC_{ext} = 0.9849$, $s = 0.1120$, $F = 838.6887$.

Polymeric column:

$$\log I = -7.11 + 0.0970nR10 + 1.95EEig01x + 0.169L1m + + 1.41H5v + 0.905HATS6v \tag{8}$$

$R^2 = 0.9677$, $Q^2_{LOO} = 0.9623$, $Q^2_{LMO} = 0.9617$, $RMSE_{cv} = 0.1263$, $RMSE_{tr} = 0.1083$, $CCC_{tr} = 0.9836$, $RMSE_{ext} = 0.1292$, $R^2_{ext} = 0.9603$, $Q^2_{F1} = 0.9584$, $Q^2_{F2} = 0.9565$, $Q^2_{F3} = 0.9605$, $CCC_{ext} = 0.9770$, $s = 0.1209$, $F = 514.9955$.

The statistical parameters of the developed models prove that the established models are stable, robust and predictive. Thus, the two models were approved, R^2 values greater than 0.7 and CCC_{tr} values greater than 0.85. Additionally, these two models had the smallest $RMSE_{tr}$ values and the greatest CCC_{tr} values, which indicate that these models presented the least error and the smallest differences between the experimental and predicted data. Also, Q^2_{LOO} and Q^2_{LMO} values for models (polymeric and monomeric) are greater than 0.6 and very close to R^2. Additionally, the developed models presented the smallest $RMSE_{cv}$ values, which confirm that these are the best models. The external validation results of the developed models indicate that they have good predictive power, given that all presented R^2_{ext} values greater than 0.7, CCC_{ext} values are also greater than 0.85. The external validation results (Q^2_{F1}, Q^2_{F2} and Q^2_{F3}) for each subset make it clear that the two models were approved, in agreement with the criteria recommended in the literature.[22,24] Then, the built models were used to predict the prediction set data (Table S-I).

Table I shows the statistical and the definition of the selected descriptors. The regression coefficients of the descriptors presented in the models are significantly larger than the standard deviation indicated by the high absolute *t*-values. The values of probability (*P*) are less than 0.05 for each descriptor that means the presence of every descriptor is statistically significant and indicates that the models are not a result of mere chance. As can be seen from Table I, the variance inflation factor (*VIF*) values of all descriptors are less than five.[35] Thus, there is no collinearity between the selected descriptors, and the obtained models are stable.

TABLE I. Names, definitions and coefficients of selected descriptors in the developed models

Descriptor	Descriptor definition	Coeff	SE. Coeff	*T*	*P*	*VIF*
	Polymeric					
Constant		–7.110	0.627	–11.33	0.000	–
nR10	Number of 10-memberd rings	0.097	0.007	12.62	0.000	1.460
EEig01x	Eigen value 01 from edge adj. matrix weighted by edge degrees	1.945	0.136	14.30	0.000	1.789
H5v	H autocorrelation of lag 5 / weighted by atomic van der Waals volumes	0.168	0.007	23.24	0.000	1.951
L1m	1st component size directional WHIM index / weighted by atomic masses	1.410	0.265	5.31	0.000	2.347
HATS6v	Leverage-weighted autocorrelation of lag 6 / weighted by van der Waals volume	0.904	0.262	3.44	0.001	1.496
	Monomeric					
Constant		1.397	0.114	12.160	0.000	–
nCIR	Number of circuits	0.017	0.002	7.210	0.000	3.670
GGI3	Topological charge index of order 3	0.441	0.035	12.590	0.000	1.793
GGI4	Topological charge index of order 4	0.733	0.039	18.640	0.000	2.518
JGT	Global topological charge index	1.362	0.371	3.670	0.000	1.788
DP14	Molecular profile no. 14	0.130	0.007	17.98	0.000	1.544

As shown in Fig. 1, the experimental and predicted values are very close. This model fits well the experimental data (R^2 = 0.96, 0.97, *RMSE* = 0.11, 0.10 for the training set and R^2_{ext} = 0.96, 0.97, *RMSE* = 0.13, 0.11 for the prediction set) for polymeric and monomeric column; respectively. A good internal robustness (Q^2_{LMO} = 0.97, 0.96). So, the proposed models show an excellent agreement between the experimental and predicted values.

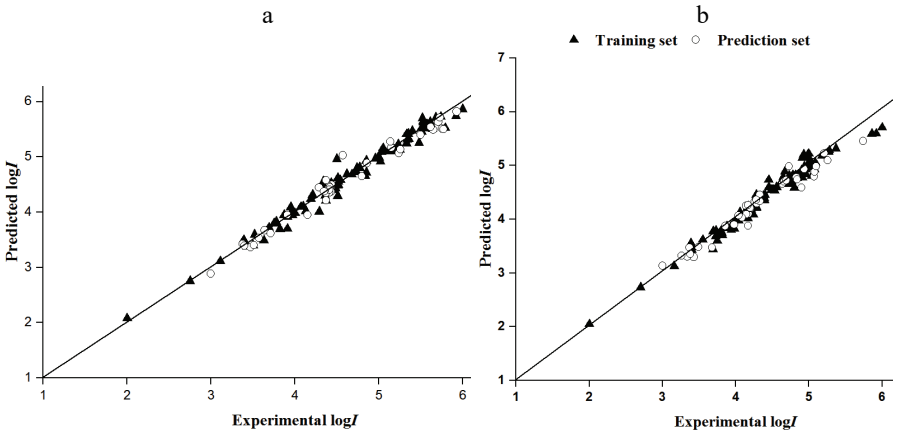

Fig. 1. Predicted versus experimental values of log *I*: a) monomeric column; b) polymeric column.

Fig. 2 shows the residuals of the training and prediction data set. All the residuals, that are distributed on both sides of the zero line uniformly and randomly, indicated the absence of the systematic error in the developed model.

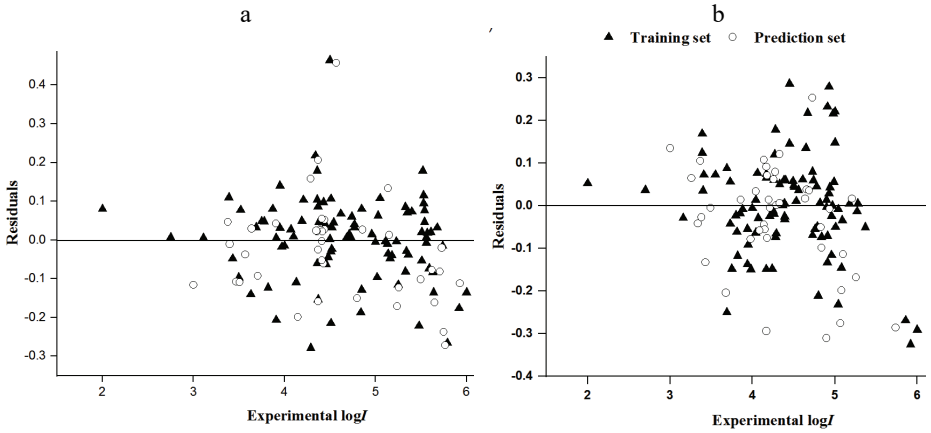

Fig. 2. The residuals *vs.* training and prediction values for the developed models: a) monomeric column; b) polymeric column.

The built models were analyzed using Williams plots. The results show that most of 132 compounds are within the area of the applicability domain of the model and have been well predicted (Fig. 3). The leverage value of Naphthalene for the polymeric column model is greater than the threshold $h^* = 0.195$, while for the monomeric column model four compounds (Indeno[1,2,3-*cd*]fluoranthene, naphthalene, benzo[ghi]perylene and dibenzo[def,mno]chrysene) from the training set exceed the h^* value ($h^* = 0.195$). But their standardized residual values are less than 3s. Thus, these compounds can stabilize the models and make them more precise.[33]

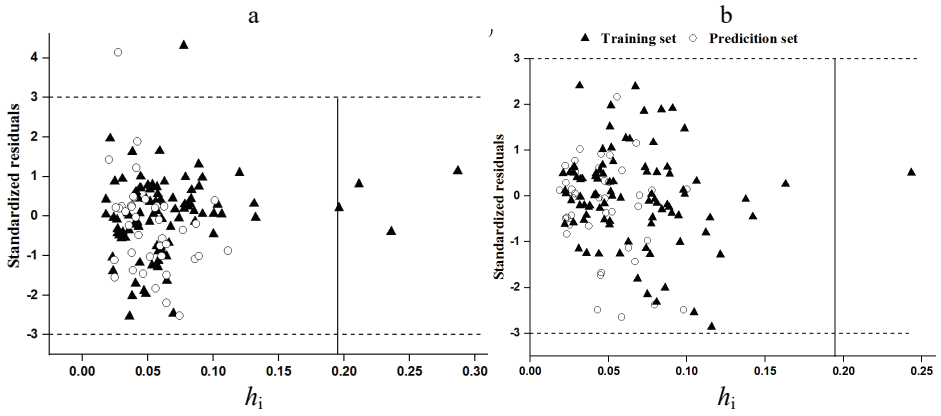

Fig. 3. Williams plot: a) monomeric column; b) polymeric column.

In order to identify outlier compounds, Williams plot shows that the standardized residuals for all molecules in the training and prediction sets are smaller than three standard deviation units (±3s) in absolute value, except for monomeric model only one compound in the training set (Benzo[a]naphthacene) and one in the prediction set (perylene-3-methyl) were wrongly predicted, but have lower leverage values, which means that they belong to the applicability domain of the developed models. When the statistical parameters Q^2_{F1}, Q^2_{F2}, Q^2_{F3} and $CCC_{ext,}$, which are indicators of the predictive ability have high values. Then, the predicted log I by the developed model is reliable. Perhaps, the wrong predictions may have happened due to incorrect experimental values.

In the goal of verifying the robustness of the developed models, Y-randomization test was applied. The dependent variable vector (log RI) was shuffled randomly within the training set by using 200 iterations, knowing that on every iteration a novel model will be generated.

Figure 4 (A-B) which represents the diagram of the statistical coefficients Q^2_{Yscr} and R^2_{Yscr} makes it possible to compare the results obtained for the randomized models (squares) with the developed model (ring). It is clear that R^2

and Q^2 values of the model are very high compared to the values obtained for the randomized models. These results indicate that the robustness and the reliability of the developed models are not due to chance correlation.

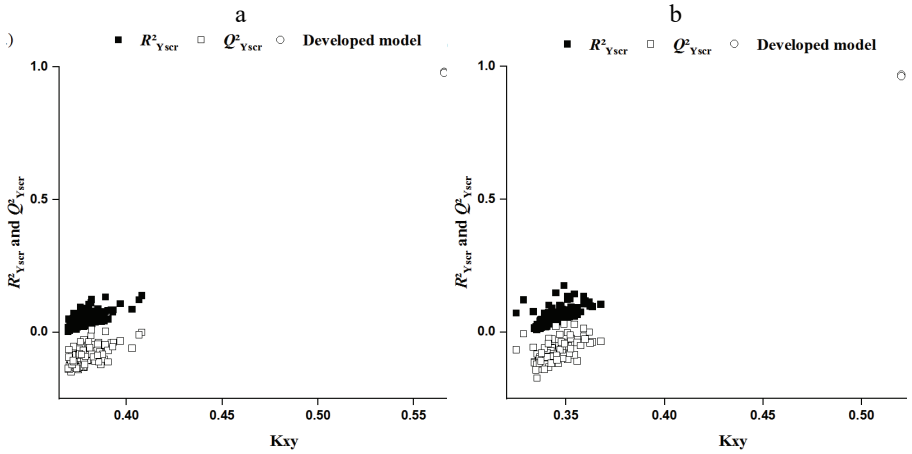

Fig. 4. Y-Scramble plot of R^2 and Q^2 *vs*. *Kxy* for random models (*Kxy*: correlations among the block of the descriptors and the experimental data).

The orders of importance for the selected descriptors in monomeric and polymeric columns are as follow:

For the monomeric column: *GGI4* (27.4862 %) > *DP14* (26.2492 %) > *nCIR* (19.7418 %) > *GGI3* (14.2261 %) > > *JGT* (12.2967 %).

For polymeric column: *L1m* (32.419 %) > *EEig01x* (22.102 %) > *nR10* (19.789 %) > *H5v* (13.444 %) > > *HATS6v* (12.2434 %).

The two descriptors belonged to the GETAWAY-type descriptor[36] are namely *H5v* and *HATS6v*. *H5v* which belongs to the GETAWAY *H*-indices-type descriptors that was calculated by *H* autocorrelation function along with the topological structure and weighted by atomic van der Waals volumes.[36] The diagonal elements of the molecular influence matrix were used to calculate the *HAT6v* descriptor taking into account the relative position of each atom in the three-dimensional molecular space weighted by van der Waals volume.[36] The *HAT6v* values are directly proportional to the ramification of molecules. The positive influence of *H5v* and *HATS6v* on the log *I* indicated that the logarithm of *RI* in the polymeric column will be increased when the volume of a solute is increased.

The WHIM descriptor[37] involved in polymeric model *L1m*, represent different sources of chemical information for the entire three-dimensional molecular structure such as size, shape, symmetry, and atom distribution. They are calculated by carrying out a PCA on a weighted covariance matrix of the centred rectangular coordinates of a molecule obtained from different atoms weighting

schemes.[37] *L1m* encodes the size of the molecule along with the second component weighted *via* atomic masses. In Eq. (8), *L1m* showed a positive effect, indicating that the increase of the molecule size increases the log *I*.

GGI3 and *GGI4* are topological charge indexes of order 3 and 4 respectively, while *JGT* is the global topological charge index which belongs to the Galvez topological charge indices. Topological descriptors facilitate the identification of the molecules through to their size, degree of ramification, flexibility and global shape.[38] Topological charge indices describe the charge transfer between atoms, and therefore the global charge transfer in the molecule as it relates to the topology.[39] These descriptors have a positive sign in the model equation which means log *I* increase with the increasing of these predictors.

The two constitutional descriptors *nR10* and *nCIR* are reported in the built models reflecting the molecular composition of a compound without connectivity and geometry information. The *nR10* descriptor explains the presence of either independent or fused 10-membered rings in molecules which play the main role in the determination of physicochemical properties.[38] While the *nCIR* descriptor is the number of the circuit and includes both rings and circuits. The positive coefficient of *nR10* and *nCIR* suggests that the log *I* increase with the increasing number of *n*-member rings.

The *EEig01x* is an edge adjacency index, that belongs to topological descriptor obtained from the edge adjacency matrix, which encodes the connectivity between graph edges. The positive coefficient of *EEig01x* descriptor indicates that the *RI* increases with the increasing of *EEig01x* values.[38] The Randić molecular profile *DP14*[40] can characterize the three-dimensional structure of each molecule. The Randić molecular profile descriptors are particularly suitable in similarity/diversity analysis since each profile well characterizes a molecule. The positive sign of *DP14* coefficient suggests that the log *I* increase with the molecule branching.

CONCLUSION

QSRR method was utilized to investigate the relationship between the molecular structure of PAHs and their retention indices. The good performance of statistical parameters (R^2, Q^2_{LOO}, $Q^2_{F1\text{-}F3}$ and *CCC*) and low *RMSE* values suggest that the developed models possess a good predictive capacity, which helps to estimate the *RI* of PAHs in cases where *RI* values are not available. The results provide a simple and straightforward way to predict the *RI* just from the molecular structures and gave some insight into the structural features related to *RI* of the PAHs.

Acknowledgement. The authors are grateful to the Directorate General for Scientific Research and Technological Development DGRSDT of Algeria for the financial support to this work.

SUPPLEMENTARY MATERIAL

Additional data are available electronically at the pages of journal website: https://www.shd-pub.org.rs/index.php/JSCS/index, or from the corresponding author on request.

И З В О Д

ПРЕДВИЂАЊЕ РЕТЕНЦИОНИХ ИНДЕКСА ПОЛИЦИКЛИЧНИХ АРОМАТИЧНИХ УГЉОВОДОНИКА У РЕВЕРСНО-ФАЗНОЈ ТЕЧНОЈ ХРОМАТОГРАФИЈИ: ПРИСТУП КВАНТИТАТИВНЕ РЕЛАЦИЈЕ СТРУКТУРЕ И РЕТЕНЦИОНИХ ИНДЕКСА

NABIL BOUARRA[1,2], NADJI NAWEL[1], NOURI LOUBNA[1], AMEL BOUDJEMAA[1], KHALDOUN BACHARI[1] и DEJLLOUL MESSADI[2]

[1]*Centre de Recherche Scientifique et Technique en Analyses Physico–Chimiques, BP 384, Zone Industrielle Bou-Ismail, 42004 Tipaza, Algeria* и [2]*Laboratory of Environmental and Food Safety, Department of Chemistry, Badji Mokhtar– Annaba University, PB 12, 23000, Annaba, Algeria*

У овом раду су истраживана ретенциона времена у мономерним и полимерним стационарним фазама полицикличних ароматичних угљоводоника (ПАУ) у течној хроматографији. Приступ квантитативном релацијом структуре и ретенције успешно је спроведен. Почето је са 3224 молекулска дескриптора израчунатим за оптимизоване структуре ПАУ помоћу Dragon софтвера. Затим је, моделовани скуп података подељен користећи CADEX алгоритам у два подскупа за интерну и екстерну валидацију. Генетички алгоритам заснован на вишеструкој линеарној регресији употребљен је да се изврши избор карактеристика најзначајнијих дескриптора и развој модела. Одабрани модели који укључују пет дескриптора: *nCIR*, *GGI3*, *GGI4*, *JGT* и *DP14* употребљени су за мономерне колоне, а *nR10*, *EEig01x*, *L1m*, *H5v* и *HATS6v* су уведени за полимерну колону. Робустност и ваљаност предвиђања сугерисаних модела проверене су и интерном и екстерном статстичком валидацијом. Висок квалитет статистичких параметара указује на стабилност и способност предвиђања сугерисаних модела. Ова студија демонстрира погодност утврђених модела за предвиђање ретенционих индекса код течне хроматографије ПАУ.

(Примљено 19. фебруара 2019, ревидирано 24. марта, прихваћено 16. априла 2020)

REFERENCES

1. M. Pogorzelec, K. Piekarska, *Sci. Total Environ*. **631** (2018)1431 (https://dx.doi.org/10.1016/j.scitotenv.2018.03.105)
2. H. I. Abdel-Shafy, M. S. M. Mansour, *Egypt. J. Petrol*. **25** (2016) 107 (https://dx.doi.org/10.1016/j.ejpe.2015.03.011)
3. N. E. Kaminski, B. L. Faubert Kaplan, M. P. Holsapple, *Casarett and Doull's Toxicology, the basic science of poisons*, C. D. Klaassen (Ed.), Mc-Graw Hill, Inc., New York, 2008, p. 1280 (ISBN: 978-0071470513)
4. R. Put, Y. Vander Heyden, *Anal. Chim. Acta* **602**(2007) 164 (https://dx.doi.org/10.1016/j.aca.2007.09.014)
5. K. D. Bartle,M. L Lee,S. A. Wise, *Chem. Soc. Rev*. **10** (1981) 113 (https://dx.doi.org/10.1039/CS9811000113).
6. *EPA Test Method, Polynuclear Aromatic Hydrocarbons- Method 610*, US Environmental Protection Agency, Environmental Monitoring and Support Laboratory, 1982 (https://www.epa.gov/sites/production/files/2015-10/documents/method_610_1984.pdf)
7. R. Kaliszan, *Chem. Rev*. **107** (2007) 3212 (https://dx.doi.org/10.1021/cr068412z)
8. N.Goudarzi, D. Shahsavani,F. Emadi-Gandaghi, M. Arab Chamjangali, *J. Chromatogr., A* **1333** (2014) 25 (https://dx.doi.org/10.1016/j.chroma.2014.01.048)

9. M. M. C. Ferreira, *Chemosphere* **44** (2001) 125 (https://dx.doi.org/10.1016/S0045-6535(00)00275-7)
10. F. A. L. Ribeiro, M. M. C. Ferreira, *J. Mol. Struct.: Theochem*. **663** (2003) 109 (https://dx.doi.org/10.1016/j.theochem.2003.08.107)
11. T. Moon, M. W. Chi, S. J. Park, C. N. Yoon, *J. Liq. Chromatogr. Rel. Technol*. **26** (2003) 2987 (https://dx.doi.org/10.1081/JLC-120025413)
12. K. A. Lippa, L. C. Sander, S. A. Wise, *Anal. Bioanal. Chem*. **378** (2004) 365 (https://dx.doi.org/10.1007/s00216-003-2419-7)
13. L. C. Sander, S. A.Wise, *J. Chromatogr. Libr*. **57**(1995) 337 (https://dx.doi.org/10.1016/S0301-4770(08)60622-3)
14. M. Popl, V. Dolansky,J.Mostecky, *J. Chromatogr*. **117** (1976) 117 (https://doi.org/10.1016/S0021-9673(00)81072-9)
15. National institute of standards and technology, https://webbook.nist.gov/chemistry/
16. A. D. Becke, *J. Chem. Phys*. **98** (1993) 5648 (https://dx.doi.org/10.1063/1.464913)
17. *TaleteSrl. Dragon for windows (Software for Molecular Descriptor Calculation), version 5.5*, Milano, 2007 (software available at: http://www.talete.mi.it)
18. R. W. Kennard, L. A. Stone, *Technometrics* **11** (1969) 137 (https://dx.doi.org/10.1080/00401706.1969.10490666)
19. P. Gramatica, N. Chirico, E. Papa, S. Cassani, S. Kovarich, *QSARINS, Software for the Development and validation of QSAR MLR Models* (available on request at http://www.qsar.it)
20. R. Todeschini, A. Maiocchi, V. Consonni, *Chemometr. Intell. Lab. Sys*. **46** (1999) 13 (https://dx.doi.org/10.1016/S0169-7439(98)00124-5)
21. P. Gramatica, *QSAR Comb. Sci*. **26** (2007) 694 (https://dx.doi.org/10.1002/qsar.200610151)
22. N. Chirico, P. Gramatica, *J. Chem. Inf. Model*. **51** (2011) 2320 (https://dx.doi.org/10.1021/ci200211n)
23. D. W. Osten. *J. Chemometr.* **2** (1998) 39 (https://dx.doi.org/10.1002/cem.1180020106)
24. N. Chirico, P. Gramatica, *J. Chem. Inf. Model*. **52** (2012) 2044 (https://dx.doi.org/10.1021/ci300084j)
25. R. Kiralj, M. M. C. Ferreira, *J. Braz. Chem. Soc*. **20** (2009) 770 (https://dx.doi.org/10.1590/S0103-50532009000400021)
26. P. Gramatica, *Mol. Inf*. **33** (2014) 311 (https://dx.doi.org/ 10.1002/minf.201400030)
27. G. Schüürmann, R. Ebert, J. Chen, B. Wang, R. Kühne. *J. Chem. Inf. Model*. **48** (2008) 2140 (https://doi.org/10.1021/ci800253u)
28. V. Consonni, D. Ballabio, R. Todeschini, *J. Chem. Inf. Model*. **49** (2009) 1669 (https://dx.doi.org/10.1021/ci900115y)
29. V. Consonni, D. Ballabio, R. Todeschini, *J. Chemometr.* **24** (2010) 194 (https://dx.doi.org/10.1002/cem.1290)
30. L. I. Lin, *Biometrics* **45** (1989) 255 (https://dx.doi.org/10.2307/2532051)
31. A. O. Aptula, N. G. Jeliazkova, T. W. Schultz, M. T. D. Cronin, *QSAR Comb. Sci*. **24** (2005) 385 (https://dx.doi.org/10.1002/qsar.200430909)
32. A. Tropsha, P. Gramatica, V. K. Gombar, *QSAR Comb. Sci*. **22** (2003) 69 (https://dx.doi.org/10.1002/qsar.200390007)
33. L. Eriksson, J. Jaworska, A. P. Worth, M. T. D. Cronin,R. M. McDowell, P. Gramatica. *Environ. Health Perspect*. **111** (2003)1361(https://dx.doi.org/10.1289/ehp.5758)
34. S. Kherouf, N. Bouarra,A. Bouakkadia, D. Messadi**,** *J. Serb. Chem. Soc*. **84** (2019) 575 (https://dx.doi.org/10.2298/JSC180820016K)

35. S. Chatterjee, A. Hadi, B. Price, *Regression Analysis by Examples*, Wiley-VCH, New York, 2000, p. 368 (ISBN-13: 978-0471319467)
36. V. Consonni, R. Todeschini, M. Pavan. *J. Chem. Inf. Comput. Sci.* **42** (2002) 682 (https://dx.doi.org/10.1021/ci015504a)
37. R. Todeschini, P. Gramatica, *Quant. Struct.-Act. Relat.* **16** (1997) 113 (https://dx.doi.org/10.1002/qsar.19970160203)
38. R. Todeschini, V. Consonni, *Molecular Descriptors for Chemoinformatics*, Wiley-VCH, New York, 2009, p.1257 (ISBN-13: 978-3527318520)
39. J. Galvez, R. Garcia-Domenech, J. V. de Julian-Ortiz, R. Soler, *J. Chem. Inf. Comput. Sci*. **35** (1995) 272(https://dx.doi.org/10.1021/ci00024a017)
40. M. Randic, G. Krilov, *Chem. Phys. Lett*. **272** (1997) 115 (https://dx.doi.org/10.1016/S0009-2614(97)00447-8).

Journal of the Serbian Chemical Society
JSCS-info@shd.org.rs • www.shd.org.rs/JSCS
J. Serb. Chem. Soc. 86 (1) S8–S14 (2020) *Supplementary material*

SUPPLEMENTARY MATERIAL TO

Predicting retention indices of PAHs in reversed-phase liquid chromatography: Quantitative structure retention relationship approach

NABIL BOUARRA[1,2]*, NAWEL NADJI[1], LOUBNA NOURI[1], AMEL BOUDJEMAA[1], KHALDOUN BACHARI[1] and DEJLLOUL MESSADI[2]

[1]*Centre de Recherche Scientifique et Technique en Analyses Physico–Chimiques, BP 384, Zone Industrielle Bou-Ismail, 42004 Tipaza, Algeria and* [2]*Laboratory of Environmental and Food Safety, Department of Chemistry, Badji Mokhtar– Annaba University, PB 12, 23000, Annaba, Algeria*

J. Serb. Chem. Soc. 86 (1) (2021) 63–75

TABLE S-I. Experimental (Exp.), predicted (Pred.) and residual (Res.) values of log *I* for PAHs

Name	log *I*					
	Polymeric			Monomeric		
	Exp.	Pred.	Res.	Exp.	Pred.	Res.
Naphthalene	2	2.0532	0.0532	2	2.0802	0.0802
Fluorene	2.7	2.7374	0.0374	2.75	2.7566	0.0066
Anthracene	3.16	3.132	-0.028	3.11	3.1157	0.0057
Fluoranthene	3.39	3.5593	0.1693	3.43	3.3816	-0.0484
Aceanthrylene	3.39	3.5146	0.1246	3.39	3.4995	0.1095
pyrene	3.55	3.6231	0.0731	3.63	3.4899	-0.1401
11H-Benzo[a]fluorene	3.81	3.749	-0.061	3.75	3.7988	0.0488
11H-Benzo[b]fluorene	3.82	3.7031	-0.1169	3.78	3.828	0.048
Cyclopenta[cd]pyrene	3.94	3.8861	-0.0539	3.95	4.0903	0.1403
Benzo[ghi]fluoranthene	3.95	3.8594	-0.0906	4.07	4.0969	0.0269
Triphenylene	3.75	3.6021	-0.1479	3.82	3.6972	-0.1228
Benzo[c]phenanthrene	3.69	3.7788	0.0888	3.91	3.7039	-0.2061
Benz[a]anthracene	4	3.995	-0.005	4	3.9853	-0.0147
Chrysene	4.06	4.1373	0.0773	3.97	3.9523	-0.0177
Benz[e]aceanthrylene	4.25	4.2389	-0.0111	4.34	4.5578	0.2178
Benz[l]aceanthrylene	4.26	4.2413	-0.0187	4.38	4.4269	0.0469
Benz[k]acephenanthrylene	4.39	4.3584	-0.0316	4.43	4.5273	0.0973
Benz[a]aceanthrylene	4.24	4.0922	-0.1478	4.45	4.4899	0.0399
Benzo[j]fluoranthene	4.26	4.3209	0.0609	4.37	4.4568	0.0868
Benzo[k]fluoranthene	4.38	4.4403	0.0603	4.5	4.5022	0.0022

* Corresponding author. E-mail: bouarranabil@yahoo.com

Benzo[e]pyrene	4.29	4.2252	-0.0648	4.51	4.4802	-0.0298
Perylene	4.33	4.3808	0.0508	4.52	4.497	-0.023
Benzo[a]pyrene	4.51	4.5548	0.0448	4.68	4.6848	0.0048
13H-Dibenzo[a,g]fluorene	4.53	4.5413	0.0113	4.62	4.6876	0.0676
11H-Indeno[2,1-a]phenanthrene	4.91	4.8396	-0.0704	4.74	4.8004	0.0604
13H-Dibenzo[a,h]fluorene	4.96	4.8445	-0.1155	4.77	4.8101	0.0401
Indeno[1,2,3-cd]pyrene	4.84	4.7669	-0.0731	5.23	5.2265	-0.0035
Indeno[1,2,3-cd]fluoranthene	4.93	4.9587	0.0287	5.05	5.1578	0.1078
Benzo[ghi]perylene	4.76	4.7061	-0.0539	5.36	5.3214	-0.0386
Dibenzo[def,mno]chrysene	5.08	4.9348	-0.1452	5.61	5.6305	0.0205
Dibenzo[c,g]phenanthrene	4.07	4.0412	-0.0288	4.51	4.2953	-0.2147
Benzo[b]triphenylene	4.4	4.4598	0.0598	4.73	4.7379	0.0079
Benzo[g]chrysene	4.27	4.3909	0.1209	4.71	4.7247	0.0147
Benzo[c]chrysene	4.45	4.7367	0.2867	4.85	4.7213	-0.1287
Dibenz[a,j]anthracene	4.56	4.5969	0.0369	4.84	4.653	-0.187
Pentaphene	4.67	4.8886	0.2186	4.96	4.9748	0.0148
Benzo[a]naphthacene	4.99	5.0465	0.0565	4.5	4.964	0.464
Benzo[b]chrysene	5	5.1483	0.1483	5	4.9949	-0.0051
Picene	5.18	5.1848	0.0048	5.02	4.9239	-0.0961
Dibenz[a,e]acephenanthrylene	4.8	4.5894	-0.2106	5.48	5.2584	-0.2216
Dibenzo[j,l]fluoranthene	4.79	4.7415	-0.0485	5.35	5.4208	0.0708
Naphth[2,3-a]aceanthrylene	4.91	4.7772	-0.1328	5.51	5.4563	-0.0537
Naphth[2,3-e]acephenanthrylene	5.27	5.257	-0.013	5.64	5.5046	-0.1354
Naphtho[2,3-j]fluoranthene	4.98	5.1963	0.2163	5.4	5.4736	0.0736
Dibenz[e,k]acephenanthrylene	5.28	5.2857	0.0057	5.59	5.5167	-0.0733
7H-Benzo[c]fluorene	3.49	3.4851	-0.0049	3.64	3.6692	0.0292
Benz[j]aceanthrylene	4.26	4.3223	0.0623	4.29	4.4481	0.1581
Benz[e]acephenanthrylene	4.29	4.2918	0.0018	4.44	4.4668	0.0268
Dibenzo[b,g]phenanthrene	4.33	4.4514	0.1214	4.8	4.6493	-0.1507
Dibenz[a,h]anthracene	4.73	4.9839	0.2539	4.86	4.8862	0.0262
Dibenz[a,e]aceanthrylene	4.9	4.5897	-0.3103	5.5	5.3982	-0.1018
Indeno[1,2,3-fg]naphthacene	5.07	4.7944	-0.2756	5.71	5.628	-0.082
Benzo[rst]pentaphene	5.74	5.4542	-0.2858	5.93	5.8178	-0.1122
Anthracene, 1-methyl	3.43	3.2975	-0.1325	3.57	3.5323	-0.0377
Phenanthrene, 2-methyl	3.68	3.476	-0.204	3.71	3.6171	-0.0929
Phenanthrene, 3-methyl	3.34	3.2989	-0.0411	3.47	3.362	-0.108
Phenanthrene, 4-methyl	3.26	3.3252	0.0652	3.4	3.3892	-0.0108
Phenanthrene, 9-methyl	3.38	3.3532	-0.0268	3.51	3.4003	-0.1097
Fluoranthene, 3-methyl	3.86	3.8745	0.0145	3.91	3.9518	0.0418
Pyrene, 1-methyl	3.98	3.9024	-0.0776	4.15	3.9512	-0.1988
Benz[a]anthracene, 1-methyl	4.18	4.1046	-0.0754	4.39	4.4171	0.0271
Benz[a]anthracene, 2-methyl	4.14	4.0963	-0.0437	4.43	4.3685	-0.0615
Benz[a]anthracene, 4-methyl	4.33	4.3361	0.0061	4.44	4.4917	0.0517
Benz[a]anthracene, 6-methyl	4.15	4.0944	-0.0556	4.41	4.4644	0.0544
Benz[a]anthracene, 8-methyl	4.21	4.2051	-0.0049	4.4	4.4258	0.0258
Benz[a]anthracene, 10-methyl	4.18	4.2514	0.0714	4.42	4.4419	0.0219
Benz[a]anthracene, 12-methyl	4.14	4.2485	0.1085	4.37	4.5758	0.2058

Benzo[c]phenanthrene, 3-methyl	4.09	4.0318	-0.0582	4.41	4.357	-0.053
Benzo[c]phenanthrene, 5-methyl	4.04	4.0741	0.0341	4.37	4.3441	-0.0259
Benzo[c]phenanthrene, 6-methyl	4.17	3.8761	-0.2939	4.37	4.2106	-0.1594
Chyrsene, 3-methyl	4.28	4.3594	0.0794	4.41	4.4067	-0.0033
Chyrsene, 4-methyl	4.2	4.2145	0.0145	4.36	4.3813	0.0213
Chyrsene, 6-methyl	4.17	4.2617	0.0917	4.35	4.3736	0.0236
Benzo[a]pyrene, 1-methyl	4.83	4.7796	-0.0504	5.24	5.0683	-0.1717
Benzo[a]pyrene, 4-methyl	4.84	4.7412	-0.0988	5.26	5.1368	-0.1232
Benzo[a]pyrene, 5-methyl	4.64	4.6567	0.0167	5.15	5.1626	0.0126
Benzo[a]pyrene, 11-methyl	4.66	4.6984	0.0384	5.14	5.2735	0.1335
Benzo[a]pyrene, 1,2-dimethyl	5.21	5.2264	0.0164	5.73	5.7094	-0.0206
Benzo[a]pyrene, 1,3-dimethyl	5.26	5.0922	-0.1678	5.75	5.512	-0.238
Benzo[a]pyrene, 1,4-dimethyl	5.08	4.8818	-0.1982	5.77	5.4979	-0.2721
Benzo[a]pyrene, 1,6-dimethyl	5.1	4.9867	-0.1133	5.65	5.4879	-0.1621
Benzo[a]pyrene, 3,12-dimethyl	4.94	4.9331	-0.0069	5.62	5.5425	-0.0775
Perylene, 3-methyl	4.69	4.7255	0.0355	4.57	5.0275	0.4575
Naphtho[1,2-k]fluoranthene	5	5.2213	0.2213	5.34	5.3113	-0.0287
Naphtho[2,3-k]fluoranthene	5.92	5.5952	-0.3248	5.79	5.5242	-0.2658
Dibenzo[def,p]chrysene	4.65	4.7862	0.1362	5.57	5.5884	0.0184
Benzo[a]perylene	4.93	5.2096	0.2796	5.54	5.6166	0.0766
Naphtho[1,2,3,4-def]chrysene	4.97	4.9702	0.0002	5.56	5.5666	0.0066
Dibenzo[de,qr]naphthacene	4.91	5.143	0.233	5.53	5.625	0.095
Dibenzo[fg,op]naphthacene	5.04	5.0321	-0.0079	5.52	5.699	0.179
Benzo[b]perylene	5.04	4.8086	-0.2314	5.56	5.5531	-0.0069
Naphtho[2,1,8-qra]naphthacene	5.86	5.5916	-0.2684	5.92	5.7437	-0.1763
Dibenzo[b,def]chrysene	6	5.7094	-0.2906	6	5.8644	-0.1356
Phenanthro[3,4-c]phenanthrene	4.21	4.1858	-0.0242	4.77	4.8017	0.0317
Dibenzo[g,p]chrysene	4.45	4.5961	0.1461	5.53	5.6454	0.1154
Anthracene, 2-methyl	3.69	3.4408	-0.2492	3.69	3.723	0.033
Anthracene, 9-methyl	3.41	3.4833	0.0733	3.52	3.5974	0.0774
Phenanthrene, 1-methyl	3.4	3.4359	0.0359	3.5	3.4035	-0.0965
Fluoranthene, 1-methyl	3.73	3.6879	-0.0421	3.87	3.9504	0.0804
Fluoranthene, 7-methyl	3.8	3.7781	-0.0219	3.91	3.9149	0.0049
Fluoranthene, 8-methyl	3.85	3.8324	-0.0176	3.95	3.9809	0.0309
Pyrene, 2-methyl	4.04	3.9772	-0.0628	4.21	4.3139	0.1039
Pyrene, 4-methyl	3.98	3.8308	-0.1492	4.13	4.0205	-0.1095
Benz[a]anthracene, 3-methyl	4.39	4.365	-0.025	4.51	4.6163	0.1063
Benz[a]anthracene, 5-methyl	4.28	4.2072	-0.0728	4.48	4.4358	-0.0442
Benz[a]anthracene, 7-methyl	4.17	4.2448	0.0748	4.36	4.4645	0.1045
Benz[a]anthracene, 9-methyl	4.37	4.3714	0.0014	4.52	4.5525	0.0325
Benz[a]anthracene, 11-methyl	4.17	4.0218	-0.1482	4.36	4.2997	-0.0603
Benzo[c]phenanthrene, 1-methyl	3.73	3.787	0.057	4.1	4.1087	0.0087
Benzo[c]phenanthrene, 2-methyl	3.94	3.8032	-0.1368	4.29	4.0115	-0.2785
Benzo[c]phenanthrene, 4-methyl	4.04	4.0541	0.0141	4.37	4.2163	-0.1537
Chyrsene, 1-methyl	4.39	4.3954	0.0054	4.46	4.3979	-0.0621
Chyrsene, 2-methyl	4.49	4.5481	0.0581	4.54	4.5851	0.0451

Chyrsene, 5-methyl	4.17	4.2363	0.0663	4.36	4.5387	0.1787
Triphenylene, 1-methyl	3.88	3.8721	-0.0079	4.19	4.2392	0.0492
Benzo[a]pyrene, 2-methyl	4.94	4.9836	0.0436	5.33	5.4154	0.0854
Benzo[a]pyrene, 3-methyl	4.9	4.8976	-0.0024	5.25	5.1346	-0.1154
Benzo[a]pyrene, 6-methyl	4.73	4.8103	0.0803	5.11	5.1064	-0.0036
Benzo[a]pyrene, 7-methyl	4.74	4.7999	0.0599	5.13	5.1202	-0.0098
Benzo[a]pyrene, 8-methyl	4.96	4.9365	-0.0235	5.33	5.2481	-0.0819
Benzo[a]pyrene, 9-methyl	4.78	4.8255	0.0455	5.18	5.1402	-0.0398
Benzo[a]pyrene, 10-methyl	4.73	4.6615	-0.0685	5.16	5.1126	-0.0474
Benzo[a]pyrene, 12-methyl	4.61	4.6717	0.0617	5.14	5.1044	-0.0356
Benzo[a]pyrene, 2,3-dimethyl	5.37	5.3198	-0.0502	5.74	5.7253	-0.0147
Benzo[a]pyrene, 3,6-dimethyl	5.09	5.0559	-0.0341	5.63	5.5467	-0.0833
Benzo[a]pyrene, 3,11-dimethyl	5.01	4.9604	-0.0496	5.68	5.7123	0.0323
Benzo[a]pyrene, 4,5-dimethyl	4.9	4.9148	0.0148	5.54	5.5869	0.0469
Benzo[a]pyrene, 7,10-dimethyl	4.82	4.8266	0.0066	5.51	5.53	0.02
Perylene, 1-methyl	4.28	4.4591	0.1791	4.85	4.9304	0.0804
Perylene, 2-methyl	4.5	4.5484	0.0484	5.03	5.093	0.063
Phenanthrene	3	3.1353	0.1353	3	2.8838	-0.1162
Acephenanthrene	3.37	3.4751	0.1051	3.38	3.4265	0.0465

TABLE S-II. Training and prediction sets for both columns by using Kennard and Stone algorithm

ID	Name	Status	ID	Name	Status
1	Naphthalene	Training	44	Naphtho[2,3-j]fluoranthene	Training
2	Fluorene	Training	45	Dibenz[e,k]acephenanthrylene	Training
3	Anthracene	Training	46	Naphtho[1,2-k]fluoranthene	Training
4	Fluoranthene	Training	47	Naphtho[2,3-k]fluoranthene	Training
5	Aceanthrylene	Training	48	Dibenzo[def,p]chrysene	Training
6	pyrene	Training	49	Benzo[a]perylene	Training
7	11H-Benzo[a]fluorene	Training	50	Naphtho[1,2,3,4-def]chrysene	Training
8	11H-Benzo[b]fluorene	Training	51	Dibenzo[de,qr]naphthacene	Training
9	Cyclopenta[cd]pyrene	Training	52	Dibenzo[fg,op]naphthacene	Training
10	Benzo[ghi]fluoranthene	Training	53	Benzo[b]perylene	Training
11	Triphenylene	Training	54	Naphtho[2,1,8-qra]naphthacene	Training
12	Benzo[c]phenanthrene	Training	55	Dibenzo[b,def]chrysene	Training
13	Benz[a]anthracene	Training	56	Phenanthro[3,4-c]phenanthrene	Training
14	Chrysene	Training	57	Dibenzo[g,p]chrysene	Training
15	Benz[e]aceanthrylene	Training	58	Anthracene, 2-methyl	Training
16	Benz[l]aceanthrylene	Training	59	Anthracene, 9-methyl	Training
17	Benz[k]acephenanthrylene	Training	60	Phenanthrene, 1-methyl	Training
18	Benz[a]aceanthrylene	Training	61	Fluoranthene, 1-methyl	Training
19	Benzo[j]fluoranthene	Training	62	Fluoranthene, 7-methyl	Training
20	Benzo[k]fluoranthene	Training	63	Fluoranthene, 8-methyl	Training

21	Benzo[e]pyrene	Training	64	Pyrene, 2-methyl	Training
22	Perylene	Training	65	Pyrene, 4-methyl	Training
23	Benzo[a]pyrene	Training	66	Benz[a]anthracene, 3-methyl	Training
24	13H-Dibenzo[a,g]fluorene	Training	67	Benz[a]anthracene, 5-methyl	Training
25	11H-Indeno[2,1-a]phenanthrene	Training	68	Benz[a]anthracene, 7-methyl	Training
26	13H-Dibenzo[a,h]fluorene	Training	69	Benz[a]anthracene, 9-methyl	Training
27	Indeno[1,2,3-cd]pyrene	Training	70	Benz[a]anthracene, 11-methyl	Training
28	Indeno[1,2,3-cd]fluoranthene	Training	71	Benzo[c]phenanthrene, 1-methyl	Training
29	Benzo[ghi]perylene	Training	72	Benzo[c]phenanthrene, 2-methyl	Training
30	Dibenzo[def,mno]chrysene	Training	73	Benzo[c]phenanthrene, 4-methyl	Training
31	Dibenzo[c,g]phenanthrene	Training	74	Chyrsene, 1-methyl	Training
32	Benzo[b]triphenylene	Training	75	Chyrsene, 2-methyl	Training
33	Benzo[g]chrysene	Training	76	Chyrsene, 5-methyl	Training
34	Benzo[c]chrysene	Training	77	Triphenylene, 1-methyl	Training
35	Dibenz[a,j]anthracene	Training	78	Benzo[a]pyrene, 2-methyl	Training
36	Pentaphene	Training	79	Benzo[a]pyrene, 3-methyl	Training
37	Benzo[a]naphthacene	Training	80	Benzo[a]pyrene, 6-methyl	Training
38	Benzo[b]chrysene	Training	81	Benzo[a]pyrene, 7-methyl	Training
39	Picene	Training	82	Benzo[a]pyrene, 8-methyl	Training
40	Dibenz[a,e]acephenanthrylene	Training	83	Benzo[a]pyrene, 9-methyl	Training
41	Dibenzo[j,l]fluoranthene	Training	84	Benzo[a]pyrene, 10-methyl	Training
42	Naphth[2,3-a]aceanthrylene	Training	85	Benzo[a]pyrene, 12-methyl	Training
43	Naphth[2,3-e]acephenanthrylene	Training	86	Benzo[a]pyrene, 2,3-dimethyl	Training
87	Benzo[a]pyrene, 3,6-dimethyl	Training	110	Benz[a]anthracene, 1-methyl	Prediction
88	Benzo[a]pyrene, 3,11-dimethyl	Training	111	Benz[a]anthracene, 2-methyl	Prediction
89	Benzo[a]pyrene, 4,5-dimethyl	Training	112	Benz[a]anthracene, 4-methyl	Prediction
90	Benzo[a]pyrene, 7,10-dimethyl	Training	113	Benz[a]anthracene, 6-methyl	Prediction
91	Perylene, 1-methyl	Training	114	Benz[a]anthracene, 8-methyl	Prediction
92	Perylene, 2-methyl	Training	115	Benz[a]anthracene, 10-methyl	Prediction
93	Phenanthrene	Prediction	116	Benz[a]anthracene, 12-methyl	Prediction
94	Acephenanthrene	Prediction	117	Benzo[c]phenanthrene, 3-methyl	Prediction
95	7H-Benzo[c]fluorene	Prediction	118	Benzo[c]phenanthrene, 5-methyl	Prediction

96	Benz[j]aceanthrylene	Prediction	119	Benzo[c]phenanthrene, 6-methyl	Prediction
97	Benz[e]acephenanthrylene	Prediction	120	Chyrsene, 3-methyl	Prediction
98	Dibenzo[b,g]phenanthrene	Prediction	121	Chyrsene, 4-methyl	Prediction
99	Dibenz[a,h]anthracene	Prediction	122	Chyrsene, 6-methyl	Prediction
100	Dibenz[a,e]aceanthrylene	Prediction	123	Benzo[a]pyrene, 1-methyl	Prediction
101	Indeno[1,2,3-fg]naph-thacene	Prediction	124	Benzo[a]pyrene, 4-methyl	Prediction
102	Benzo[rst]pentaphene	Prediction	125	Benzo[a]pyrene, 5-methyl	Prediction
103	Anthracene, 1-methyl	Prediction	126	Benzo[a]pyrene, 11-methyl	Prediction
104	Phenanthrene, 2-methyl	Prediction	127	Benzo[a]pyrene, 1,2-dimethyl	Prediction
105	Phenanthrene, 3-methyl	Prediction	128	Benzo[a]pyrene, 1,3-dimethyl	Prediction
106	Phenanthrene, 4-methyl	Prediction	129	Benzo[a]pyrene, 1,4-dimethyl	Prediction
107	Phenanthrene, 9-methyl	Prediction	130	Benzo[a]pyrene, 1,6-dimethyl	Prediction
108	Fluoranthene, 3-methyl	Prediction	131	Benzo[a]pyrene, 3,12-dimethyl	Prediction
109	Pyrene, 1-methyl	Prediction	132	Perylene, 3-methyl	Prediction

TABLE S-III. Evaluation metrics formulas and their accepted thresholds

Metric	Threshold
$R^2_{ext} = 1 - \frac{\sum_{i=1}^{n_{ext}} \left(y_i - \hat{y}_i\right)^2}{\sum_{n=1}^{n_{ext}} \left(y_i - \bar{y}\right)^2}$	$R^2ext > 0.7$
$Q^2_{F1} = 1 - \frac{\sum_{i=1}^{n_{ext}} \left(y_i - \hat{y}_i\right)^2}{\sum_{i=1}^{n_{ext}} \left(y_i - \bar{y}_{tr}\right)^2}$	$Q^2F1 > 0.6$
$Q^2_{F2} = 1 - \frac{\sum_{i=1}^{n_{ext}} \left(y_i - \hat{y}_i\right)^2}{\sum_{i=1}^{n_{ext}} \left(y_i - \bar{y}_{ext}\right)^2}$	$Q^2F2 > 0.6$
$Q^2_{F3} = 1 - \frac{\sum_{i=1}^{n_{ext}} \left(y_i - \hat{y}_i\right)^2 / n_{ext}}{\sum_{i=1}^{n_{tr}} \left(y_i - \hat{y}_{tr}\right)^2 / n_{tr}}$	$Q^2F3 > 0.6$
$CCC = \frac{2\sum_{i=1}^{n_{ext}} \left(y_i - \bar{y}\right)\left(\hat{y}_i - \bar{\hat{y}}\right)}{\sum_{i=1}^{n_{ext}} \left(y_i - \bar{y}_{ext}\right)^2 + \sum_{i=1}^{n_{ext}} \left(\hat{y}_i - \bar{\hat{y}}\right)^2 + n_{ext}\left(\bar{y}_{ext} - \bar{\hat{y}}\right)^2}$	$CCC > 0.85$

In Table S-III, y_i is the predicted value calculated using the regression of the predicted and experimental data of the prediction set, y_n the mean experimental value in the training set and n_{ext} the number of molecules in the validation set, y_{ext} the mean experimental value in the prediction set, y is the mean predicted values.

Journal of the Serbian Chemical Society
JSCS-info@shd.org.rs • www.shd.org.rs/JSCS
J. Serb. Chem. Soc. *86* (1) 77–90 (2021)
JSCS–5405
Original scientific paper

Headspace gas chromatography–mass spectrometry method for the determination of total cyanide concentration in water and *post-mortem* blood samples

ORHAN DESTANOĞLU* and İSMAİL ATEŞ

Council of Forensic Medicine (ATK), Department of Chemistry, 34196 Bahçelievler, Istanbul, Turkey

(Received 22 April, revised 2 July, accepted 27 September 2020)

Abstract: In this study, we aimed to develop a headspace gas chromatography––mass spectrometry method for determining the total cyanide concentration in the forensic evidences. Total cyanide content of the samples was calculated based on the hydrogen cyanide gas concentration evaporated from the liquid sample in the headspace vial. Hexacyanoferrate(II) was used for the optimization of headspace oven temperature. We have found that iron–cyanide bonds were completely degraded after 0.2 mL of the sample was treated with 1 mL of 1 M sulfuric acid under the optimized headspace conditions where the temperature and the heating time were 120 °C and 12.5 min, respectively. Satisfactory recovery results for both aqueous and blood samples were obtained. The method was linear in the range 0.05–10 μg mL^{-1} of cyanide which was a suitable range for toxicological investigations. The proposed method was validated and applied to the *post-mortem* blood samples, drinking waters, and the other forensic evidences. The proposed method can easily be performed not only in the forensic laboratories, but in the related laboratories where the total cyanide analysis is a critical issue.

Keywords: analytical toxicology; cyanide poisoning; evidence; forensic chemistry.

INTRODUCTION

Cyanides are the potent toxic agent for humans, animals and aquatic life. Hydrogen cyanide (HCN), which is a weak acid (pK_a 9.2), and CN^- can interconvert based on temperature and pH.[1] HCN is a colorless gas, and it has an almond-like odor, but half of the population is unable to smell it.[1,2] Acute toxic effect of cyanide mainly stems from inhibiting the final stage of the oxidative

* Corresponding author. E-mail: orhan.destanoglu@istanbul.edu.tr; present address: Istanbul University-Cerrahpaşa, Institute of Forensic Sciences and Legal Medicine, Department of Science, 34500, Istanbul, Turkey.
https://doi.org/10.2298/JSC200422063D

phosphorylation, which is essential for the aerobic cell respiration, by ligating to the haem group of the cytochrome c oxidase enzyme (EC 1.9.3.1).[3] In addition to cytochrome c oxidase, it disrupts activities of the many metalloenzymes such as catalase – Fe(III) (EC 1.11.1.6), iron–sulfur protein succinate dehydrogenase (EC 1.3.5.1), superoxide dismutase – Cu, – Zn (EC 1.15.1.1), carbonic anhydrase – Zn (EC 4.2.1.1), alkaline phosphatase – Zn (EC 3.1.3.1), alcohol dehydrogenase – Zn (EC 1.1.1.1), xanthine oxidase – Mo (EC 1.17.3.2), xanthine dehydrogenase – Mo (EC 1.17.1.4), aldehyde oxidase – Mo (EC 1.2.3.1), sulfite oxidase – Mo (EC 1.8.3.1) and glutathione peroxidase – Se (EC 1.11.1.9).[3,4] Moreover, it leads to the production of cyanohydrins by binding to carbonyl groups in the center of some enzymes.[3]

The most poisonous cyanide compounds are the hydrogen cyanide gas, the water-soluble salts of cyanide (sodium cyanide; potassium cyanide), and the weak acid dissociable (WAD) cyanide complexes of zinc, nickel, copper and cadmium. Whether voluntarily (committing suicide) or involuntarily (accidentally or fire exposure) ingestion of these cyanide solids or inhalation of HCN most likely results in death when the concentration of cyanide in the blood reaches about 4–5 mg L^{-1}.[2,5–7] 98 % of the total CN^- concentration in blood is distributed to erythrocytes (also called red blood cells) containing hemoglobin while the 2 % part of it could be present in the plasma either in the free form or bound to methemoglobin protein, the ferric form of hemoglobin.[2,8] It was reported that about 100 mg of HCN or 300 mg of KCN intake are the lethal doses for the humans.[2]

In nature, the primary source of CN^- comes from anthropogenic activities such as synthetic fibers, resins, herbicides, electroplating, mining, metal finishing, steel, petroleum and chemical industries, and gold extraction processes. Cyanide intoxication from HCN inhalation commonly arises from tobacco smokes and pyrolysis of nitrogen-containing polymers such as melamine, nylon, polyurethanes, polyamides, wool and silk. On the other hand, cyanide compounds are found in almonds, millet sprouts, lima beans, soy, spinach, bamboo shoots, sorghum and cassava roots. Due to its military use, authorities also identify HCN as a chemical terrorist agent.[1,4,9,10] In *post-mortem* blood samples, cyanide concentration can reach to 20 mg L^{-1} in the suicide cases or industrial exposure while it exceeds 1 mg L^{-1} in fire victims.[2] Although the concentration of cyanide seems to be low, the reason why the fire victims die is carbon monoxide and cyanide exhibiting synergistic effects.[4]

The toxicity of cyanide species differs depending on whether free cyanide or HCN is easily formed or not in the physiological conditions. Therefore, simple cyanide salts and WAD cyanide complexes are the most hazardous compounds, whereas strong acid dissociable (SAD) cyanide complexes like hexacyanoferrate(II,III) are the less toxic species. To degrade the metal–cyanide bonds of the

SAD complexes, a process needs more heavier conditions such as UV radiation, higher temperatures, and strong acids.[5,7,11]

Many methods have been developed for the determination of the cyanide species in different types of samples including ion chromatography (IC),[6,7] capillary electrophoresis (CE),[12,13] headspace gas chromatography (HS-GC),[14] GC–mass spectrometry (MS),[15–18] electrochemicalsensors,[8,19–21] headspace (HS)-single-drop microextraction (SDME)-NanoDrop® microspectrophotometry (ND),[11] HS-GC-atomic emission detector (AED),[22] HS-GC-electron capture detector (ECD),[23] HS-GC-ECD/photoionization detection (PID),[24] HS-GC-nitrogen–phosphorus detector (HS-GC-NPD),[25–30] HS-solid-phase microextraction (HS-SPME)-NPD,[31] HS-SPME-CE,[32] HS-GC–MS[9,15,33,34] and HS-SPME-GC–MS.[35]

Cyanide poisoning, which is an important issue in forensic sciences, is often caused by exposure to cyanide-containing compounds in committing suicide, homicide attempt, and accidental digestion cases. According to the Official Gazette of the Republic of Turkey, cyanide sales to the public have been banned because the number of cases of cyanide suicides increased in the past years.[36] The available cyanides (free and WAD species) rapidly act in the body, whereas the SAD species could not lead to death. Therefore, death does not occur in some cases where people who do not have any idea about toxic effect of the SAD species intentionally use these cyanides. Accordingly, even if someone else does not die, the suspect may be punished for attempting homicide.

Thus, a reliable method for the determination of total cyanide concentration in postmortem blood samples, environmental samples, and any evidence have vital importance, especially for forensic science. In this paper, as can be seen, we aimed to present an HS-GC–MS method for the total cyanide analysis in both postmortem blood samples and aqueous solutions. We carried out the method optimizations by using hexacyanoferrate(II) ($[Fe(CN)_6]^{4-}$) as SAD complex, and the temperature values were checked by calculating recovery values instead of optimizing HS conditions only by vapor pressure equilibrium.[9,33,34] Though the proposed method is highly accurate, it does not give any information relating to the cyanide species. Consequently, because the proposed method is fast (no derivatization) and reliable, it is very suitable for the related laboratories.

EXPERIMENTAL

Reagents

1000 mg L^{-1} of certified cyanide standard solution (CL01.0371.0100) was purchased from Chem-Lab (Zedelgem, Belgium). Aqueous certified reference material (CRM) of cyanide (lot: LRAA3393) was obtained from Sigma–Aldrich. Potassium hexacyanoferrate(II) trihydrate ($K_4[Fe(CN)_6]\cdot 3H_2O$, 99.5 %) was procured from Carlo Erba Reagents (Val de Reuil Cedex, France). Sulfuric acid (95–97 %) for analysis Emsure® ISO was supplied by Merck.

Ultrapure water was acquired from a New Human Power I Scholar UV system (Human Corporation, Seoul, South Korea).

Instrumentation

We carried out the analysis of cyanide by utilizing a Perkin Elmer Clarus 680 gas chromatograph equipped with a Clarus SQ 8 T mass spectrometer and HS40 headspace (HS) autosampler. A Perkin Elmer Elite – free fatty acid phase (FFAP) GC column providing appropriate separation of acidic compounds with a crossbond carbowax-PEG structure was used. Dimensions of the column were 30 m long, 0.25 mm i.d. and 0.5 μm df. The constant flow rate of the carrier gas (He) was adjusted at 1 mL min^{-1} with an HS pressure of 30 psi.

HCN gas liberated from all of the possible cyanide species by keeping the vials in the HS oven set at 120 °C for 13 min. The HS needle temperature and the transfer line temperatures were 130 and 150 °C, respectively. The authors used a stainless-steel needle jet to achieve minimum carryover from the adsorption of cyanide on the needle surface.[33] After the incubation time finished, pressure was the applied to the vial by the needle for 1.0 min, and then the gas sample was injected for 0.1 min (loopless). HCN was successfully separated from the other peaks on the column by the optimized GC oven temperature program which was set initially 40 °C for 7 min, then ramped at 25 °C min^{-1} to 220 °C, and finally, held at 220 °C for 2 min. The equilibration time of the GC oven was 30 s. GC injector temperature was 200 °C, total analysis time was 16.20 min.

Electron energy was 70 eV of the EI+ source. Mass detection was performed at 200 °C. The authors utilized a TurboMass (version 6.1.0.1963) software for data acquisition and instrumental control for GC and MS, while the headspace autosampler was controlled by computer using PerkinElmer HS Driver v2.5.0.0125 software. The software simultaneously collected the data by both the full scan between 12–150 atomic mass units (amu) for identification of the peaks during 5-8 min and the selected-ion recording (SIR) of *m*/*z* 27 ($^{1}H^{12}C^{14}N^{+}$) for quantitative analysis at a dwell time of 40 ms between 5-7.5 min. Solvent delay was set for the first 5 min. We measured the concentration of HCN in the samples using a standard calibration curve prepared by plotting the peak area against the designated concentrations (0.05-10 μg mL^{-1}).

Preparation of the $[Fe(CN)_6]^{4-}$ solutions

To prepare the stock solution of $[Fe(CN)_6]^{4-}$ in which the CN^- equivalent concentration was 100 mg L^{-1}, 27.1 mg of $K_4[Fe(CN)_6]\cdot 3H_2O$ was dissolved in a 100 mL volumetric flask. Then, we diluted this solution to obtain an aqueous $[Fe(CN)_6]^{4-}$ solution to be equivalent to 5 mg L^{-1} of CN^-. Similarly, we spiked the blood samples from the blood stocks with same concentration of $[Fe(CN)_6]^{4-}$.

Samples and sample preparation

The *post-mortem* blood samples were sent to our laboratory after the autopsies conducted at the Council of Forensic Medicine (ATK). We carried out this study by the permission of ATK Chairmanship, Education and Scientific Research Commission (decision number: 2018/737; date: September 18, 2018). The informed consent was waived. We pledged to comply with all ethical rules during the application. The authors confirm that this research was conducted according to the principles expressed in the Declaration of Helsinki.

The authors prepared the standard solutions and the samples as follows: we added 0.2 mL of the sample solution into 22 mL headspace vial, which was in a tube holder placed on an icebox with an appropriate size. Then, 1 mL of 1 M H_2SO_4 was added above the cold sample. After we instantly sealed the vial with a gas-tight polytetrafluoroethylene (PTFE)-lined rubber

septum cap, it was vortexed for 1 min. Finally, we loaded the vials to the HS autosampler for analyzing.

RESULTS AND DISCUSSION

Optimization of the HS temperature

In the first experiments, we calculated the recoveries from the aqueous iron cyanide complex solutions. By this means, we prepared a series of solutions with the same concentration: 200 μL of the $[Fe(CN)_6]^{4-}$ of which CN^- concentration was equivalent to 5 mg L^{-1} and 200 μL 1 M H_2SO_4 solutions were added into a cold 22 mL headspace vial, respectively. After immediate sealing, each vial was vortexed. The solutions were analyzed after 20 min of incubation at 80, 90, 100, 110, 120 and 130 °C. Three of the solutions containing the complex and three standard solutions of 5 mg L^{-1} CN^- were analyzed in parallel for each temperature point. The recoveries of the parallel measurements were calculated. CN^- have been measured until a plateau was observed. As seen in Fig. 1, 120 °C was found to be the adequate temperature with 102 % recovery to completely degrade the Fe–CN bonds. Therefore, all subsequent experiments were carried out at 120 °C. It is noteworthy that the available cyanide species could be measured with good recoveries at the lower temperatures, but this does not allow accurate analyzing of the SAD species in the complex matrices possessing transition metals. Furthermore, approximately 10 % recovery values were obtained when the temperatures were exerted between 80–90 °C while 50 % recovery was calculated at 100 °C. These recovery values indicated not only that merely controlling the vapor pressure equilibrium was unsufficient, but they could contribute to finding positive cyanide concentrations when the available cyanides were analyzed in complex matrices as well. Therefore, it should be taken into account not to be given misleading results for both SAD and WAD cyanide species.

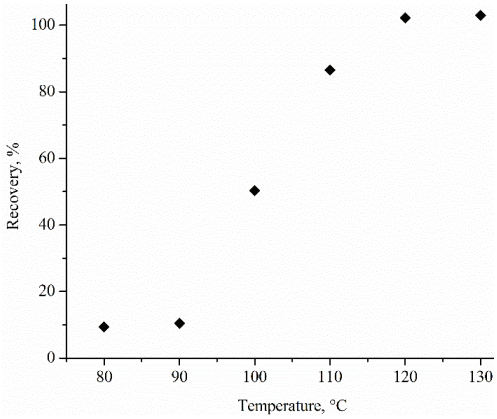

Fig. 1. Effect of HS oven temperature time on the recovery of 5 mg L^{-1} CN from $[Fe(CN)_6]^{4-}$ complex in aqueous solution.

To calculate the recovery from the blank blood samples, three different HS vials containing 200 µL of the blood sample spiked with $[Fe(CN)_6]^{4-}$ to obtain 5 mg L^{-1} of CN^- and 200 µL of 1 M H_2SO_4 were prepared, and also three different standard solutions with 5 mg L^{-1} of CN^- (*vide supra*). Recovery was 71.5±1.5 %. The low recovery value resulted from the vapor pressure difference between the standard solution and the sample solution. Hereafter, we decided to increase the volume of the acid. In the next study, 200 µL of the blood sample similarly spiked with $[Fe(CN)_6]^{4-}$ and 1.0 mL of 1 M H_2SO_4 were mixed. The recovery rose to 96.0±2.9 %. Besides, we have found the recovery value to be 100.6±1.7 %.

Optimization of the HS heating time

To optimize the heating time of the HS oven, we analyzed the solutions containing 200 µL of same aqueous $[Fe(CN)_6]^{4-}$ solution and 1.0 mL of 1 M H_2SO_4 after keeping in the HS oven throughout 1, 2.5, 5, 7.5, 10, 12.5, 15, 17.5 and 20 min. As can be seen from Fig. 2, the peak areas reached a plateau after 12.5 min. Hence, we optimized the heating time to 13 min of the HS oven.

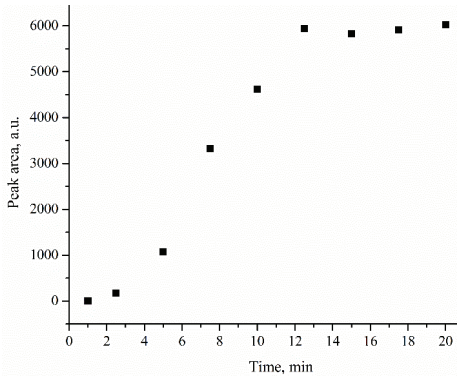

Fig. 2. Effect of heating time of the HS oven on HCN peak area. Aqueous solutions containing 200 µL of $[Fe(CN)_6]^{4-}$ (equivalent to 5 mg L^{-1} of CN^-) and 1 mL of 1 M H_2SO_4 were injected.

Optimization of the H_2SO_4 concentration

We put 1 mL of H_2SO_4 solutions with increasing concentrations from 0.1 to 5.0 M in the HS vials containing 200 µL of aqueous $[Fe(CN)_6]^{4-}$ which was equivalent to 5 mg L^{-1} of CN^-. We determined the optimal H_2SO_4 concentration to be 1.0 M (see Fig. 3).

Method performance characteristics

The authors investigated the method validation parameters, which were sensitivity, linearity, selectivity, accuracy and precision.

Linearity and sensitivity. Table I summarizes the linear range, retention time, regression equation, the limit of detection (*LOD*), and limit of quantification (*LOQ*) values. We calculated *LOD* and *LOQ* concentrations as 3×standard devi-

ations (*SD*) and 10*SD* of the very low concentration (signal-to-noise ratio: 3) of cyanide, respectively, obeying the Eurachem Guide.[37]

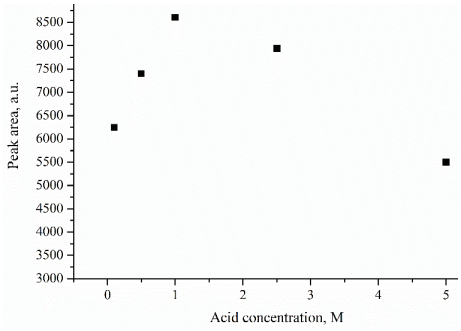

Fig. 3.++ Effect of H_2SO_4 concentration on HCN peak area. 1 mL of 0.1, 0.5, 1.0, 2.5 and 5.0 M H_2SO_4 were added onto the HS vial containing aqueous $[Fe(CN)_6]^{4-}$ which was equivalent to 5 mg L^{-1} of CN^- solutions, respectively.

TABLE I. The linearity, retention time, *LOD* and *LOQ* parameters of the proposed method

Analyte	Linear calibration range, μg mL^{-1}	Regression equation	Regression coefficient	Retention time, min	*LOD* ng mL^{-1}	*LOQ* ng mL^{-1}
Cyanide	0.05–10	$y = 3917.6x - 55.4$	0.9996	6.20	27	41

Linear range (0.05–10 μg mL^{-1}) was useful for the routine toxicological analyses. The calibration curves were prepared monthly. We allowed every sequence to start as long as we find QC (total cyanide 0.76 μg mL^{-1}) measurements in the acceptable range. We reconstructed the calibration without waiting for monthly repetition if QC controlling did not pass somehow. Also, after each blood sample run, a blank measurement was conducted owing to the observation of carry-over. We encountered no carry-over problem at all since we employed the stainless steel needle jet, and adjusted (loopless) injection time to above 0.05 min. Even though increasing injection time gave rise to both elevated sensitivity and decreased carry-over it caused expansion, of the width of the HCN peak, above 0.12 minutes. Thereby, we optimized 0.1 minute for the injection time. On the other hand, sensitivity of the method could be enhanced either by adding Na_2SO_4 leading to salt-out effect or by increasing sample volume. Yet, we did not need more sensitivity.

Selectivity. The Elite-FFAP was a suitable column for the separation of polar substances. No interference on the HCN peak (*m*/*z* 27) has been observed in the samples at optimized conditions, even it contained many volatile compounds. As the filament switched off before 5th min and after the 8th min of the analysis, data were collected between 5th to 8th min. Therefore, acetaldehyde, diethyl ether, acetone, ethyl acetate, methanol, 2-propanol, ethanol and benzene eluted before 5th min and 1-butanol, 3-methyl-1-butanol, *o*-,*m*-,*p*-xylenes, acetic acid and formic acid eluted after 8th min were not detected. Only chloroform, toluene and 1-propanol with the retention times of 5.86, 6.50 and 6.62 min, respectively, were

observed between 5th and 8th min. Some of these compounds, especially alcohols, could be formed endogenously in the postmortem blood samples while the source of the other compounds might be huffing glue or paint thinners (by abusers) due to their psychoactive effects. To check out the interference effect, a solution containing 0.5 μg mL^{-1} of CN^- and 100 μg mL^{-1} of the other compunds, described above, was prepared. No HCN peak was observed between chloroform and toluene peaks on the total ion current (TIC) chromatogram (see Fig. 4c) while HCN was successfully separated on the SIR chromatogram (*m*/*z* 27) as seen in Fig. 4a with 103.3 % of recovery value. In other words, cyanide could be determined by the proposed method, even if a sample had high concentrations of chloroform and toluene.

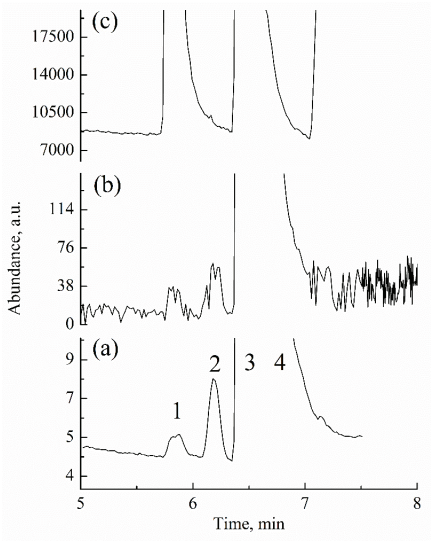

Fig. 4. Overlaid chromatograms of: a) SIR (*m*/*z* 27), b) *m*/*z* 27 ion in the full scan and c) TIC (12–150 amu); 1: chloroform, 2: HCN, 3: toluene, 4: 1-propanol.

It can be assumed that CN^- is formed as a result of the conversion of SCN^- at low levels in the blood. Though the addition of ascorbic acid inhibits this conversion, we did not use it because this conversion at the trace level is negligible for toxicological analysis.[33] Eventually, it was clear that the proposed method was quite selective for cyanide present in many sample matrices.

Trueness. The authors calculated the bias (*b*) of the method by using the reference material. The significance test (*t*-test) exerted to certified reference material (CRM) and recovery values obtained from two spike levels applied to a positive *post-mortem* blood sample with 6.40 μg mL^{-1} of mean concentration of CN^-. As seen in Table II, after the post-mortem blood sample was spiked with cyanide at 3.00 and 6.00 μg mL^{-1}, the average recovery values were found to be 101.1 and 94.5 %, respectively. Eq. (1) was employed for calculation of recovery, %, as:

$$\text{Recovery} = 100\frac{C_f - C_m}{C_a} \quad (1)$$

where C_f is the total found concentration value of the spiked blood sample; C_m is the mean concentration of the unspiked sample; C_a is the added concentration value of standard cyanide in the blood sample. We could not perform more than three times for the number of analyses of the positive *post-mortem* blood sample and its spiked solutions since the sample volume was limited. According to the results exhibited in Table II, calculated t values were well below the critical *t*-values. It indicated that there was no difference between our results and the reference concentrations at the 95 % confidence level.

TABLE II. Results of the accuracy experiments. For CRM, *t*-values were calculated by using certificate value and our results while recoveries were used for calculating *t*-values of spiked blood sample

Sample	Number of analyses	Measured mean concentration of cyanide ± *SD* μg mL^{-1}	*RSD* %	CRM results			Spike results of blood			*t*-Test results	
				Certified concentration of cyanide μg mL^{-1}	Bias	Bias %	Added μg mL^{-1}	Found μg mL^{-1}	Recovery %	*t* Value calculated	*t* Value reference
CRM	10	0.760 ± 0.039	5.19	0.757	0.003	0.40	–	–	–	0.24	2.26
Blood	3	6.40 ± 0.27	4.22	–	–	–	3.00	9.43	101.1	0.3	4.3
							6.00	12.27	94.5	2.0	

Precision. To investigate the precision of the developed method, the researchers carried out inter-day (three days×six replicates) and intra-day (one-day×six replicates) repeatability studies for the concentration and t_R by using CRM. Table III presents the repeatability results expressed as *RSD*. *RSD* values found <11 both in the trueness and in the precision studies were acceptable according to the AOAC guideline.[38] Consequently, the proposed method was successfully validated.

TABLE III. Inter-day and intra-day precision values of the concentration and retention time parameters. CRM solution of cyanide was analyzed six times in one day and three different days with six replicates for intra-day and inter-day repeatability studies, respectively

Examination	Parameter	*RSD* / %
Intra-day study	Concentration	3.66
	Retention time	0.14
Inter-day study	Concentration	5.93
	Retention time	0.21

Analysis of the real samples

The specialists should transfer the postmortem blood samples of the cyanide poisoning cases into the grey-colored tubes containing fluoride and EDTA during the autopsy. Then, they should quickly deliver the blood samples to toxicology laboratories for analysis. Bacteria and fungi might increase or decrease the cyanide concentration in the body or the other samples. Fluoride can inhibit *post-mortem* bacterial enzymatic reactions. Although fluoride and EDTA help to keep cyanide concentration stable, one should conduct the analysis as soon as possible to prevent the loss of analyte. In this study, we applied the proposed method to the real samples, and we found that total cyanide concentrations were in the range of 3.67-24 μg mL^{-1} and 0.66–2.40 μg mL^{-1} in the *post-mortem* blood samples of victims who ingested cyanide salts or were exposed to the smoke of the fire, respectively (see Table IV). In general, after the cyanide concentration was about 1–2 μg mL^{-1} in a blood sample with no case story, the stomach content was qualitatively analyzed for the presence of cyanide. If the result was negative, the reason for death most probably was that the victim has been exposed to carbonmonoxide also. Here, cyanide and carbonmonoxide, which are the two strong field ligands, could synergistically result in the death of the fire victims. The affinity of carbon monoxide for haemoglobin is 200–300 times higher than that of oxygen. Therapeutic and toxic concentration of carboxyhaemoglobin (COHb) are 1–5 % and > 20 %, respectively. Elevated COHb causes nausea, headache, gastrointestinal upset, hypertension, hyperventilation and drowsiness to coma. When the concentration of COHb reaches to 40–50 %, reddish colour on skin and cyanosis can occur. We observed when cyanide was not detected, the concentration of COHb was found up to 80–90 % in the *post-mortem* blood samples. However, its concentration range was between 25–45 % when the concentration of cyanide was determined at 1–2 μg mL^{-1}.

TABLE IV. Distribition of cyanide concentration in the *post-mortem* blood samples by cyanide intake and fire cases

Case	Number of cases	Concentration of cyanide, μg mL^{-1}		
		Range	Mean	Median
Cyanide intake	13	3.7–24.0	9.1	6.4
Fire	9	0.7–2.4	1.4	1.3

People who commit suicide at home sometimes leave a note in front of the door or on walls so that nobody could be harmed from the HCN gas. 6.40 μg mL^{-1} of cyanide was measured in the blood of a person found dead in an industrial zone. On the other hand, ten commercial drinking water samples, purchased from Istanbul markets, were analyzed and cyanide was not detected in the samples. The chromatograms, of the blood sample with 6.40 μg mL^{-1} of cyanide and a

drinking water sample, are given in Fig. 5. To sum up, the validated method was successfully applied to the real samples.

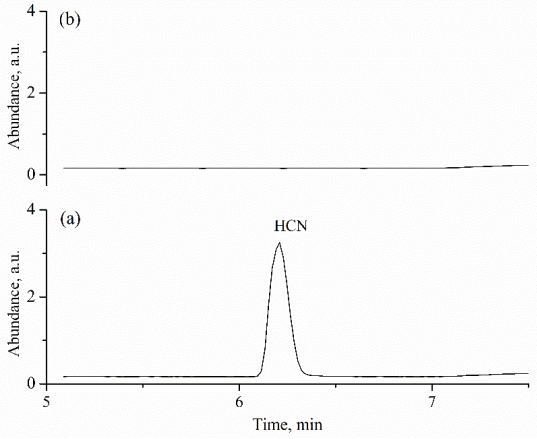

Fig. 5. Overlaid chromatograms (SIR acquisition *m*/*z* 27) of: a) blood sample with 6.40 μg mL^{-1} of cyanide and b) drinking water sample (cyanide was not detected).

A male, falling deeper into debt, have decided to commit suicide by intaking a cyanide compound. He drank the solution containing a cyanide compound from a small bottle, after parking his car. The statement told that after a while, he was nauseated and then his health got worse, but he survived and called the emergency. The crime scene investigation team took a swab sample from the bottle and sent it to our laboratory. We mixed the yellowish tip of the swab with 5 mL of 0.1 M NaOH. After analysis, we found 11 mg $swab^{-1}$ cyanide in the sample. We decided to carry out an experiment by ICP–MS for analysis of iron in the extracted solution. About six to one of molar ratio was determined as expected. We found out that the reason for his survival was that he drank a solution containing iron cyanide complex, which was most likely purchased as a cyanide--containing pesticide.

In addition to the analysis of the forensic evidences, the proposed method could be performed for the determination of total cyanide content in the environmental samples and in the industrial wastewaters. It is crucial that HCN may be released to the air from the industrial wastewater when acidic wastes are mixed with cyanide-containing wastes or when the wastewaters are directly exposed to the sunlight during the treatment processes. Thus, the related laboratories may easily adapt our method to control total cyanide concentration in the wastewaters.

CONCLUSION

In this work, a reliable HS-GC–MS method was developed for the determination of total cyanide in the forensic evidences such as postmortem blood

samples and aqueous samples. We attained very good recovery values from the whole blood sample, even $[Fe(CN)_6]^{4-}$ was used as a SAD complex, so we successfully validated the method. The proposed method has many advantages: the sample preparation procedure is simple, it does not require any derivatization step or clean-up procedure, and it is adequately rapid, sensitive, and selective for the routine toxicological investigations.

Acknowledgment. The authors are grateful to the Council of Forensic Medicine (ATK) Chairmanship, Turkey, for permitting, supporting and encouraging us to conduct this research.

ИЗВОД

МЕТОДА „HEADSPACE“ ГАСНЕ ХРОМАТОГРАФИЈЕ–МАСЕНЕ СПЕКТРОМЕТРИЈЕ ЗА ОДРЕЂИВАЊЕ УКУПНЕ КОНЦЕНТРАЦИЈЕ ЦИЈАНИДА У ВОДИ И *POST-MORTEM* УЗОРЦИМА КРВИ

ORHAN DESTANOĞLU и İSMAİL ATEŞ

Council of Forensic Medicine (ATK), Department of Chemistry, 34196Bahçelievler, İstanbul, Turkey

У овој студији имали смо за циљ да развијемо методу *headspace* гасне хроматографије–масене спектрометрије за одређивање укупне концентрације цијанида у форензичким доказима. Укупни садржај цијанида у узорцима израчунат је на основу концентрације цијановодоника испареног из течног узорка у вијали. Током оптимизације температуре пећи коришћен је хексацијаноферат(II). Утврђено је да се везе гвожђе-цијанид у потпуности разлажу након што је 0,2 mL узорка третирано са 1 mL 1 M сумпорне киселине, при температури од 120 °C и времену загревања од 12,5 min. Добијани су задовољавајући резултати процента приноса (*recovery*) и из водених и узорака крви. Метода је била линеарна у распону 0,05–10 μg mL^{-1} цијанида, што је било погодно за токсиколошка испитивања. Предложени метод је валидиран и примењен на узорке крви после смрти, воде за пиће и остале форензичке доказе. Предложена метода се може применити не само у форензичким, већ и у другим лабораторијама у којима је се анализирају узорци на садржај цијанида.

(Примљено 22. априла, ревидирано 2. јула, прихваћено 27. септембра 2020)

REFERENCES

1. U.S. Environmental Protection Agency, *EPA/635/R-08/016F Toxicological Review Of Hydrogen Cyanide And Cyanide Salts*, https://cfpub.epa.gov/ncea/iris/iris_documents/documents/toxreviews/0060tr.pdf, (accessed February 17th 2020)
2. S. Jickells, A. Negrusz, *Clarke's Analytical Forensic Toxicology*, Pharmaceutical Press, London, 2008, p. 111 (ISBN: 9780853697053)
3. H. Marquardt, S. Schäfer, R. O. McClellan, F. Welsch, *Toxicology*, 1st ed., Academic Press-Elsevier, Cambridge, 1999, p. 851 (https://doi.org/10.1016/B978-012473270-4/50094-8)
4. A. E. Lindsay, A. R. Greenbaum, D. O'Hare, *Anal. Chim. Acta* **511** (2004) 185 (https://dx.doi.org/10.1016/j.aca.2004.02.006)
5. A. Zheng, D. A. Dzomba, R. G. Luthy, B. Sawyer, W. Lazouskas, P. Tata, M. F. Delaney, L. Zilitinkevitch, J. R. Sebroski, R. S. Swartling, S. M. Drop, J. M. Flaherty, *Environ. Sci. Technol.* **37** (2003) 107 (https://dx.doi.org/10.1021/es0258273)

6. O. Destanoğlu, G. Gümüş Yılmaz, R. Apak, *J. Liq. Chromatogr. Relat. Technol.* **38** (2015) 1537 (https://dx.doi.org/10.1080/10826076.2015.1076460)
7. O. Destanoğlu, G. Gümüş Yılmaz, *J. Liq. Chromatogr. Relat. Technol.* **39** (2016) 465 (https://dx.doi.org/10.1080/10826076.2016.1192044)
8. A. E. Lindsay, D. O'Hare, *Anal. Chim. Acta* **558** (2006) 158 (https://dx.doi.org/10.1016/j.aca.2005.11.036)
9. K. E. Murphy, M. M. Schantz, T. A. Butler, B. A. Benner, L. J. Wood, G. C. Turk, *Clin. Chem.* **52** (2006) 458 (https://dx.doi.org/10.1373/clinchem.2005.061002)
10. J. Ma, P. K. Dasgupta, *Anal. Chim. Acta* **673** (2010) 117 (https://dx.doi.org/10.1016/j.aca.2010.05.042)
11. A. Jain, A. K. K. V. Pillai, N. Sharma, K. K. Verma, *Talanta* **82** (2010) 758 (https://dx.doi.org/10.1016/j.talanta.2010.05.048)
12. L. Meng, X. Liu, B. Wang, G. Shen, Z. Wang, M. Guo, *J. Chromatogr., B* **877** (2009) 3645 (https://dx.doi.org/10.1016/j.jchromb.2009.09.006)
13. M. Aguilar, A. Farran, V. Martí, *Fresenius J. Anal. Chem.* **363** (1999) 121 (https://doi.org/10.1007/s002160051153)
14. A. M. Calafat, S. B. Stanfill, *J. Chromatogr., B* **772** (2002) 131 (https://dx.doi.org/10.1016/s1570-0232(02)00067-3)
15. B. Desharnais, G. Huppé, M. Lamarche, P. Mireault, C. D. Skinner, *Forensic Sci. Int.* **222** (2012) 346 (https://dx.doi.org/10.1016/j.forsciint.2012.06.017)
16. G. Liu, J. Liu, K. Hara, Y. Wang, Y. Yu, L. Gao, L. Li, *J. Chromatogr., B* **877** (2009) 3054 (https://dx.doi.org/10.1016/j.jchromb.2009.07.029)
17. R. K. Bhandari, R. P. Oda, S. L. Youso, I. Petrikovics, V. S. Bebarta, G. A. Rockwood, B. A. Logue, *Anal. Bioanal. Chem.* **404** (2012) 2287 (https://dx.doi.org/10.1007/s00216-012-6360-5)
18. S. Kage, T. Nagata, K. Kudo, *J. Chromatogr., B* **675** (1996) 27 (https://dx.doi.org/10.1016/0378-4347(95)00344-4)
19. A. A. Cárdenas Riojas, A. Wong, G. A. Planes, M. D. P. T. Sotomayor, A. La Rosa-Toro, A. M. Baena-Moncada, *Sensors Actuators, B* **287** (2019) 544 (https://dx.doi.org/10.1016/j.snb.2019.02.053)
20. L. Zhang, H. H. Quan, K. Yang, M. Li, C. P. Chen, J. H. Ahn, J. Hahn, *Sensors Actuators, B.* **259** (2018) 926 (https://dx.doi.org/10.1016/j.snb.2017.12.143)
21. A. Yari, R. Sepahvand, *Microchim. Acta* **174** (2011) 321 (https://dx.doi.org/10.1007/s00604-011-0629-9)
22. M. L. Koskinen-Soivi, E. Leppämäki, P. Stahlberg, *Anal. Bioanal. Chem.* **381** (2005) 1625 (https://dx.doi.org/10.1007/s00216-005-3129-0)
23. C. Zhang, H. Zheng, J. Ouyang, S. Feng, Y. E. C. Taes, *Anal. Lett.* **38** (2005) 247 (https://dx.doi.org/10.1081/AL-200045143)
24. A. J. Curtis, C. C. Grayless, R. Fall, *Analyst* **127** (2002) 1446 (https://dx.doi.org/10.1039/b205378k)
25. G. Roda, S. Arnoldi, M. D. Cas, V. Ottaviano, E. Casagni, F. Tregambe, G. L. Visconti, F. Farè, R. Froldi, V. Gambaro, *J. Anal. Toxicol.* **42** (2018) e51 (https://dx.doi.org/10.1093/jat/bky015)
26. D. Marton, A. Tapparo, V. B. Di Marco, C. Repice, C. Giorio, S. Bogialli, *J. Chromatogr., A* **1300** (2013) 209 (https://dx.doi.org/10.1016/j.chroma.2013.03.004)
27. V. Gambaro, S. Arnoldi, E. Casagni, L. Dell'Acqua, C. Pecoraro, R. Froldi, *J. Forensic Sci.* **52** (2007) 1401 (https://dx.doi.org/10.1111/j.1556-4029.2007.00570.x)

28. M. Shibata, K. Inoue, Y. Yoshimura, H. Nakazawa, Y. Seto, *Arch. Toxicol.* **78** (2004) 301 (https://dx.doi.org/10.1007/s00204-004-0545-4)
29. Y. Seto, N. Tsunoda, H. Ohta, T. Shinohara, *Anal. Chim. Acta* **276** (1993) 247 (https://dx.doi.org/10.1016/0003-2670(93)80391-W)
30. G. Nota, V. R. Maraglia, C. Improta, A. Acampora, *J. Chromatogr., A* **207** (1981) 47 (https://dx.doi.org/10.1016/S0021-9673(00)82691-6)
31. P. Boadas-Vaello, E. Jover, J. Llorens, J. M. Bayona, *J. Chromatogr., B* **870** (2008) 17 (https://dx.doi.org/10.1016/j.jchromb.2008.05.031)
32. S. Jermak, B. Pranaityte, A. Padarauskas, *Electrophoresis* **27** (2006) 4538 (https://dx.doi.org/10.1002/elps.200600295)
33. L.-L. Løbger, H. W. Petersen, J. E. T. Andersen, *Anal. Lett.* **41** (2008) 2564 (https://dx.doi.org/10.1080/00032710802363248)
34. P. Dumas, G. Gingras, A. LeBlanc, *J. Anal. Toxicol.* **29** (2005) 71 (https://dx.doi.org/10.1093/jat/29.1.71)
35. G. Frison, F. Zancanaro, D. Favretto, S. D. Ferrara, *Rapid Commun. Mass Spectrom.* **20** (2006) 2932 (https://dx.doi.org/10.1002/rcm.2689)
36. Republic of Turkey, Ministry of Environment and Urbanisation, *Regulation of the registration, evaluation, permission and restriction of chemicals*, https://www.resmigazete.gov.tr/eskiler/2019/11/20191129-4.htm (accessed September 8th 2020)
37. *Eurachem The Fitness for Purpose of Analytical Methods, A Laboratory Guide to Method Validation and Related Topics*, https://www.eurachem.org/index.php/publications/guides/mv (accessed January 23th 2019)
38. *Appendix F: Guidelines for Standard Method Performance Requirements, in AOAC official methods of analysis*, http://www.eoma.aoac.org/app_f.pdf (accessed January 23th 2019).

Journal of the Serbian Chemical Society
JSCS-info@shd.org.rs • www.shd.org.rs/JSCS
J. Serb. Chem. Soc. *86* (1) 91–102 (2021)
JSCS–5406
Original scientific paper

Solid–liquid phase equilibria of H_2O–$Mn(H_2PO_2)_2$–$MnCl_2$–NaCl, H_2O–$Mn(H_2PO_2)_2$–$MnCl_2$ and (H_2O–NaCl–$MnCl_2$ systems at 323.15 K

VEDAT ADIGUZEL*

Department of Chemical Engineering, Kafkas University, Kars 36100, Turkey

(Received 21 May, revised 25 August, accepted 5 September 2020)

Abstract: The solid–liquid phase equilibria (SLE) and densities of H_2O–NaCl–$MnCl_2$–$Mn(H_2PO_2)_2$ quaternary system and H_2O–NaCl–$MnCl_2$ and H_2O–$MnCl_2$–$Mn(H_2PO_2)_2$ ternary systems were investigated at 323.15 K by the isothermal solution saturation method. The analyses of the liquid and solid phases were used to determine the composition of the solid phase using the Schreinemakers graphic method. The ternary systems contain one invariant point, two invariant curves and two crystallization regions. In the quaternary system, there is one invariant point, three invariant curves and three crystallization areas corresponding to NaCl, $MnCl_2{\cdot}4H_2O$ and $Mn(H_2PO_2)_2{\cdot}H_2O$. The crystallization area of $Mn(H_2PO_2)_2{\cdot}H_2O$, being the largest in comparison with those of other salts, occupied 80.75 % of the total crystallization area.

Keywords: manganese hypophosphite; manganese chloride; ternary system; Schreinmakers method; density.

INTRODUCTION

Apart from being environmentally friendly, the metal hypophosphite salts $M(H_2PO_2)_n$ draw great attention, due to their high thermal and chemical stabilities, good reducing, and mechanical features.[1] These salts are used as reductive, antioxidant, anticorrosive, animal feed, flame retardant in polymer, medicine, metal and food industry.[1-7]

$Mn(H_2PO_2)_2$ is used as a chemical intermediate in pharmacy and polymer technology, and to increase fiber quality in nylon carpet fiber production.[4,5] In a study, Yang *et al.* has determined that $Mn(H_2PO_2)_2$ has high flame-retardant effect.[2]

In laboratory synthesis the hypophosphites are generally synthesized from sulphate, hydroxide, oxide, and nitrates of metals. The synthesis of hypophos-

* Corresponding author. E-mail: vedatnursen@gmail.com
https://doi.org/10.2298/JSC200521059A

phites obtained from hydroxides of insoluble elements in the water is generally synthesized both via multi-step reactions and expensively.[4,8–15]

Phase equilibriums are widely used as a method in the study of equilibrium relationships. In the salt industry, they are used to increase production efficiency, and also for the recovery of valuable chemicals. Besides, they are used in the recycling and disposal of harmful wastes in terms of environmental pollution. In addition to all of these, they are used in economic synthesis by obtaining chemicals that can be synthesized by multi-step reactions in fewer reaction steps in a laboratory.[16,17]

In this study, H_2O–$Mn(H_2PO_2)_2$–$MnCl_2$–NaCl, H_2O–$Mn(H_2PO_2)_2$–$MnCl_2$ and H_2O–NaCl–$MnCl_2$ systems were analyzed, and an economic method was proposed for the separation process of $Mn(H_2PO_2)_2$ salt used in the industrial field.

SLE data of salts including $H_2PO_2^-$ were given in Table I.[8–15,18–22]

TABLE I. SLE ternary and quaternary systems including $H_2PO_2^-$

Researchers	Systems
Alisoglu and Necefoglu[9]	Na^+, Mn^{2+}//NO_3^-, $(H_2PO_2)^-$–H_2O at 273.15 K
Alişoglu[11]	K^+, Mn^{2+}//Br^-, $(H_2PO_2)^-$–H_2O at 298.15 K
Alişoglu[8]	Na^+, Mn^{2+}//Cl^-, $(H_2PO_2)^-$–H_2O at 298.15 K
Alişoglu[10]	Na^+, Mn^{2+}//Br^-, $(H_2PO_2)^-$–H_2O at 298.15 K
Alisoglu and Adıguzel[12]	K^+, Mn^{2+}/Br^-, $(H_2PO_2)^-$//H_2O at 298.15 K
Erge *et al.*[13]	Na^+, Ba^{2+}//$(H_2PO_2)^-$–H_2O at 273.15 K
	Na^+//Cl^-, $(H_2PO_2)^-$–H_2O at 273.15 K
	Ba^{2+}//Cl^-, $(H_2PO_2)^-$–H_2O at 273.15 K
	Na^+, Ba^{2+}//Cl^-, $(H_2PO_2)^-$–H_2O at 273.15 K
Adıguzel *et al.*[14]	Na^+, Zn^{2+}//$(H_2PO_2)^-$–H_2O at 273.15 K
	Zn^{2+}//Cl^-, $(H_2PO_2)^-$–H_2O at 273.15 K
	Na^+, Zn^{2+}//Cl^-, $(H_2PO_2)^-$–H_2O at 273.15 K
Demirci *et al.*[15]	NaH_2PO_2–NaCl–H_2O at 298.15 K
	NaH_2PO_2–$Zn(H_2PO_2)_2$–H_2O at 298.15 K
	NaCl–$Zn(H_2PO_2)_2$–H_2O at 298.15 K
	NaH_2PO_2–NaCl–$Zn(H_2PO_2)_2$–H_2O at 298.15 K
Tan *et al.*[18]	$Ca(H_2PO_2)_2$ – $CaCl_2$ – H_2O at 298.15 K
	$Ca(H_2PO_2)_2$–NaH_2PO_2–H_2O at 298.15 K
Cao *et al.*[22]	$Ca(H_2PO_2)_2$ + $CaCl_2$ + H_2O at 323.15 K
	$Ca(H_2PO_2)_2$ + NaH_2PO_2 + H_2O at 323.15 K
Gao *et al.*[20]	$Mg(H_2PO_2)_2$ + NaH_2PO_2 + H_2O at 298 K
	$Mg(H_2PO_2)_2$ +$MgCl_2$ + H_2O at 298 K
Yin *et al.*[19]	$Ca(H_2PO_2)_2$ + $CaCl_2$ + H_2O
	$Ca(H_2PO_2)_2$ + NaH_2PO_2 + H_2O
Shi *et al.*[21]	$Mg(H_2PO_2)_2$ + NaH_2PO_2 + H_2O
	$Mg(H_2PO_2)_2$ + $MgCl_2$ + H_2O

EXPERIMENTAL

Apparatus and reagents

The commercial chemicals used in the study were given in Table II. The solution condition was provided with the use of pure water whose pH was 6.6 and conductivity was $<10^{-4}$ S m^{-1}.

TABLE II. Source and mass fraction concentration of the used chemicals

Chemical	CAS No	Source	Mass fraction[a]
NaCl	7647-14-5	Merck	0.999
$MnCl_2 \cdot 4H_2O$	13446-34-9	Merck	0.999
$Mn(H_2PO_2)_2 \cdot H_2O$	7783-16-6	Sigma-Aldrich	≥0.985
$CuCl_2 \cdot 2H_2O$	10125-13-0	Sigma-Aldrich	0.999
$C_{10}H_{14}N_2Na_2O_8$	6381-92-6	Riedel-de Haen	0.98
HCl	7647-01-0	Riedel-de Haen	0.37
$K_2Cr_2O_7$	7778-50-9	Merck	0.98
K_2CrO_4	7789-00-6	Merck	0.98

[a]Mass fraction values were measured by the supplier of the chemicals

The density analyses were detected with the device of Mettler Toledo 30PX (accuracy ±0.001 g cm^{-3}).

The titration measurements were conducted with Hirscmann Solarus automatic burette (accuracy 0.2 %). The stable experimental temperature was provided with a Polyscience branded cooler and a mixer water bath (accuracy ± 0.05 K).

Experimental methods

The phase equilibria were determined according to isothermal solubility saturation method.[12,15]

All the experiments were carried out at atmospheric pressure (0.1025 MPa).

The general procedure of the experiment is as below:

1) In the ternary system, the binary system saturated solution was prepared in a waterproof isolated tube, and placed in a water bath stabilized at 323.15 K.

2) The second salt was added at a certain amount to this solution. The solution was stirred for one day.

3) The solution was kept until the phase separation was observed clearly.

4) Later on, the samples were obtained from solid and liquid phases, and the necessary analyses were done.

5) The first forth steps of the procedure were repeated until the invariant point was reached.

6) In quaternary systems, the process was completed with the invariant point solution of the ternary system in the first step. In the second step, the third salt was added, and the whole process was performed, respectively.

All the density measurements were taken using a density measurement device which was stabilized at 323.15 K. The measurements were carried out in triplicate, and the calibration of the device was controlled by using pure water.

The solid phase compositions were detected according to the wet residue method of Schreinmakers.[12,15,23]

All the tests were repeated three times for the reliability of the test results, and the results were expressed as ± standard deviation value.

All the tables and graphics were formed after the mathematical calculations necessary for all the data were conducted, and results were interpreted.

Analytical methods

Cl^-(aq), $H_2PO_2^-$(aq) and Mn^{2+}(aq) analyses were respectively determined by the titration with standard solutions of $AgNO_3$, $K_2Cr_2O_7$ and EDTA.[24,25] The expanded uncertainties (u_r) for Mn^{2+}, Cl^- and $H_2PO_2^-$ analyses were respectively 1.32, 2.99 and 1.92 mass % (at the level of confidence of 0.95). Na^+ amounts were calculated according to the total ion balance.

RESULTS AND DISCUSSION

Solubility data of H_2O–$MnCl_2$–NaCl ternary system at 323.15 K

The solubility and the density values of NaCl–H_2O and $MnCl_2$–H_2O binary systems were respectively detected as 26.86 mass % NaCl and 49.54 mass % $MnCl_2$, 1.191 g cm^{-3}, and 1.568 g cm^{-3} at 323.15 K. The solid phases belonging to these compositions were found to be NaCl and $MnCl_2{\cdot}4H_2O$, and NaCl and $MnCl_2$. The H_2O compositions and the density in the invariant point of the H_2O––$MnCl_2$–NaCl system at 323.15 K were respectively 3.14, 47.48 and 49.38 mass %, and 1.583 g cm^{-3}. The solid phase of the invariant point consisted of NaCl and $MnCl_2{\cdot}4H_2O$ salts.

The solubility and density data belonging to this system are given in Table III and Figs. 1 and 2.

TABLE III. SLE data for the H_2O–$MnCl_2$–NaCl ternary system at 323.15 K; standard uncertainties (u) are $u(\rho)$ = 0.001 g cm^{-3}, $u(T)$ = 0.05 K, $u_r(P)$ = 5 % and $u(w)$ = 0.01w, w is the mass fraction; N = NaCl; M = $MnCl_2{\cdot}4H_2O$

No.	Content, mass %				100 w of salts in the liquid phase		P / g cm^{-3}	Solid phase
	Liquid phase		Solid phase					
	$MnCl_2$	NaCl	$MnCl_2$	NaCl	$MnCl_2$	NaCl		
1A	0.00	26.86	0.00	93.44	0.00	100	1.191	N
2	6.21	20.65	1.64	81.01	12.24	87.76	1.225	N
3	14.69	15.29	3.22	82.15	30.85	69.15	1.279	N
4	21.39	11.33	5.52	77.9	46.71	53.29	1.325	N
5	27.86	9.00	6.51	79.68	58.98	41.02	1.383	N
6	36.01	6.18	8.43	78.39	73.02	26.98	1.460	N
7E	47.48	3.14	39.76	49.82	87.54	12.46	1.583	N+M
8E	47.48	3.14	59.42	18.97	87.54	12.46	1.583	N+M
9	48.60	1.63	56.16	1.17	93.26	6.74	1.572	M
10B	49.54	0.00	58.36	0.00	100	0.00	1.568	M

In Fig. 1, there are two crystallization areas. The first one is CAE corresponding to the crystallization area of NaCl, and the second is BFE corresponding to the crystallization area of $MnCl_2$ $4H_2O$. Point A and F are the invariant points of the binary systems of NaCl−H_2O and $MnCl_2$−H_2O. Point E represents the

invariant of the system. Points C and B show the amount of salt by the weight of NaCl and $MnCl_2 \cdot 4H_2O$ salt molecules and the amount of water as hydrate, respectively. The areas of AEB0 and CEBD represent the unsaturated and saturated solutions of both salts, respectively. The curves AE and EB represent the saturation curves of NaCl and $MnCl_2$, respectively.

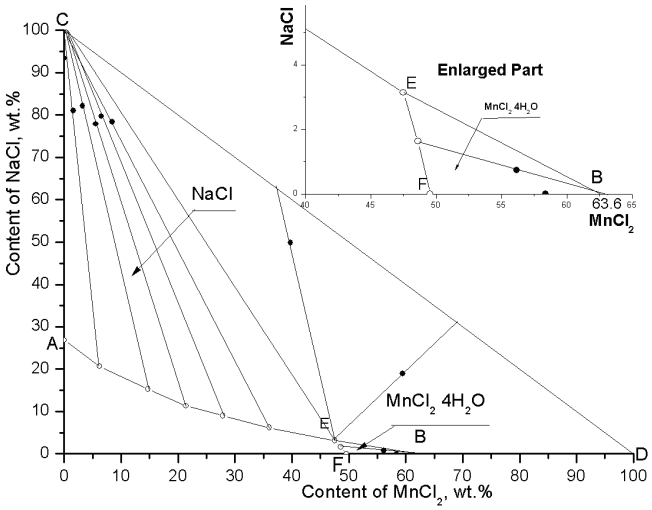

Fig. 1. SLE diagram for theH_2O–$MnCl_2$–NaCl ternary system at 323.15 K.

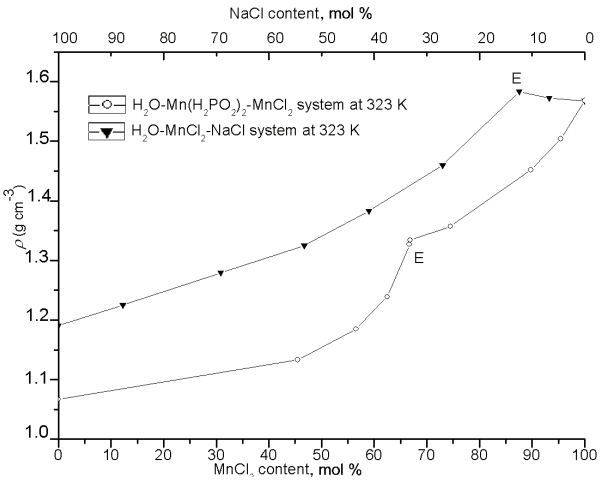

Fig. 2. Density *vs.* composition diagram for the ternary systems at 323.15 K.

Solubility data of H_2O–$MnCl_2$–$Mn(H_2PO_2)_2$ ternary system at 323.15 K

The solubility and density values of $Mn(H_2PO_2)_2$–H_2O and $MnCl_2$–H_2O binary systems were respectively detected as 11.14 mass % $Mn(H_2PO_2)_2$ and

49.54 mass % $MnCl_2$, 1.067 and 1.568 g cm^{-3} at 323.15 K. The solid phases belonging to these compositions were found as $Mn(H_2PO_2)_2{\cdot}H_2O$ and $MnCl_2{\cdot}4H_2O$.

$Mn(H_2PO_2)_2$, $MnCl_2$ and H_2O compositions and the density in the invariant point of H_2O + $MnCl_2$ + $Mn(H_2PO_2)_2$ system at 323.15 K were respectively 15.34, 21.02 and 63.64 mass % and 1.334 g cm^{-3}. The solid phase of the invariant point consists of $Mn(H_2PO_2)_2{\cdot}H_2O$ and $MnCl_2{\cdot}4H_2O$ salts. The solubility and density data belonging to this system are given in Table IV and Fig. 2 and 3.

TABLE IV. SLE data for theH_2O–$MnCl_2$–$Mn(H_2PO_2)_2$ ternary system at 323.15 K; standard uncertainties, u, are $u(\rho)$ = 0.001 g cm^{-3}, $u(T)$ = 0.05 K, $u_r(P)$ = 5 % and $u(w)$ = 0.01w, w is the mass fraction; M – $MnCl_2{\cdot}4H_2O$; H – $Mn(H_2PO_2)_2{\cdot}H_2O$

No.	Content, mass %				100w of salts in liquid phase		ρ g cm^{-3}	Solid phase
	Liquid phase		Solid phase					
	$MnCl_2$	$Mn(H_2PO_2)_2$	$MnCl_2$	$Mn(H_2PO_2)_2$	$MnCl_2$	$Mn(H_2PO_2)_2$		
1A	0.00	11.14	0.00	90.13	0.00	100	1.067	H
2	6.73	11.77	0.58	88.57	45.45	54.55	1.133	H
3	11.07	12.50	1.2	84.72	56.55	43.45	1.185	H
4	15.02	13.26	3.4	74.58	62.46	37.54	1.239	H
5	20.76	15.23	2.83	82.42	66.72	33.28	1.327	H
6E	21.02	15.34	28.02	52.46	66.82	33.18	1.334	H+M
7E	21.02	15.34	56.35	32.15	66.82	33.18	1.334	H+M
8	25.1	12.63	50.29	4.13	74.48	25.52	1.357	M
9	36.7	6.17	55.24	1.91	89.75	10.25	1.452	M
10	43.4	3.03	56.09	0.91	95.46	4.54	1.504	M
11F	49.54	0.00	60.86	0.00	100	0.00	1.568	M

In Fig. 3, there are two crystallization areas. The first one is HAE corresponding to the crystallization area of $Mn(H_2PO_2)_2$ H_2O, and the second is BFE corresponding to the crystallization area of $MnCl_2$ $4H_2O$. Point A and F are the invariant points of the binary systems of $Mn(H_2PO_2)_2$–H_2O and $MnCl_2$–H_2O. Point E represents the invariant of the system.

Point H and Point B show the amount of salt by weight of $Mn(H_2PO_2)_2$ H_2O and $MnCl_2{\cdot}4H_2O$ salt molecules and the amount of water as hydrate, respectively. The areas of AEF0 and CHEBD represent the unsaturated and saturated solutions of both salts, respectively. The curves AE and EF represent the saturation curves of $Mn(H_2PO_2)_2$ and $MnCl_2$, respectively.

Solubility data of H_2O–$Mn(H_2PO_2)_2$–NaCl–$MnCl_2$ system at 323.15 K

The solubility data belonging to the quaternary system are given in Table V and Fig. 4.

The invariant point data of H_2O–$Mn(H_2PO_2)_2$–NaCl system are 69.52, 6.02 and 24.46 mass %, respectively.

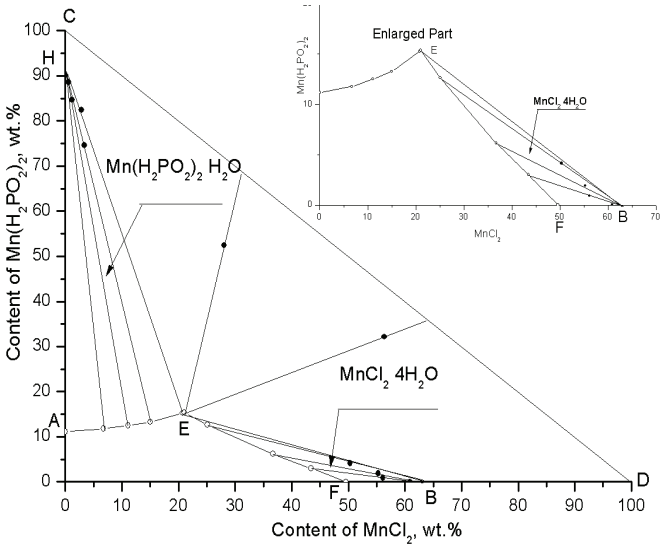

Fig. 3. SLE diagram for theH_2O–$MnCl_2$–$Mn(H_2PO_2)_2$ ternary system at 323.15 K.

TABLE V. SLE data for the quaternary H_2O–$Mn(H_2PO_2)_2$–NaCl–$MnCl_2$ system at 323.15 K; Jänecke index (J) = mol per 100 mol of dry salt ($2Na^+ + Mn^{2+}$); standard uncertainties (u) are $u(\rho)$ = 0.001 g cm^{-3}, $u(T)$ = 0.05 K, $u_r(P)$ = 5 % and $u(w) = 0.01w$, w is the mass fraction, N – NaCl; M – $MnCl_2{\cdot}4H_2O$; H – $Mn(H_2PO_2)_2{\cdot}H_2O$

No	100w				100J			Solid phase
	Mn^{2+}	Na^+	Cl^-	H_2PO_2	Mn^{2+}	$2Cl^-$	H_2O	
1	20.73	1.23	28.63	0.00	93.98	99.90	680.67	N+M
2	18.28	2.37	26.60	1.19	86.58	97.60	746.93	N+M
3	16.08	2.59	23.94	1.47	83.85	96.73	891.89	N+M
4E	14.28	2.95	21.91	1.95	80.19	95.33	1011.86	N+M+H
5	13.72	0.00	11.83	10.78	100	66.80	1419.43	M+H
6	13.29	1.45	16.26	5.73	88.46	83.85	1288.10	M+H
7	12.76	2.00	17.62	3.52	84.21	90.05	1293.63	M+H
8E	14.28	2.95	21.91	1.95	80.19	95.33	1011.86	N+M+H
9	1.79	9.61	14.85	4.23	13.46	86.62	1601.20	H+N
10	4.32	7.36	14.94	3.67	32.91	88.22	1625.10	H+N
11	5.49	7.02	15.97	3.59	39.54	89.10	1496.39	H+N
12	7.57	4.76	15.73	2.53	57.07	91.87	1600.66	H+N
13E	14.28	2.95	21.91	1.95	80.19	95.33	1011.86	N+M+H

The invariant point data of H_2O–$Mn(H_2PO_2)_2$–NaCl–$MnCl_2$ quaternary system are respectively 58.89, 2.77, 7.5 and 30.84 mass %.

In Fig. 4, there are three crystallization areas. The first one is AECH corresponding to the crystallization area of $Mn(H_2PO_2)_2$ H_2O, the second one is DBEA corresponding to the crystallization area of NaCl, and the third is BECF corresponding to the crystallization area of $MnCl_2{\cdot}4H_2O$. Points A, B and C are the

invariant points of the ternary systems. Point E represents the invariant of the quarternary system.

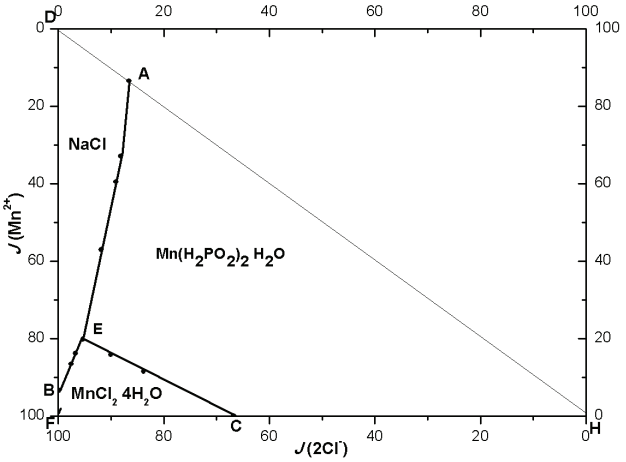

Fig. 4. SLE diagram for the H_2O–$Mn(H_2PO_2)_2$–NaCl–$MnCl_2$ system at 323.15 K.

As it is seen in Fig. 4, which shows the crystallization area of the quaternary system, $Mn(H_2PO_2)_2$ 80.75 %, NaCl 11.63 %, and $MnCl_2$ 7.62 % cover the area. These values were obtained by calculating the area of the DFH triangle in Fig. 4. When the study is compared with literature data of the binary, ternary and quarternary systems, it is seen that the solubility of $Mn(H_2PO_2)_2$ and NaCl in binary systems slightly change with the increase of temperature, but the solubility of $MnCl_2$ increases significantly with the increase in temperature.[26]

The solubility of $MnCl_2$ changed as respectively 49.54 and 56.1 mass % between 273 and 373 K. The solubility of NaCl changed as respectively 26.28 and 28.05 mass % between 273 and 373 K.[26]

There is limited data available for $Mn(H_2PO_2)_2$ solubility. According to the data, the solubility of it is between 12.20 and 11.14 mass% at between 273 and 298K.[8–12]

The quaternary systems of this study and ref. 8 were compared (Fig. 5).

When the temperature increased from 298.15 to 323.15 K, the crystallization areas of NaCl and $Mn(H_2PO_2)_2$ decreased; thus, their corresponding solubilities increased. In contrast to this, the crystallization area of $MnCl_2$ increased and its solubility decreased.

In this study, the invariant points of the quaternary system were respectively 30.84, 7.5 and 2.77 mass% ($MnCl_2$, NaCl and $Mn(H_2PO_2)_2$). According to this, there is mostly $MnCl_2$ and at least $Mn(H_2PO_2)_2$ in the solution. Because of this, these are the important data for the separation of $Mn(H_2PO_2)_2$ from the solution.

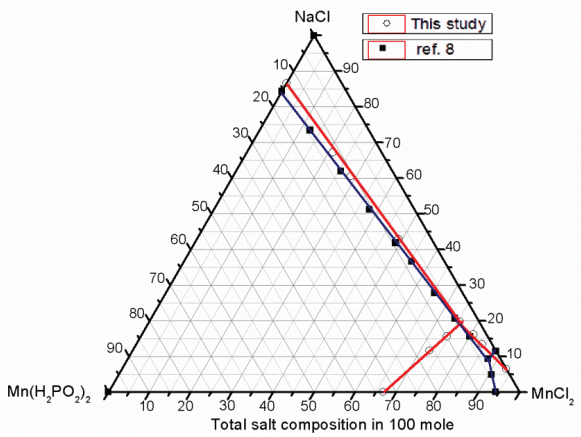

Fig. 5. Comparison of the data obtained in this study with those of reference 8 related to the same salts studied at 298.15 K.

CONCLUSION

Two ternary systems and one quaternary system were investigated in this study.

First of all, in the $MnCl_2$–NaCl–H_2O system, NaCl solubility reduced from 26.86 to 3.14 mass % in the existence of $MnCl_2$, and $MnCl_2$ solubility reduced from 49.54 to 47.48 mass % in the existence of NaCl. It is clearly seen that $MnCl_2$ has a sharp salting-out effect on NaCl. The density of the invariant point was determined as 1.583 g cm^{-3}.

Secondly, in $MnCl_2$–$Mn(H_2PO_2)_2$–H_2O system, the solubility of $Mn(H_2PO_2)_2$ increased from 11.14 to 15.34mass % in the existence of $MnCl_2$, and $MnCl_2$ decreased from 49.54 to 21.02 mass %. Here, $MnCl_2$ has a salting-on effect on $Mn(H_2PO_2)_2$. The density of the invariant point was 1.334g cm^{-3}.

Thirdly, as the crystallizing area of the quaternary system is clearly observed, $Mn(H_2PO_2)_2$ has the greatest area with 80.75 %, NaCl follows it with 11.63 % and $MnCl_2$ has the smallest area with 7.62 % in the solution including all the three salts.

When literature data is analyzed, it is seen that the solubility and the density of $Mn(H_2PO_2)_2$–H_2O binary system are respectively 12.20 mass % and 1.089 g cm^{-3} at 273 K. This result was found by Alisoğlu and Necefoğlu.[9] Furthermore, it has been found that the solubility is 12.48 mass % and the density is 1.086 g cm^{-3} at 298 K. It is apparently seen that the solubility and the densities of $Mn(H_2PO_2)_2$–H_2O binary system changed slightly at 273 and 298 K, but when the temperature reached 323.15 K, the solubility and the densities decreased to 11.14 mass % and 1.067 g cm^{-3}, respectively.

It has been seen in the literature that $MnCl_2$–H_2O binary system has 43.60 mass % solubility and 1.491 g cm^{-3} density at 298 K, and 49.40 mass % sol-

ubility at 323 K. When it is compared with the data obtained from this study and the literature cited above, it can be concluded that the solubility of $MnCl_2$–H_2O binary system is in the range 43.60 to 49.54 mass %. Moreover, the density of the system increased from 1.491 to 1.568 g cm^{-3} in parallel with the increase of the temperature.

Finally, it has been observed that solubility of NaCl–H_2O binary system at 273, 298 and 323 K is respectively 26.25, 26.42 and 26.84 mass %, and the density is 1.201, 1.199 and 1.191 g m^{-3}, respectively, again.

$Mn(H_2PO_2)_2$ is obtained by a displacement reaction of $MnCl_2$ with NaH_2PO_2 in order to produce $Mn(H_2PO_2)_2$ and NaCl. The salts can be separated from each other as a result of their solubility differences by creating Na^+, Mn^{2+}/Cl^-, $(H_2PO_2)^-//H_2O$ reciprocal quaternary system. In this study, a method has been proposed for purification of $Mn(H_2PO_2)_2$ by separating it from the solution medium by using phase equilibrium method, which enables the synthesis of $Mn(H_2PO_2)_2$ more economically and easily than the synthesis method used in the traditional laboratory.

In the study with the same quaternary system at 298 K, it is seen that the crystallizing area of $Mn(H_2PO_2)_2$ covers 82.9 % of the total area. A method can be proposed to separate these salts using temperature and phase changes with the joint evaluation from literature and this study. Especially, the separation of $Mn(H_2PO_2)_2$ which has the highest crystallization area, is an important result since it is more economical than the traditional method. According to this, it has been concluded that $Mn(H_2PO_2)_2$ can be separated via temperature change.

Therefore, this study suggests an economic method for the separation of $Mn(H_2PO_2)_2$ which solves the least (2.77 %) and covers the most crystallizing area (80.75 %) in the solution including three salts mentioned.

Acknowledgment. The authors would like to thank the referees for their valuable comments, which helped to improve the manuscript.

ИЗВОД

РАВНОТЕЖА ФАЗА ЧВРСТО–ТЕЧНО У H_2O–$Mn(H_2PO_2)_2$–$MnCl_2$–NaCl, H_2O–$Mn(H_2PO_2)_2$–$MnCl_2$ и H_2O–NaCl–$MnCl_2$ СИСТЕМИМА НА 323,15 K

VEDAT ADIGUZEL

Department of Chemical Engineering, Kafkas University, Kars 36100, Turkey

Равнотежа фаза чврсто–течно и густине у кватернарном систему H_2O–NaCl–$MnCl_2$–$Mn(H_2PO_2)_2$, као и у тернарним системима H_2O–NaCl–$MnCl_2$ и H_2O–$MnCl_2$–$Mn(H_2PO_2)_2$, испитане су применом методе мерења засићења раствора при изотермским условимана на 323,15 K. Анализом течне и чврсте фазе утврђен је састав чврсте фазе коришћењем Schreinemaker графичке методе. Тернарни системи садрже једну инваријатну тачку, две криве растворљивости и два поља кристализације. У кватернарном систему постоји једна инваријантна тачка, три криве растворљивости и три поља кристализације која одговарају чврстим фазама NaCl, $MnCl_2{\cdot}4H_2O$ и $Mn(H_2PO_2)_2{\cdot}H_2O$.

Поље кристализације $Mn(H_2PO_2)_2 \cdot H_2O$, као највеће у поређењу са областима кристализације осталих чврстих фаза, заузима 80,75 % укупне површи кристализације.

(Примљено 21. маја, ревидирано 25. августа, прихваћено 5. септембра 2020)

REFERENCES

1. W. Wu, S. Lv, X. Liu, H. Qu, H. Zhang, J. Xu, *J. Therm. Anal. Calorim.* **118** (2014) 1569 (https://doi.org/10.1007/s10973-014-4085-8)
2. W. Yang, W. J. Yang, B. Tawiah, Y. Zhang, L. L. Wang, S. E. Zhu, T. B. Y. Chen, A. C. Y. Yuen, B. Yu, Y. F. Liu, *Compos. Sci. Technol.* **164** (2018) 44 (https://doi.org/10.1016/j.compscitech.2018.05.023)
3. G. A. Bhat, P. Vishnoi, S. K. Gupta, R. Murugavel, *Inorg. Chem. Commun.* **59** (2015) 84 (https://doi.org/10.1016/j.inoche.2015.07.006)
4. P. Noisong, C. Danvirutai, *Spectrochim. Acta, A* **77** (2010) 890 (https://doi.org/10.1016/j.saa.2010.08.028)
5. P. Noisong, C. Danvirutai, T. Srithanratana, B. Boonchom, *Solid State Sci.***1 0** (2008) 1598 (https://doi.org/10.1016/j.solidstatesciences.2008.02.020)
6. A. Suekkhayad, P. Noisong, C. Danvirutai, *J. Therm. Anal. Calorim.* **129** (2017) 123 (https://doi.org/10.1007/s10973-017-6156-0)
7. Y. Zeng, J. Yi, H. Wang, G. Zhou, S. Liu, *J. Mol. Struct.THEOCHEM* **724** (2005) 81 (https://doi.org/10.1016/j.theochem.2005.03.014)
8. V. Alisoğlu, *C.R. Chim.* **5** (2002) 547 (https://doi.org/10.1016/S1631-0748(02)01411-X)
9. V. Alisoglu, H. Necefoglu,*C.R. Acad. Sci., Ser. IIb: Mec., Phys., Chim., Astron.* **324** (1997) 139 (https://doi.org/10.1016/S1251-8069(99)80017-7)
10. V. Alisoğlu, *C.R. Chim.* **8** (2005) 1684 (https://doi.org/10.1016/j.crci.2004.11.041)
11. V. Alisoglu, *C.R. Acad. Sci., Ser. IIc: Chim.* **1** (1998) 781 (https://doi.org/10.1016/S1251-8069(99)80046-2)
12. V. Alisoglu, V. Adiguzel, *C.R. Chim.* **11** (2008) 938 (https://doi.org/10.1016/j.crci.2007.12.001)
13. H. Erge, V. Adiguzel, V. Alisoglu, *Fluid Phase Equilib.* **344** (2013) 13 (https://doi.org/10.1016/j.fluid.2012.12.033)
14. V. Adiguzel, H. Erge, V. Alisoglu, H. Necefoglu, *J. Chem. Thermodyn.* **75** (2014) 35 (https://doi.org/10.1016/j.jct.2014.04.014)
15. S. Demirci, V. Adıgüzel, Ö. Şahin, *J. Chem. Eng. Data* **61** (2016) 2292 (https://doi.org/10.1021/acs.jced.5b00988)
16. Y. Mastai, *Advances in Crystallization Processes,* InTech, Rijeka, 2012, pp. 400–413 (https://doi.org/10.5772/2672)
17. H. Civelekoğlu, R. Tolun, N. Bulutçu, *İnorganik teknolojiler*, İTÜ Maden Fakültesi Ofset Atölyesi, İstanbul, 1987, pp. 80–103 (http://www.ituyayinlari.com.tr/kitapdetay.asp?KitapID=34&inorganik-Teknolojiler)
18. L. Tan, J. Wang, H. Zhou, L. Wang, P. Wang, X. Bai, *Fluid Phase Equilib.* **388** (2015) 66 (https://doi.org/10.1016/j.fluid.2014.12.047)
19. J. Yin, X. Shi, H. Zhou, J. Tang, Y. Dai, X. Bai, *J. Chem. Eng. Data* **62** (2017) 744 (https://doi.org/10.1021/acs.jced.6b00813)
20. S. Gao, X. Shi, J. Yin, Z. Wan, H. Zhou, G. Li, *Fluid Phase Equilib.* **411** (2016) 7 (https://doi.org/10.1016/j.fluid.2015.11.033)
21. X. Shi, J. Yin, H. Zhou, X. Gu, Y. Dai, J. Tang, *J. Chem. Eng. Data* **62** (2017) 1011 (https://doi.org/10.1021/acs.jced.6b00828)

22. H. Cao, H. Zhou, X. Bai, R. Ma, L. Tan, J. Wang, *J. Chem. Thermodyn.* **93** (2016) 255 (https://doi.org/10.1016/j.jct.2015.09.006)
23. H. Schott, *J. Chem. Eng. Data* **6** (1961) 324 (https://doi.org/10.1021/je00103a002)
24. J. R. Van Wazer, *Phosphorus and its Compounds*, Interscience Publishers, New York, 1958, pp. 60–62 (https://doi.org/10.1002/ange.19610731513)
25. T. Gündüz, *Kantitatif analiz laboratuvar kitabı*, Gazi Büro Kitabevi, Ankara, 2012, pp. 280–282 (ISBN 9799757313457)
26. D. R. Lide, *CRC handbook of chemistry and physics*, CRC Press, Boca Raton, FL, 2012, pp. 468–469 (https://doi.org/10.1080/08893110902764125)
27. A. R. Kul, H. Erge, İ. Meydan, *Yüzüncü Yıl Üniversitesi Fen Bilim. Enstitüsü Derg.* **19** (2014) 62 (https://dergipark.org.tr/en/download/article-file/204648).

Journal of the Serbian Chemical Society
JSCS-info@shd.org.rs • www.shd.org.rs/JSCS
J. Serb. Chem. Soc. *86* (1) 103–113 (2021)
JSCS–5407
Original scientific paper

The influence of the annealing mode on stress elimination in a foam glass structure

IRINA GRUSHKO*

Platov South-Russian State Polytechnic University (NPI), Novocherkassk 346428 and Don State Technical University, Rostov-on-Don 344000, Russian Federation

(Received 19 December 2019, revised 24 May, accepted 28 May 2020)

Abstract: The purpose of this work was to establish the influence of features of the annealing mode on the value of residual stresses in the structure of porous inorganic materials using foam glass as an example. A single-stage uniform cooling mode at three different speeds was considered. The study was performed using a mathematical model. The algorithm for analyzing the stress–strain state of the foam glass sample consisted in solving a system of equations by the finite element method. The calculation results are presented in graphic form. The graphics show the changes in stress in the foam glass upon cooling at speeds of 100, 10 and 1 °C min^{-1}. The temperature difference and the viscosity values of the foam glass subsurface and central layers in dependency on different temperatures of the cooling onset are presented. It was concluded that it is necessary to carry out the annealing mode of foam glass in three stages: initial, glass transition step and stabilization step, meaning different cooling rates have to be applied in different stages.

Keywords: Strain; slags; cooling; silicates; finite element method; energy efficiency.

INTRODUCTION

Currently, heat-insulating materials based on dense porous structures, which are used as insulation of facades of buildings and structures for civil and industrial purposes, are becoming more popular.[1–5] A similar material with a dense porous structure is foam glass, which is characterized by its high thermal insulation ability, mechanical strength, and chemical resistance.[6–9]

The properties of foam glass depend, for the most part, on the composition of raw materials and the production method.[10,11]

One of the main technological operations that determines the mechanical strength of foam glass is annealing.[12,13] However, upon obtaining foam glass that is optimal in all aspects, poor-quality annealing can lead to a sharp increase

* Correspondence E-mail: grushkois@srspu.ru
https://doi.org/10.2298/JSC191218034G

in defects in the finished product.[14] At this stage, because of the limited thermal conductivity of the material, changes in the environmental temperature of the foam glass leads to a gradual transfer of heat from one layer of the sample to another. This, in turn, leads to a temperature difference between the outer and inner layers, which cause inner stresses. Those stresses affect the foam glass quality. Thus, it is relevant to study the annealing process and identify patterns of stress formation in foam glass.

Previously,[15] the successful use of mathematical modelling to describe physical and chemical processes at all stages of foam glass production with sufficient accuracy, including at the annealing stage, was established. It seems promising to use the mathematical model proposed by Alekseev and Yashurkaev,[14,16–18] developed based on the relaxation-kinetic theory of glass transition of Mazurin and Lalykina.[19,20] Grushko[21] describes developed software that allows, with minimal time and adequate accuracy, a numerical study of the annealing process to be performed based on the presented mathematical models.

The purpose of this work was to determine the effect of the features of the annealing mode on the value of residual stresses in the structure of porous inorganic materials using foam glass as an example. To achieve this goal, the following objectives have to be solved: identification of the influence of the main parameters of the technological stage of "annealing" (cooling rate and initial annealing rate). Thus, a single-stage uniform cooling mode of foam glass at three speeds was considered: 1 °C min^{-1} (typical cooling rate for glass products), 10 and 100 °C min^{-1} (chosen for a more visual demonstration of the processes that occur during annealing of foam glass) and a study of a nonlinear ("three-stage") annealing mode.

EXPERIMENTAL

The study of the stress-strain state of the foam glass sample during annealing was realized with numerical simulation by solving a system of equations[20] by the finite element method in the ANSYS software package,[22] according to a previously proposed technique[23] that allows relaxation of the material properties to be taken into account:

$$T_{\text{f}\tilde{\imath}} = T - \int_0^t \exp\left[-\int_{t'}^{t} \frac{\mathrm{d}t''}{\tau_i\left(t''\right)}\right] \frac{\mathrm{d}T\left(t'\right)}{\mathrm{d}t'} \mathrm{d}t' \tag{1}$$

$$T_{\text{f}\tilde{\imath}} = \sum_{i=1}^{n} g_{i\tau} T_{\text{f}\tilde{\imath}}, \text{ where } \sum_{i=1}^{n} g_{i\tau} = 1 \tag{2}$$

$$\lg \tau_i = \left(A + \frac{B}{T_{\text{fp}} - T_0} - \lg K_i\right) \frac{T_{\text{f}\tau}}{T} - \lg \tau_0 \left(\frac{T_{\text{f}\tau}}{T} - 1\right) \tag{3}$$

$$T_{\text{fp}} = \sum_{i=1}^{n} g_{iP} T_{\text{f}\tilde{\imath}}, \text{ where } \sum_{i=1}^{n} g_{iP} = 1 \tag{4}$$

$$P = P_i\left(T_{\mathrm{fp}}\right) + \int_{T_{\mathrm{fP}}}^{T} \left(\frac{\partial P}{\partial T'}\right)_{T_{\mathrm{fP}}} \mathrm{d}T' \tag{5}$$

where T is the temperature, T_f is the structural temperature, t is the time, τ is the relaxation time, g_i are the weight coefficients, n is the number of internal parameters characterizing the structure of the substance, A, B and T_0 are the constants in the Fulcher–Tamman equation; P is property; P_i is the property of a substance in an equilibrium (liquid) state; $K_i = \eta/\tau_i$, here η is the viscosity.

Mathematical modelling of the heat transfer process in the studied object is based on the numerical solution of the initial-boundary-value problem:

$$\rho c = \frac{\partial T}{\partial \tau} = \frac{\partial}{\partial x}\left(\lambda_x \frac{\partial T(x,y,z,\tau)}{\partial x}\right) + \frac{\partial}{\partial y}\left(\lambda_y \frac{\partial T(x,y,z,\tau)}{\partial y}\right) + \frac{\partial}{\partial z}\left(\lambda_z \frac{\partial T(x,y,z,\tau)}{\partial z}\right) \tag{6}$$

where $T(x, y, z, \tau)$ is the desired temperature distribution function; λ_x, λ_y, λ_z are the thermal conductivity coefficients in the direction of the x, y, z axes; ρ is the density; c is the specific heat of the medium.

The stationary heat equation for an isotropic medium has the form:

$$\mathrm{div}\left(\lambda \,\mathrm{grad}\, T\right) = 0 \tag{7}$$

where T is the desired temperature distribution function; λ is the coefficient of thermal conductivity.

It should be noted that the results of calculating the thermal state are the basis for solving the strength problem.

In this regard, determination of stresses is realized for a system of equations with the following form:[24]

$$\sigma_{ik} = 2G\left[\varepsilon_{ik} + \frac{\mu}{1+\mu}\frac{S}{2G}\delta_{ik} - \alpha T \delta_{ik}\right] \tag{8}$$

$$\varepsilon_{ik} = \varepsilon_{ki} = \frac{1}{2}\left(\frac{\partial U_k}{\partial x_i} + \frac{\partial U_i}{\partial x_k}\right),\ i, k=1,2,3 \tag{9}$$

$$\sum \frac{\partial \sigma_{ki}}{\partial x_k} = 0 \tag{10}$$

where σ_{ik} are stresses (σ_{ii} are normal stresses, σ_{ik} ($i \neq k$) are shear stresses; ε_{ik} are distortions; U_i is displacement; $S = \sum \sigma_{ii}$ is the sum of the normal stresses, T is the medium temperature, G is the shear modulus, $2G = E / (1+\mu)$, E is Young's modulus, μ – Poisson's ratio; α – coefficient of thermal expansion and

$$\delta_{ik} = \begin{cases} 1, i = k \\ 0, i \neq k \end{cases} \text{ – Kronecker symbol.}$$

The main steps in solving this problem are setting the source data (including the implementation of the solid-state model) and solving and processing the results.

The object of study (Fig. 1) is a sample of foam glass with dimensions of 30×30×30 mm^3, placed on a stand with dimensions of 100×100×3 mm^3, created by powder technology.[25]

The raw materials were ground in a ball mill with a volume of 5 L to the point of completely passing through a sieve No. 0315, and the batch mixture specific surface area value

was 552 $m^2 g^{-1}$. The batch mixture composition, in mass %: ash and slag waste, 30; crushed glass, 70; borax, 5; anthracite, 5; this composition is 5 over 100 % of the basic components. The estimated chemical composition of the foam glass is given in Table I.

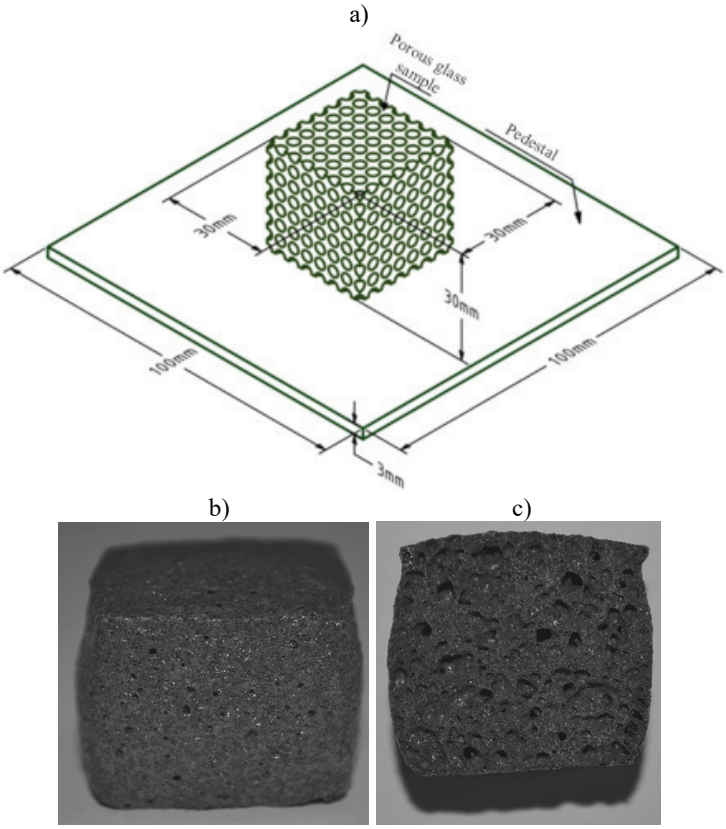

Fig. 1. Object of the study: a) object model view; b) object real view; c) object, longitudinal section.

TABLE I. Composition of the synthesized foam glass

Oxide	Content, mass %	Oxide	Content, mass %
SiO_2	67.33	CaO	7.78
Al_2O_3	6.88	K_2O	1.05
Fe_2O_3	3.73	MgO	0.77
Na_2O	10.71	TiO_2	0.07
P_2O_5	–	SO_3	1.68
PPP	–	Σ	100.00

During heating the ground glass matrix and porous agent batch mixture to 825 °C, the gases formed as a result of oxidation or dissociation of the porous agent, the softened glass mass swelled. The sample was foamed and annealed in a muffle furnace with electrical

heaters at a preset temperature–time mode.[26] The preset temperature–time mode was as follows: prepared samples were loaded into a cold oven and then heated at 16 °C min^{-1} to 500 °C, the temperature for complete combustion of the contained volatile substances. This temperature was maintained for 20 min to ensure an even warming-up of the sample, which has a positive effect on the further process of foaming. Then the temperature was further increased to 825 °C, the foaming temperature, and maintained for 20 min. Subsequently, the glass was rapidly cooled to 600 °C to fix the structure of the material. Finally, the sample was cooled to 25 °C at a rate of 2.8 °C min^{-1}.

The physical properties of the obtained foam glass sample were determined by building its solid-state model (the visual inspection method was used (Fig. 1) using a ShTs-150 calliper): sample geometry, location and pore size (usually uniformly distributed pore arrangement having an average diameter of 3 mm with a constant gas composition). The construction of a solid model of the foam glass sample was performed using the CAD system software package ANSYS "Space Claim".

Next, the following physical properties of the obtained sample were determined: thermal conductivity, heat capacity, radiation characteristics, sample geometry, mass, density, Young's modulus, and Poisson's ratio.

The calculations used the real thermophysical and radiative properties of carbon dioxide, the foam glass matrix and the steel standard 2Kh18N9T.[27-30]

The values of the thermal conductivity of carbon dioxide at the upper and lower boundary curves, at the critical point and on isobars from 30 to 200 kg cm^{-2} to a temperature of 1000 °C are presented as a function of temperature. For the gas emission process, the ambient temperature and the emissivity of the body were set.

According to the theory of the radiation heat transfer between a radiating and absorbing gas and the surrounding enclosed grey clad, the required emissivity coefficient of the radiative components is given by:

$$\varepsilon_{CO_2} = f\left(\rho_{CO_2}, l, T_g\right) \tag{11}$$

where ρ_{CO_2} is the partial pressure of the gas mixture and T_g is the temperature of the gas mixture.

For a spherical pore with diameter D = 3 mm, the effective thickness of the gas radiating layer is l = 1.8 mm:

$$l = 0.6D \tag{12}$$

The intensity of gas emission inside the pores of the foam glass decreased in proportion to a decrease in the temperature of the inorganic frame of the foam glass. At the end of the foam glass manufacturing process (at the end of the last production stage), the gas pressure inside the pores was approximately equal to atmospheric pressure. Upon further cooling through the annealing process, the gas pressure decreased by the required amount in certain cells, so that the completely annealed glass exhibited a substantial pressure drop of 33.8 kPa in the cells.[31] Then, the required emissivity coefficient within the temperature decrease range was 0.01 on average. To estimate the contribution of the radiative compound to the overall temperature distribution, it was assumed that the emissivity coefficient was equal for both the working batch and initial foam glass (ε_{gl} = 0.94).[29]

The radiation from the surface of the stand was set in a similar way with its values of the degree of blackness. At the same time, in the block for setting the properties of radiation heat transfer (the variable "Correlations"), the value "Emissions to the environment" was set ("To ambient").

The thermal conductivity and specific thermal capacity of the foam glass matrix were determined by the laser burst method[32] within the temperature range of 25–700 °C using the thermal conductivity measuring system TC-9000H (ULVAC, Japan) at the Common Use Center "Technologies and Materials of National Research University BelSU," Belgorod, Russia.

TABLE II. Results of the determined thermal conductivity and specific heat of the foam glass

t / °C	T / K	A / cm^2 s^{-1}	C_p / J g^{-1} K^{-1}	k / W cm^{-1} K^{-1}
31.1	304.1	0.00592	0.87296	0.00757
101.1	374.1	0.00567	0.85875	0.00714
200.1	473.1	0.00538	0.93964	0.0074
300.4	573.4	0.00528	1.18179	0.00913
399.7	672.7	0.0052	1.20185	0.00914
499.3	772.3	0.00553	1.19574	0.00968
599.3	872.3	0.00572	1.37081	0.01149
699.4	972.4	0.00517	1.62584	0.0123

The value of thermal conductivity λ was calculated by the formula:

$$\lambda = \alpha C_p \rho_k \tag{13}$$

where ρ_k = 146 kg m^{-3} is the sample density.

The density of the sample was calculated by the formula EN 1602:1996 "Thermal insulating products for building applications – Determination of apparent density":

$$\rho_k = \frac{m}{V} \tag{14}$$

where m is the mass of material, kg; V is the volume of the material, including pores and voids, m^3, and ρ_k = 146 kg m^{-3}.

To determine Young's modulus, tests of foam glass samples were carried out according to the procedure presented in EN 13167:2012 "Thermal insulation for building – Factory made cellular glass (CG) products – Specification" was applied. The essence was to measure the value of the compressive forces necessary to destroy the sample under appropriate test conditions.

Cubic samples with sizes of 30×30×30 mm^3 were mounted in a hydraulic press so that the compressive force was directed along the vertical axis of the sample. Additionally, one 250 UW strain gauge with a vertical axis (longitudinal strain gauge) and one gauge with a horizontal axis (transverse strain gauge) were glued on the sides of the cross-section of the foam glass sample, each of which was connected *via* a half-bridge circuit to a separate channel of the UTS-1 strain gauge station. The process of loading the sample had an initial load of 500 N in increments of 250 N until the visual destruction of the sample. In addition, by sequentially switching the corresponding channels of the strain gauge station, the readings of each of the strain gauges were taken.

The sample pressure, σ, Pa, is determined by the formula:

$$\sigma = \frac{P}{lb} \tag{15}$$

where P is the applied load, N; l is the sample length, m, and b is the sample width, m.

The relative longitudinal strain, ε_{long}, was determined by the formula:

$$\varepsilon_{\text{long}} = \frac{\Delta l}{l_0} \tag{16}$$

where Δl is the defined elongation and l_0 is the initial sample length.

The relative transverse strain, $\varepsilon_{\text{transv}}$, was determined by the formula:

$$\varepsilon_{\text{transv}} = \frac{\Delta d}{d_0} \tag{17}$$

where Δd is the transverse sample size and d_0 is the initial sample size.

When the force reached 2250 N, the pressure on the sample created a stress exceeding the shear stress, and the material entered the stage of plastic deformation. At a moment corresponding to a force of 2500 N, destruction of the material occurred.

In accordance with Hooke's Law, the elastic modulus of the sample material was determined:

$$E = \frac{\sigma}{\varepsilon} \tag{18}$$

therefore, σ = 2.6 MPa, ε = 0.002070 and E = 1256 MPa.

According to the results of tensometric measurements, the dependence of the transverse strain on the longitudinal strain under compression was obtained.

The experimental results were approximated by a straight line using the least squares method. The result of the standard error was 1.07×10^{-8}.

The determined value of the Poisson's ratio was:

$$\mu = \frac{\varepsilon_{\text{transv}}}{\varepsilon_{\text{long}}} = \frac{0.0004554}{0.002070} = 0.22 \tag{19}$$

where μ is the Poisson's ratio, $\varepsilon_{\text{transv}}$ = 0.0004554 is the lateral relative deformation and $\varepsilon_{\text{long}}$ = = 0.002070 is the longitudinal relative deformation.

The obtained values of the physical properties of the matrix material of the foam glass sample using the module "Engineering Data" with the additional shell interface "Workbench" used descriptions of the properties of materials, and input parameters of the mathematical models are listed in the created mathematical model.

To solve unsteady heat conduction problems, a transient thermal module with the following boundary conditions was used.

The boundary conditions were specified in the form of temperature $T = f$(time) on the outer surface of the foam glass sample in the study. The calculation was performed under the assumption that the temperature of the surface of the sample changed according to a given mode (the physical possibility of the claimed mode could be achieved due to the significant convective heat transfer of heat from the foam glass surface, providing a given cooling rate of the sample (the temperature of the gaseous medium around the sample should be much lower than its surface temperature)).

The maximum time step value was determined to be 10 s according to the literature.[33]

RESULTS AND DISCUSSION

The stress changes in the sample during cooling starting from 600 °C at different speeds: a) 100, b) 10 and c) 1 °C min^{-1} are shown in Fig S-1 of the

Supplementary material to this paper. As can be seen from Fig. S-1, the stress increase occurs in two stages.

In the initial period of uniform cooling, there is a rapid increase in the temperature difference between the centre (Fig. S-2 of the Supplementary material) and the surface of the object in question, which leads to an increase in temperature stresses and their subsequent decrease due to an intense relaxation process.[34] In the second stage of annealing, which occurs in the glass transition region (the range of the decimal logarithm of the viscosity of the foam glass is 10–16 Pa·s, Fig. S-3 of the Supplementary material), the stress values increase, the rate of change of which becomes minimal, which leads to the appearance of residual stresses. It should be noted that the available stress effects are inversely proportional to the rate of annealing.

The temperature difference between the subsurface and central layers of a sample depending on various temperatures of cooling onset are shown in Fig. S-2 of the Supplementary material. The cooling rate was set as a constant, and its value was 1.5 °C min^{-1} regardless of the initial annealing temperature.

With uniform cooling, the stresses in the subsurface layers of the foam glass are compression stresses (Fig. S-1), since at the beginning of the annealing process, the temperatures of the subsurface layers were lower than the temperatures of its central layer (Fig. S-2), while the free dimensions of the surface layers decreased to a greater extent than the dimensions of the central layer. However, in the glass transition interval, the free sizes of the inner layers decrease to a greater extent than the free sizes of the outer layers. As a result of these processes, the residual stresses in the subsurface layers are compression stresses, and in the central layers, tensile stresses.

The viscosity values of the subsurface and central layers in dependence on different temperatures of cooling onset are shown in Fig. S-3. The cooling rate is set as a constant, and its value was 1.5 °C min^{-1} regardless of the initial annealing temperature.

The stresses occurring in the foam glass during annealing with different initial temperatures are presented in Figure S-4 of the Supplementary material. Evidently, an increase in the initial annealing temperature (while maintaining a constant rate of the cooling process) practically does not change the value of the residual stresses and retains the shape of the curve.

Thus, the heat treatment of foam glass during the annealing process has a different effect on the formation of its stress–strain state, which allows us to conclude that different values of the rate of temperature change at different stages are necessary. The foam glass annealing mode is nonlinear and it is advisable to divide it into three stages: initial (stage 1), glass transition (stage 2) and stabilization stage (stage 3), and the cooling rates in the first and third stages are much higher than in

the second stage, the temperature range of which is the critical cooling interval.[14,16–18] As a rule, the cooling rates at different stages differ several times.[13]

Consideration of a three-stage annealing mode. The dependence of stress, viscosity and temperature of the subsurface and central layers on time are shown in Figs. S-5–S-7 of the Supplementary material.

In the temperature range of 600 °C, an increase in stresses is formed, associated with the beginning of the glass transition interval, the viscosity of the layers is relatively small, the significant stresses that arise begin to relax initially at a high speed, then gradually reduce it. The cooling rate again increases from a temperature of 460 °C. In this case, the temperature difference between the centre and the surface of the foam glass increases again, however, these changes are significantly slower than after a sharp decrease in speed. Moreover, the total value of the effect in this case is more significant than in the case of a decrease in the cooling rate, as a consequence of 3–4 orders of magnitude higher viscosity at 460 °C than viscosity at 600 °C, so stress relaxation is practically absent. Thus, stress relaxation in the second cooling stage affects residual stresses favourably.

CONCLUSIONS

Analysis of the information presented allows the following conclusions to be drawn:

1) with uniform cooling, the growth of stresses is occurs in two stages, the value of which is proportional to the rate of annealing: the first stage is determined by temperature stresses and their subsequent decreases due to the intense relaxation process; the second stage corresponds to the glass transition area (the range when the decimal logarithm of the viscosity of the foam glass is 10–16 Pa s), where there is a new increase in stresses, the rate of change of which becomes minimal, and then leads to the appearance of residual stresses;

2) the residual stresses in the subsurface layers are compression stresses, and in the central layers tensile stresses, due to the fact that at the beginning of annealing, the temperature of the subsurface layers was lower than that of its central layer, while the free dimensions of the surface layers decrease to a greater extent than the dimensions of the central layer, but then, in the glass transition interval, the free sizes of the inner layers decrease to a greater extent than the free sizes of the outer layers;

3) the heat treatment of foam glass during the annealing process has a different effect on the formation of its stress–strain state, which allows us to conclude that different values of the rate of temperature change at different stages are necessary. It is advisable to divide the foam glass annealing mode into three stages: initial (step 1), glass transition (step 2) and stabilization step (step 3);

4) stress relaxation at the glass transition stage favourably affects the residual stresses because the viscosity values at a temperature of 460 °C are 3–4

orders of magnitude higher than the corresponding values at a temperature of 600 °C and stress relaxation is practically absent.

SUPPLEMENTARY MATERIAL

Additional data are available electronically at the pages of journal website: https://www.shd-pub.org.rs/index.php/JSCS/index, or from the corresponding author on request.

ИЗВОД

УТИЦАЈ РЕЖИМА ОДГРЕВАЊА НА УКЛАЊАЊЕ НАПРЕЗАЊА У ПЕНАСТОМ СТАКЛУ

IRINA GRUSHKO

Platov South-Russian State Polytechnic University (NPI), Novocherkassk 346428 и Don State Technical University, Rostov-on-Don 344000, Russian Federation

Циљ овог рада је дефинисање утицаја начина одгревања на заостала напрезања у структури порозних неорганских материјала, на примеру пенастог стакла. Разматран је утицај три брзине током једностепеног униформног режима хлађења. Коришћењем математичког модела који је добијен методом коначних елемената анализирана су настала напрезања у стаклу. Графички су приказане зависности напрезања од времена при брзинама хлађења 100, 10 и 1 °C min^{-1}. Приказане су разлике температуре и вискозности потповршинског и централног слоја од времена, за различите почетне температуре одгревања. Закључено је да режим одгревања мора да се изводи у три корака различитих брзина: почетни, прелазни и стабилизациони.

(Примљено 19. децембра 2019, ревидирано 24. маја, прихваћено 28. маја 2020)

REFERENCES

1. K. S. Ivanov, *Mag. Civ. Eng.* **5** (2019) 52 (https://dx.doi.org/10.18720/MCE.89.5)
2. Y. V. Selivanov, A. D. Shiltsina, V. M. Selivanov, Y. V. Loginova, N. N. Korolkova, *Mag. Civ. Eng.* **3** (2012) 35 (https://dx.doi.org/10.5862/MCE.29.4)
3. B. S. Semukhin, O. V. Kazmina, A. Y. Volkova, V. I. Suslyayev, *Rus. Phys. J.* **12** (2017) 2130 (https://dx.doi.org/10.1007/s11182-017-1024-8)
4. L. Lakov, B. Jivov, M. Aleksandrova, Y. Ivanova, K. Toncheva, *J. Chem. Tech. Met.* **6** (2018) 1081 (https://dl.uctm.edu/journal/node/j2018-6/8_17-204_p_1081-1086.pdf)
5. S. Schiavoni, F. D'Alessandro, F. Bianchi, F. Asdrubali, *Renew. Sust. Energy Rev.* **62** (2016) 988 (https://dx.doi.org/10.1016/j.rser.2016.05.045)
6. J. Zach, M. Sedlmajer, J. Bubenik, M. Drdlova, *IOP Conf. Ser.: Mater. Sci. Eng.* **583** (2019) 012016 (https://dx.doi.org/10.1088/1757-899X/583/1/012016)
7. Z. Qin, G. Li, Y. Tian, Y. Ma, P. Shen, *Mater.* **12** (2018) 54 (https://dx.doi.org/10.3390/ma12010054)
8. C. Xi, F. Zheng, J. Xu, W. Yang, Y. Peng, Y. Li, P. Li, Q. Zhen, S. Bashir, J.L. Liu, *Constr. Build. Mater.* **190** (2018) 896 (https://dx.doi.org/10.1016/j.conbuildmat.2018.09.170)
9. O. V. Puchka, V. S. Lesovik, N. I. Minko, S. S. Vaysera, M. A. Frolova, *Res. J. Appl. Sci.* **10** (2014) 674 (https://medwelljournals.com/abstract/?doi=rjasci.2014.674.679)
10. O. V. Kazmina, S. N. Volland, M. A. Dushkina, *IOP Conf. Ser.: Mater. Sci. Eng.* **64** (2014) 012015 (https://dx.doi.org/10.1088/1757-899X/64/1/012015)
11. R. R. Petersen, J. König, Y. Yue, *J. Non-Cryst. Solids* **425** (2015) 74 (https://dx.doi.org/10.1016/j.jnoncrysol.2015.05.030)
12. I. I. Kitajgorodskiy, *Penosteklo*, Strojizdat, Moscow, 1958
13. B. K. Demidovich, *Penosteklo*, Nauka i Technika, Minsk, 1975

14. A. I. Shutov, L. I. Yashurkaeva, S. V. Alekseev, T. V. Yashurkaev, *Glass Ceram*. **64** (2007) 397 (https://dx.doi.org/10.1007/s10717-007-0099-z)
15. I. S. Grushko, *Glass Ceram*. **73** (2017) 355 (https://dx.doi.org/10.1007/s10717-017-9888-1)
16. A. I. Shutov, S. V. Alekseev, T. V. Yashurkaev, *Glass Ceram*. **63** (2006) 213 (https://dx.doi.org/10.1007/s10717-006-0082-0)
17. A. I. Shutov, L. I. Yashurkaeva, S. V. Alekseev, T. V. Yashurkaev, *Glass Ceram*. **64** (2007) 297 (https://dx.doi.org/10.1007/s10717-007-0074-8)
18. A. I. Shutov, S. V. Alekseev, T. V. Yashurkaev, *Tech. Technol. Silic*. **13** (2006) 14 (https://elibrary.ru/item.asp?id=12909525)
19. O. V. Mazurin, *Steklovanije & Stabilizacija Neorganicheskih Stekol*, Nauka, Leningrad, 1978
20. O. V. Mazurin, *Steklovanije*, Nauka, Leningrad, 1986
21. I. S. Grushko, *Izv. Vish. Uch. Zav. Sev.-Kav. Reg. Ser.: Tech. Sci.* **2** (2018) 90 (https://dx.doi.org/10.17213/0321-2653-2018-2-90-95)
22. N. N. Fedorova, S. A., Valger, M. N. Danilov, Yu. V. Zaharova, *Osnovi raboti v Ansys 17*, DMK Press, Moscow, 2017
23. O. Yu. Smetannikov, N. A. Trufanov, *Vich. Mech. Splosh. Sred*. **1** (2008) 92.
24. E. Melan, G. Parkus, *Termouprugie naprjazhenija, vizvannie stacionarnimi temperaturnimi poljami*, Fizatgiz, Moscow, 1958
25. I. Grushko, in *13th International Scientific-Technical Conference on Dynamic of Technical Systems*, 2017, Rostov-on-Don, Russia, *XIII International Scientific-Technical Conference "Dynamic of Technical Systems" (DTS-2017)*, MATEC Web Conf., EDP Sciences, Les Ulis, France, 2017, Abstract No. 03006 (https://dx.doi.org/10.1051/matecconf/201713203006)
26. I. S. Grushko, *IOP Conf. Ser.: Mater. Sci. Eng.* **389** (2018) 012001 (https://dx.doi.org/10.1088/1757-899X/389/1/012001)
27. GSSSD 101-86: *Diocsid ugleroda. Koefficienti vjazkosti, teploprovodnosti i chislo Prandtlja razrezhennogo gaza v diapazone temperatur 150–2000 K / Tablici spravochnih dannih*, 1986
28. N. V. Cederberg, *Teploprovodnost gazov i zhidkostej*, Gosenergoizdat, Moscow, 1963
29. L. N. Latyev, V. A. Petrov, V. Ya. Chehovskij, E. N. Shestakov, *Izluchatelnije svojstva tverdih materialov: spravochnik*, Energija, Moscow, 1974
30. A. Minsar, *Teploprovodnost tverdih tel, zhidkostej, gazov i ih kompozicij*, Mir, Moscow, 1968
31. F. Shill, *Penosteklo*, Izdatelstvo literaturi po stroitelstvu, Moscow, 1965
32. V. G. Baranov, A. V. Tenishev, A. V. Lunev, S. A. Pokrovskij, A. V. Hlunov, *Jad. Fiz. Inzhin.* **4** (2011) 291
33. O. V. Mazurin, Yu. K. Starcev, R. Ya. Hodakovskaja, *Relaksacionnaja teorija otzhiga stekla i raschet na ee osnove rezhimov otzhiga*. Uchebnoe posobie. MHTI named by D.I. Mendeleev, Moscow, 1987
34. O. V. Mazurin, Yu. L. Belousov, *Otzhig I Zakalka Stekla*, MISI&BTISM, Moscow, 1984.

Journal of the Serbian Chemical Society
JSCS-info@shd.org.rs • www.shd.org.rs/JSCS
J. Serb. Chem. Soc. 86 (1) S15–S18 (2021)
Supplementary material

SUPPLEMENTARY MATERIAL TO

The influence of the annealing mode on stress elimination in a foam glass structure

IRINA GRUSHKO*

Platov South-Russian State Polytechnic University (NPI), Novocherkassk 346428 and Don State Technical University, Rostov-on-Don 344000, Russian Federation

J. Serb. Chem. Soc. 86 (1) (2021) 103–113

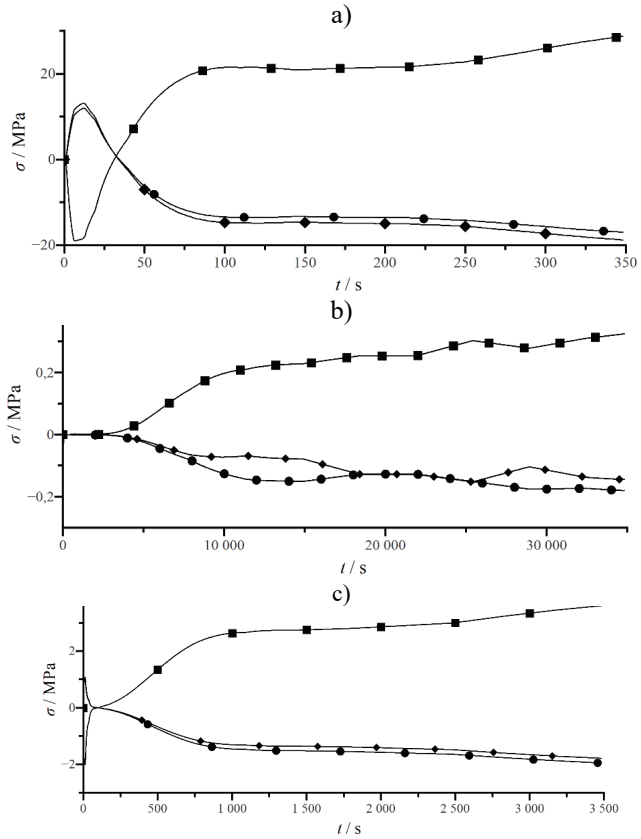

Fig. S-1. Stresses during cooling of foam glass at different rates: a) 100 ºC min^{-1}; b) 10 ºC min^{-1}; c) 1 ºC min^{-1}. Layers: ♦ – upper, ■ – centre, ● – bottom.

* Correspondence E-mail: grushkois@srspu.ru

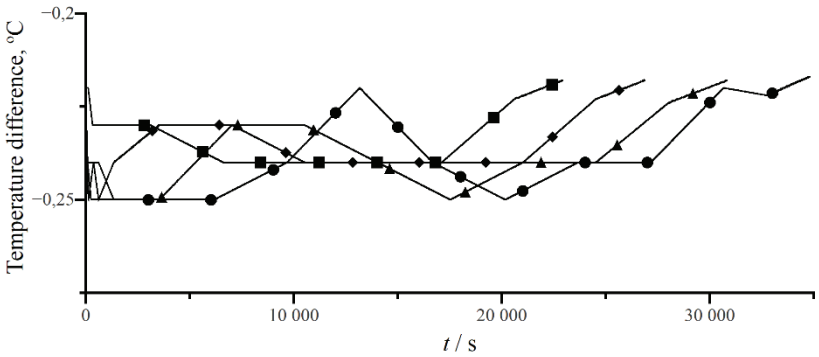

Fig. S-2. The temperature difference of the subsurface layer of the sample depending on various temperatures from the onset of cooling, initial annealing temperature: ■ – 600 °C, ♦ – 700 °C, ▲ – 800 °C, ● – 900 °C.

a)

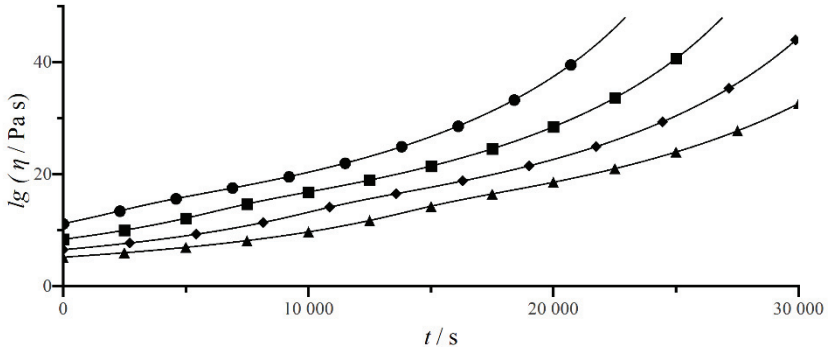

b)

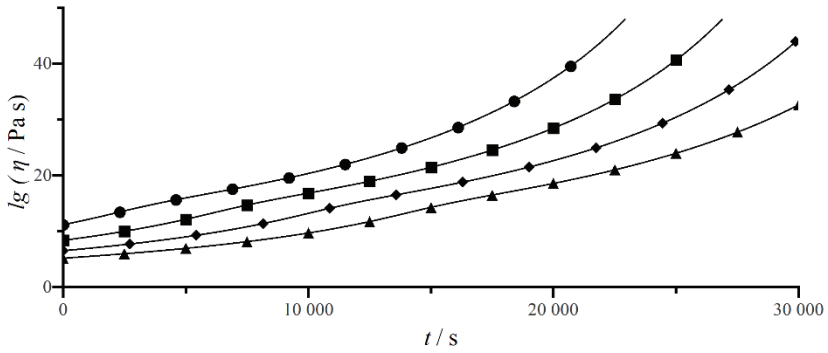

Fig. S-3. The viscosity of the layers in dependence on different temperatures at the beginning of cooling: a) the viscosity of the subsurface layer, initial annealing temperature; b) the viscosity of the Central layer, initial annealing temperature. ● – 600 °C, ■ – 700 °C, ♦ – 800 °C, ▲ – 900 °C.

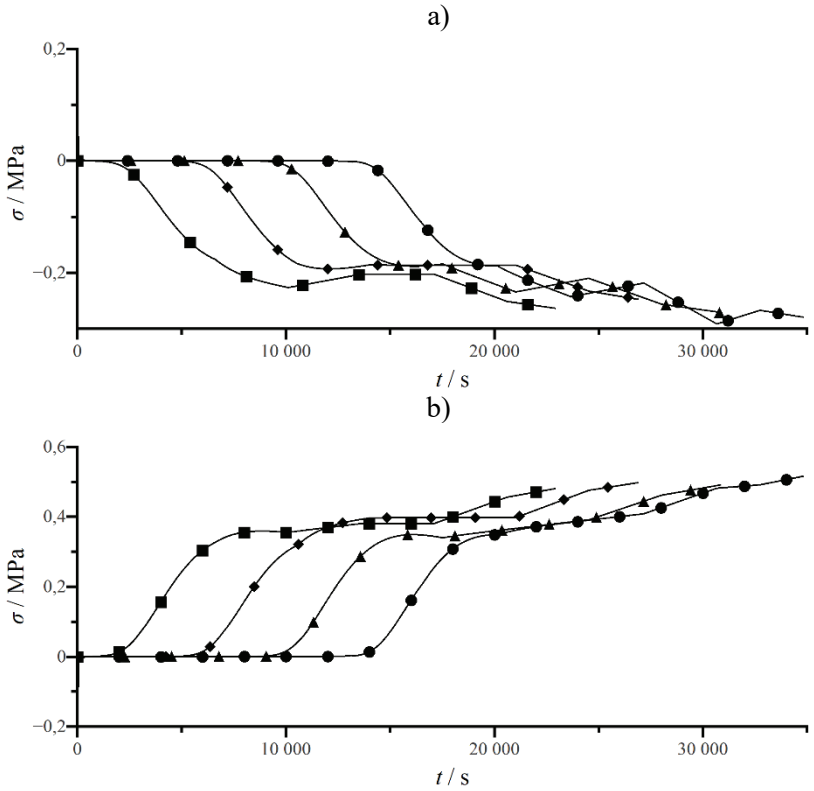

Fig. S-4. Stresses in foam glass during cooling with different initial annealing temperatures: a) surface layer, initial annealing temperature b) the central layer, initial annealing temperature. ■ – 600 °C, ♦ – 700 °C, ▲ – 800 °C, ● – 900 °C.

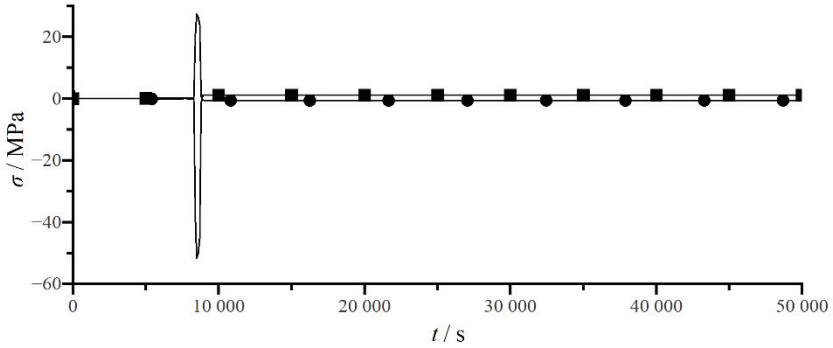

Fig. S-5. Stresses in foam glass, layers: ● – subsurface, ■ – centre.

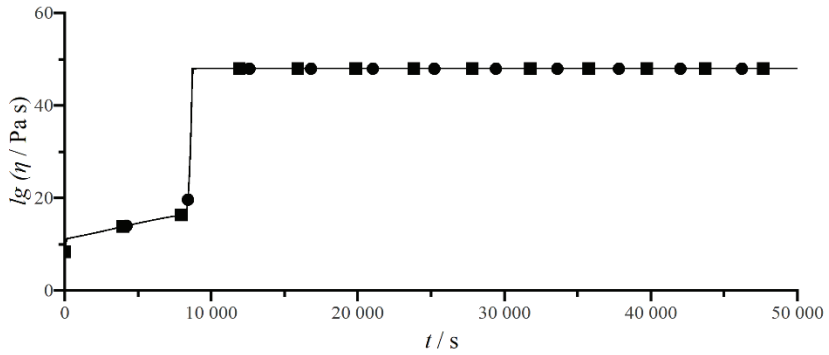

Fig. S-6. The viscosity of the layers of foam glass, layers: ● – subsurface, ■ – centre.

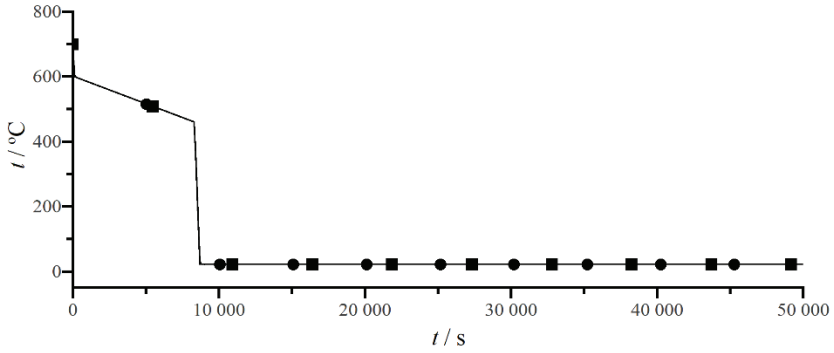

Fig. S-7. The temperature of the layers of foam glass, layers: ● – subsurface, ■ – centre.